INFRARED PHOTOCURRENT SPECTROSCOPY OF DEEP LEVELS IN Mg-DOPED GaN AND $Al_xGa_{1-x}N$

by

Paolo Batoni

A dissertation submitted to the faculty of
The University of North Carolina at Charlotte
in partial fulfillment of the requirements
for the degree of Doctor of Philosophy in
Electrical Engineering

Charlotte

Spring 2009

Approved by:

____
Dr. Edward B. Stokes

____
Dr. Stephen M. Bobbio

____
Dr. Michael A. Fiddy

____
Dr. Vasily Astratov

©2009
Paolo Batoni
ALL RIGHTS RESERVED

ABSTRACT

PAOLO BATONI. Infrared photocurrent spectroscopy of deep levels in Mg-doped GaN and $Al_xGa_{1-x}N$.
(Under the direction of DR. EDWARD B. STOKES)

Recently, there is an increasing demand for III-nitride semiconductor based optoelectronic devices, and especially for ultraviolet (UV) and Deep UV sources and sensors; however, the development and the performance of such devices is fundamentally limited by low carrier concentration, especially in p-type GaN and its alloys with aluminum, p-type $Al_xGa_{1-x}N$. Common acceptors such as magnesium (Mg), which function adequately in GaN, are often too deep in AlGaN alloys to allow significant acceptor ionization at room temperature. Various strategies such as short period superlattices are often incorporated into device architectures in order to enhance carrier levels in p-AlGaN. In this work, IR photocurrent spectroscopy in Mg doped GaN, and Mg-doped $Al_xGa_{1-x}N$ ($0.15 < x < 0.52$) was conducted by means of a YAG-pumped OPO/OPA system tunable from 250 meV to 1.75 eV with the goal of observing and identifying energy levels associated with acceptor atoms of Mg in GaN and $Al_xGa_{1-x}N$. Infrared photocurrent spectra are presented from a variety of GaN and $Al_xGa_{1-x}N$ test structures. Non-zero background response is associated with shallow extrinsic impurities and/or a continuum of shallow levels, photocurrent response peaks observed and associated with deep level donors. No evidence of acceptor ionization associated with Mg in magnesium-doped GaN and $Al_xGa_{1-x}N$ is observed. A number of deep levels are observed in photocurrent spectra, including several 400 meV in GaN and low aluminum alloys, and one around 800 meV in higher aluminum alloys. Thermal analysis of

Mg:GaN photocurrent data is consistent with the deep levels being electron donors. Finally, the effects of IR radiation on the UV optical output of forward biased commercial 365nm UV LEDs is investigated and reported.

DEDICATION

When I ponder upon the factors that have affected my life as a student at the University of North Carolina at Charlotte, my Alma Mater, I consider how lucky I have been for having had such an extraordinary experience. I also think of those who supported and made me strong while walking on my own path to truth, and I then think of Bonnie Cone and the benevolence of the institution she founded, which allows many to achieve their dream of a higher education with scholarships, fellowships, and many opportunities for research.

While traveling from country to country, I have learned that “no man is an island.” I have seen my own world becoming smaller and smaller, and I have pleasurably discovered that I am not an isolated individual, yet an element of a large network. I have hence become aware of the invisible thread that keeps me connected with everyone, even those who are remotely located in this corner of the Universe, where success and failure are never single handed, and where one’s success is also the success of everyone. Thus, I dedicate this work to all of us: far and close, faraway and near, sometimes far in space and yet so indescribably dear.

ACKNOWLEDGMENTS

The work presented in this dissertation was performed under the direction of Dr. Edward B. Stokes at the Infrared Spectroscopy Laboratory and the Center for Optoelectronics and Optical Communications, at the University of North Carolina at Charlotte. I have had the privilege of working under the guidance of Professor Edward B. Stokes since the summer of 2003, when I was a rising undergraduate senior in the Electrical and Computer Engineering Department at the University of North Carolina at Charlotte (UNC Charlotte), and I here acknowledge his significant contribution to both my personal, and professional growth; indeed, his genuine interest in my personal development, sharp insight, and constant support throughout the entire course of my graduate education has made it possible for me to achieve the ultimate level of higher education. Moreover, I would like to acknowledge the assistance of Professor Stephen M. Bobbio for providing direction and advice on specialized research as a graduate student at (UNC Charlotte), the input of Professor Vasily Astratov, and the support of Professor Michael M. Fiddy through the Center for Optoelectronics and Optical Communications.

I would also like to express my gratitude for the technical assistance that I received from Dr. Dean R. Guyer of LaserVision, Dr. Lou Deguzman, Dr. Robert Hudgins, Dr. Oleg Smolski, John Hudak, Bruce Dudley, Alec Martin, and Scott Williams, Faculty Associates at the Center for Optoelectronics Optical Communications, and for the use of the clean room facilities provided by the Charlotte Research Institute. Special thanks go to Dr. Stuart Smith and the Center for Precision Metrology at UNC Charlotte for the assistance I received in obtaining precision measurements of various test structures used in my work. Furthermore, I would like to acknowledge the invaluable assistance that I

have received while working with my colleagues, and special mention goes out to the contributions made by Kinnari Patel, Jennifer Pagan, Casey Burkhart, M. Dave Hodge, Vikram Iyengar, Trushant Shah, and the rest of the Stokes Research Group.

A special thanks goes out to Joe Smart of Crystal IS, Thomas Nohava of Honeywell Labs, ATMI (J. J. Flynn, H. Xian, J. Dion, and G. R. Brandes), Epitex, ATMI, and Technologies and Devices Incorporated Devices (TDI) for providing III-nitride samples and many helpful conversations.

In addition, I am extremely appreciative of the financial assistance received from the Institute of Electrical and Electronics Engineers (IEEE), which entrusted me with the honor of being the recipient of the prestigious Charles LeGeyt Fortescue Scholarship during the academic year 2005-2006, and the Defense Advanced Research Projects Agency (DARPA) for financial support (W911NF-04-1-0319).

Special thanks goes out to Dr. Steven F. LeBoeuf, Dr. Danielle W. Merfeld, Dr. Vinayak Tilak, Dr. Ho-Young Cha, Dr. Xian-An Cao, Peter Sandvik, and the Staff of the Micro and Nano Structures Technology Laboratory, at GE Global Research Center in Niskayuna, NY, for providing me with the opportunity of shadowing highly respected scientists, learning from them, and sharpening my professional skills; Pat Winter, Shirley Joyner, Billie Jo Schweitzer, Dodie Hart, Margaret Williams for their constant support, and their invaluable contribution as administrative assistants; Zoya Volynskaya for her adamantine friendship and love.

Finally, I want give a heartfelt thanks to my own family and all of my loved ones for their moral support and their constant encouragement through my academic and professional endeavors.

INTRODUCTION

Recently, there is an increasing demand for nitride semiconductor based optoelectronic devices, and especially for ultraviolet (UV) and Deep UV sources and sensors. The implementation of such devices would certainly address the needs of the very promising general illumination market, and also enable a proliferation of a new class of solid-state chemical and biological detectors, and optoelectronic components of UV and Deep UV sources to kill bacteria and detect their UV-fluorescent proteins.[1,2,3]

The nitrides of group III elements (III-Nitrides), such as indium nitride (InN), aluminum nitride (AlN), gallium nitride (GaN) and its alloys with aluminum ($Al_xGa_{1-x}N$), typically form crystalline structures with hexagonal symmetry (Wurtzite), and are polar; hence they posses potentially useful properties such as piezoelectricity, piezoresistivity, pyroelectricity, and second harmonic generation.[4,5,6] GaN and $Al_xGa_{1-x}N$ are commonly grown on c-plane sapphire (0001), and this leads to the growth of polar GaN and $Al_xGa_{1-x}N$. Polarization in GaN (and $Al_xGa_{1-x}N$ for that matter) is stable at high temperature; therefore, such compound semiconductors are suitable for high temperature devices such as strain gauges. GaN based, metal-insulator semiconductor (MIS) capacitors have been fabricated and used as high temperature strain gauges by the author, while interning for the MNST laboratory of GE Global Research (Niskayuna, NY).[7] As shown in Figure 1, a MIS capacitor fabricated on a cantilever made of a film of GaN grown on c-plane sapphire is used to measure a change in strain in the material; when a force is applied to the cantilever, piezoelectric charges are generated, and cause an increase in capacitance, which can be measured.

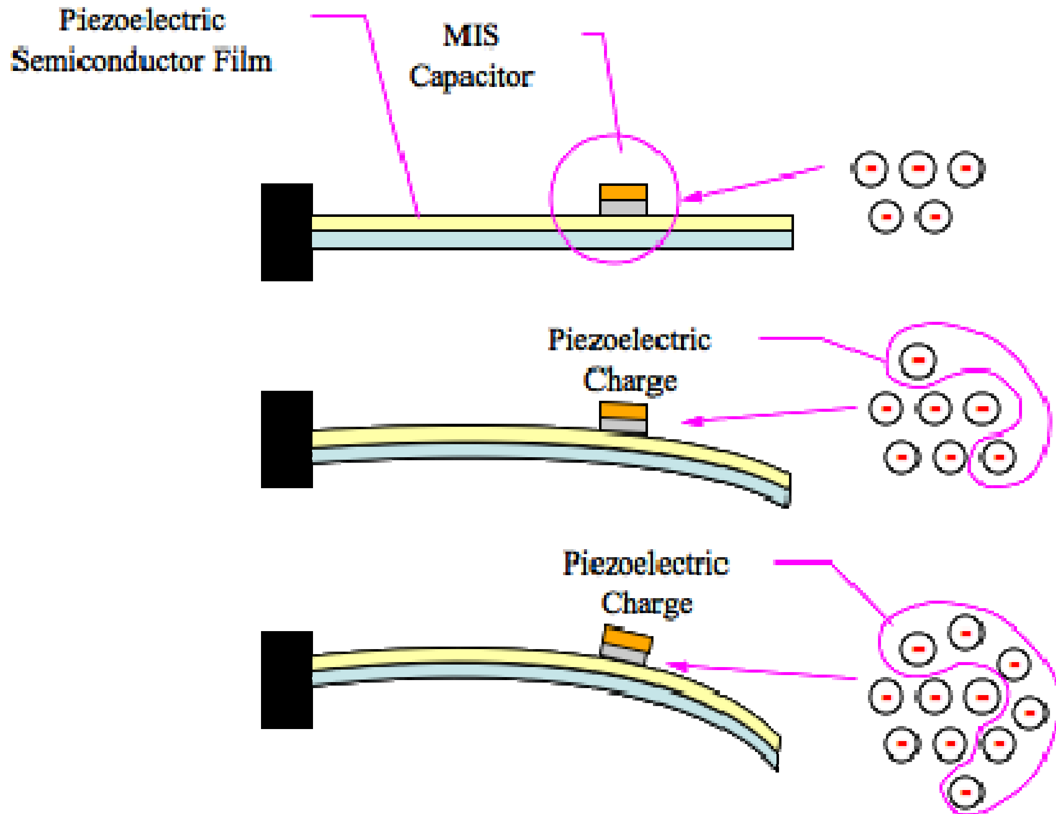

Figure 1: Schematics of a MIS capacitor fabricated on cantilever made of a film of GaN grown on c-plane sapphire.

Non-polar GaN and $Al_xGa_{1-x}N$ are commonly grown with a crystalline orientation parallel to the a-plane $(11\bar{2}0)$, m-plane $(10\bar{1}0)$, or r-plane $(1\bar{1}02)$, and are typically grown on r-plane sapphire. Non polar GaN and $Al_xGa_{1-x}N$ have less intrinsic defects, and hence allow the fabrication of optoelectronic devices with an enhanced optical output, shorter radiative recombination lifetimes, and emissions that are blueshifted with respect to comparable devices made with polar GaN and $Al_xGa_{1-x}N$. Since spontaneous polarization is not an issue in non-polar GaN and $Al_xGa_{1-x}N$, optoelectronic devices made with said compound semiconductors do not suffer from a quantum confined Stark effect.

Due to the large difference in electronegativity between the elements from group III, and the elements from group V, III-Nitrides are characterized by very strong bonds that are responsible for many of the amazing physical properties of this class of compound semiconductors. For instance, the strong chemical bonds of III-Nitrides make the former insoluble in all mineral acids and bases at room temperature and hence resistant to conventional wet etchants.[8] As a direct consequence of the strong chemical bonds of III-Nitrides is the size of their "wide forbidden gap" (wide bandgap), which spans from 1.9 eV to 6.2 eV. As shown in Figure 2 and Figure 3, the class of III-Nitrides is the only class of semiconductors that offers such a tuning potential; in fact, the spectral range of III-Nitrides covers the visible spectrum, and well as the Near UV, UV, and Deep UV regions.

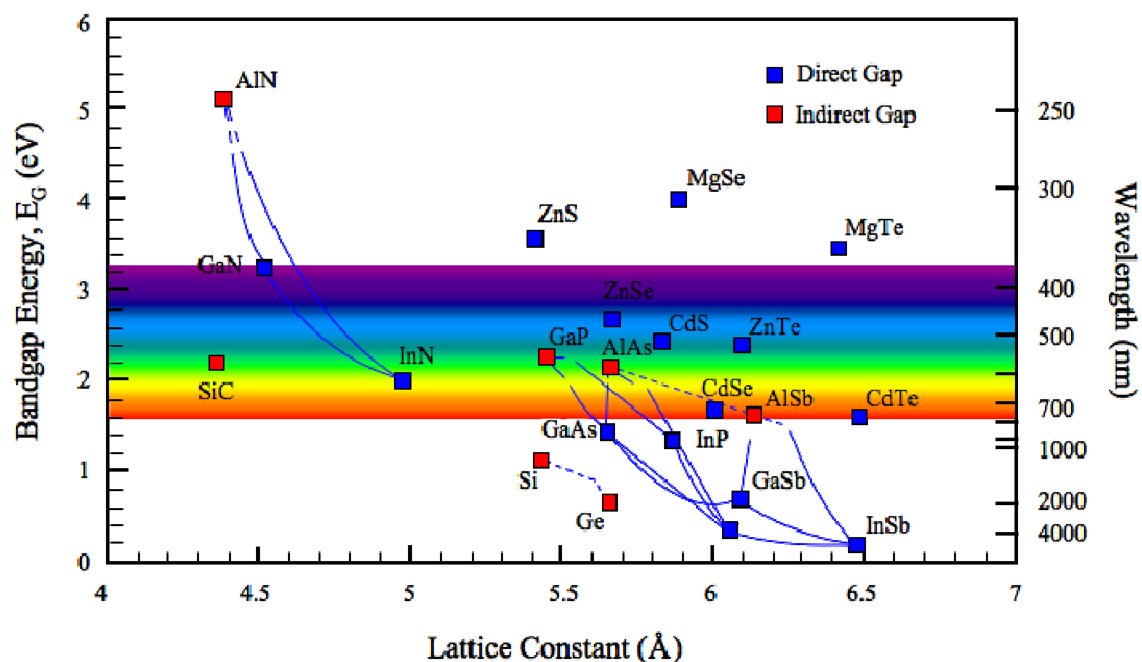

Figure 2: Diagram showing the bandgap values of most cubic semiconductors (elemental and compound) versus their lattice constant at 300 °K. The right-hand scale indicates the spectral range. Adapted from Montanari.[9]

Within the group of III-Nitrides, GaN and $Al_xGa_{1-x}N$ undoubtedly are the most promising wide bandgap semiconductor materials. As shown in Figure 3, GaN and $Al_xGa_{1-x}N$ have a bandgap that can be adjusted continuously between 3.4 eV (356 nm) and 6.2 (eV); therefore, they are suitable for the fabrication of both UV and Deep UV sources and sensors. In addition, they are also candidates for applications including solid-state lighting for general illumination, sources fluorescence microscopy, components of biochemical sensors, and both high power microelectronic and optoelectronic devices operating at high temperature.

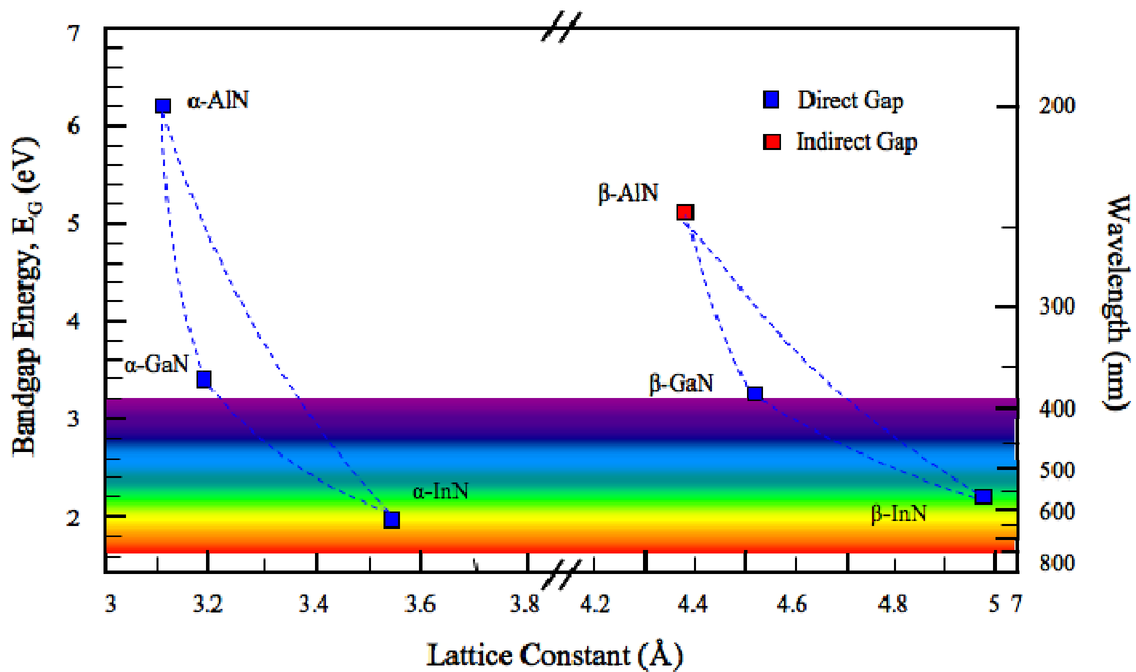

Figure 3: Diagram showing the bandgap values of III-N semiconductors with wurtzite (α), and cubic (β) versus their lattice constant at 300 °K. The right-hand scale indicates the spectral range. Adapted from Montanari.[9]

Several different techniques have been adopted to improve the p-type conductivity in p-type GaN, and p-type $Al_xGa_{1-x}N$: some of these techniques induce a higher concentration of acceptor atoms (typically Mg), or holes, while other techniques aim to

lower the ionization energy of the acceptor atoms. Two of the most popular techniques are 1) Short Period Superlattices (SPSL), and 2) High Temperature Anneal (HTA).

SPSL is a term used to indicate a heterostructure composed by a vertically grown, periodic arrangement of layers of p-type doped GaN, and ad-hoc tailored p-type doped $Al_xGa_{1-x}N$; typically, Mg atoms are used as the substitutional acceptor atoms to achieve p-type doping. A SPSL structure is characterized by a short-period oscillation of the valence band, and acceptor atoms are ionized when the balance band edge is located below the Fermi level. As a result, in a Mg-doped GaN/AlGaN SPSL, holes are accumulated in the region where the band edge is close to the Fermi level; more precisely, the carriers are confined within parallel sheets whose carrier density is much higher than that of a simple bulk film.[124] As proposed by Schubert *et al.*, a SPSL increases the hole concentration by allowing deep acceptors in the layers with the larger bandgap ($Al_xGa_{1-x}N$) to ionize into the valence band of the adjacent material with a lower bandgap (GaN). Such applications have been successfully attempted both with n-type, and p-type $Al_xGa_{1-x}N$/GaN structures, and data also suggest that in such cases the ionization energy of acceptor is reduced. [84,130]

HTA is a technique used to lower the ionization energy of acceptor atoms in p-type doped GaN, and p-type doped $Al_xGa_{1-x}N$. Again, Mg atoms are typically used as the substitutional acceptor atoms to achieve p-type doping. Following this technique, samples of Mg-doped GaN, and Mg-doped $Al_xGa_{1-x}N$ are encapsulated in silicon dioxide (SiO_2) and subjected to two consecutive anneal treatments. The first anneal takes place at 700 °C for 30 minutes, and the second anneal at a temperature ranging between 1000 °C and

1300 °C for 5 minutes. Upon the completion of the anneal process, the SiO_2 capsule is dissolved with diluted hydrofluoric acid (HF).[110]

In this work, photocurrent spectroscopy was conducted by means of a YAG pumped Optical Parametric Oscillator/Optical Parametric Amplifier (OPO/OPA) system tunable from 250 meV to 1.75 eV on test structures fabricated on magnesium doped $Al_xGa_{1-x}N$ with an aluminum mole fraction ranging 0% to 52%. The goal of this work was the observation and identification of energy levels associated with acceptor atoms of Mg in GaN and $Al_xGa_{1-x}N$. Photocurrent response peaks at Mg energy levels in Mg-doped GaN, and $Al_xGa_{1-x}N$ would indicate transient optical ionization of acceptor atoms in III-nitrides, and hence enable a transient, enhanced excess of hole (or “hot” holes) and improved p-type conductivity in said materials. In this case, the term “enhanced p-type conductivity by means of IR optical pumping” will be used. Here it is necessary to specify that this kind of “optical pumping” is different from the kind of optical pumping of solid-state lasers, where valence electrons are excited into the conduction band; in fact, in this work “optical pumping” is the steady-state continuous optical ionization of acceptor atoms of Mg in Mg-doped GaN, and Mg-doped $Al_xGa_{1-x}N$. This work was inspired by the experimentation conducted on the investigation of acceptors in diamond semiconductor by means of Fourier-transform photocurrent spectroscopy, Infrared, and Raman spectroscopy conducted by various research groups in the early 2000’s [10,11], and the initial results on the optical acceptor ionization in III-Nitrides conducted at the MNST Laboratory, of the General Electric Corporate Research & Development (GE CRD, Niskayuna, NY).[12] Initial photoconduction experiments on the optical acceptor ionization in III-Nitrides focused on Fourier Transform Infrared (FTIR) analysis, and despite the

observation of small increases in photoconductivity were observed upon exposure to IR radiation, FT spectral profiles were not determined due to the low intensity of the IR source in accordance with the theoretically proven fact that carrier cross section of IR radiation absorbed by deep acceptors in GaN, and $Al_xGa_{1-x}N$ sharply peak at a photon energy larger than the acceptor ionization energy.[12] The transient optical ionization of acceptors in Mg-doped GaN, and Mg-doped $Al_xGa_{1-x}N$ would enable the creation of a new class of optically pumped devices, with enhanced performance. Also, it would allow the circumvention of the problems due to poor p-type conductivity in p-type $Al_xGa_{1-x}N$ in III-Nitride based heterostructure Light-Emitting Diodes (LEDs) and other p-n junction based optoelectronic devices, and achieve transient enhanced UV emission in III-Nitride based heterostructure UV and Deep UV LEDs, as shown in Figure 4.

This work presents IR photocurrent spectroscopy spectra from a variety of Ni-Au metal-semiconductor-metal (MSM) test structures fabricated on Mg-doped GaN, and Mg-doped $Al_xGa_{1-x}N$ with Al mole fraction ranging from 15% to 52%. A non-zero background response was associated with shallow extrinsic impurities and/or a continuum of shallow levels with ionization energy ranging from 50 meV to 100 meV. In addition, peaks in the photocurrent response obtained from test structures were observed and associated with deep level donors. No evidence of deep levels associated with Mg in magnesium-doped GaN and $Al_xGa_{1-x}N$ were observed. Finally, the effects of IR radiation on the UV optical output of forward biased commercial 365nm UV LEDs were investigated and reported.

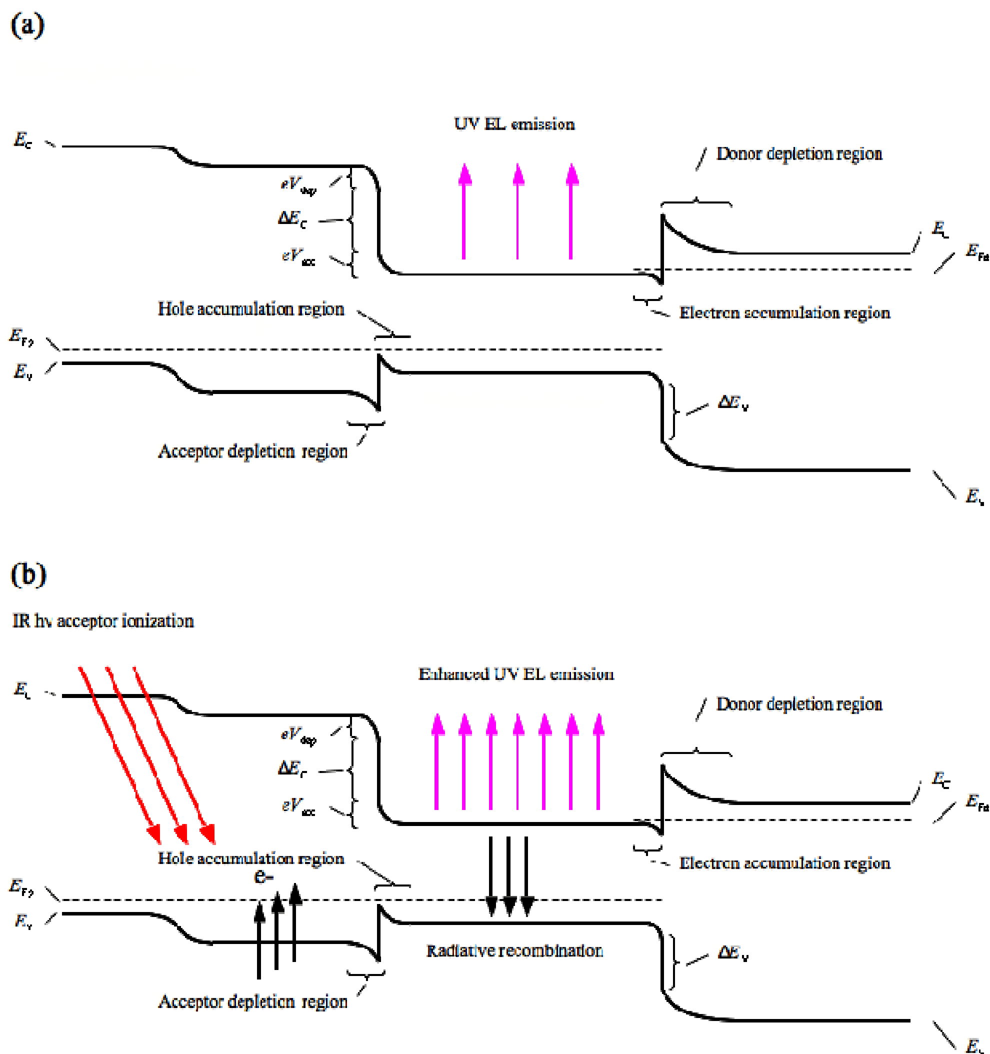

Figure 4: (a) Schematic diagram of a III-Nitride based heterostructure UV LED under no IR optical pumping, and (b) under IR pumping. Adapted from Schubert.[13]

TABLE OF CONTENTS

LIST OF SYMBOLS AND ABBREVIATIONS xx

CHAPTER 1: GaN AND $Al_xGa_{1-x}N$ GROWTH AND CHARACTERIZATION 1

1.1. Growth of GaN and $Al_xGa_{1-x}N$ by HVPE 2

1.2. Growth of GaN and $Al_xGa_{1-x}N$ by MOPVE (MOCVD) 3

1.3. Growth of GaN and $Al_xGa_{1-x}N$ by MBE 5

1.3.1. Reactive MBE (RMBE) 7

1.3.1.1. Reactive Ion MBE (RIMBE) 8

1.3.2. Plasma Enhanced MBE (PEMBE) 8

1.4. Commonly used substrates to grow GaN and $Al_xGa_{1-x}N$ 9

1.5. Characterization of GaN and $Al_xGa_{1-x}N$ 9

1.6. Hall effect: a method to determine the conductivity type of GaN and $Al_xGa_{1-x}N$ 10

1.7. Transmission Line Method (TLM): a method to characterize metal to semiconductor contacts 13

1.8. Circular Transmission Line Method (CTLM): a variation TLM 17

1.8.1. Marlow & Das' CTLM: a variation of Reeve's CTLM 18

CHAPTER 2: P-TYPE GaN AND P-TYPE $Al_xGa_{1-x}N$ 21

2.1. Acceptor substitutional elements in GaN and $Al_xGa_{1-x}N$ 24

2.1.1. Mg as the most successful acceptor substitutional element in GaN and $Al_xGa_{1-x}N$ 27

2.1.2. P-type doping of GaN, and $Al_xGa_{1-x}N$: ionization energy of Mg 28

2.1.3. P-type doping of GaN, and $Al_xGa_{1-x}N$: counteracting role of hydrogen 33

2.1.4. P-type doping of GaN, and $Al_xGa_{1-x}N$: activation of Mg acceptor atoms 36

2.2. Deep Level Defects in GaN and $Al_xGa_{1-x}N$ 38

2.2.1. Deep Level Defects in GaN 39

2.2.2. Deep Level Defects in $Al_xGa_{1-x}N$ 40

2.3. Enhanced p-type doping in GaN and $Al_xGa_{1-x}N$ 40

CHAPTER 3: METAL-SEMICONDUCTOR CONTACTS 42

3.1. Energy Band Theory of Metal Semiconductor Junctions: Schottky and Ohmic Contacts 42

3.1.1. Schottky and Ohmic Contacts 46

3.1.2. Schottky Barrier Lowering 52

3.1.3. Schottky Barrier Lowering 61

3.1.4. Metal Contacts to GaN and $Al_xGa_{1-x}N$ 63

3.1.5. GaN and $Al_xGa_{1-x}N$ surface preparation 71

3.1.6. GaN and $Al_xGa_{1-x}N$ contact anneal 73

CHAPTER 4: KELVIN SENSE MEASUREMENT METHOD 77

4.1. Two-Terminal vs. Four-Terminal Sensing 77

CHAPTER 5: PROCEDURE 82

5.1. LaserVision OPO/OPA System Alignment 82

5.1.1. LaserVision OPO/OPA System Components 82

5.1.2. Coarse Alignment of the Nd:YAG Laser and OPA/OPA System 84

5.1.3. Fine Alignment of the Nd:YAG Laser and OPO/OPA System 86

5.1.4. LaserVision OPO/OPA System Use in the Near Infrared Range 100

5.1.5. LaserVision OPO/OPA System Use in the Intermediate Infrared Range 101

5.1.6. LaserVision OPO/OPA System Use in the Mid Infrared Range 104

5.2. Tooling factor determination of the Kurt J. Lesker PDV 75 Deposition System for the deposition of Au, and Ni thin films 107

5.2.1. Preparation of masked samples for metal deposition trials with the Kurt J. Lesker PDV 75 Deposition System 110

5.2.1.1. Masking and Patterning 111

5.2.1.2. Au film deposition, and determination of relative tooling factor 112

5.2.1.3. Ni film deposition, and determination of relative tooling factor 114

5.2.1.4. Metal Lift-off Patterning 116

5.3. Fabrication of Ni-Au Ohmic contacts to Mg:doped GaN and $Al_xGa_{1-x}N$ 118

5.4. Test Bed Setup 134

5.5. Origin of Mg-doped GaN, and Mg-doped $Al_xGa_{1-x}N$ samples 139

5.5.1. IV Characterization of Mg-doped GaN, and Mg-doped $Al_xGa_{1-x}N$ test structures 140

CHAPTER 6: RESULTS 157

6.1. Infrared Photocurrent Spectra from Mg-doped $Al_{0.52}Ga_{0.48}N$ Test Structures 157

6.2. Infrared Photocurrent Spectra from Mg-doped $Al_{0.42}Ga_{0.58}N$ Test Structures 166

6.3. Infrared Photocurrent Spectra from Mg-doped $Al_{0.20}Ga_{0.80}N$ Test Structures 176

6.4. Infrared Photocurrent Spectra from Mg-doped $Al_{0.15}Ga_{0.85}N$ Test Structures 184

6.5. Infrared Photocurrent Spectra from Mg-doped GaN Test Structures 192

6.6. Comprehensive Plot of the IR Photocurrent Response Peaks 217

6.7. Temperature Dependent Infrared Photocurrent Spectra from Mg-doped GaN Test Structures 218

6.8. Time Decay of the Infrared Photocurrent Spectra from Mg-doped GaN and $Al_xGa_{1-x}N$ Test Structures 224

6.9. Effects on Forward Current and Light Output from Commercial UV III-nitride LEDs under IR Irradiation 231

CHAPTER 7: DISCUSSION AND CONCLUSIONS 236

7.1. Future Work 249

REFERENCES 252

APPENDIX A: AUTHOR'S CURRENT LIST OF PUBLICATIONS 271

LIST OF SYMBOLS AND ABBREVIATIONS

ε_0	Permittivity of Free Space
ε_s	Permittivity of Semiconductor
Φ_M	Schottky Barrier Height
Φ_i	Built-in Potential
Φ_B	Work Function of Metal
Φ_S	Work Function of Semiconductor
E_f	Fermi Level Energy
E_0	Energy of Free Electron
Χ	Electron Affinity
E_v	Energy Level of the Valence Band Edge
E_c	Energy Level of the Conduction Band Edge
E_H	Hall Field
V_H	Hall Voltage
B	Magnetic Field
Ω	Ohm
$(C_5H_5)_2Mg$	Bis-cyclopentadienyl Magnesium
$(CH_3)_3Al$	Trimethylaluminum (TMA)
$(CH_3)_3Ga$	Trimethylgallium (TMG)
$(NH_4)2S_x$	Ammonium Sulfides
A	Ampere
Å	Angstrom (10^{-10} m)
Al	Aluminum

Al_2O_3	Aluminum Oxide
AlCl	Aluminum Monochloride
$AlCl_3$	Aluminum Chloride
AlN	Aluminum Nitride
$Al_xGa_{1-x}N$	Aluminum-Gallium-Nitride Alloys
Ar	Argon
Au	Gold (*Au*rum)
BCl_3	Boron Tricholoride
Be	Beryllium
BOE	Buffered Oxide Etch (HF:H_2O – 1:10)
C	Carbon
C_3H_6O	Acetone (2-Propanone)
Ca	Calcium
Ca^+	Calcium Ion
CCl_2F_2	Dichlorodifluoromethane
ccm	Cubic Centimeter per Minute
ccs	Cubic Centimeter per Second
Cd	Cadmium
CH_4O	Methanol (Monohydroxymethane)
Cl_2	Chlorine
cm	centimeter (10^{-2} m)
Cp2Mg	Bis-cyclopentadienyl Magnesium
Cr	Chromium

DC	Direct Current
DI-H_20	De-ionized Water
DTLS	Deep Level Transient Spectroscopy
ECR	Electron Cyclotron Resonance
EHP	Electron Hole Pair
eV	Electron Volt
F_2	Fluorine
Fe	Iron (*Fe*rrum)
G	Gauss
GaAs	Gallium-Arsenide
GaCl	Gallium Chloride
GaN	Gallium-Nitride
Ge	Germanium
GHz	Giga Hertz (10^9 Hertz)
H^+	Hydrogen Ion
H_2	Hydrogen
H_2O	Water
H_3PO_4	Phosphoric-Acid
HCl	Hydrochloric Acid
HCl:H_2O	Diluted Hydrochloric Acid
HCl:H_2O	Diluted Hydrofluoric Acid
HEMT	High Electron Mobility Transistor
HF	Hydrofluoric Acid

Hg	Mercury *(Hydrargyrum)*
HNO_3	Nitric Acid
HTA	High Temperature Anneal
HVPE	Hydride Vapor Phase Epitaxy
in	inch
InN	Indium Nitride
Ir	Iridium
IR	Infrared
J	Current Density (A/cm^2)
k	Boltzmann's constant (8.62×10^{-5} eV K^{-1})
k*J*	Kilo Joule (10^3 Joule)
KOH	Potassium Hydroxide
kW	Kilo Watt (10^3 Watt)
LED	Light Emitting Diode
LEEBI	Low Energy Electron Beam Irradiation
Li	Lithium
MΩ	Mega Ohm (10^6 Ohm)
mA	milli Ampere (10^{-3} A)
MBE	Molecular Beam Epitaxy
m_e	Mass of Electron
meV	milli eV (10^{-3} eV)
MFC	Mass Flow Control
Mg	Magnesium

$MgAl_2O_4$	Spinel
MgO	Magnesium Oxide
MHz	Mega Hertz (10^6 Hertz)
Mm	milli meter (10^{-3} m)
Mo	Molybdenum
MOCVD	Metal Organic Chemical Vapor Deposition
MOVPE	Metal Organic Vapor Phase Epitaxy
MSM	Metal Semiconductor Metal
mtorr	milli torr (10^{-3} torr)
mW	milli Watt (10^{-3} W)
n	Electron concentration (carriers/cm^3)
N	Atomic Nitrogen
N_2	Nitrogen
N_2H_4	Hydrazine
N_2O	Nitrous Oxide
NaCl	Sodium Chloride
n-$Al_xGa_{1-x}N$	n-type Aluminum-Gallium-Nitride Alloys
Nb	Niobium
n-GaN	n-type Gallium Nitride
NH_3	Ammonia
NH_4OH	Ammonium Hydroxide
Ni	Nickel
NiO	Nickel Oxide

nm	Nanometer (10^{-9} m)
N_V	Nitrogen Vacancy
O	Atomic Oxygen
O_2	Oxygen
ºC	Degree Celsius
ODTLS	Optical Deep Level Transient Spectroscopy
ºK	Degree Kelvin
p	Hole concentration (carriers/cm^3)
P^+	Phosphorus Ion
p-$Al_xGa_{1-x}N$	p-type Aluminum-Gallium-Nitride Alloys
Pd	Palladium
PEDOT	Poly-3,4-ethylenedioxythiophene
PEMBE	Plasma Enhanced Molecular Beam Epitaxy
p-GaN	p-Type Gallium-Nitride
Pt	Platinum
q	Charge of a particle expressed in coulombs
R	Resistance
Re	Rhenium
RF	Radio Frequency
RHEED	Reflection High Energy Electron Diffraction
RIE	Reactive Ion Etch
RMBE	Reactive Molecular Beam Epitaxy
RTA	Rapid Thermal Anneal

RTP	Rapid Thermal Processing
sccm	Standard Cubic Centimeter per Minute
SEM	Scanning Electron Microscope
SF_6	Sulfur Hexafluoride
Si	Silicon
SiC	Silicon Carbide
$SiCl_4$	Silicon Tetrachloride
SiO_2	Silicon Oxide
Sn	Tin (*S*tag*n*um)
SUVOS	Semiconductor Ultra Violet Optical Sources
TAS	Thermal Admittance Spectroscopy (TAS)
Ti	Titanium
$TiAl_x$	Titanium-Aluminum Alloys
TiO_2	Titanium Oxide
torr	A unit of pressure, equal to 1.316×10^{-3} atmosphere
UHV	Ultra High Vacuum
UV	Ultraviolet
V	Volt
W	Watt
W	Tungsten
Zn	Zinc
ZnO	Zinc Oxide
μm	micron (10^{-6} m)

CHAPTER 1: GaN AND $Al_xGa_{1-x}N$ GROWTH AND CHARACTERIZATION

In order to grow high quality, single crystalline III-nitrides (GaN and $Al_xGa_{1-x}N$ included), nearly every crystal growth methodology, substrate kind and orientation has been investigated and tested since the first synthesis of AlN[14], and GaN[15] over fifty years ago. Such a scenario has slowly emerged in light of two major facts: 1) a very challenging bulk growth that requires both high temperature, and high pressure, and 2) a lack of native III-nitride semiconductor material substrates, which has enabled the proliferation of various heteropitaxial growth methodologies.

Recently, GaN[16,17,18] and AlN[19] bulk crystals have been produced, and a limited supply of native substrates made commercially available; nonetheless, most of the GaN and $Al_xGa_{1-x}N$ thin films are made available via epitaxial growth on a non-native substrate. The principal drawback of GaN and $Al_xGa_{1-x}N$ is that N_2 has both a low solubility in Ga, and a high vapor pressure on the former; thus, independent of the chosen crystal growth methodology, the main challenge with the growth of GaN and $Al_xGa_{1-x}N$ is to incorporate stoichiometric quantities of N_2 in the crystalline semiconductor film. Typically, the growth of GaN and $Al_xGa_{1-x}N$ is accomplished by forcing the combination of vapor-phase Ga, atomic nitrogen (N), and Al onto a substrate at very high temperature, and such process is achieved via Hydride Vapor Phase Epitaxy (HVPE), Metal Organic Vapor Phase Epitaxy (MOPVE), which is also known as Metal Organic Chemical Vapor

Deposition (MOCVD), and Molecular Beam Epitaxy (MBE) techniques, which will be described below.

1.1. Growth of GaN and $Al_xGa_{1-x}N$ by HVPE

One interesting method to grow crystalline GaN and $Al_xGa_{1-x}N$ semiconductor materials is hydride vapor phase epitaxy (HVPE). The core of this crystal grow methodology consists of passing hydrochloric acid (HCl) vapor over molten Ga, and Al sources; from the reaction of the metals and the HCl vapor, gallium chloride (GaCl) and aluminum chloride ($AlCl_3$) are formed, and then transported downstream toward the substrate by a carrier gas (N_2, or H_2). At the substrate, which is kept at a temperature as high as 1100 °C, GaCl and $AlCl_3$ are combined with ammonia (NH_3); from the high temperature decomposition of these three compounds, Ga, Al, and N are made available for their recombination into $Al_xGa_{1-x}N$. It should be obvious that for the formation of GaN, the molten Al source is not used. In any case, by means of HVPE, it is possible to obtain free standing and/or templates, and bulk GaN and $Al_xGa_{1-x}N$.

Growth rates are usually quite high for both GaN (0.5 μm/min)[20], and $Al_xGa_{1-x}N$ (30 μm/min)[21], and semiconductor materials tend to exhibit a strong n-type carrier concentration. Typically, the formation of $Al_xGa_{1-x}N$ via HVPE is challenging because of the rather violent reaction between metastable aluminum monochloride (AlCl) and the silicon oxide (SiO_2) of the quartz reactor, which leads to a rapid deterioration of the reactor; hence, means to refine $AlCl_3$ (which does not react with the SiO_2 of the quartz reactor) are necessary. A schematic diagram of a HVPE reactor is shown in Figure 5.

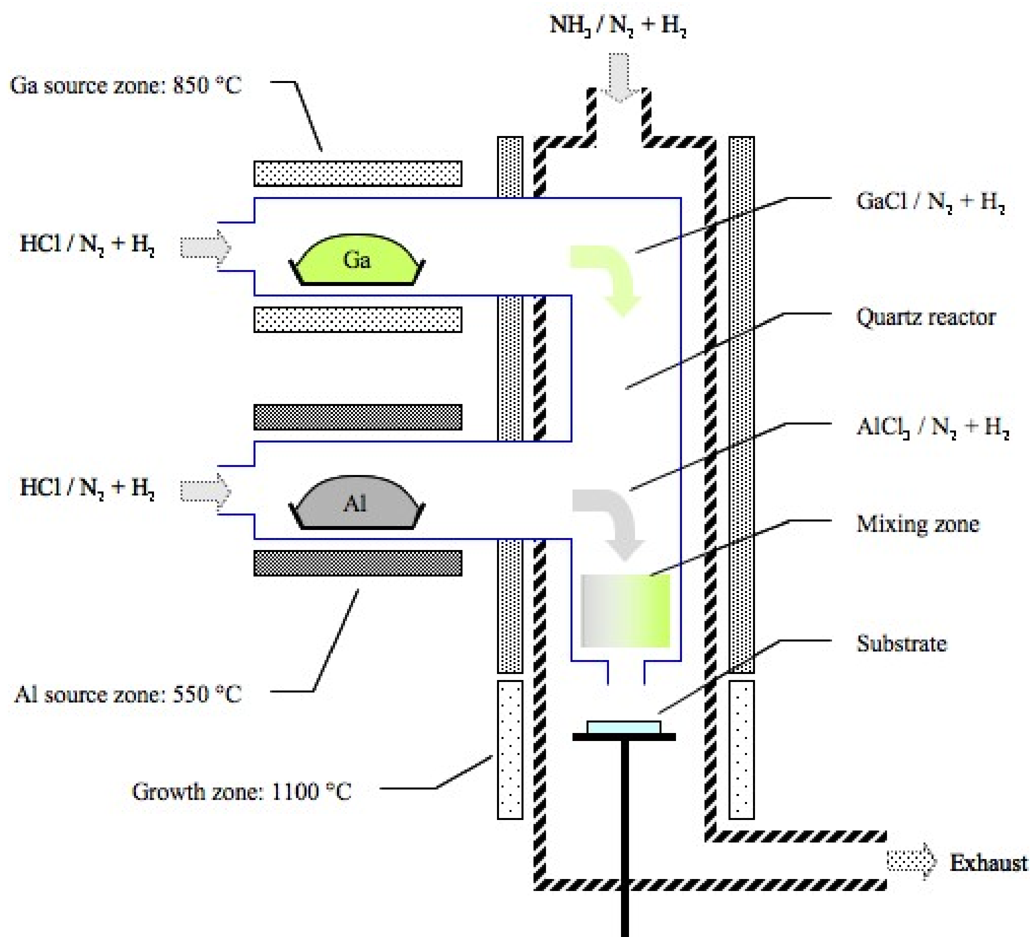

Figure 5: Schematic diagram of a HVPE reactor. Adapted from Yamane *et al.*[21]

1.2. Growth of GaN and $Al_xGa_{1-x}N$ by MOPVE (MOCVD)

MOPVE, also known as MOCVD, is a flexible method to deposit crystalline films of GaN and $Al_xGa_{1-x}N$ on a non-native substrate; such method involves the controlled reaction of the group-III metalorganics trimethylaluminum (TMA), and trimethylgallium (TMG) with ammonia (NH_3) at a substrate that is heated to a temperature ranging between 700 °C and 1100 °C[22,20], in the chamber of an atmospheric-pressure or nearly atmospheric[1] pressure reactor. In order to avoid the reaction of the reactants before they

[1] Some MOCVD reactors are designed to operate in the order of tens of mtorr of pressure.

reach the surface of the substrate, the reactants are diluted in a carrier gas, which typically is H_2; nonetheless, N_2, and a combination of H_2 and N_2 have been also used[23]. Most recent MOCVD reactors utilize an activated form of nitrogen, so that the deposition of GaN and $Al_xGa_{1-x}N$ can occur at a lower temperature. Dependent on the methodology used to activate nitrogen, the chemical vapor deposition of GaN and $Al_xGa_{1-x}N$ is called "remote plasma enhanced", "laser assisted", "ECR plasma assisted", "RF plasma assisted", or "photo assisted".[20] Conventionally, p-type GaN and p- $Al_xGa_{1-x}N$, which are of interest in this work, are achieved via MOCVD growth followed by a post-growth anneal process aimed to active the substitutional acceptor impurities[24,25,26]. A schematic diagram of a MOCVD reactor based on design of the Vertical Modulation Flow MOCVD reactor installed in Grigg Hall, at the University of North Carolina at Charlotte is shown in Figure 6.

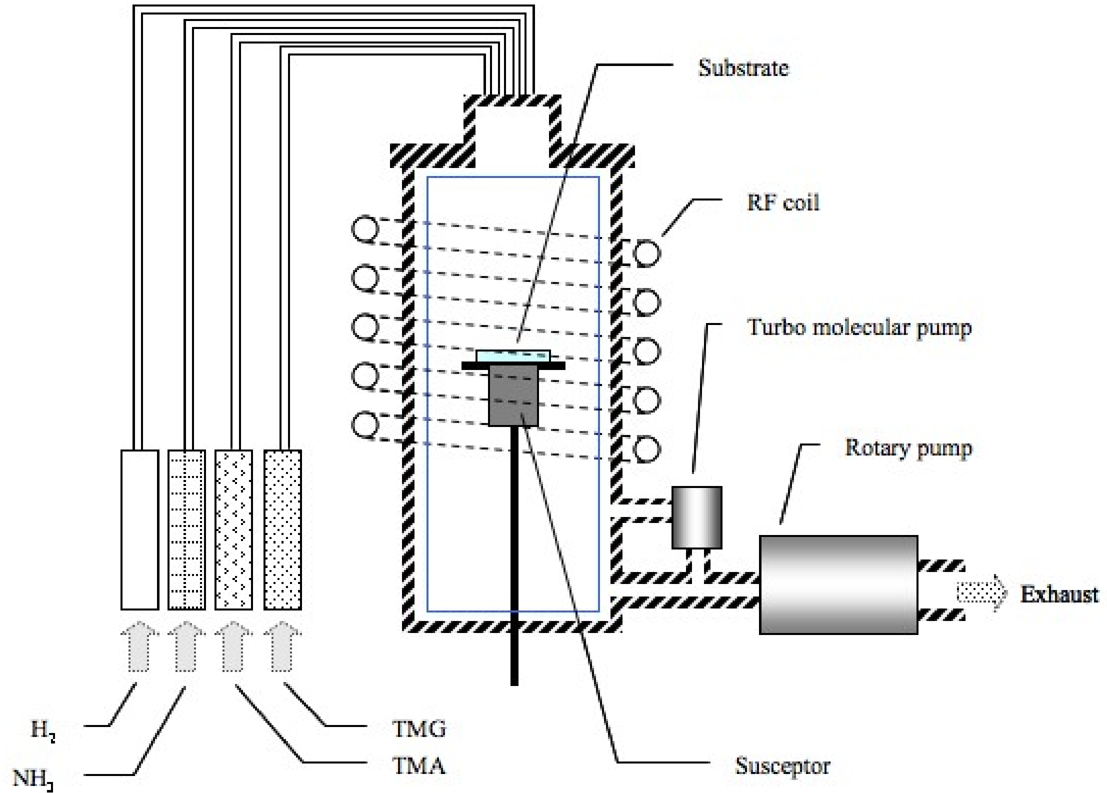

Figure 6: Schematic diagram of a MOCVD reactor.

1.3. Growth of GaN and $Al_xGa_{1-x}N$ by MBE

MBE is an ultra high vacuum (UHV) crystal growth method that is hinged on the interaction of one or more molecular or atomic beams at the surface of a heated substrate. The nature of this deposition technique allows both a very refined control of the growth parameters, and the in-situ monitoring of the growth by means of characterization tools such as the reflection high energy electron diffraction system (RHEED). A schematic cross sectional diagram of an MBE system is shown in Figure 7.

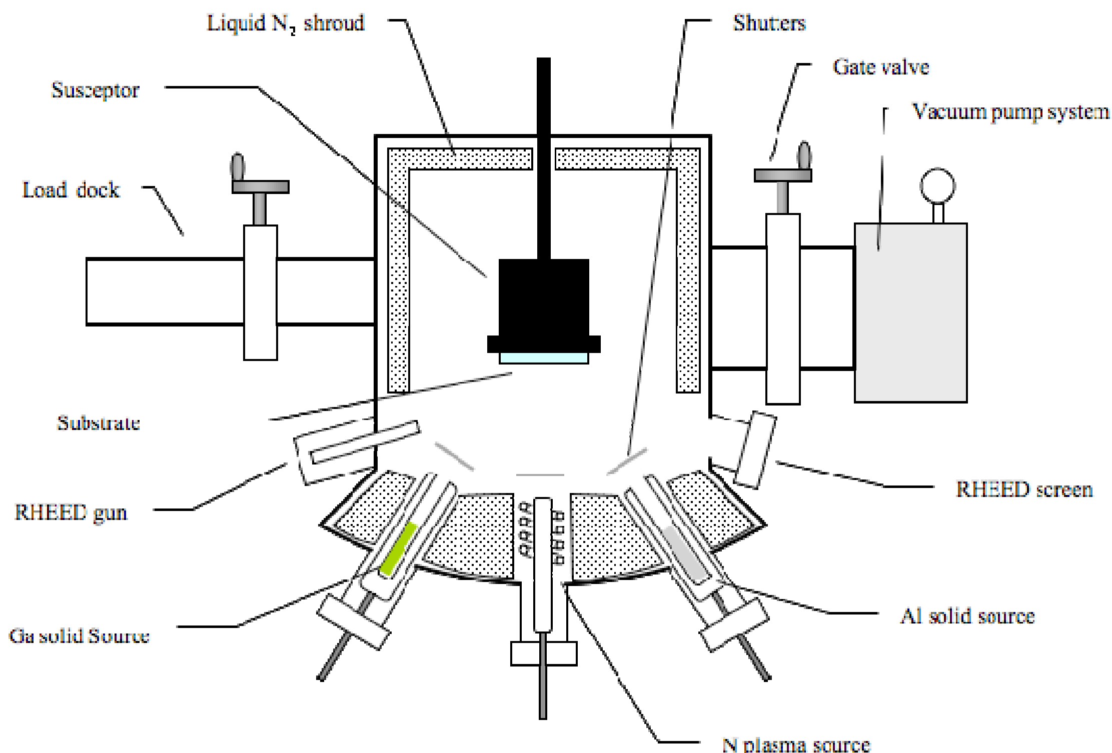

Figure 7: A schematic cross sectional diagram of an MBE system based on the design of the MBE system installed in the clean room, in Cameron Hall, at the University of North Carolina at Charlotte.

Solid elements Ga and Al are heated in special effusion cells, also known as Knudsen cells, and combined to either a NH_3 injector or a source of activated nitrogen (N); the chamber pressure of an MBE reactor prior epitaxial growth or heating or degassing of the sources and substrate is in the order of 10^{-10} torr, and does not exceed 10^{-5} torr during the epitaxial growth so that the mean free path of the particles does not exceed the geometrical dimension of a typical MBE chamber. Solid elements heated in effusion cells are also used as the source of substitutional impurities to obtain n-type and p-type, GaN and $Al_xGa_{1-x}N$: silicon (Si) and magnesium (Mg) are the most commonly, and successfully used elements for achieving n-type and p-type conductivity, respectively. MBE growth is conducted at a relatively low temperature with respect to the growth

temperature of a typical MOCVD reactor, and it can range from 650 °C to 800 °C[20,24] for both GaN and $Al_xGa_{1-x}N$. P-type conductivity in MBE grown GaN, and $Al_xGa_{1-x}N$ has been proven, and typically no post-growth anneal process is required. MBE growth rates range from 0.2 µm to 1 µm per hour, and are hence not suitable for a large-scale production.

Since molecular nitrogen (N_2) is characterized by a strong covalent bond (ΔH°= 946 kJ/Mole)[27], N_2 molecules do not chemisorb on the surface of GaN below 950 °C[20]; hence atomic nitrogen (N), or nitrogen containing molecules with weak inter-atomic bonds have been considered as a nitrogen source for MBE system. This also induced the proliferation of various kinds of MBE systems that have been modified to be suitable for growing III-nitride semiconductor materials, GaN and $Al_xGa_{1-x}N$ included. A few of these MBE systems will be described below.

1.3.1. Reactive MBE (RMBE)

The growth mechanism of GaN and $Al_xGa_{1-x}N$ in RMBE involves the pyrolysis of ammonia (NH_3), and the reaction of atomic nitrogen (N) with Ga, and Al at the surface of a heated substrate. In order to obtain a thermal decomposition of NH_3, the temperature of the substrate must range between 750 °C and 850 °C. Slow growth rates are usually achieved, which is typical of MBE-based growing techniques, but the crystalline quality of III-nitride semiconductor material films grown with this technique can be pretty good, especially in the case of GaN.[28] RMBE is a rather interesting crystal growing technique, as it allows the formation of nano-structures, nanorods included; this property is enabled by the fact that the thermal cracking of NH_3 may or may not be able to provide a sufficiently large N-flow to match the Ga-flow. In the case that there is a surplus of Ga at

the surface of the heated substrate, Ga will thermally desorb, nucleate, and form GaN or $Al_xGa_{1-x}N$ clusters with a locally accelerated growth rate known as "hillocks".[29,30]

1.3.1.1.Reactive Ion MBE (RIMBE)

A variation of the RMBE methodology is known as RIMBE, which is hinged on pyrolysis of hydrazine (N_2H_4), and the reaction of atomic nitrogen (N) with Ga, and Al at the surface of a heated substrate. The use of (N_2H_4) is believed to increase the reactivity of nitrogen-containing species[20]; this would hence allow a higher nitrogen flow, and the reduction of both the pyrolysis, and substrate temperature. GaN films have been grown via RIMBE[31,32,33]; US patents protecting proprietary methods to grow $Al_xGa_{1-x}N$ via RIMBE have been issued[34,35,36], but currently there is virtually no trace of such experimentation mentioned in the literature. A possible explanation is that the use of N_2H_4 has been restricted because of its intrinsic toxicity and its challenging handling, and simultaneously curbed by the development of plasma enhanced MBE (PEMBE), which will be described below.

1.3.2. Plasma Enhanced MBE (PEMBE)

PEMBE is a crystal growth technique characterized by a compact plasma-based nitrogen source, which is commercially available either in RF or ECR compatible design; in any case, the function of the plasma nitrogen source is to crack N_2 molecules, and provide ionic nitrogen that reacts with atomic Ga, and Al at the surface of a heated substrate. ECR plasma sources operate at the electron cyclotron frequency of 2.45 GHz, and approximately 10% of N_2 molecules are converted into atomic nitrogen, while RF plasma sources operate at a relatively lower frequency of 13.56 MHz.[20]

1.4. Commonly used substrates to grown GaN and $Al_xGa_{1-x}N$

Although GaN bulk crystals have been recently produced, and a limited supply of native substrates made commercially available, most of the GaN and $Al_xGa_{1-x}N$ thin films are made available via epitaxial growth on a non-native substrate. So far, the best results in terms of commercially growing GaN and $Al_xGa_{1-x}N$ thin films have been obtained by growing such III-nitride semiconductors on c-plane (0001) sapphire (Al_2O_3) substrates; in addition, a-plane $(11\bar{2}0)$, m-plane $(10\bar{1}0)$, and r-plane $(1\bar{1}02)$ Al_2O_3 substrates have also been used with excellent results.[37,38,39,40,41]

Additional substrates used to grown GaN and $Al_xGa_{1-x}N$ thin films are silicon carbide (SiC), zinc oxide (ZnO), silicon (Si), gallium arsenide (GaAs), magnesium oxide (MgO), sodium chloride (NaCl), tungsten (*W*), titanium oxide (TiO_2), and spinel ($MgAl_2O_4$).[20, 42]

1.5. Characterization of GaN and $Al_xGa_{1-x}N$

Characterizing a given semiconductor material literally implies the investigation, marking, and distinguishing of certain characteristics that pertain to one, or more than one specific field; thus it is a very broad definition. For instance, the characterization of GaN and $Al_xGa_{1-x}N$ may be aimed to define their electronic properties, crystalline structure and quality, surface morphology, or even the mapping of very specific kinds of macro defects; in addition, non invasive probing such the one conducted either via cathodoluminescence (CL), or photoluminenscence (PL) may be considered a way to characterize their optoelectronic properties.

In this work, however, the discussion about the characterization of GaN and $Al_xGa_{1-x}N$ will be limited to the characterization of the type of conductivity of a given

semiconductor (n-type, or p-type), and contact resistivity of metal-to-semiconductor contacts.

1.6. Hall effect: a method to determine the conductivity type of GaN and $Al_xGa_{1-x}N$:

The so-called *Hall effect* is a phenomenon first investigated in 1879 by the American physicist E. H. Hall, who observed the occurrence of a small, localized, transverse voltage in a metal strip, in which a current was flowing, immersed in an applied magnetic field. [132,43] Currently, Hall effect measurement methodologies are used as accurate means to determine the carrier mobility and density, and electrical resistivity of a given semiconductor; in addition, by investigating the sign of the Hall voltage, it is possible to determine if an unknown sample of semiconductor show p-type, or n-type conductivity.

The basic physical principle of the Hall effect is the Lorentz force, which is the force exerted on a particle with charge q that moves in a magnetic field $\vec{B}$ with velocity $\vec{v}$, which is given in vector notation by

$$\vec{F} = q\vec{v} \times \vec{B} \qquad \text{Equation 1}$$

where $\times$ indicated the vector cross product of the vector velocity $\vec{v}$, and the vector magnetic field $\vec{B}$; in other words, the product of the magnitude of each two vectors, and the sine of the angle between them.

According to Equation 1, when carriers (electrons or holes) are moving in a conductor (hence, a current), they will experience a force (Lorentz force) in a direction perpendicular to both the direction of the magnetic field, and the direction of their velocity. Such a force will be balanced by an induced electric field that is generated by a slight redistribution of the carriers, and, in this particular case, this induced electric field

is known as *Hall field*, E_H. By integrating E_H with respect to space, the so-called *Hall voltage*, V_H can be dutifully determined. A schematic of the Hall effect is illustrated in Figure 8.

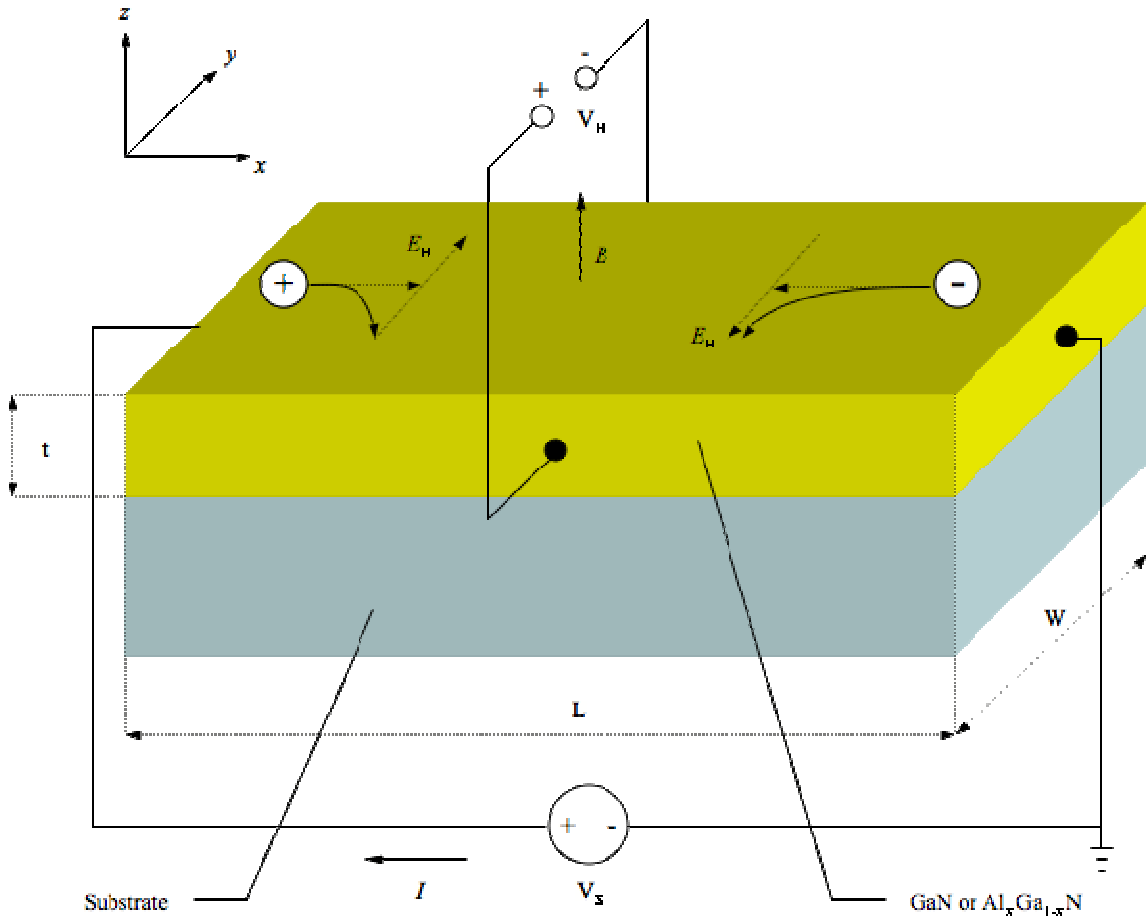

Figure 8: Schematics of the Hall effect occurring in a GaN or $Al_xGa_{1-x}N$ sample. A current (electrons or holes) flows along the positive x-direction, and carriers are deviated in the negative y-direction by the presence of the magnetic field *B* in the positive z-direction. The redistribution of the carrier generates the Hall field, E_H, which is directed in the positive y-direction for an accumulation of holes, and in the positive y-direction for an accumulation of electrons. The Hall voltage, V_H, can be measured by a voltmeter along the y-direction. Adapted from Muller *et al.*[132]

From Figure 8, it can be inferred that a predominantly sample of n-type semiconductor (rich with electrons), and a sample of p-type semiconductor (rich with

holes) would show a Hall voltage with opposite polarity, and this is the concept used to distinguish the type of conductivity of an unknown semiconductor sample when using a Hall effect measuring system.

The Hall field can be expressed as a function of current, and the applied magnetic field; for holes it can be written as

$$E_H = \frac{J_x B}{qp} \qquad \text{Equation 2}$$

where J_x is the current density per unit area in the x-direction, B is the magnitude of the magnetic field in the z-direction, q is the hole charge, and p is concentration of holes per volume unit area.

For electrons Equation 2 can be written as

$$E_H = -\frac{J_x B}{qn} \qquad \text{Equation 3}$$

where J_x is the current density per unit area in the x-direction, B is the magnitude of the magnetic field in the z-direction, q is the hole charge, and n is concentration of electrons per volume unit area.

Both equations can be expressed as

$$E_H = R_H J_x B \qquad \text{Equation 4}$$

where J_x is the current density per unit area in the x-direction, B is the magnitude of the magnetic field in the z-direction, and R_H is the *Hall coefficient* which is equal to $\frac{1}{qp}$ for holes, and to $-\frac{1}{qn}$ for electrons.

A final note goes to address the magnitude of the magnetic field that is typically necessary for a Hall effect measurement with wide bandgap semiconductor materials such as GaN and $Al_xGa_{1-x}N$: 6000 to 10000 Gauss.

1.7. Transmission Line Method (TLM): a method to characterize metal to semiconductor contacts.

One of the most widely used methods to characterize the quality of ohmic, metal to semiconductor contacts, by determining the specific contact resistance, is the so-called Transmission Line Method (TLM), also occasionally called Transfer Length Method, which was first introduced by W. Shockley in 1964.[44] In his original approach, Shockley fabricated an array of metal contacts with increasingly gap between them, and determined the resistance as a function of the gap spacing. A schematic diagram of a semiconductor material (GaN or $Al_xGa_{1-x}N$) with a set of metal contacts for TLM analysis is shown in Figure 9.

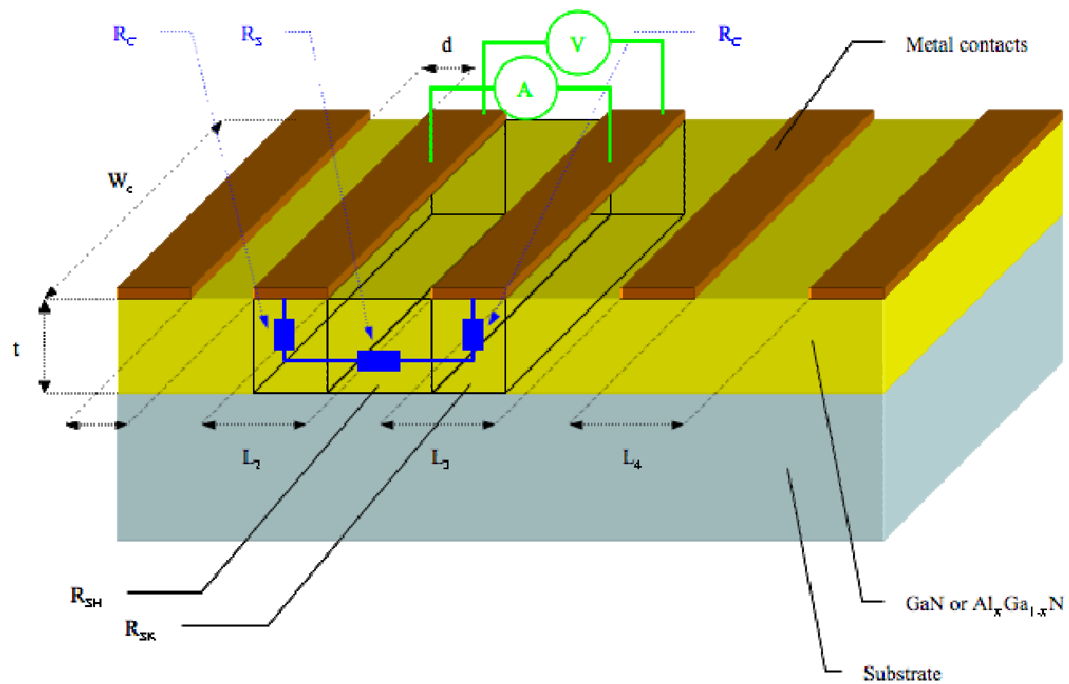

Figure 9: A schematic diagram of a semiconductor (GaN or AlGaN) with a set of metal contacts for TLM analysis. Adapted from Bashar.[45]

In order to determine the resistance as a function of the gap between two adjacent contacts, a constant current is passed between them, while a second set of probes is used to measure the voltage drop across the same two adjacent contacts. This process is repeated for all of the contacts, and the values of the gap-dependent resistance (total resistance, R_T) are plotted on a liner graph, as shown in Figure 10.

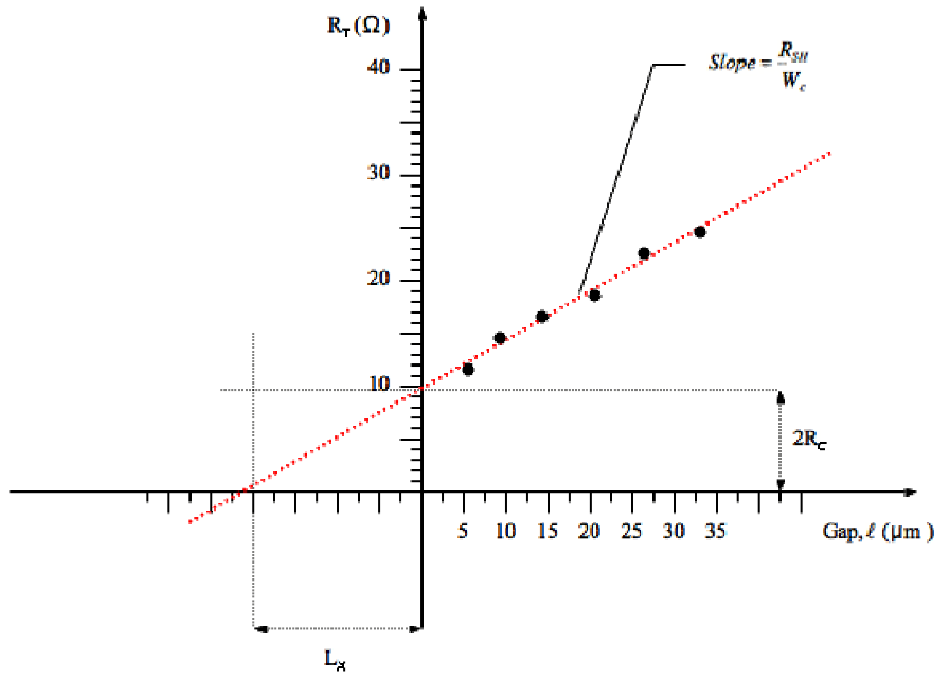

Figure 10: Variation of the resistance with respect to TLM contact spacing. Adapted from Morkoç[20] and Bashar.[45]

From Figure 9 it can be observed that the resistance between two adjacent TLM contacts is given by

$$R = 2R_C + R_S \quad \text{Equation 5}$$

where R_C is the resistance due to the contact, and R_S is the resistance due to the semiconductor material. The resistance due to the semiconductor material, R_S, can be expressed by

$$R_S = \frac{\rho L}{tW_c} \quad \text{Equation 6}$$

where ρ is the resistivity of the semiconductor material, L is the dimension of a given gap spacing, t is the thickness of the semiconductor layer beneath the TLM contact, and W_c is width of the semiconductor layer beneath the TLM contact.

Since the sheet resistance of a semiconductor is given by

$$R_{SH} = \frac{\rho}{t} \qquad \text{Equation 7}$$

therefore Equation 6 can be rewritten as

$$R_S = L\left(\frac{R_{SH}}{W_c}\right) \qquad \text{Equation 8}$$

and Equation 5 can be rewritten as

$$R = 2R_C + L\left(\frac{R_{SH}}{W_c}\right) \qquad \text{Equation 9}$$

Using Equation 9, the total resistance, R_T, is given by

$$R_T = 2R_C + \ell\left(\frac{R_{SH}}{W_c}\right) \qquad \text{Equation 10}$$

where ℓ is the length (independent variable) of each of the TLM contact gaps

$$\ell = L_1, L_2, L_3 ... L_n \qquad \text{Equation 11}$$

From the graph shown in Figure 10, which plots Equation 10, it can be seen that the contact resistance can be extrapolated from the values of y-intercept, $2R_C$, and the Transfer Length, L_T, can be extrapolated from the value of the x-intercept, L_X, using

$$L_T = \frac{L_X}{2} \qquad \text{Equation 12}$$

For the sake of this discussion, it is interesting to notice that L_T can be used as an indicator of the quality of an Ohmic metal to semiconductor contact; more precisely, the shorter L_T, the better the Ohmic quality of the contact.

Assuming that the sheet resistance under the contact is not modified, or that the changes of the sheet resistance due to the contact are negligible, the value for the sheet resistance can be extrapolated from the slope of Equation 10.[20,45,46,47]

1.8. Circular Transmission Line Method (CTLM): a variation TLM

A variation of the TLM method described above employs concentric, circular patterns, and it is knows as Circular Transmission Line Method (CTLM). Such method was first introduced in the late 70's by G. K. Reeves[48], and was conceived around the need of fabricating very simple test structures that did not need mesa isolation processing. Reeve's original test structure consisted of three concentric, circular metal contacts deposited onto the surface a semiconductor; more precisely, one central solid, and two annular pads. Using Reeve's CLTM, two resistance values are determined: R_1, which is the resistance measured across the inner two pads (r_0, r_1), and R_2, which is the resistance measured across the outer two pads (r_1, r_2). In addition, the ratio of the output voltage of the middle ring contact to the current input, with current output equal to zero, is called the end resistance, R_E.[150] Reeve's CTLM method reduces the complexity in terms of contact mesa isolation processing; on the other end, it introduces a more complex mathematical term derivation with respect to TLM. Reeve's CTLM has been object of criticism since its introduction, and found to be unable to determine very accurate[49,50], and precise[51] values of R_E when the sheet resistance beneath the metal pad is not negligible, or when the specific contact resistance is small. A diagram of Reeve's CTLM structure for contact characterization is shown in Figure 11.

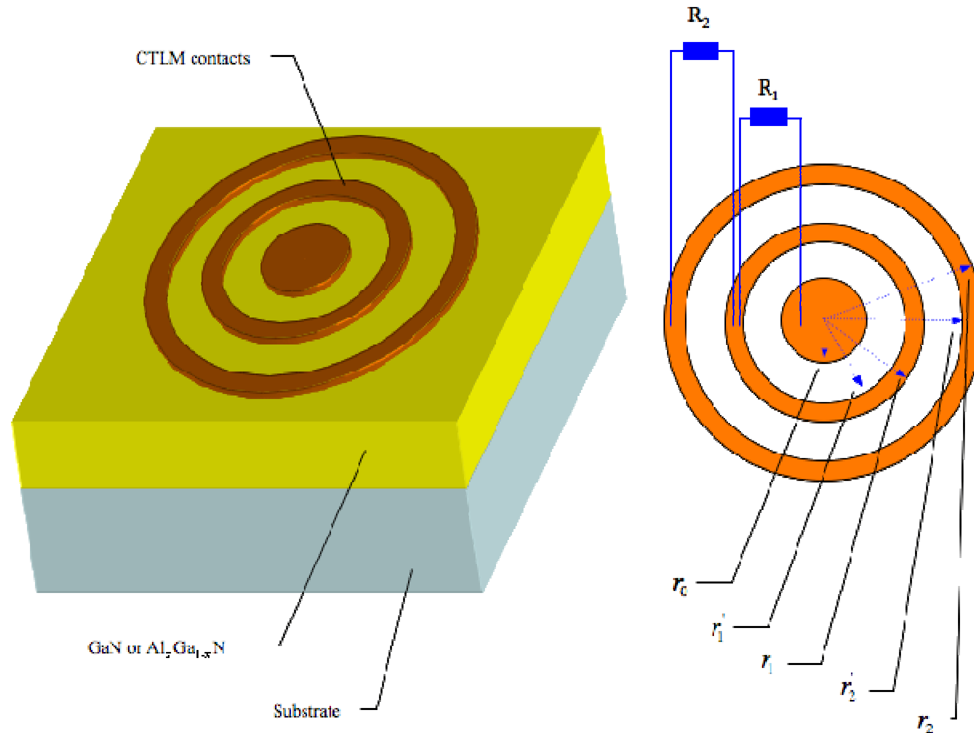

Figure 11: A diagram of Reeve's CTLM structure for metal to semiconductor contact characterization. Adapted from Reeves.[48]

1.8.1. Marlow & Das' CTLM: a variation of Reeve's CTLM

A variation of Reeve's CTLM was introduced by Marlow and Das in 1982 [52], and it has been extensively used in the literature [53,54,55,56,57]. Marlow and Das' CTLM test structures have been used in this work as well, and a schematic diagram of such test structures is depicted in Figure 12.

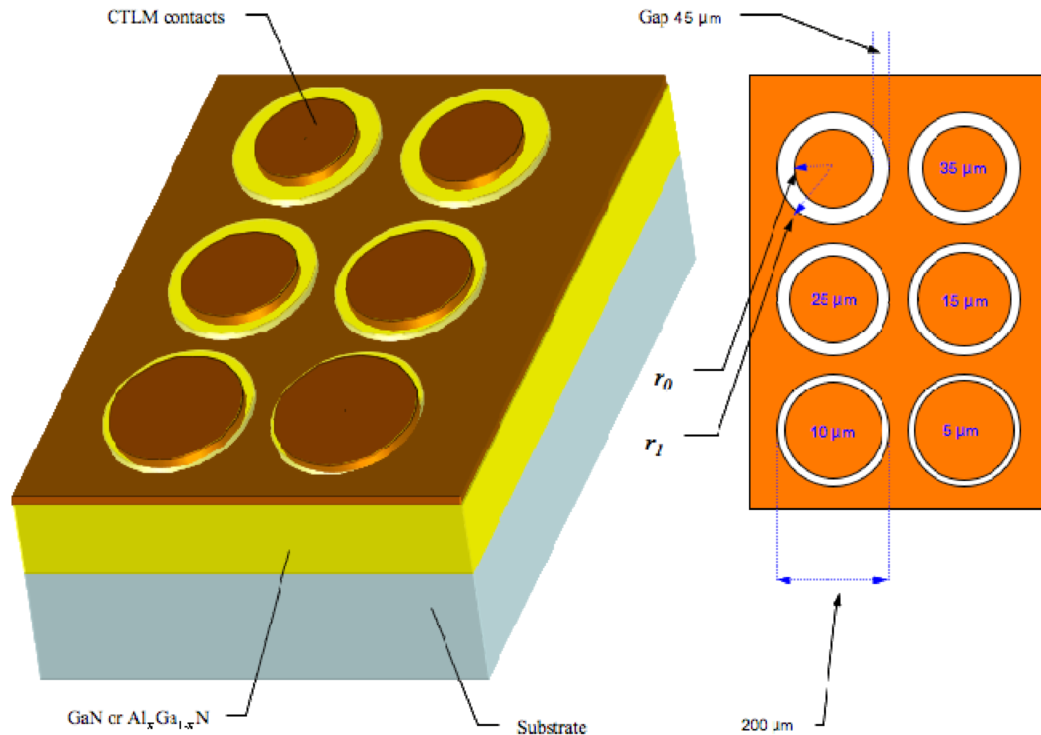

Figure 12: Schematic diagram of a CTLM test structure based on the one suggested by Marlow and Das.[52] The values shown in this figure reflect the dimension of CTLM test structures used in this work.[150]

As shown in Figure 12, test structures maintain a circular pattern for the metal to semiconductor contacts, and are characterized by a variable "gap" between a constant-radius (r_0 = 200 µm) outer circle, and a variable radius inner circle (r_1); the dimension of the gap varies as 5 µm, 10 µm, 15 µm, 25 µm, 35 µm, and 45µm.[150]

When a Marlow and Das' CTLM test structure is used, six independent measurements are carried out to determine the value of the resistance across each of the six gaps; the value of the resistance obviously varies as a function of the gap given that the there is no fluctuation in the sheet resistance of the semiconductor material. The resistance values are plotted as a function of the gap spacing in order to produce a graph similar to the one depicted in Figure 10.

Once again, from the graph shown in Figure 10, the values for the contact resistance, $2R_C$, can be extrapolated by the y-intercept, the normalized contact resistance, R_T, is then given by the product of R by the area of the contact pad, and the transfer length, L_T, can be extrapolated from the x-intercept by using Equation 12. The resistance, R_T, is determined experimentally, and used in to extrapolate the value of the sheet resistance, R_{SH}

$$R_T = \frac{R_{SH}}{2\pi}\left[\ln\left(\frac{r_0}{r_1}\right) + L_T\left(\frac{1}{r_0} + \frac{1}{r_1}\right)\right] \qquad \text{Equation 13}$$

where r_0, and r_1 are radii of the outer and inner rings of the CTLM structure.

The contact resistance, R_C, is then given by

$$R_C = R_{SH}\left(L_T\right)^2 \qquad \text{Equation 14}$$

and the resistivity of the semiconductor material, σ, can be determined by rearranging Equation 7 in

$$\sigma = R_{SH}t \qquad \text{Equation 15}$$

A set of photolithographic masks to fabricate Marlow and Das' CTLM test structures for this work was provided by the Micro & Nano Structures Technologies (MNST) laboratory of GE Global Research, Niskayuna, NY.[150]

CHAPTER 2: P-TYPE GaN AND P-TYPE $Al_xGa_{1-x}N$

Despite the fact that GaN is a semiconductor material that was first synthesized in 1932[15], GaN and its alloys still represent a real technological conundrum. GaN became the hinge of a scientific curiosity in the late 1960's with the introduction of epitaxial growth on sapphire by means of hydride vapor phase epitaxy (HVPE)[58], but it was not until the 1990's that applications of GaN and its alloys in optoelectronic devices became possible; indeed, successful GaN p-type doping was only achieved in 1990[59]. To say the least, it is interesting to notice that the achievement of p-type doping of $Al_xGa_{1-x}N$ is still one of the most pervasive challenges; perhaps the "mother of all bottlenecks" involving the development of III-nitride semiconductor materials.

Since 1989, there have been countless, yet often-unsuccessful efforts to obtain p-type GaN, and several kinds of substitutional elemental impurities have been investigated. This kind of trend basically embraces most wide bandgap nitride semiconductor materials (GaN an $Al_xGa_{1-x}N$ included), and it is due to a lack of shallow acceptor levels, which is a characteristic that is attributed to the high electronegativity of nitrogen. As a matter, of fact, nitrogen is a highly electronegative element with a deep 2*p* atomic orbital; thus the valence band maximum of most nitride semiconductors, which contains N 2*p* orbital, is low in energy, and this leads to a rather deep acceptor energy level.[60,61,62,63]

A large variety of elemental substitutional impurities have been investigated, and the p-type doping of GaN, and $Al_xGa_{1-x}N$ has been attempted with the intentional

introduction of Group I, Group II, and Group IV; nonetheless, both GaN, and $Al_xGa_{1-x}N$ have a natural, and strong tendency to exhibit n-type conductivity, which was initially associated with the presence intrinsic defects, such as vacancies, self-interstitials, dislocations, and antisites.[64]

These kinds of defects either introduce deep donor levels in the bandgap, or act as compensating centers that mitigate the functions of the intentionally incorporated substitutional impurities; however, shallow donor levels can be occasionally introduced in the bandgap by intrinsic defects, and the former can behave as dopants. For instance, nitrogen vacancies (N_V) can act as donors, and they can be responsible for n-type conductivity in GaN, or $Al_xGa_{1-x}N$; this kind of vacancy can occur during ion implantation, and in such a scenario an increased electron concentration can be observed.[65] Moreover, it is also possible that N_V act as compensating center in p-type GaN, and in this case the function of the intentionally incorporated acceptor substitutional impurity would be abated; the likelihood of such a scenario is supported by the fact that N_V in p-GaN are know to have a low formation energy, and in the case of p-$Al_xGa_{1-x}N$, N_V assume a more relevant role as the Al mole fraction increases.[64]

Recent findings, however, suggest that the proclivity of GaN and $Al_xGa_{1-x}N$ to show n-type conductivity is caused by unintentionally incorporated impurities.[66] Oxygen and silicon, for instance, can be incorporated within the lattice of GaN, and $Al_xGa_{1-x}N$ with a concentration that can induce n-type conductivity. The unintentional n-type doping of GaN and $Al_xGa_{1-x}N$ can occur in many different ways. In the case of oxygen, contamination can occur through a water-contaminated ammonia (NH_3) source, which is a typical precursor of III-nitride semiconductors materials grown by means of MOCVD,

or through an oxygen-contaminated nitrogen (N_2) source when III-nitride semiconductor materials are grown by means of MBE. In the case of silicon contamination, contamination can occur if III-nitride semiconductors are grown on a silicon carbide (SiC) substrate.[64]

Early studies and experiments suggested that zinc (Zn), and magnesium (Mg) were promising substitutional impurities that could be used to obtain p-type GaN, and p-type $Al_xGa_{1-x}N$; however, it was later on demonstrated that Zn tends to compensate III-nitride semiconductors, and leads to the production of very resistive semiconductor materials.[20] On the other hand, Mg is currently the most successfully used kind of substitutional impurity used to obtain p-type GaN, and p-type $Al_xGa_{1-x}N$. For the sake if this discussion, it is worth mentioning, that the very first breakthrough in terms of p-type doping of GaN was achieved by Amano *et al.*[59], who were able convert highly compensated Mg-doped GaN samples, into p-type conductive by means of Low Energy Electron Beam Irradiation (LEEBI) post-growth anneal. Later on, improvements based on the work of Amano *et al.* were achieved by Nakamura *et al.*[145], who obtained samples of p-type GaN with hole concentration $p = 3x10^{18} cm^{-3}$, and a resistivity $\sigma = 0.2\,\Omega cm$ by means of post-growth anneal at 700 °C in a N_2 environment. The post-growth p-type conversion mechanism was later on understood, and associated with the activation of hydrogen-passivated Mg atoms in the lattice of Mg-doped GaN; in fact, in MOCVD grown Mg-doped GaN, and $Al_xGa_{1-x}N$, hydrogen atoms passivate Mg acceptor by forming a Mg-H complex, which can be cracked at a temperature higher than 700 °C in a neutral environment. Such topic will be discussed later on in this work. Furthermore, other kinds of substitutional impurities have been investigated, and they too will be discussed later on in this work.

2.1. Acceptor substitutional elements in GaN and $Al_xGa_{1-x}N$

There are three main criteria that can be used to evaluate the role of an acceptor substitutional elemental impurity (acceptor) in a semiconductor material: 1) solubility, 2) compensation stability, and 3) ionization energy. The solubility of an acceptor is defined as the equilibrium concentration of the impurity in the lattice of the semiconductor material, the compensation stability defines the stability of a given acceptor against compensation by other configurations, and the ionization energy is the energy required to ionize the acceptor atoms.[64]

The p-type doping of GaN, and AlGaN has bee attempted with the intentional incorporation of elements from Group I, and Group II, and research results have indicated that elements from Group II outperforms elements from Group I in terms of solubility.[67,68,69] Amphoteric elements of Group IV have been also considered.[20] Following is a summarization of the research results relative to the acceptors used in order to achieve p-type doping in GaN, and $Al_xGa_{1-x}N$:

- **Elements Group I**
  - *Lithium* (Li):
    - It is favorable for interstitial configurations because of its small atomic radius.[64]
    - It suffers from incorporation in interstitial sites, where it acts as a donor.[64]
- **Elements Group II**
  - *Beryllium* (Be):

  - It is favorable for interstitial configurations because of its small atomic radius.[64]
  - Its solubility is comparable to that of Mg.[64]
  - Its calculated ionization energy is slightly smaller than that of Mg, but results are not conclusive[69]; nonetheless, there is evidence that Be is marginally shallower than Mg, Zi, Ca, and C[70]. Based on luminescence, values for ionization energy vary from 250 meV to 290 meV in GaN.[71,72]
  - Controversial experimental results indicate MBE p-type doping with oxygen as a co-dopant. Be-O co-doping in cubic GaN grown on GaN was reported to have a carrier concentration in excess of 10^{20} cm^{-3}, and hole motilities in the 100 cm^2/Vs range.[69,73,74]

- *Cadmium* (Cd):
  - Luminescence analysis indicated a deep acceptor energy level.[75]
- *Calcium* (Ca):
  - It has poor solubility, and high formation energy.[64]
  - Its ionization energy is large compared to that of Mg.[64]
  - It is subject to hydrogen passivation at low temperatures (250 °C).[20]
  - P-type doping was achieved by ion implantation of Ca^+, or Ca^+ and P^+ followed by rapid thermal anneal at a temperature

higher than 1100 °C. The measured ionization energy was established to be 169 meV.[76]

- *Magnesium* (Mg):
  - Currently, magnesium is the prevalent p-type impurity, and it is commonly employed to achieve p-type conductivity both in GaN and $Al_xGa_{1-x}N$ alloys. This specific kind of acceptor will be discussed in detail in a dedicated session later on in this discussion.
- *Mercury* (Hg):
  - Luminescence analysis indicated emission peaks at 2.43 eV[77], and 2.9 eV, and an extrapolated ionization energy of 410 meV.[78]
- *Zinc* (Zn):
  - It has poor solubility, and high formation energy.[64]
  - The calculated ionization energy is large compared to that of Mg, and photoluminescence experiments suggest that the value for the ionization energy is 340 meV.[64,77,78]

- **Elements Group IV**
  - *Carbon* (C):
    - It was found to be amphoteric in GaN. It acts as donor if C is located on a Ga-site, and as an acceptor if C is located on a N-site.[79]

- Computational results indicate that it acts as an acceptor, and the experimental value for the ionization energy is 230 meV.[80,81,82]

2.1.1. Mg as the most successful acceptor substitutional element in GaN and $Al_xGa_{1-x}N$

Currently, Mg is the kind of elemental substitutional impurity that is most prevalently used to obtain p-type conductivity in GaN, and $Al_xGa_{1-x}N$; however, p-type doping levels, and the relative hole concentrations are acceptable in GaN, but decisively unsatisfactory in $Al_xGa_{1-x}N$. Hole concentrations of Mg-doped GaN, and Mg-doped $Al_xGa_{1-x}N$ at room temperatures are generally speaking less than $3x10^{18}$ cm^{-3} with a mobility of $9cm^2/Vs$[83]; however, hole concentrations larger than 10^{18} cm^{-3} are possible, but at the expense of low mobility. Due to the high binding energy (~200 meV) of Mg in GaN, acceptor activation ratios range between 10^{-2} and 10^{-3}; moreover, it is required to incorporate Mg in chemical concentrations in the 10^{20} cm^{-3}.[20] This scenario becomes even more challenging in the case of Mg-doped $Al_xGa_{1-x}N$, as the binding energy of Mg in $Al_xGa_{1-x}N$ increases with increasing Al mole fraction; hence, the hole concentration of Mg-doped $Al_xGa_{1-x}N$ decreases as the Al mole fraction decreases.[84] In addition, the negative correlation between the hole concentration in Mg-doped $Al_xGa_{1-x}N$, and the Al mole fraction of the former, is exacerbated by the compensation effect due to native defects such as nitrogen vacancies, and cation interstitials.[85]

Magnesium can be introduced in the lattice of GaN, or $Al_xGa_{1-x}N$ using a variety of crystalline growth methods; nonetheless, such a task is typically achieved either by means of MOCVD, or MBE: in the first case, a typical precursor is bis-cyclopentadienyl

magnesium [Cp_2Mg or $(C_5H_5)_2Mg$], and in the second case Mg is evaporated from a highly pure solid source, heated inside an effusion cell. The concentration of Mg as a substitutional impurity can be increased, but it was observed that he hole concentration levels off, and sometimes decreases after a certain Mg concentration is reached.[86] An investigation of this phenomenon was first conducted in 1996, and research results suggested that the solubility of Mg is the most limiting factor, in combination with incorporation of Mg on substitutional nitrogen sites, or on interstitial sites.[82]

2.1.2. P-type doping of GaN, and $Al_xGa_{1-x}N$: ionization energy of Mg

Despite the extensive investigation of the role of Mg as a substitutional acceptor in GaN, and $Al_xGa_{1-x}N$, a lot about its electrical activity still waits to be revealed. For instance, the ionization energy of Mg in GaN has been found to have a broad range of values that have been determined by using a variety of different investigation techniques. By means of Hall Effect measurements, Tanaka *et al*. attributed two values to the ionization energy of Mg in MOVPE grown Mg-doped GaN: 125 meV, and 157 meV.[25] Huang *et al*. reported ionization energies of 136 meV, 124 meV, and 160 meV in MOVPE grown Mg-doped GaN samples[87], and 131 meV in MOCVD grown Mg-doped GaN was reported by Johnson *et al*.[88] Katsuragawa et al.[89] reported ionization energy of 157 meV, and a value of 208 meV was reported by Götz *et al*.[90] By means of optical deep-level transient spectroscopy (ODTLS), Seghier *et al*.[91] reported Mg ionization Energy of 130 meV in MOCVD grown Mg-doped GaN samples. Using thermal admittance spectroscopy (TAS), Nakano and Jimbo[92] reported Mg ionization energy of ~135 meV in MOCVD grown GaN based Shottky diodes; a value of ~160 meV was instead determined by means of deep level transient spectroscopy (DTLS).[92]

Investigations of the ionization of Mg in MOCVD grown Mg-doped GaN by means of time resolved photoluminescence (PL) conducted by Smith *et al.*[93] suggested a Mg ionization energy of 290 meV. For what concerns Mg-doped $Al_xGa_{1-x}N$, it has been determined that the ionization energy of Mg increases with increasing percentage of Al.[84,94,95,89,25,26,] Ionization energies relative to Mg incorporated in $Al_xGa_{1-x}N$ have been reported to ~260 meV, and ~310 meV for an Al mole fraction of ~27%, and ~30% respectively by Saxler *et al.*[84], 232 meV, and 252 meV for an Al mole fraction of 15%, and 20% respectively by Chernyak *et al.*[96] As shown in Figure 13, ionization energy values for Mg in $Al_xGa_{1-x}N$ have been observed in increasing range from 185 meV to 500 meV for an increasing range of Al mole fraction from 0% to 45%, and estimated to be 565-665 meV for 60% Al mole fraction by Johnson.[97]

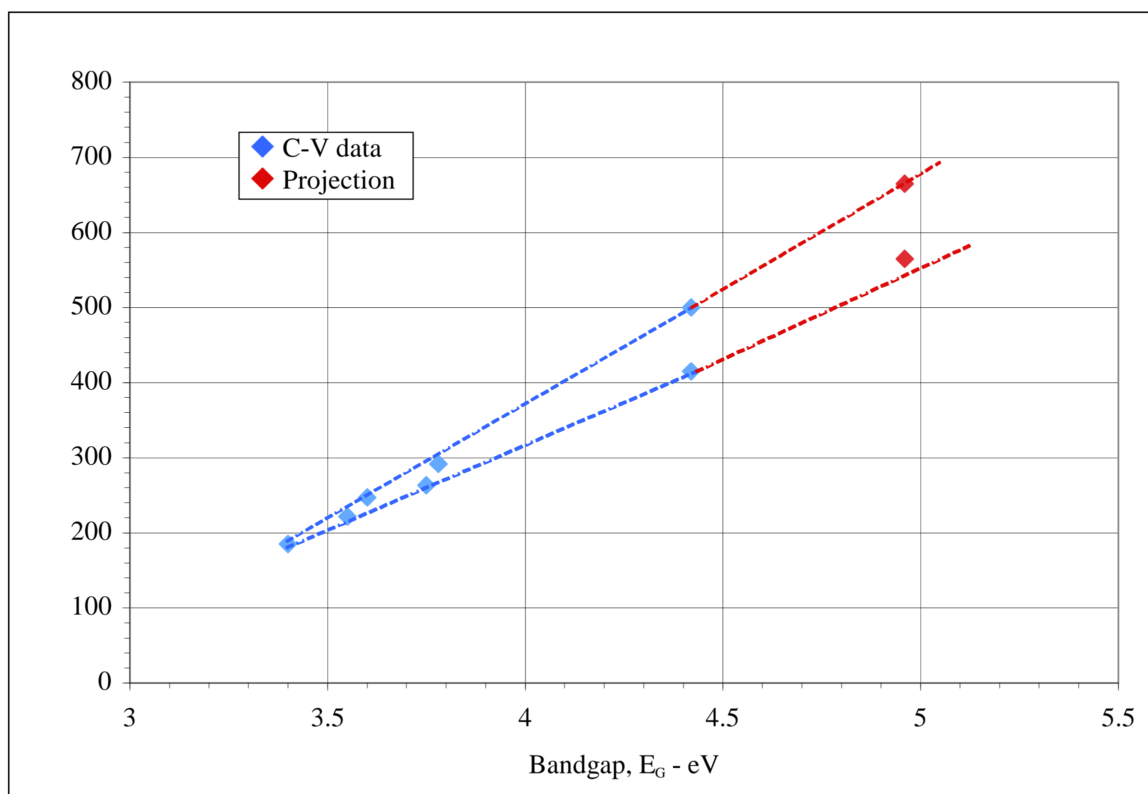

Figure 13: Ionization energy values for Mg in $Al_xGa_{1-x}N$. Adapted from Johnson.[97]

For the sake of the reader's comprehension, the value for the Al mole fraction is extrapolated from the value of the bandgap of $Al_xGa_{1-x}N$ shown in Figure 13 by using

$$E_g(x) = E_g(AlN)x + (1-x)E_g(GaN) - bx(1-x) \qquad \text{Equation 16}$$

where x is the Al mole fraction, $E_g(AlN) = 6.2\ eV$, $E_g(GaN) = 3.4\ eV$, and

$b = 0.89 \quad bowing\ parameter$[2].

In Figure 14, ionization energy values for Mg in $Al_xGa_{1-x}N$ have been plotted as a function of Al mole fraction; the values of the former were extrapolated from Johnson[97], by using Equation 16.

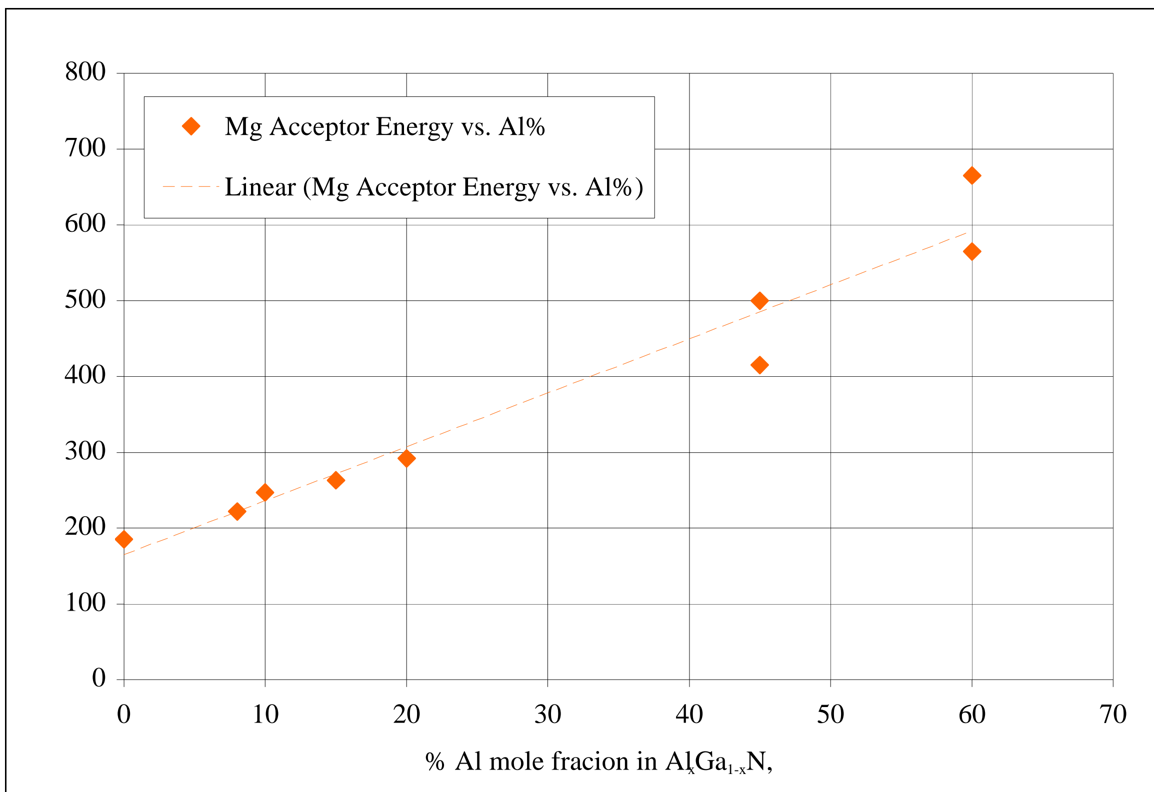

Figure 14: Mg acceptor energy as a function of Al mole fraction. Extrapolated from Johnson.[97]

Figure 15 plots the bandgap of $Al_xGa_{1-x}N$ as determined by using by using Equation 16 with bowing parameter *b*=0.89, and the bandedge emission of $Al_xGa_{1-x}N$ as a function of Al mole fraction.

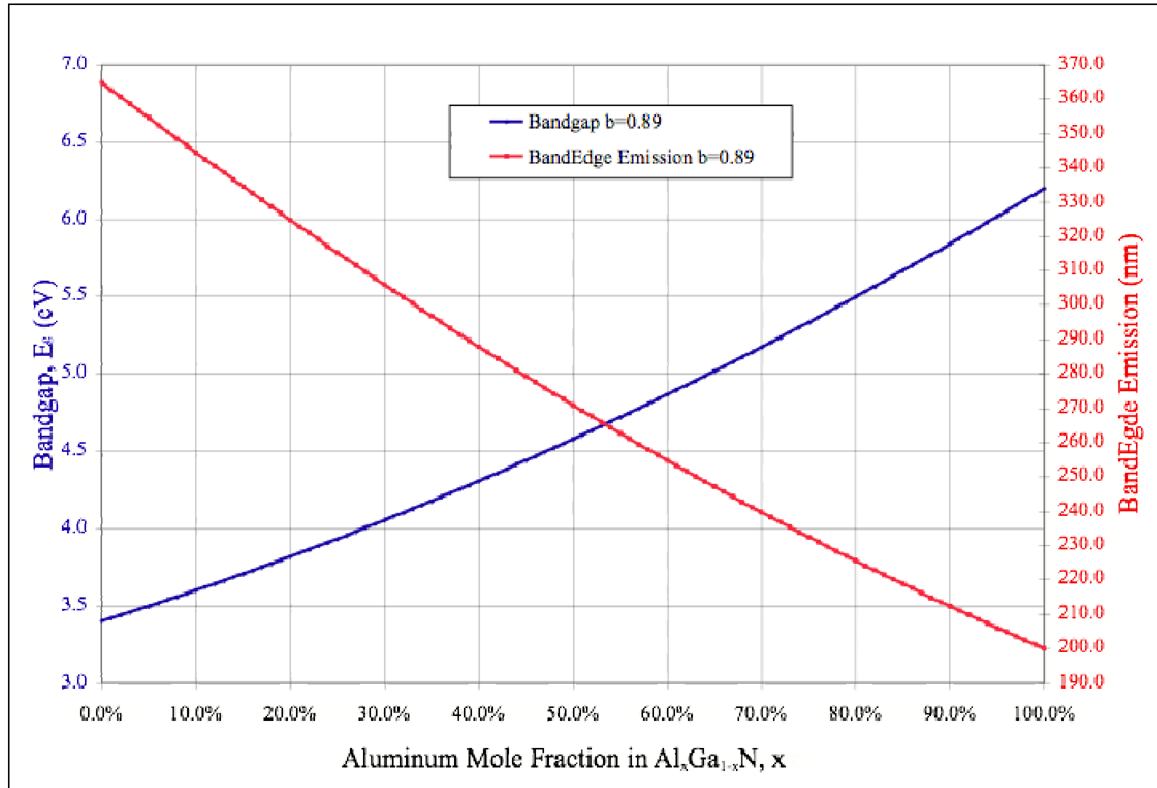

Figure 15: Plot of the band bandgap of $Al_xGa_{1-x}N$ as determined by using by using Equation 16 with bowing parameter *b*=0.89, and the bandedge emission of $Al_xGa_{1-x}N$ as a function of Al mole fraction.

The bowing parameter, *b*, has controversial parameters, and still is object of discussion. Negative (-1.0 eV), zero (0 eV), and positive (0.25, and 1.0 eV) values of the bowing parameters were compiled by Yoshida *et al.*[98], and Wickended *et al.*[99] Positive bowing parameters were also determined by Lee *et al.*[100] (0.69 eV), Angerer *et al.*[101] (1.3 eV), Lin *et al.*[102] (0.35 eV), Khan *et al.*[103] (0.89 eV). Figure 16 plots the bandgap of

[2] A value of 0.89 eV was used for the computation of the Al mole fraction.

$Al_xGa_{1-x}N$ as determined by using by using Equation 16 with various bowing parameter*s*, and the bandedge emission of $Al_xGa_{1-x}N$ as a function of Al mole fraction.

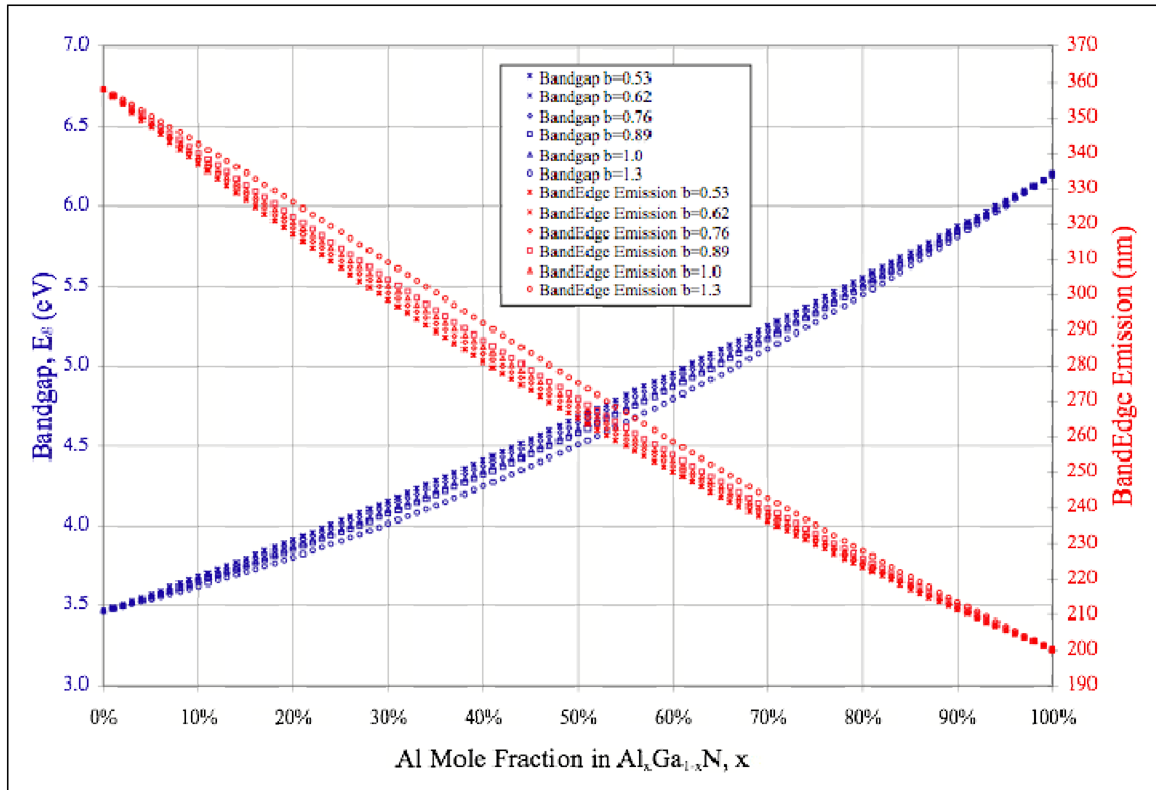

Figure 16: Plot of the band bandgap of $Al_xGa_{1-x}N$ as determined by using by using Equation 16 with various bowing parameters, and the bandedge emission of $Al_xGa_{1-x}N$ as a function of Al mole fraction.

2.1.3. P-type doping of GaN, and $Al_xGa_{1-x}N$: counteracting role of hydrogen

Hydrogen contamination is a phenomenon that can be hardly controlled, as the very small atomic radius of this element allows the former to easily diffuse through high density materials, such as the walls of a MOCVD, or MBE reactor; furthermore, hydrogen contamination can occur during MOCVD, or HVPE growth, since hydrogen is used a carrier gas.[85]

This kind of contamination can greatly affect the electrical behavior of Mg-doped GaN, and $Al_xGa_{1-x}N$ films, which very often result to be highly resistive; in fact, hydrogen atoms act as donors (H^+) in Mg-doped GaN, and Mg-doped AlGaN, and passivate the acceptor atoms of Mg by forming a Mg-H complex, which is depicted in Figure 17.[85,20]

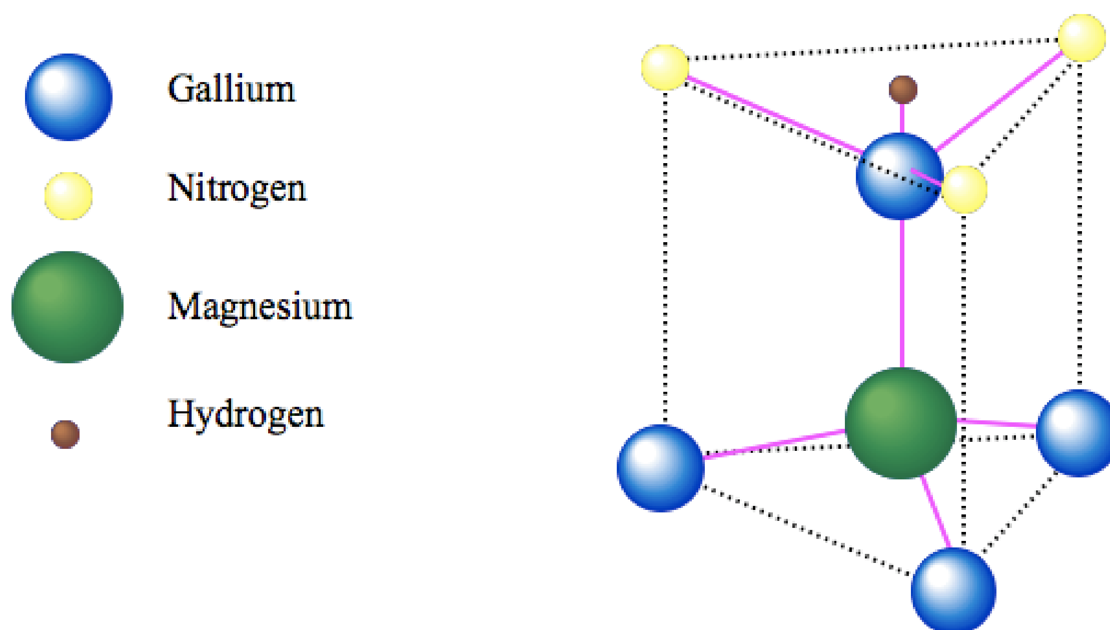

Figure 17: Schematic diagram illustrating the Mg-H complex in GaN. The atom of hydrogen is spatially located in the anti-bonding site, which is though to be the most plausible location. Adapted from Nakamura *et al.*[85]

Theoretical efforts have been attempted to explain the dynamics of the Mg-H complex, and the spatial position of the atom of hydrogen with respect to nitrogen, gallium, and nitrogen has been the hinge of controversy. According to Neugebauer *et al.*[104], the anti-bonding site illustrated in Figure 17 is energetically speaking more likely to be favorable with respect to the bond-center site; au contraire, Okamoto *et al.*[105] determined that the energetically favorable position of hydrogen is the bond-center, or rather in between the substitutional atom of magnesium and its nearest nitrogen atoms. Recent findings, however, support the idea that the anti-bonding site is the more plausible.[20,85] The Mg-H complex with hydrogen positioned in the bond-center site is illustrated in Figure 18.

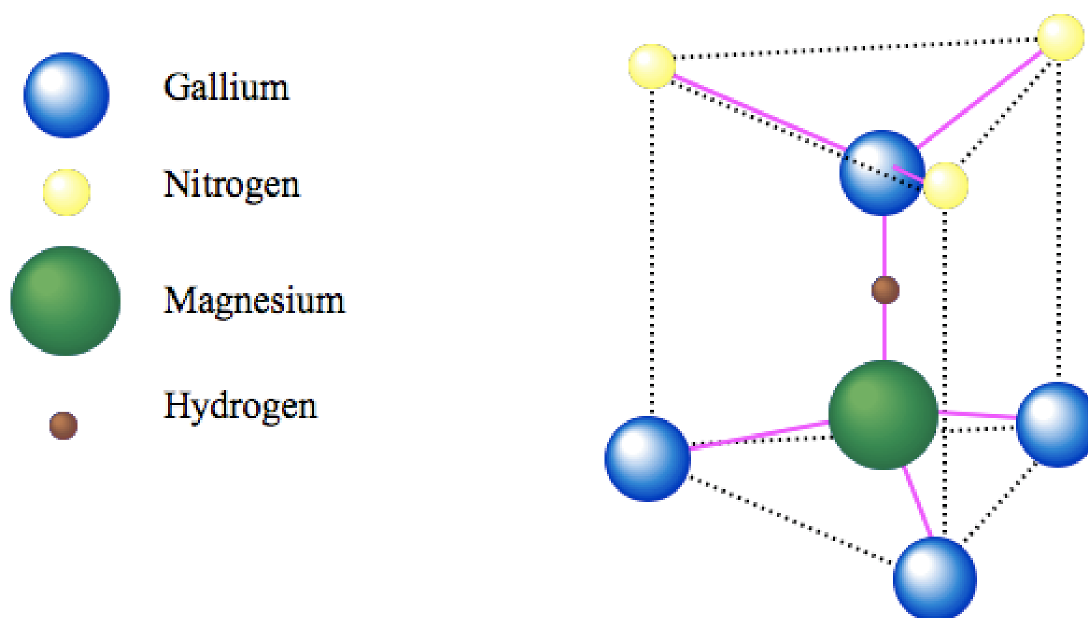

Figure 18: Schematic diagram illustrating the Mg-H complex in GaN. The atom of hydrogen is spatially located in the bond-center site. Adapted from Nakamura *et al.*[85]

Recent findings reported that acceptor passivation in Mg-doped $Al_xGa_{1-x}N$ can occur if a hydrogen plasma treatment is used; such treatment is often employed to prepared the surface of sapphire (Al_2O_3) wafers prior to the deposition of an aluminum nitride (AlN) buffer layer is deposited, or to passivate surfaces as a post-growth treatment. On this front, Polyakov *et al*. observed that the concentration of magnesium acceptors in Mg-doped $Al_xGa_{1-x}N$ with an Al mole fraction of 15% decreases as a result of hydrogen passivation by an order of magnitude after a half an hour hydrogen plasma treatment at a temperature of 250 °C.[106]

Growing Mg-doped GaN, and $Al_xGa_{1-x}N$ by means of RMBE can reduce hydrogen passivation, and there is evidence of RMBE grown Mg-doped GaN films deposited in a hydrogen-contaminating environment that showed p-type conductivity prior to any post-grown anneal process.[107] It is believed that Mg-doped GaN, and AlGaN grown by means of RMBE are subjected to an in-situ annealing effect that takes place during the cooling process that follows the material growth.[20] For the sake of the reader's comprehension, the passivation of a Mg acceptor atom in the crystalline lattice of GaN, due to the presence of hydrogen is illustrated in Figure 19.

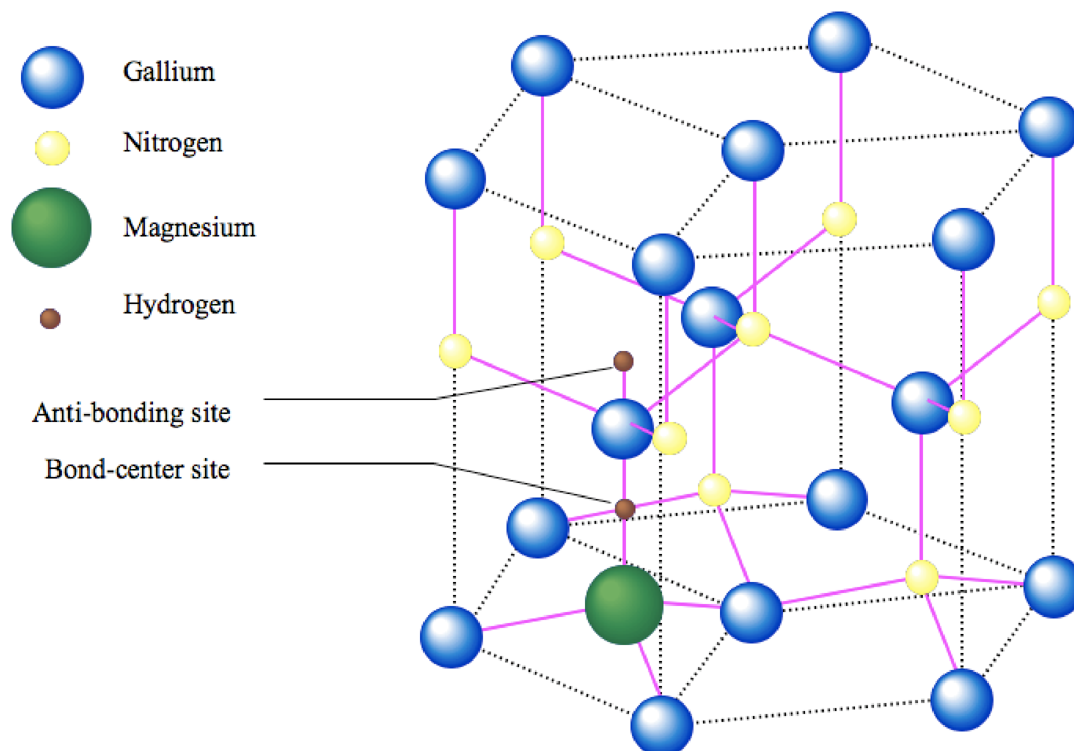

Figure 19: Schematic diagram of a Mg-doped GaN crystalline lattice. The illustration shows the passivation of the Mg accept atom due to the presence or of a Mg-H complex. The proposed bond-center, and anti-bonding sites for the hydrogen atom are also illustrated. Adapted from Nakamura *et al.*[85]

2.1.4. P-type doping of GaN, and $Al_xGa_{1-x}N$: activation of Mg acceptor atoms

The Mg-H complex, which is responsible for the passivation of Mg acceptor atoms in Mg-doped GaN and $Al_xGa_{1-x}N$ can be broken by means Low Energy Electron Beam Irradiation (LEEBI), which is a technique that was actually used to produce the very first samples of Mg-doped GaN that showed p-type conductivity.[108,109] Although the implications of the post-grown LEEBI activation process are not fully understood, it is believed that an electron beam generates electron-hole pairs (EHPs) in the semiconductor material that can either provide enough energy to provoke the dissociation of the Mg-H complex, or lower the energy level of the former.[59,85] Nonetheless, more recently the

activation of Mg acceptor atoms in Mg-doped GaN and $Al_xGa_{1-x}N$ is achieved either by means rapid thermal anneal (RTA), or high temperature anneal (HTA), which is often conducted in situ, as a post-growth treatment. As reported by Akano *et al.*, from the room-temperature of C-V measurements of MOCVD grown samples of Mg-doped GaN that were subjected to HTA, the effective hole concentration is seen to increase monotonically with the rise of the anneal temperature, as the latter progressively reaches 1300 °C.[110] From both thermal admittance and current DLTS measurements, Akano *et al.* observed that the depth of the acceptor level decreased from 136 meV to 117 meV with an anneal temperature up to 1200 °C.[110] The treatment used by Akano *et al.* consisted of a first anneal conducted for 30 minutes in a N_2 environment, with SiO_2 encapsulation layer at 700 °C, and a second anneal treatment conducted minutes in a N_2 environment, with SiO_2 encapsulation layer at a temperature in the range 1000 °C – 1300 °C.[110]

Investigations on the activation of Mg acceptor atoms in GaN and $Al_xGa_{1-x}N$ achieved by means of RTA confirmed that the RTA method is unquestionably valid. Götz *et al*. demonstrated an increased hole concentration, and a reduced resistivity in their Mg-doped GaN samples grown by means of MOCVD, and annealed by means of RTA over the temperature range of 500 °C – 850 °C, with time increments of 5 minutes.[119,111] More recently, p-type conductivity in Mg-doped $Al_xGa_{1-x}N$ with Al mole fraction up to 70% have been obtained by means or RTA in a nitrogen environment at temperature as high as 950 °C, with anneal time that can go from as low as 8 seconds, up to 10 minutes.[112,113,114,115]

2.2. Deep Level Defects in GaN and $Al_xGa_{1-x}N$

Deep level defects can function as carrier traps, recombination or generation centers de fact affecting the properties of a given semiconductor material. Generally speaking, deep level defects are energy states located in the bandgap of a semiconductor, with a binding energy larger than 100 meV (100 meV above the valence band, or 100 meV below the conduction band), or, in other terms, with a binding energy approximately larger than $4kT^3$ at room temperature. [116,117] A schematic diagram illustrating the concept of deep level defects in a semiconductor material is available in Figure 20.

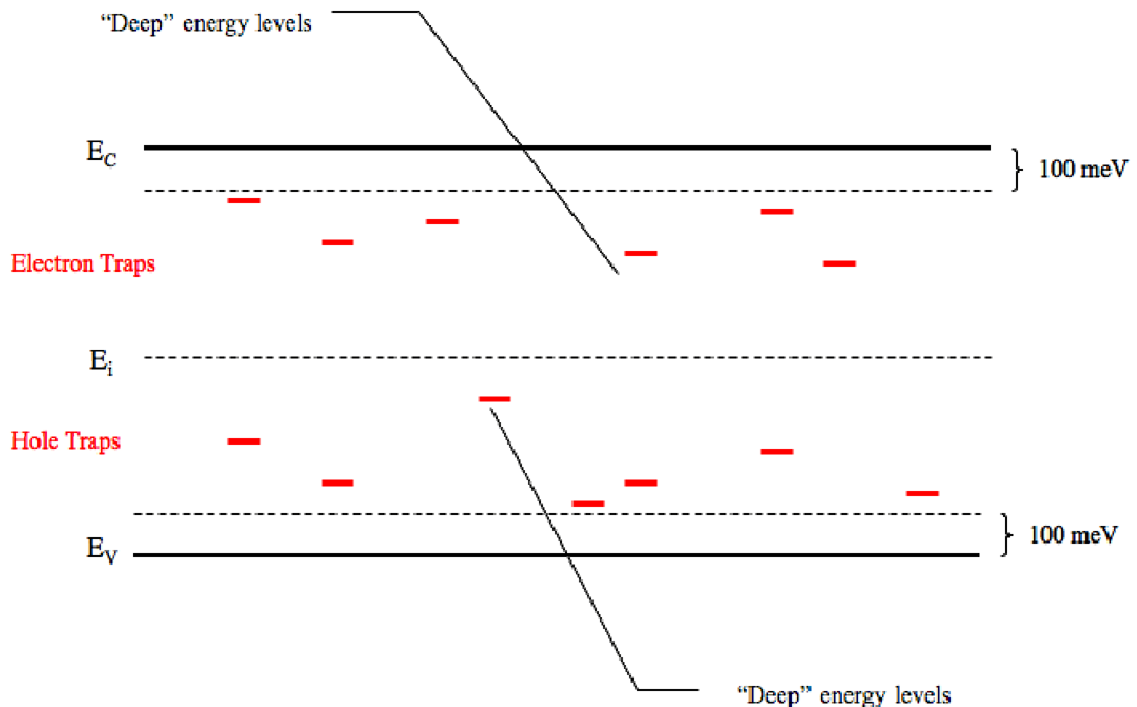

Figure 20: Schematics illustrating the concept of "deep level defects" in the bandgap of a semiconductor material.

---

[3] k is the Boltzmann's constant, $8.62\times10^{-5} eVK^{-1}$, and T is the temperature expressed in degree Kelvin, with T= 300°K at room temperature.

Deep level defects usually are isolated point defects, such atoms of metallic contaminants in the crystalline lattice of the semiconductor material, but they are also known to be caused by extended defects, such as Frenkel pairs, dislocations, and stacking faults. As shown in Figure 20, deep level defects that are located in the upper bandgap half are known as electron trap; hole traps instead indicate deep level defects locate in the lower bandgap half. Moreover, deep level defects can act as donors (charge state 0 / -), double donors (charge state 0 / - / --), acceptors (charge state + / 0), double acceptors (charge state ++ / + / 0), or amphoteric (- / 0 / +); however, the charge state does not affect the position in the band gap.[116]

2.2.1. Deep Level Defects in GaN

Deep level defects in MOCVD grown samples of GaN termed E1, E2, and E3, have been identified; they have energies in the range of 264 meV to 269 meV, 530 meV to 590 meV, and 662 meV to 686 meV, respectively.[20,118,119,120] Electron traps with energy levels of 490 meV, 580 meV, and 620 meV have been identified in n-type GaN, and hole traps with energy levels of 410 meV, 490 meV, and 590 meV have been identified in p-type GaN films. In addition, an electron trap with an energy level of ~ 600 meV in ion implanted n-type GaN, and an electron trap in the p-region of an MOVPE grown p-n$^+$ junction having an energy level of 590 meV have been identified; the latter is believed to be caused by a nitrogen vacancy/magnesium complex.[116] Similar deep level defects have been identified by Martin et *al.*: 285 meV, 310 meV due to implantation damage, 425 meV, 450 meV, and 600 meV due to RTA.[121] Zhu *et al*. reported deep level traps in MOVPE grown samples of Mg-doped GaN having 416 meV, 496 meV, and 596 meV, respectively. [122]

2.2.2. Deep Level Defects in $Al_xGa_{1-x}N$

Deep level defects in MBE grown n-$Al_xGa_{1-x}N$ Schottky photodiodes have been identified by Legodi *et al.,* and observed as being independent of Al mole fraction below a temperature of 320 °K; their energy level were reported as 274 meV, and 610 meV.[123] Mizutani *et al.* have identified electron, and hole traps by means of DLTS of MBE grown $Al_{0.3}Ga_{0.7}N$/GaN high electron mobility transistors (HEMTs): one electron trap at 590 meV, and two hole traps at 290 meV, and 550 meV, respectively.[124] Polyakov *et al.*[106] have reported electron, and hole traps in AlGaN-based LEDs due to Mg in-diffusion; such traps were determined to have 550 meV and 850 meV (electron traps), and 400 meV and 850 meV (hole traps). Seghier *et al*. have reported metastable deep level defects in $Al_{0.3}Ga_{0.7}N$ with emission energy of 800 meV, and optical ionization energy of 1.2eV.[125,126] Deep level defects in $Al_{0.12}Ga_{0.88}N$ having ionization, and optical energies of 610 meV, and 770 meV, respectively were determined via DTLS, and optical DTSL.[127,128] Recently, Kikawa *et al*. have reported an Al mole fraction dependence of deep level defects in $Al_xGa_{1-x}N$; the result of their work, indicates that the energy depth of deep level defects is distributed from 320 meV to 470 meV from the conduction band for Al mole fraction from 19% to 30% respectively.[129]

2.3. Enhanced p-type doping in GaN and $Al_xGa_{1-x}N$

Different strategies have adopted to improve the p-type doping of GaN, and $Al_xGa_{1-x}N$, and the employment of short period super lattices (SPSLs) is currently one of the most successfully used. A SPSL is term used to indicate a heterostructure composed by a vertically grown, periodic arrangement of layers of Mg-doped GaN, and ad-hoc tailored Mg doped: $Al_xGa_{1-x}N$; such structure is also characterized by a short-period oscillation of

the valence band, and acceptor atoms are ionized when the balance band edge is located below the Fermi level. As a result, in a Mg-doped GaN/AlGaN SPSL, holes are accumulated in the region where the band edge is close to the Fermi level; more precisely, the carriers are confined within parallel sheets whose carrier density is much higher than that of a simple bulk film.[124]

As proposed by Schubert *et al*., a SPSL increases the hole concentration by allowing deep acceptors in the layers with the larger bandgap ($Al_xGa_{1-x}N$) to ionize into the valence band of the adjacent material with a lower bandgap (GaN). Such applications have been successfully attempted both with n-type, and p-type $Al_xGa_{1-x}N$/GaN structures, and data also suggest that in such cases the ionization energy of acceptor is reduced.[130,84]

CHAPTER 3: METAL-SEMICONDUCTOR CONTACTS

In this chapter, theory pertaining the nature of metal semiconductor contacts, and the fabrication of the former will be described.

3.1. Energy Band Theory of Metal Semiconductor Junctions: Schottky and Ohmic Contacts

Most if not all of the electronic devices that are integrated in a circuit rely on a metal-semiconductor junction, which is a transitional spatial region in which a semiconductor material and a metal establish an intimate contact. The nature of such a junction is explained by the well-understood Schottky theory, which was developed as early as 1932[131]; nonetheless, for the sake of the reader's perspective it is worth summarizing a few key concepts, starting with idealized scenario of a representative metal and a representative semiconductor that are not in contact, and hence do not interact. Such idealized scenario, which is illustrated in Figure 21, comprises two systems: System 1, a qualitative representation of a metal, and System 2, a qualitative representation of a semiconductor[132]. Assuming that each of the systems have a density of allowed electronic states per unity energy, $g(E)$, and that $n(E)$, and $v(E)$ are the density of occupied, and empty states per unit energy, respectively, then Fermi-Dirac distribution functions for the

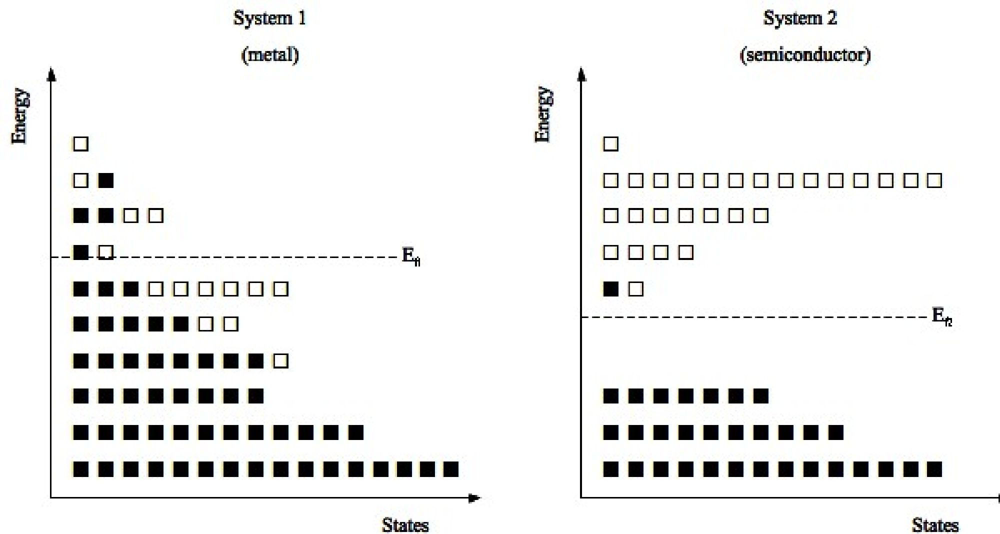

Figure 21: Qualitative representation of a metal (System 1), and a semiconductor (System 2) that are not interacting. Fermi level, and allowed electronic energy states for each of the systems are depicted as well. Empty electronic energy states are represented with □, while ■ indicates a filled electronic state. After Muller *et al.*[132]

the two systems are given by

$$f_{D_{1,2}}(E) = \frac{1}{1 + e^{\left(\frac{E - E_{f_{1,}}}{kT}\right)}} \qquad \text{Equation 17}$$

where $E_{f_{1,2}}$ is the Fermi level (eV), k is the Boltzmann's constant (eV K^{-1}), and T (K) is the temperature. The density of the occupied electronic states per unit energy is given by

$$n_{1,2}(E) = \left[g_{1,2}(E)\right]\left[f_{D_{1,2}}(E)\right] \qquad \text{Equation 18}$$

and the density of the empty electronic states per unit energy is given by

$$v_{1,2}(E) = \left[g_{1,2}(E)\right]\left[1 - f_{D_{1,2}}(E)\right] \qquad \text{Equation 19}$$

For the sake of the reader's perspective, Figure 22 illustrates the energy band diagrams of the above-mentioned metal and semiconductor, and the position of the relative Fermi levels within the of allowed electronic states per unity energy, $g(E)$.

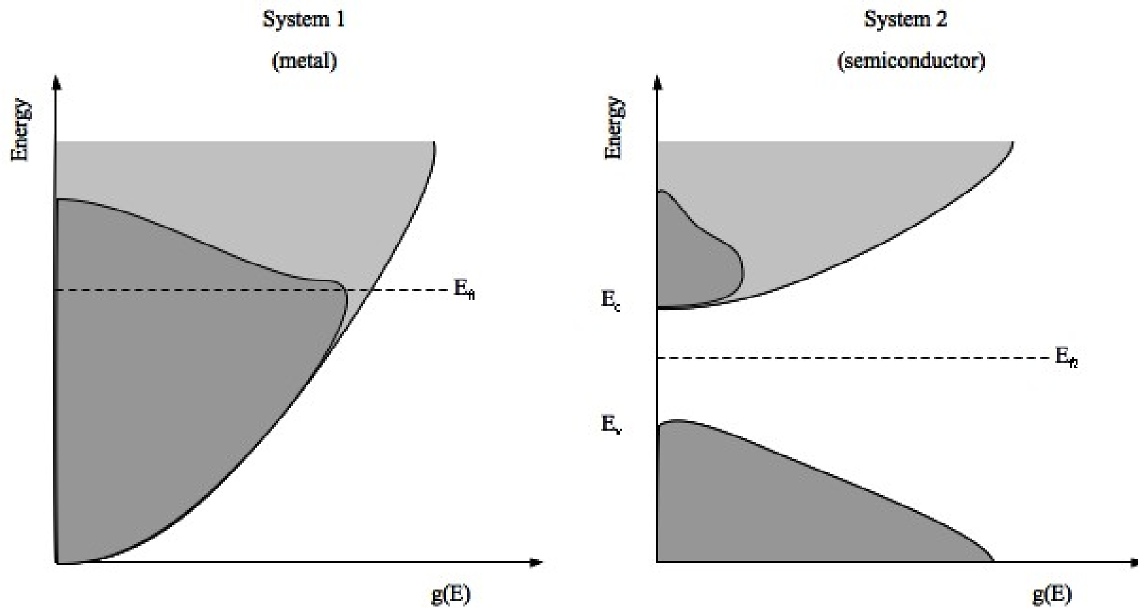

Figure 22: Allowed electronic states per unit energy, $g(E)$ for a representative metal (left) and a semiconductor (right). After Muller *et al*.[132]

As shown in Figure 22 the Fermi level in the metal is located within a continuum of allowed electronic states, while in the semiconductor the Fermi level is located in the so-called forbidden gap or "bandgap", a region in which under usual circumstances no electronic states are allowed. Again, for the sake of the reader's perspective, the diagram shown in Figure 23 must also be considered; in fact, Figure 23 illustrates the allowed energy states in the bulk of a metal and a semiconductor as a function of position, and also introduces the following quantities: E_0, Φ, and X.

The free-electron energy, E_0, is a quantity used as a reference, and it represents the energy of free standing electron; more precisely, the energy that an electron would

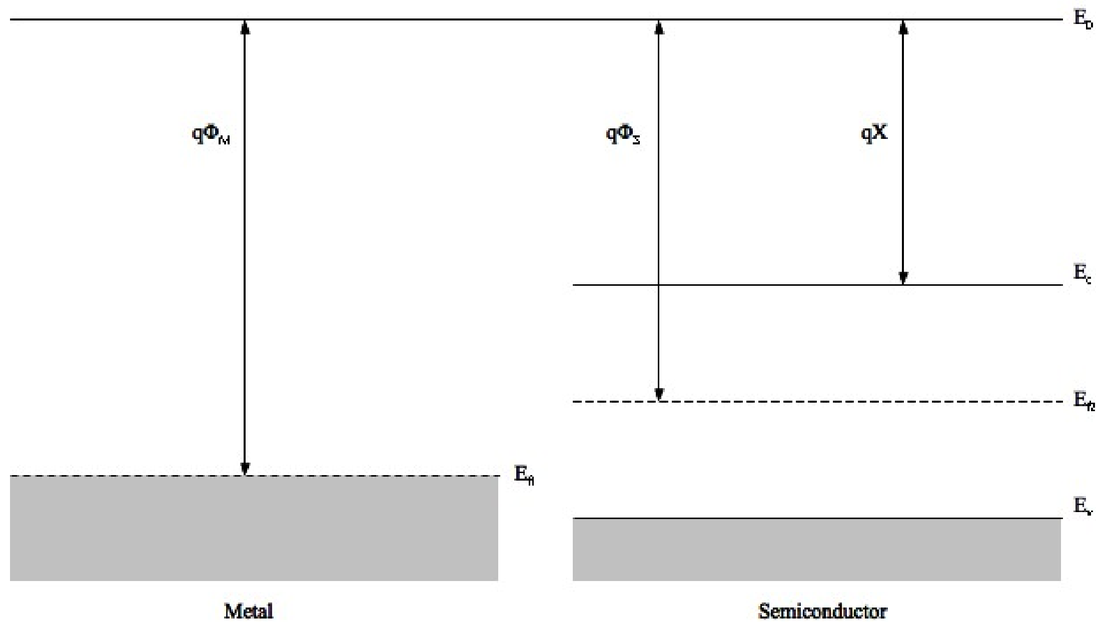

Figure 23: Allowed energy states in the bulk of a metal (left) and a semiconductor (right) as a function of position. After Muller *et al*.[132]

have if it were free from any influence of the bulk of a given material. As an alternative, E_0 can be interpreted as the amount of energy that is necessary to extract an electron from the bulk of a given material. The distance between E_0 and the Fermi level, E_f, is known as the work function, Φ, which is usually expressed in terms of eV with the symbol $q\Phi$. The distance between E_0 and the edge of the conduction band, between E_c, is known as the electron affinity, Χ, which is usually expressed in terms of eV with the symbol $q\mathrm{X}$.

When an intimate contact between the above-mentioned metal, and semiconductor (System 1, and 2) is established, an electron transfer between the two systems will take place, and eventually a condition of thermal equilibrium will be achieved; more precisely, there will be no net transfer of electrons at any energy. Such condition can be expressed mathematically by taking in consideration the fact that the transfer probability is

proportional to the density of the occupied electronic states per unit energy, $n_{1,2}(E)$, and hence to the electrons that are available for transfer at a given energy, and also proportional to density of the empty electronic states per unit energy, $v_{1,2}(E)$, and hence to the available states that electrons can occupy.[132] Moreover, by taking in consideration that the transfer probability is the same for the two systems, then it must be that

$$[n_1(E)][(v_2(E))] = [n_2(E)][(v_1(E))] \quad \text{Equation 20}$$

By using Equation 18 and Equation 19, Equation 20 can be rewritten as

$$[f_{D1}(E)][g_1(E)][1 - f_{D2}(E)][g_2(E)] = [f_{D2}(E)][g_2(E)][1 - f_{D1}(E)][g_1(E)] \quad \text{Equation 21}$$

or simply as

$$[f_{D1}(E)][g_1(E)][g_2(E)] = [f_{D2}(E)][g_2(E)][g_1(E)] \quad \text{Equation 22}$$

Equation 22 does not only implies that $f_{D1}(E) = f_{D2}(E)$, but also that $E_{f1} = E_{f2}$ (from Equation 1); consequently, when a junction between a metal, and semiconductor (System 1, and 2) has reached thermal equilibrium, their relative Fermi levels are the same, and this important piece of information is crucial to understand the nature of a metal-semiconductor junction[132].

3.1.1. Schottky and Ohmic Contacts

Considering that the work function is an inherent property of a material (metal or semiconductor in this particular case), there are at least two distinct possible scenarios: one scenario in which the work function of the metal is larger than that of the semiconductor, $\Phi_M > \Phi_S$, and another scenario in which the wok function of the metal is smaller than that of the semiconductor, $\Phi_M < \Phi_S$. These two scenarios lead to two classes of contacts (the intimate contact between a metal and a semiconductor), which are known

as rectifying or Schottky, and Ohmic. Nonetheless, for the sake of the reader's perspective it is necessary to mention that Fermi level, E_f, and hence the work function of a semiconductor, Φ_S, are affected by the substitutional impurity concentration. Having stated that, this discussion will be simplified by including an n-type semiconductor.

Figure 24a illustrates the case of an idealized junction between a metal, and an n-type semiconductor, where $\Phi_M > \Phi_S$. Figure 24a also illustrates that the Fermi level in the n-type semiconductor is placed at a higher location with respect to the Fermi level of the metal; in other words, $E_{f_S} > E_{f_M}$. According to Equation 22, when the metal and the semiconductor are intimate contact and form a junction, at equilibrium, it must be that $E_{f_S} = E_{f_M}$; thus, a charge transfer (electrons) from the semiconductor to the metal must occur so that E_{f_S} and E_{f_M} are equal. The diagram shown in Figure 24b was constructed by taking in consideration that the free-electron energy, E_0, must be continuous, and that both the electron affinity, X, which is a material property, and the Fermi level must be constant. Moreover, Figure 24b introduces the following quantities: Φ_B, and Φ_i. The effective potential barrier height between the metal and the semiconductor, Φ_B, is commonly called the Schottky barrier height, while Φ_i is known as the built-in potential. Both Φ_B, and Φ_i are usually expressed in terms of eV with the symbols $q\Phi_B$, and $q\Phi_i$ respectively. A metal-semiconductor junction of this kind hence leads to the formation of a Schottky contact.

From the investigation of Figure 24b the Schottky barrier height, Φ_B, can be determined as

$$q\Phi_B = q\Phi_M - qX \qquad \text{Equation 23}$$

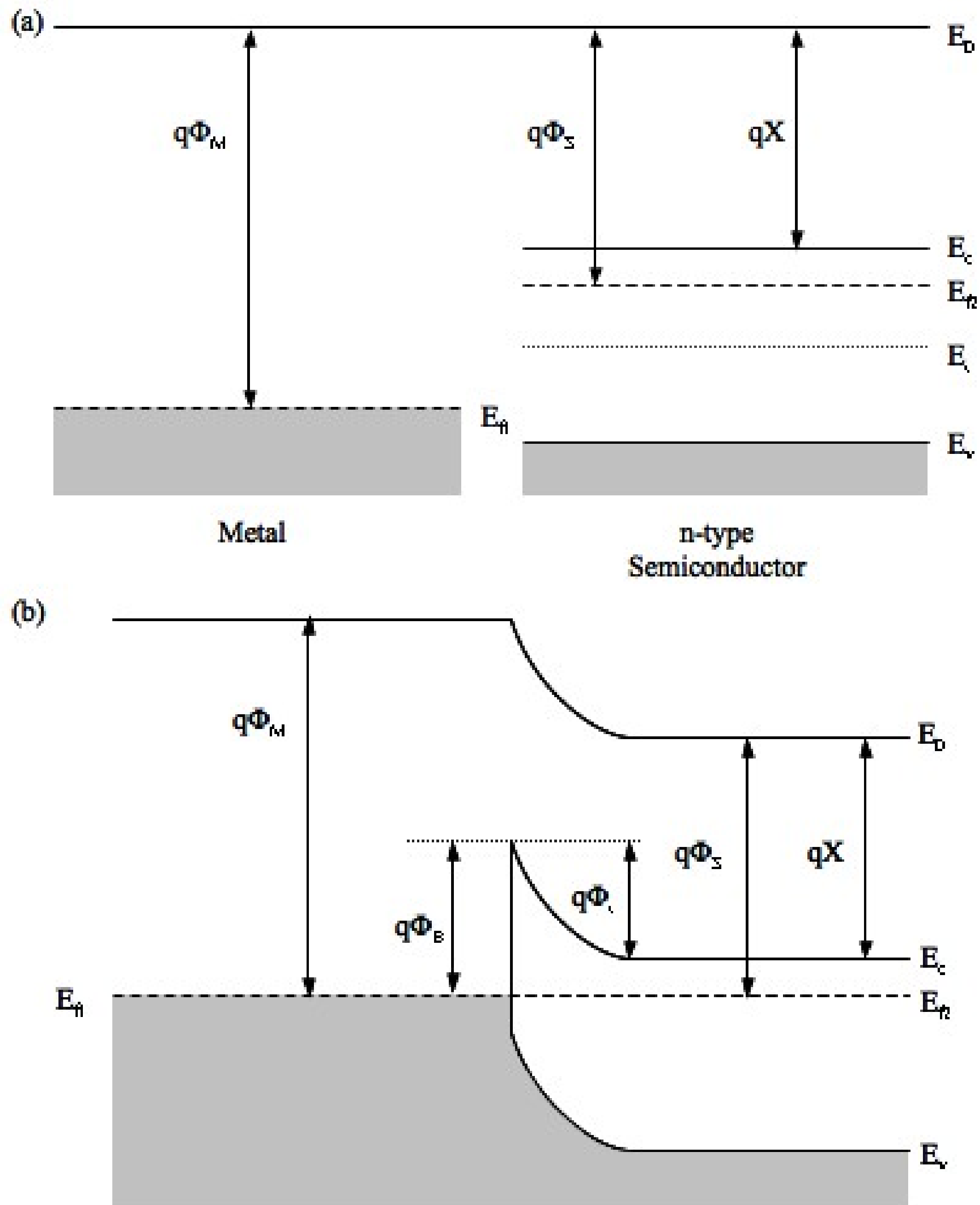

Figure 24: (a) idealized representation of allowed energy states in the bulk of a metal (left) and an n-type semiconductor (right) as function of position. (b) Idealized energy vs. space band diagram of a Schottky contact between a metal, and an n-type semiconductor at equilibrium. After Muller *et al*.[132]

Also, from the investigation of Figure 24b the built-in potential, Φ_i, can be determined as

$$q\Phi_i = q\Phi_M - q\Phi_S \qquad \text{Equation 24}$$

In addition, it is worth observing that the idealized band diagram illustrated in Figure 24b indicates that no band bending takes place in the metal, as the former can be considered as a perfect conductor with a certain degree of approximation; thus, as a perfect conductor, it does not allow the formation of a potential. The band bending in the semiconductor indicates the presence of the field generated at the junction as a consequence of the carriers that migrated from the semiconductor (which left behind an area reach with ionized donors in the semiconductor) to the metal.

A metal, and an n-type semiconductor can form an Ohmic contact when the work function of the metal is smaller than that of the semiconductor; more precisely, as shown in Figure 25a, when $\Phi_M < \Phi_S$. In this case, when an intimate contact is established between the metal, and the semiconductor, as illustrated in Figure 25b, the respective Fermi levels must align; thus carriers (electrons) flow from the metal into the semiconductor, and forcing the bands of the former to bend up and form a barrier. No depletion region is formed in the metal, as the former can be consider as a perfect conductor with a certain degree of approximation; thus, as a perfect conductor, it does not allow the formation of a potential. This feature, which is typical of an Ohmic contact, implies that the potential barrier for electrons is rather modest, and can hence be overcome by applying a relatively small voltage bias[133].

From the investigation of Figure 25b the built-in potential, Φ_i, can be determined as

$$|q\Phi_i| = q\Phi_n - (q\Phi_M - qX) \quad \text{Equation 25}$$

where $q\Phi_n = (E_C - E_f)$ in the bulk. Moreover, the condition $q\Phi_n = (q\Phi_M - qX)$ is known as the neutral contact condition; more precisely the condition of no built-in

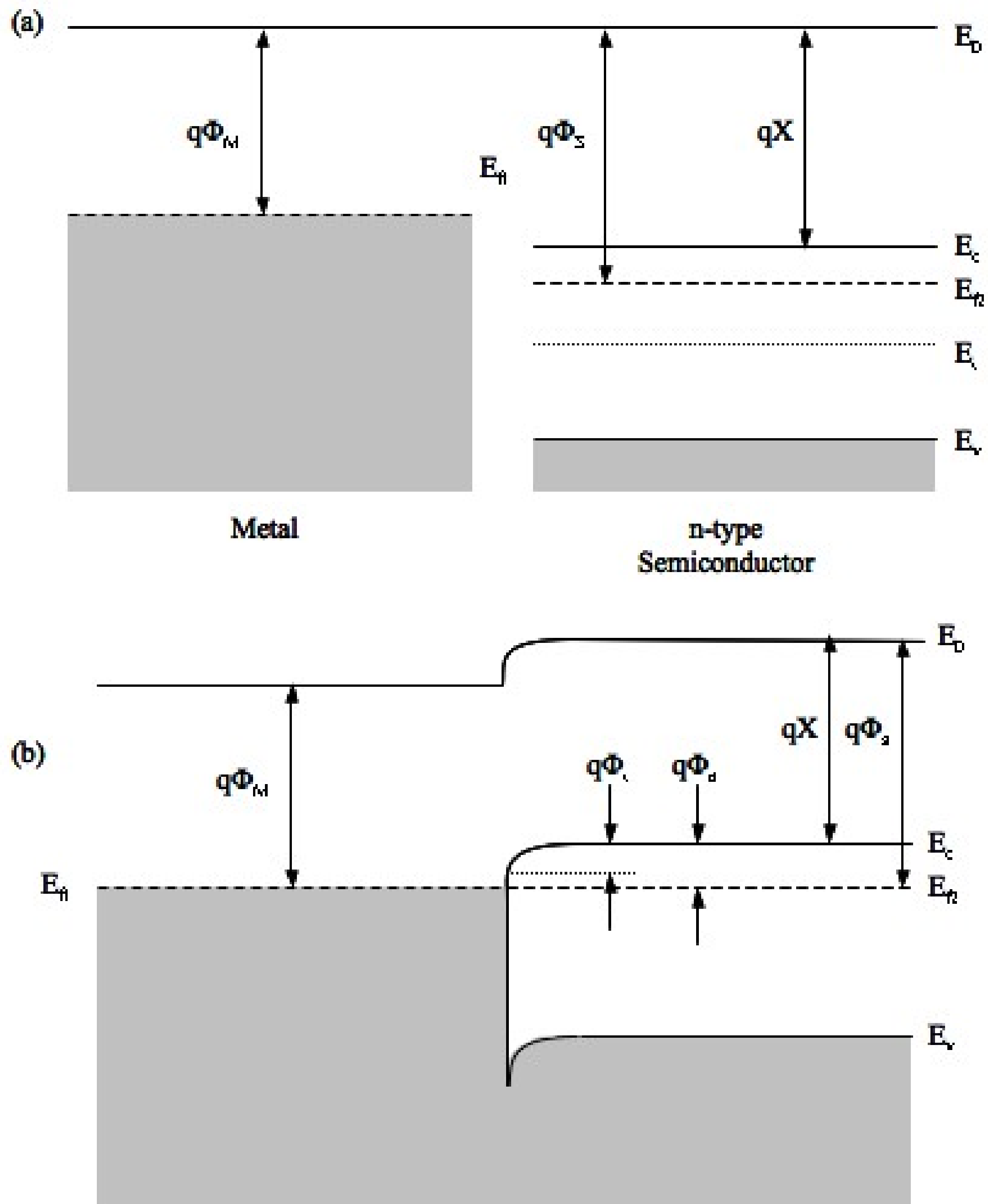

Figure 25: (a) idealized representation of allowed energy states in the bulk of a metal (left) and an n-type semiconductor (right) as function of position. (b) Idealized energy vs. space band diagram of an Ohmic contact between a metal, and an n-type semiconductor at equilibrium. Adapted from Brennan.[133]

voltage, and a surface with an electron density equivalent to that in the bulk. In summary, a contact between a metal, and an n-type semiconductor can either be Schottky, or Ohmic: in the first case, the energy bands bend up (if represented as function of position as shown in Figure 24 and Figure 25), while in the second case, the energy bands bend down. The opposite scenario occurs in the case of a contact between a metal, and a p-type semiconductor, as illustrated in Figure 26.

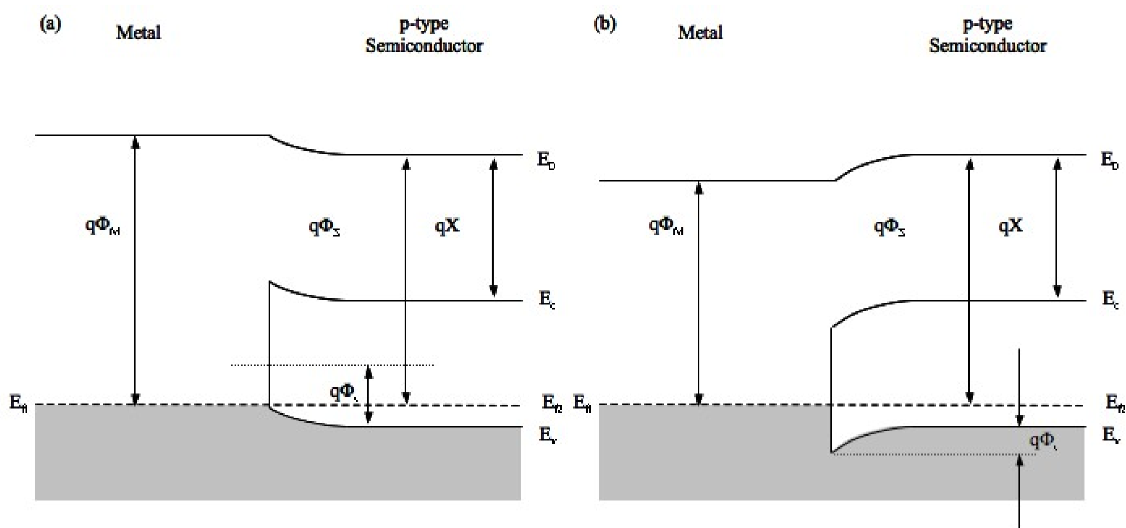

Figure 26: Energy band diagrams of metal-p-type semiconductor junction at equilibrium for (a) $\Phi_M > \Phi_S$ – Ohmic contact, and (b) (a) $\Phi_M < \Phi_S$ - Schottky contact. Adapted from Kim, and Baik[134].

Figure 26a illustrates the band structure of a junction formed by a metal, and a p-type semiconductor when the work function of the metal is larger than that of the semiconductor; more precisely, when $\Phi_M > \Phi_S$. When these two materials form a junction, the Fermi levels must align. Thus, there is a net flow of electrons from the p-type semiconductor into the metal, which produces an excess of holes in the semiconductor, and causes the energy bands in the semiconductor to band upward. In this case an Ohmic contact is obtained, and when a forward bias (a positive voltage the p-type

semiconductor, and negative voltage on the metal) is applied, the extra holes in the semiconductors will be accelerated toward the metal, therefore creating a current in the positive direction with respect to the applied voltage. Inversely, when a reverse bias is applied (a negative voltage on the p-type semiconductor, and a positive voltage on the metal) the excess electrons will be accelerated toward the semiconductor. In terms of I-V characteristics, the flowing current and the applied voltage bias have a linear relationship.

Figure 26b illustrates the band structure of a junction formed by a metal, and a p-type semiconductor when the work function of the metal is smaller than that of the semiconductor; more precisely, when $\Phi_M < \Phi_S$. When these two materials form a junction, the Fermi levels must align. Thus, there is a net flow of electrons from the metal into the p-type semiconductor, thereby decreasing its majority-carrier hole concentration. In this case a Schottky contact is obtained, and when a forward bias, V, is applied, the built-in potential, Φ_i, will be reduced to $\Phi_i - V$, and electrons in the semiconductor conduction band can diffuse across the depletion region to the metal. When a reverse bias, V_R is applied, the built-in potential, Φ_i, will be increased to $\Phi_i + V_R$; thus the electron flow is restrained.

3.1.2. Schottky Barrier Lowering

A more precise expression for the Schottky barrier (Equation 23) can be obtained if the image force barrier lowering is considered.[133] The concept of image force barrier is based on the assumption that an electron located in proximity of the junction of a metal-semiconductor interface will attract an equal, yet opposite surface charge, which is called "image charge". Moreover, it assumes that there are no mobile or fixed charges around the electron as it approached the metal-semiconductor junction, and that the time for the

surface charge to build up, as well as the time for the semiconductor to be polarized around the moving electron, is smaller than the transit time of the moving electron itself[135]. The concept of image charge is illustrated in Figure 27.

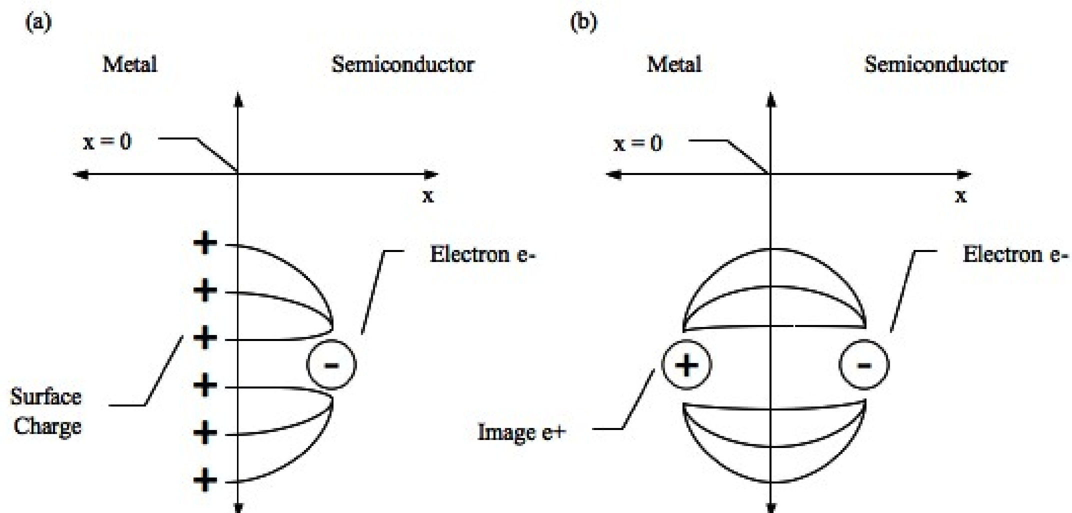

Figure 27: (a) Surface charge due to electron located in proximity of an ideal metal-semiconductor, and (b) field lines and image charge of the afore-mentioned electron. Adapted from Van Zeghbroeck [135].

As shown in Figure 27, the field lines across the metal semiconductor junction are continuous in the case of the image charge; such a concept is justified by the fact that electric field lines are perpendicular to the surface of a perfect conductor, and that the metal-semiconductor junction is thought to be ideal, and hence perfectly flat[135].

Figure 28 illustrates the concept of image-force barrier lowering, which will be discussed here in reference to a junction formed between an n-type semiconductor and a metal just like the one illustrated, in Figure 24. The Image Force Lowering shown in Figure 28 was constructed by considering the fact that a conducing metal sheet affects an electron as much as an equidistant image charge of opposite sign placed behind the plane with respect to x=0.

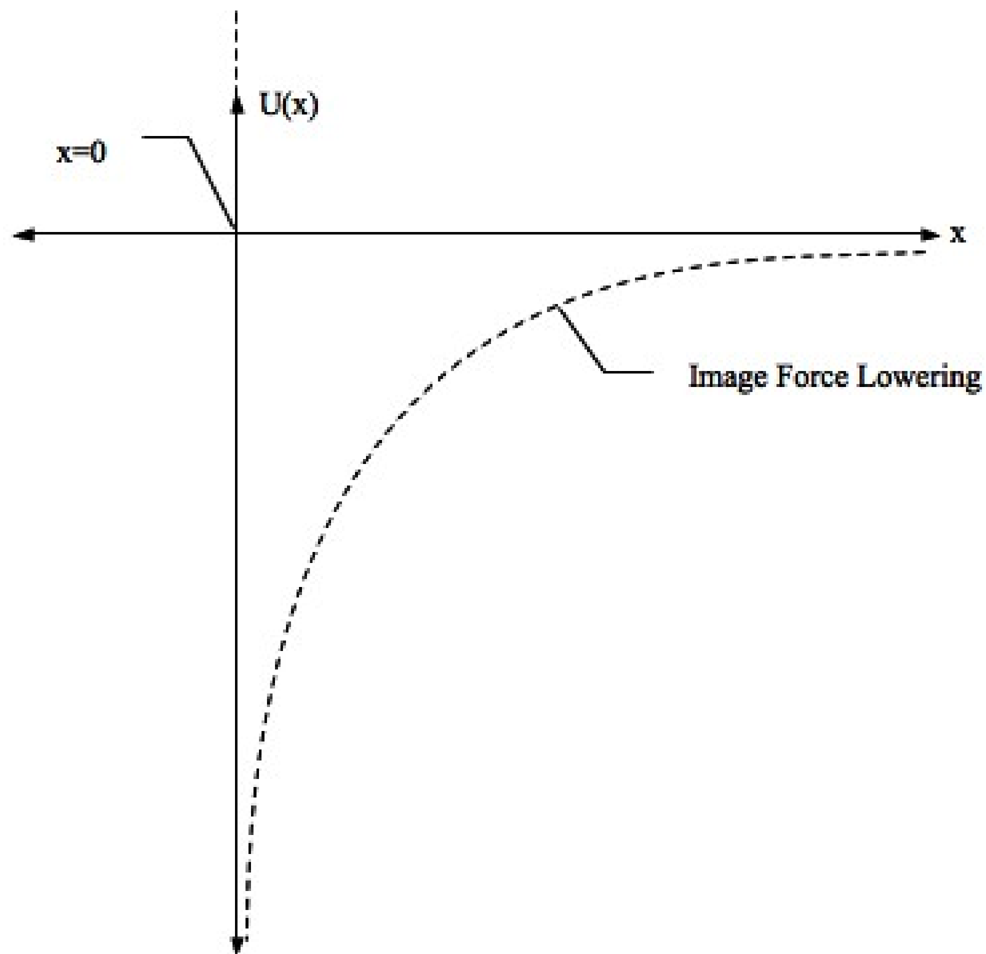

Figure 28: Potential energy diagram as a function of position for a free electron in proximity of a conducting metal sheet at equilibrium. The Image Force Lowering is shown. Adapted from Muller *et al*.[132] and Brennan.[133]

In other words, when an electron is moved away from a conducting metal plane, an equal but opposite sign charge is induced on the metal plane as described by the Gaussian law. Since an infinite conducting sheet can be placed midway between a point charge dipole without effecting the field and the potential line of the system, and since an infinite conducting sheet can only sustain perpendicular electric field components (no tangential components can be sustained by an infinite conducting sheet), the field due to an electron in proximity of an conducting sheet is identical to the one due to an equal but opposite sign charge.[132, 133]

In order to construct the Image Lowering Curve illustrated in Figure 28, let us consider a free electron moving in proximity of a conductive metal sheet, which is subjected to a coulombic force expressed by

$$F(x) = -\frac{q^2}{4\pi\varepsilon_0 (2x)^2} \qquad \text{Equation 26}$$

where x is the distance of the free electron from the conducting sheet, q is the charge of the free electron expressed in coulombs, and where ε_0 is the permittivity of space . The work done by the coulombic force of the free electron is then given by

$$U(x) = \int_{\infty}^{x} \vec{F} \cdot d\vec{x} = \int_{\infty}^{x} \frac{q^2}{4\pi\varepsilon_0 (2x)^2} dx = -\frac{q^2}{16\pi\varepsilon_0 x} \qquad \text{Equation 27}$$

In Equation 27 it is implied that the dot product *F* and *dx* is negative, as *dx* points in the negative direction of x.[133] By using Equation 27, the potential energy as a function of *x*, *U(x)*, is finally plotted and illustrated in Figure 28.

When considering the electrostatic potential due to space charge in the depletion region within the Schottky barrier, the following approximation can be formulated: a Schottky junction can be compared to a p^+n junction, which is illustrated in Figure 29.

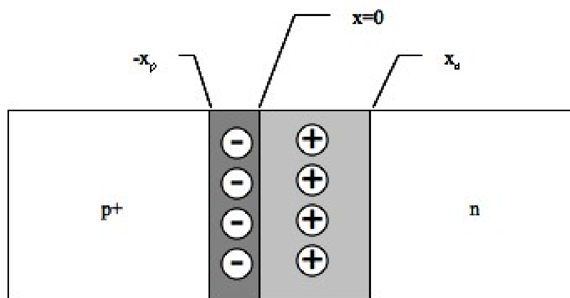

Figure 29: schematics of the space charge region within a p^+n junction.

By using Poisson's equation, which relates the gradient of the electric field to the local space charge at any point x in the to a p^+n junction illustrated in Figure 29, it must be that

$$-\frac{d^2V}{dx}=-\frac{q}{\varepsilon_s}\left[p(x)-n(x)+N_D^+(x)-N_A^-(x)\right] \qquad \text{Equation 28}$$

where q is the charge of the free electron expressed in coulombs, and where ε_s is the permittivity of the given semiconductor[4], p(x) is the intrinsic concentration of holes, n(x) is the intrinsic concentration of electrons, $N_D^+(x)$ is the concentration of ionized donors, and $N_A^-(x)$ is the concentration of ionized acceptors.

By neglecting the contribution of the intrinsic carriers, Equation 28 becomes

$$-\frac{d^2V}{dx}=-\frac{qN_D^+}{\varepsilon_s} \qquad 0\le x\le x_n \qquad \text{Equation 29}$$

$$\frac{d^2V}{dx}=\frac{qN_A^-}{\varepsilon_s} \qquad -x_p\le x\le 0 \qquad \text{Equation 30}$$

Equation 29 can be rewritten as

$$-\frac{d}{dx}\left(\frac{-dV}{dx}\right)=\frac{dF(x)}{dx}=\frac{qN_D^+}{\varepsilon_s} \qquad 0\le x\le x_n \qquad \text{Equation 31}$$

where *F(x)* is the expression for the electric field.

By integrating Equation 31, it must be that

$$\int_0^x dF(x)=\int_0^x \frac{qN_D^+}{\varepsilon_s}\,dx \quad \therefore \quad F(0)-F(x_n)=-\frac{qN_D^+x_n}{\varepsilon_s} \qquad \text{Equation 32}$$

and similarly, by integrating Equation 30, it can be obtained

$$\int_{-x_p}^{0} dF(x)=-\frac{qN_A^-x_p}{\varepsilon_s} \qquad \text{Equation 33}$$

From Equation 32 and Equation, it can be inferred that at $x = 0$ the electric field has a maximum value, which is expressed by

$$F_{MAX} = -\frac{qN_D^+ x_n}{\varepsilon_s} = -\frac{qN_A^- x_p}{\varepsilon_s} \qquad \text{Equation 34}$$

Since in a p[+]n junction, it must be

$$N_D^+ >> N_A^- \quad \therefore \quad W \approx x_n \qquad \text{Equation 35}$$

then from Equation 34, it must be that

$$F_{MAX} = -\frac{qN_D^+ W}{\varepsilon_s} \qquad \text{Equation 36}$$

Hence, within the interval $0 \le x \le x_n$, it must be that

$$F(x) = \frac{qN_D^+ (x - x_n)}{\varepsilon_s} = -\frac{qN_D^+ (W + x)}{\varepsilon_s} = -\frac{dV}{dx} \qquad \text{Equation 37}$$

By integrating Equation 37

$$\int_0^x dV = \frac{qN_D^+}{\varepsilon_s} \int_0^x (W - x)dx \quad \therefore \quad V(x) = \frac{qN_D^+}{\varepsilon_s}\left(Wx - \frac{1}{2}x^2\right) \qquad \text{Equation 38}$$

which is the expression of the electrostatic potential due to space charge within the semiconductor region in the Schottky barrier, in depletion approximation. The net potential energy within the semiconductor is given by the sum of the image force lowering, and the space charge in the semiconductor[133], which is expressed by

$$U(x) = -\frac{q^2 N_D^+}{\varepsilon_s}\left(Wx - \frac{x^2}{2} + \frac{1}{16\pi N_D^+ x}\right) \qquad \text{Equation 39}$$

A diagram illustrating the net potential energy due to image force lowering, and the space charge is shown in Figure 30.

---

[4] Assuming the p[+]n junction is a homo-junction, and hence made of the same semiconductor material.

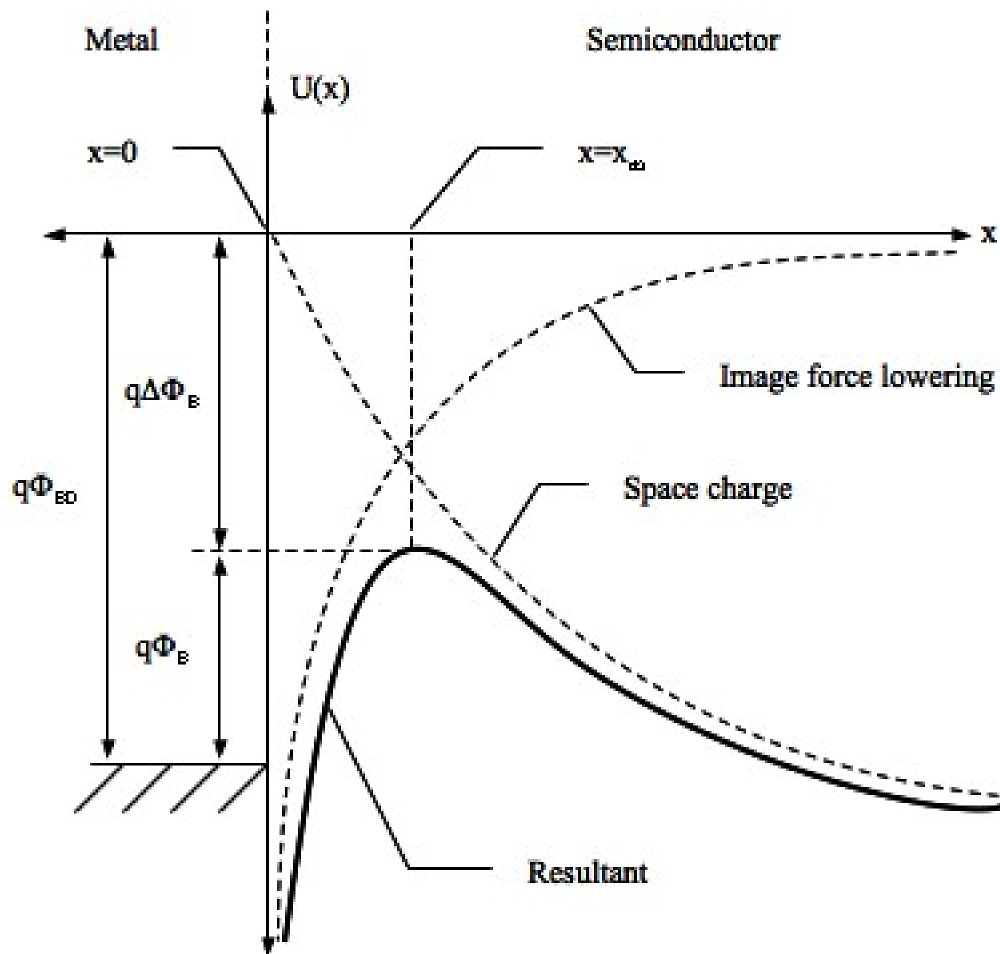

Figure 30: Energy diagram showing the net potential energy due to image force lowering, and the space charge in the semiconductor. Adapted from Muller *et al.*[132], Brennan[133], and Van Zeghbroeck[135].

As shown in Figure 30, as a result of the combined effects of the image force lowering, and the space charge in the semiconductor, the barrier that an electron has to overcome when passing from the metal into the semiconductor is lowered by an amount defined as $\Delta\Phi_B$; in other words, the Schottky barrier is lower than what it would be expected if no image charge effect is considered. Moreover, the position of the potential maximum is shifted away from the metal-semiconductor interface, to a point marked as x_m; hence, the potential energy at $x = x_m$ can be used to determine the Schottky barrier

lowering. It should be obvious that the value of x_m can be determined by finding the roots of the first derivative of Equation 23, which are given by[133]

$$x_m^2 = \frac{1}{16\pi N_D^+ (W - x_m)} \qquad \text{Equation 40}$$

Since the depletion region W is typically larger than x_m, Equation 40 can be approximated and rewritten as

$$x_m \approx \sqrt{\frac{1}{16\pi N_D^+ W}} \qquad \text{Equation 41}$$

When the approximation of x_m , and the resulting term in $1/W$ is neglected[133] the barrier lowering is given by

$$\Delta\Phi_B \approx -\frac{q}{\varepsilon_S}\sqrt{\frac{WN_D^+}{4\pi}} \qquad \text{Equation 42}$$

For the sake of this discussion, the image force also affects holes in the semiconductors by attracting them toward the metal; consequently, the image force bends the valence band upwards near the surface of the metal as illustrated in Figure 31. Differently from the bending of the conduction band, there is not a maximum or minimum point in the valence band; the bandgap is reduced in proximity of the metal-semiconductor junction[136].

There are several different methods to measure the barrier heights, but they involve an extrapolation either from, current/voltage characteristics, photoelectric or capacitance measurement, or photoelectron emission spectroscopy[136].

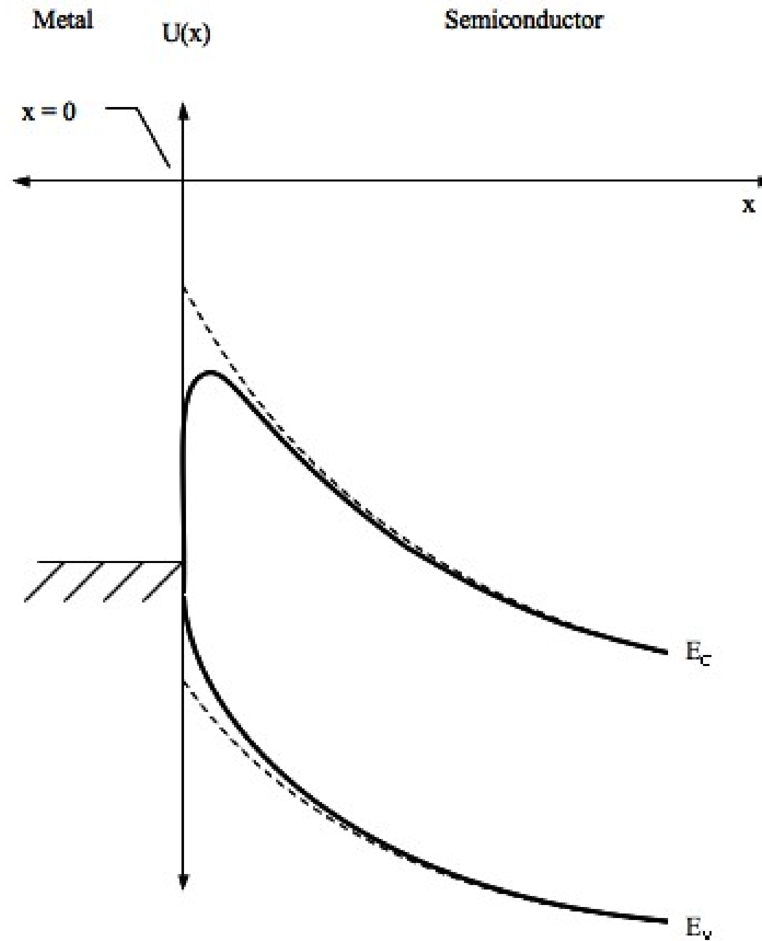

Figure 31: The effects of the image force potential on the conduction and valence bands. Adapted from Rhoderick and Wiliams[136].

As shown in Figure 30, as a result of the combined effects of the image force lowering, and the space charge in the semiconductor, the barrier that an electron has to overcome when passing from the metal into the semiconductor is lowered by an amount defined as $\Delta\Phi_B$; in other words, the Schottky barrier is lower than what it would be expected if no image charge effect is considered.

3.1.3. Schottky Barrier Lowering

In section 1.1, the concepts of free-electron energy, E_0, work function, Φ, and electron affinity, X, were introduced to explain the nature of the metal-semiconductor junction, and such concepts are indeed relevant to the Schottky-Mott theory; nonetheless, it was not mentioned that the work function of a metal, Φ_m, and the electron affinity of a semiconductor, X_s, are assumed to remain unchanged when a metal and a semiconductor make an intimate contact. In actuality, when a metal-semiconductor junction if formed, the precise atomic positions and the charge distribution at the surfaces of the metal and semiconductor cannot be determined, but it should be clear that they will differ from the atomic positions and charge distribution of their free standing surfaces. In order to overcome this problem, the electronegativity of a metal, X_m, may be used instead of its work function, Φ_m, even if the concept of electronegativity, as described by Pauling[137], [138], applies to single atoms, and cannot be readily measured. A list of values for the work functions, and electronegativity of the metals commonly used to fabricate metal-semiconductor junctions were made available in Table 1.

Table 1: Values for work functions[139], and electronegativities[138] of metals.

Metal	Symbol	Work Function, Φ_m[5] (eV)	Electronegativity, X_m (eV)
Platinum	Pt	5.65	2.2
Nickel	Ni	5.15	1.8
Palladium	Pd	5.12	2.2
Gold	Au	5.1	2.4
Cobalt	Co	5.0	1.8
Copper	Cu	4.65	1.9
Molybdenum	Mo	4.6	1.8
Tungsten	W	4.55	1.7
Iron	Fe	4.5	1.8
Chromium	Cr	4.5	1.6
Tin	Sn	4.42	1.8
Titanium	Ti	4.33	1.5
Aluminum	Al	4.28	1.5
Silver	Ag	4.26	1.9
Tantalum	Ta	4.25	1.9
Gallium	Ga	4.2	1.5
Indium	In	4.12	1.7
Magnesium	Mg	3.66	1.2
Calcium	Ca	2.87	1.0
Barium	Ba	2.7	0.9
Cesium	Cs	2.14	0.7

3.1.4. Metal Contacts to GaN and $Al_xGa_{1-x}N$

It should not be difficult for the reader that generally speaking "ideal contacts" are very much desirable when interfacing semiconductor electronic devices with the outside world, as there is always a need for increasingly efficient devices, and hence a need curb any unnecessary, spurious power losses due to parasitic resistances; in fact, an "ideal" contact to a semiconductor device is such that it does not obstruct the flow or carriers in any direction: that is from the metal to the semiconductor, or vice versa. As described earlier, in order to obtain an "ideal" metal contact to a given semiconductor material semiconductor, it is necessary that the metal and the semiconductor material have the same work function; in other words, it must be that, $\Phi_M = \Phi_S$. Despite the fact that "Mother Nature" is very often benevolent to humans, the scenario afore described rarely occurs in nature; in addition, the work function of a given semiconductor material, Φ_S, is affected by its substitutional impurity concentration, whose control is a challenge in itself. Thus, it is often acceptable to have at least an "ideal" contact in a desired direction, and this is often the case of a contact that allows an undisturbed flow of carriers from/to a metal, to/from a semiconductor material; in other words, a kind of contact that shows the so-called "Ohmic" behavior.

When dealing with GaN, or even worse with $Al_xGa_{1-x}N$ based semiconductor devices, the formation of an Ohmic contact can be quite a challenge. This is particularly true when p-type GaN (p-GaN) or p-type $Al_xGa_{1-x}N$ (p-$Al_xGa_{1-x}N$) semiconductor materials are considered, and in this case the challenge has two main obstacles. The first obstacle is

---

[5] Values for polycrystalline specimens, as determined by H. B. Michaelson.

presented by the fact that it is very difficult to grow high quality, crystalline p-GaN with a high substitutional impurity concentration; if this were not enough, both the crystalline quality of p-$Al_xGa_{1-x}N$, and its substitutional impurity concentration tend to decrease with increasing the Al mole fraction in $Al_xGa_{1-x}N$. The second obstacle is that "Mother Nature" has not made available a kind of metal sporting a work function large enough to allow the formation of "ideal" or Ohmic contacts to p- GaN or p-$Al_xGa_{1-x}N$. In order to better illustrate such a challenge, let us consider the scenario of a plausible contact formed at room temperature (300 °K) by a thin layer of metal, whose work function is 5.65 eV[138,139], and a moderately doped wurtzite p-GaN (with a Fermi level arbitrarily set at 0.2 eV from E_V for the sake of this discussion) whose bandgap is approximately 3.4 eV[140,141,142] and its electron affinity is 4.1 eV[140]; in this hypothetical scenario, a metal with a work function larger than at least 7.3 eV would be necessary to form an Ohmic contact, as shown in Figure 32.

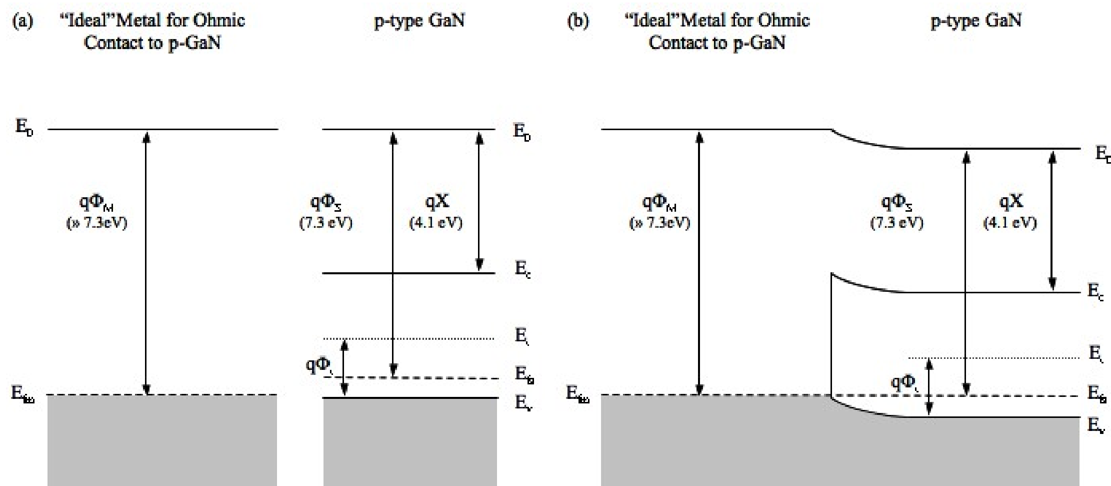

Figure 32: (a) idealized representation of allowed energy states in the bulk of an "ideal" metal for Ohmic contact to an arbitrarily selected p-GaN; (b) Idealized energy vs. space band diagram of an Ohmic contact between an "ideal" metal for Ohmic contact and an arbitrarily selected p-GaN. Adapted from Brennan[133], Kim and Baik[134].

In actuality, there is no metal with a work function larger than at least 7.3 eV, and even by employing a thin layer of platinum, whose work function is the largest with a value of 5.65 eV[138,139], a Schottky barrier would be formed at the metal-semiconductor interface, as shown in Figure 33.

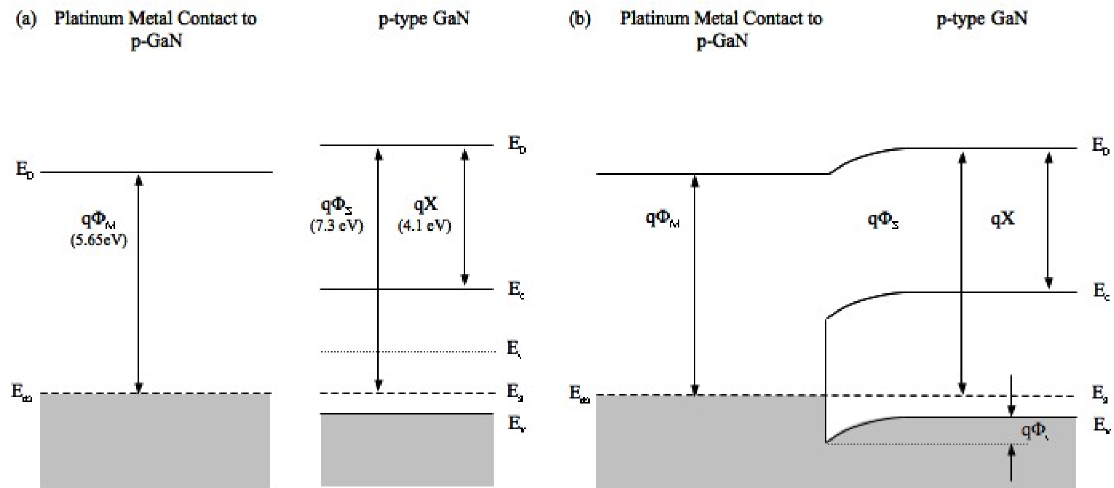

Figure 33: (a) idealized representation of allowed energy states in the bulk platinum metal for contact to an arbitrarily selected p-GaN; (b) Idealized energy vs. space band diagram of a Schottky contact between a platinum contact and an arbitrarily selected p-GaN and the resulting Schottky barrier. Adapted from Brennan[133], Kim and Baik[134].

The scenario described above turns even more dramatic when p-$Al_xGa_{1-x}N$ is considered, as the bandgap of this semiconductor material becomes larger and larger with increasing Al mole fraction; more specifically, it can vary from approximately 3.4 eV[140,141,142] for 0% Al, to 6.2 eV for 100% Al.

Despite the intrinsic challenge of growing high quality p-GaN and p- p-$Al_xGa_{1-x}N$, and the absence of metals with a work function large enough to be used as contacts to wide bandgap semiconductor materials, Ohmic contacts to both p-GaN, and p-$Al_xGa_{1-x}N$ have been obtained.

In the case of p-GaN, ohmic contacts have been obtained –for inexplicable reasons, or reasons that are often not fully understood- by using elemental metals with large work functions, such as Au, Pd, Ni, and Pt, in various combinations, and often in conjunction of Cr. Engineered, annealed in various environments, thin metal layer schemes such as Pt/Au, Pd/Au, Ni/Pt/Au, Pt/Ni/Au, Cr/Au, Ni/Cr/Au have been successfully used as Ohmic contacts to p-GaN[143], and Ni-Au (annealed in the presence of O_2) is the most extensively investigated[144, 145, 146, 147, 148, 149] and used because of its reported specific contact resistances as low as $4x10^{-6}$ Ωcm^2,[149] and a high transparency that is a very desirable characteristic for optoelectronic devices such as LEDs[150,151] and sensors.

Currently, there is still no clear understanding of the mechanism that renders a Ni/Au contact to p-GaN as a contact with Ohmic behavior; nonetheless, there is agreement that the presence of O_2 during the contact annealing process plays a predominant role in the formation of Ohmic contacts to p-GaN[152,147,153]. The presence of O_2 -even in minor concentrations- during the contact annealing process was identified as a possible active agent responsible for an increased level of conductivity in p-GaN[154]; such an enhancement was attributed to desorption of atoms of H_2 that are individually bonded to acceptor atoms of Mg (a common substitutional impurity in p-GaN), and their consequential activation[155,156,155,146].

Several theories have been formulated to explain the Ohmic nature of the Ni/Au contact to p-GaN, and many of them include the concurrent formation of non-stoichiometric nickel oxide (NiO), Ni/Au nodules, Ni/Ga alloys in proximity of the p-GaN surface while annealing in an O2 containing atmosphere.

According to the afore mentioned theories, while annealing at a temperature between 500 ºC and 700 ºC in an O_2 containing atmosphere, atoms of Au migrate from the Au layer through the Ni layer of the "as deposited" Ni/Au contact to p-GaN to form Ni/Au nodules; simultaneously, atoms of nickel react with atoms of GaN to form Ni/Ga alloys in proximity of the surface of GaN, and also diffuse from the Ni layer through the Au layer of the "as deposited" Ni/Au metallic contact to p-GaN, react with O_2 and form non-stoichiometric NiO, which tends to be a transparent, p-type oxide semiconductor[157,158,159,160]. The formation of non-stoichiometric NiO continues during the annealing process, and will continue growing downward, through the Au layer of the "as deposited" Ni/Au contact to p-GaN, and progressively segregate the former into islands, which will eventually grow more and more Au rich. During the annealing process, columnar structures made of non-stoichiometric NiO reach the surface of p-GaN, and react to form an amorphous Ni-Ga-O phase material[153,161,162,163,154,164]. For the sake of the reader's comprehension, such a process is illustrated in Figure 34.

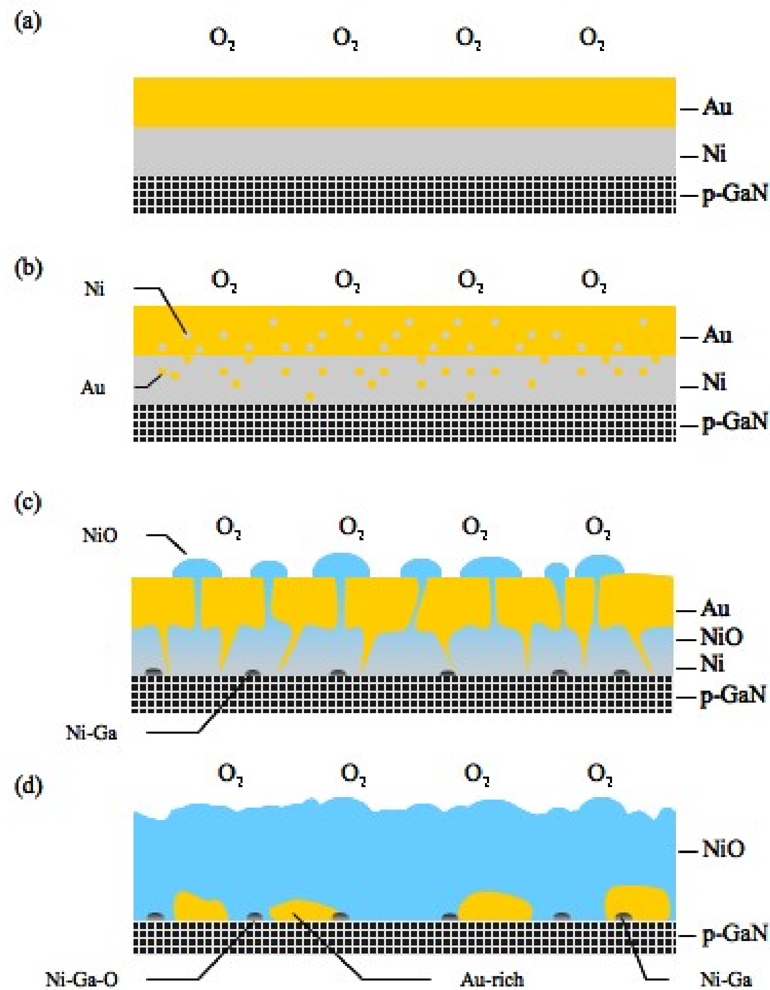

Figure 34: Formation of Ni/Au contacts to p-GaN. (a) Thin metal layers of Ni and Au are deposited onto p-GaN, and then annealed at high temperature in the presence of O_2. (b) During annealing, atoms of Ni, and Au migrate, (c) Ni-Ga compounds, and NiO are formed, and (d) and Au is segregated into Au-rich islands. Adapted with permission from J. G. Pagan[151].

In UV applications, p-$Al_xGa_{1-x}N$ with a high Al% mole fraction is currently indispensable, yet the formation of Ohmic contacts to p-$Al_xGa_{1-x}N$ is even more challenging than the formation of Ohmic contacts to p-GaN; nonetheless, Ohmic contacts to p-$Al_xGa_{1-x}N$ have been obtained, and their fabrication methodology disclosed in the literature. Similarly to the scenario of the Ohmic contacts to p-GaN, the nature of Ohmic

contacts to p-$Al_xGa_{1-x}N$ has not been yet fully understood. Most of the reported Ohmic contacts to p-$Al_xGa_{1-x}N$ have been achieved by using a multi-metallization scheme[165,166,167, 168,169,170,171], exploiting the polarization effects of standard, and recessed capping layers[172,173,174,175], non-alloyed schemes such as InN/GaN short period super lattices (SPSs)[176], polymer materials such as poly-3,4-ethylenedioxythiophene (PEDOT)[177,178,179,180], and Pd rich contacts (single Pd layer, Pd/Au, or Pt/Pd/Au annealed in N_2 at a temperature between 400 °C and 800 °C).[168,169,170] In the case of Pd rich contacts, low-resistance Ohmic contacts to p-$Al_xGa_{1-x}N$ (with $x \leq 0.15$) were obtained, and the Ohmic behavior was associated with the formation of Ga and Al vacancies near the surface region of the p-$Al_xGa_{1-x}N$[170], which function as acceptors[181,182]. Kim *et al.*[170] observed that during the annealing of Au/Pd/Pt contacts to p-$Al_xGa_{1-x}N$ alloys ($x \approx 0.1$) at 600 °C in a N_2 environment, a small amount of Pd and Pt diffused toward the interface region between the metal contact and the p-$Al_xGa_{1-x}N$, and formed Pd- and Pt-related gallide phases. The presence of Pd- and Pt-gallides at the interface between the metal contact and the and the p-$Al_xGa_{1-x}N$ indicated an out-diffusion of Ga from the surface of the semiconductor layer, and it consequential formation of Ga vacancies, which have been known to function as acceptors in p-$Al_xGa_{1-x}N$ alloys.[181,183] This progression is illustrated in Figure 35.

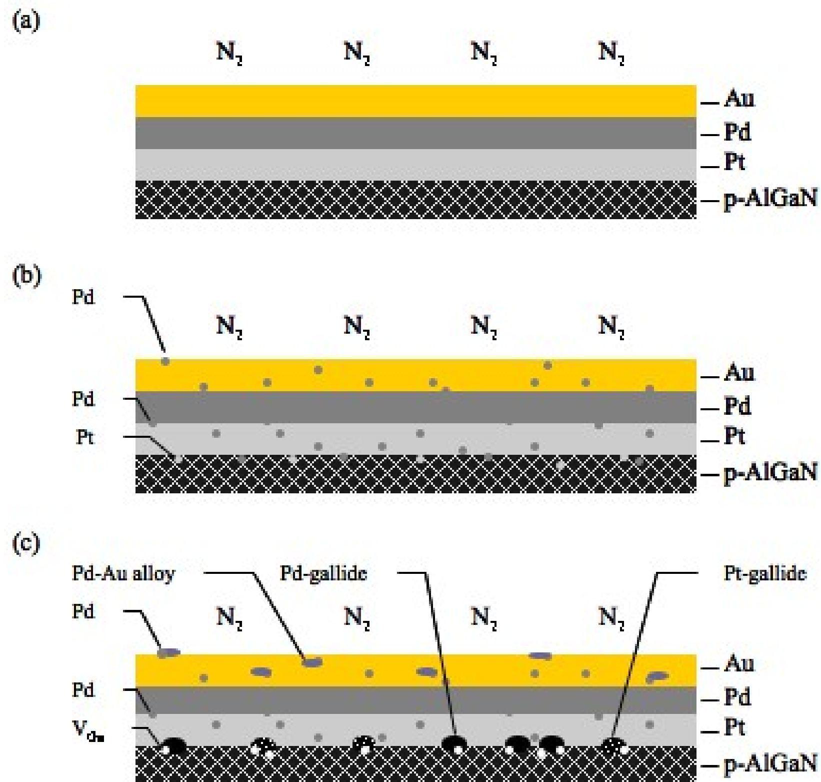

Figure 35: Formation of Au/Pd/Pt contacts to p-$Al_{0.1}Ga_{0.9}N$ as described by Kim *et al.*[170] (a) Thin metal layers of Au, Pd, and Pt are deposited onto p-$Al_{0.1}Ga_{0.9}N$, and then annealed at 600 °C in the presence of N_2. (b) During annealing, atoms of Pd out-diffuse to the surface through the Au layer, forming Pd-Au alloys; moreover, Pd and Pt diffuse to the interface between the metal contact, and the semiconductor. (c) Ga out-diffuses from the near surface of p-$Al_{0.1}Ga_{0.9}N$ leaving Ga vacancies; Pd- and Pt-gallides, which are known to behave as acceptors in p-$Al_xGa_{1-x}N$[181,183], are hence formed.

As for the formation of Ohmic contacts to n-GaN, and n-$Al_xGa_{1-x}N$, either with low or high Al% mole fraction, the scenario is certainly less challenging with respect to that of the formation of Ohmic contacts to p-GaN, and n-$Al_xGa_{1-x}N$; as a matter of fact, Ohmic contacts to n-GaN, and n-$Al_xGa_{1-x}N$ have been obtained profusely, and widely described in the literature. Nonetheless, since Ohmic contacts to n-GaN, and n-$Al_xGa_{1-x}N$ are of little or no interest in this work, this discussion will be limited to enlist some of the most popular metal schemes for n-GaN, which are based on metals with low work

functions such as Al and Ti (often use to prevent the formation of native oxide), and/or Al/Ti bi-layers[184] in conjunction with Au and/or Ni [185,186], Pd, Ta, Nd, Sc, and Hf[186], and some of the most popular metal schemes for n-$Al_xGa_{1-x}N$, which are often based on metal schemes such as Ti/Al/Ti/Au, Ti/Al/Mo/Au, Ta/Ti/Al/Mo/Au, Ti/Al/Ti/Pt, and Ti/Al/Ti/Pt/Au.[187,188,189] Titanium is often used to form an intimate contact with the surface of n-GaN or n-$Al_xGa_{1-x}N$ because it forms titanium nitride (TiN)[190,191] at the interface region between the metal and the semiconductor; such semi-metallic compound (TiN), which features a work function of 3.74 eV when annealed at temperatures of 800 °C to 900 °C [192], is believed to form an Ohmic contact to both n-GaN and n-$Al_xGa_{1-x}N$.[193] Moreover, Ti has an intrinsic property to bind with atoms of O_2, (hence functions as an oxygen getter), and desorbs oxygen atoms from the layer of native oxide that typically caps III-V semiconductor materials.[193] Aluminum is used to cap the layer of Ti, as these two elements form $TiAl_x$ intermetallics that have a high melting point, and hence tend to not ball up; nonetheless, both Al and Ti tend to oxidize fairly easy, and must therefore be capped with a metal/Au layer, where the “metal” can be Ni, Ti, Pd, Mo, Re, Ir, or Nb.[193,194,195,196,197,198,199,200,201]

3.1.5. GaN and $Al_xGa_{1-x}N$ surface preparation

In order to obtain high quality metal-semiconductor interface, it is necessary to prepare the surface of a given semiconductor material prior to the deposition of a desired metal, and here it is necessary to specify that most of the surface treatment techniques are designed for the removal of unwanted contaminants, and layers of native oxides, which tend to form rapidly on the surfaces of most III-V semiconductor materials when exposed to air. The reason that layer of native oxides are not desirable at the interface between the

metal and the semiconductor of a metal-semiconductor contact is that the native oxide is expected to obstruct the flow of carriers, accumulate the former, and hence create a parasitic capacitance. There is little or no doubt that the removal of the native oxide, which can cover the surface of a III-V semiconductor material with a film as thick as a few tens of an Å, is a "traumatic" form of action that negatively affects the quality of the surface of any given semiconductor material, and can induce the formation of undesired defects; in fact, oxide removal treatment require the use of very aggressive acids as wet etching agents, or very energetic reactive ion etch (RIE) methodologies.

As grown GaN and $Al_xGa_{1-x}N$ normally are not affected by the presence of native oxide; more precisely, a layer of native oxide does not form on the surfaces of these kinds of semiconductor materials as soon as they leave the chamber of the epitaxial growth rector in which they are grown. The formation of native oxide on the surface of GaN, and $Al_xGa_{1-x}N$ is not as rapid as in the case of the formation of native oxide on gallium arsenide (GaAs); however, an oxide layer does eventually form on the surface on both GaN and $Al_xGa_{1-x}N$ when they are exposed to air for a prolonged period of time[185], and in this case an oxide removal surface treatment becomes necessary.

Acid-based wet etching solutions such as aqua-regia (HCl and HNO_3), diluted hydrochloric acid (HCl: H_2O), and buffered oxide etch, or BOE for short (HF: H_2O), are commonly used for the native oxide surface treatment of GaN, and $Al_xGa_{1-x}N$[144,184,202,203,204,205,206], and they are usually accompanied by solvent clean (DI-H_20, Acetone, and Methanol) to remove particulate, organic, and inorganic contaminants. Pure HF, and hot phosphoric acid (H_2PO_4) have also been used.

Strong bases have also been used as oxide removal agents, and potassium hydroxide (KOH) is the most cited in the literature; in fact, KOH surface treatments are believed to be capable of both reducing the band bending by reducing the surface barrier height, and decreasing the Ga/N ration on the surface.[207,208,209] Ammonium hydroxide (NH_4OH)[204,203], and ammonium sulfides, [$(NH_4)_2S_x$][206,210] have also been used as a cleaning agent in GaN and $Al_xGa_{1-x}N$ surface treatments.

Various RIE methodologies have been used as a surface treatment to remove native oxide from the surface of GaN, and $Al_xGa_{1-x}N$; chlorine (Cl_2)[209,212,214], fluorine (F_2)[211], O_2[203], silicon tetra-chloride ($SiCl_4$)[212],[213], boron tri-chloride (BCl_3)[214], argon (Ar)[212], dichlorodifluoromethane (CCl_2F_2)[215], sulfur hexafluoride (SF_6)[211], and nitrous oxide (N_2O)[212] plasmas are the most common reactive ion sources.

3.1.6. GaN and $Al_xGa_{1-x}N$ contact anneal

After the deposition of single metal, or metal scheme contacts to GaN and $Al_xGa_{1-x}N$ a specific thermal treatment of the contacts is necessary to relieve stress in the metal layers, induce a more intimate contact at the interface between the metal and the semiconductor, the migration and/or segregation of certain metals, and the formation of alloyed compounds; these phenomena, which are crucial to the formation of Ohmic contacts to wide bandgap semiconductor materials such as GaN and GaN and $Al_xGa_{1-x}N$, have been mentioned in the section above, and illustrated in Figure 34 and Figure 35.

Without a doubt, the most common kind of thermal treatment of metal contacts is the sp-called rapid thermal anneal (RTA), which is a subset of rapid thermal processing (RTP). RTA consists of uniformly flash-heating a single wafer at a time in a controlled gaseous environment to modify metal-to-metal, and/or metal-to-wafer interfaces. In a

typical RTA furnace, a wafer is heated by two banks of high intensity (in the order of tens of kW) tungsten-halogen infrared (IR) lamps, as shown in Figure 36.

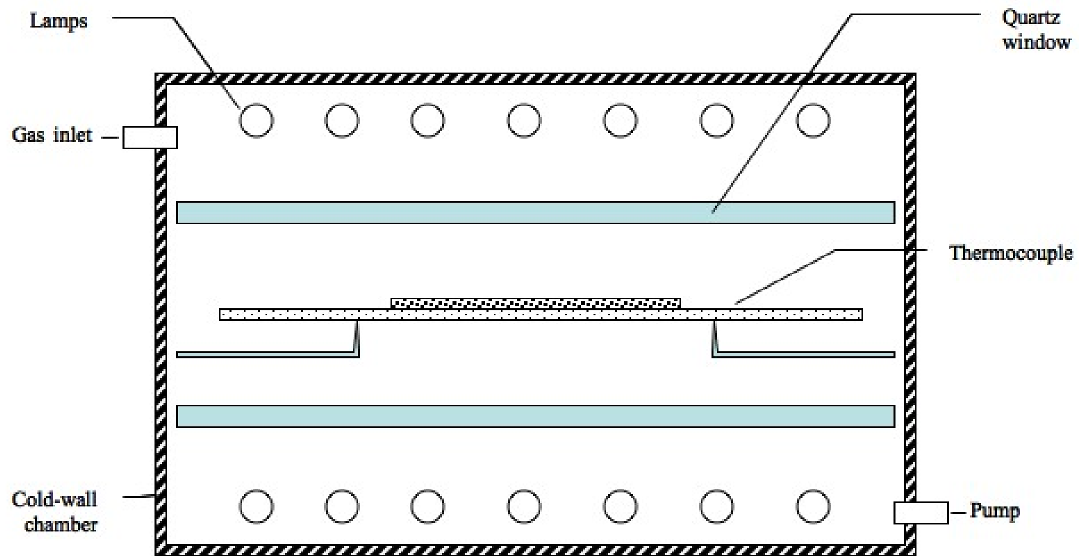

Figure 36: Schematic diagram of a rapid thermal anneal (RTA) furnace based on the Solaris 150 RTA tool available in the clean room, in Grigg Hall, at the University of North Carolina at Charlotte.

High intensity IR radiation is absorbed by the wafer (and the metal contacts as well), causing the temperature of the former to increase to a processing temperature of 200 °C to 1300 °C with ramp rates of 20 °C to 250 °C /sec. The processing temperature is reached after the gas flows in the chamber have been stabilized, and at the end of the process (which can last anywhere from a few seconds to a few minutes), the lamps are turned off to allow the temperature of the wafer (and the metal contacts as well) to drop rapidly (50 to 100 °C/sec). A typical time-temperature RTA profile is shown in Figure 37.

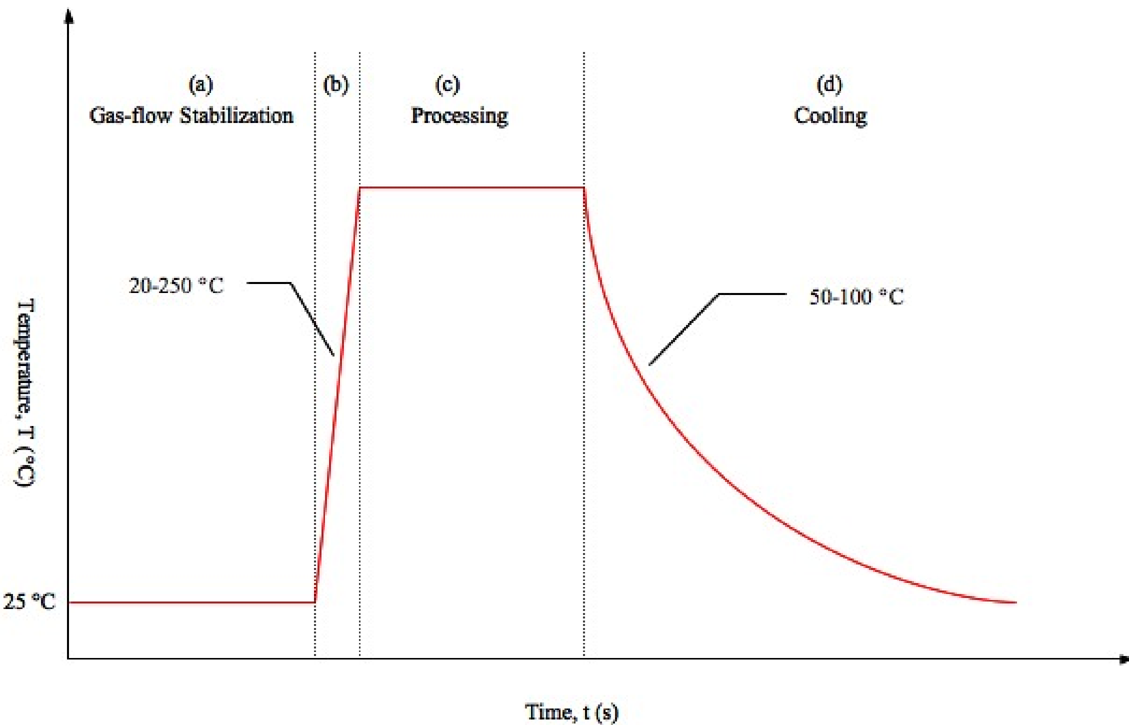

Figure 37: Typical time-temperature profile of a RTA process: (a) gases are introduced in the chamber of the RTA tool until their flows are stable, (b) lamps are turned on, and the temperature of the wafer (or sample) is increased very quickly to the desired processing temperature, (c) the annealing process takes place, (c) and finally the lamps are turned off, and wafer (or sample) cools down quickly.

Typical anneal processing temperatures for the formation of Ohmic contacts to n-GaN range between 550 ºC to 650 ºC (Al, Al/Au[216], Ti, Al/Ti metallization), and the anneal process occurs in a non-reactive environment such as Ar, or N_2. For Al/Ti contacts to n-GaN annealing temperatures can be as high as 900 ºC[217]; nonetheless, successful formation of Ohmic contacts to n-GaN has occurred at temperatures as low as 200 ºC[153]. Typical anneal processing temperatures for the formation of Ohmic contacts to n-$Al_xGa_{1-x}N$ range between 700 ºC and 900 ºC, again in a non reactive environment such as Ar, or N_2.[189,187,193,188]

Typical anneal processing temperatures for the formation of Ohmic contacts to p-GaN range between 500 ºC to 700 ºC (Ni/Au metallization), in an O_2 containing environment (O_2/20 sccm + N_2/80 sccm)[149], or simply air; 600 ºC to 750 ºC in N_2 for Ohmic contacts to p-$Al_xGa_{1-x}N$.[171,170]

CHAPTER 4: KELVIN SENSE MEASUREMENT METHOD

Advanced and very accurate current measurements across a device can be taken if a Kelvin sensing method is adopted. A Kelvin sense measuring system is hinged on a straightforward four-terminal connection typically made to a two-terminal device (or to the probes of a measuring apparatus for that matter), which separates the current path through the above-mentioned device from the voltage across the device itself, and hence excluding any additional and undesired wiring and/or contact resistance such as the one introduced by the probes of the measuring apparatus. A Kelvin sense measuring method was used to collect the data in this work.

4.1. Two-Terminal vs. Four-Terminal Sensing

Traditionally, a current measurement is taken by using a two-terminal connection made to a two-terminal device, such as the resistor named "Device" having resistance $R=R_{Device}$, illustrated in Figure 38. In Figure 38, the resistance $R=R_{Wire}$, indicates the resistance of the wires connected both to the ammeter and the device having resistance $R=R_{Device}$. In this particular case, the current measured by the ammeter is not the current flowing in the device having resistance $R=R_{Device}$, but a system with resistance is the summation of the series resistance, $R=R_{Wire}$ $R_{Device}+R_{Wire}$. Although wire resistance $R=R_{Wire}$ is typically minimal and negligible (in the order of 0.01 ohm/feet for small gauge wires), it can negatively affect measurements of a current flowing in a device having a significantly low resistance by introducing a non-negligible measurement error.

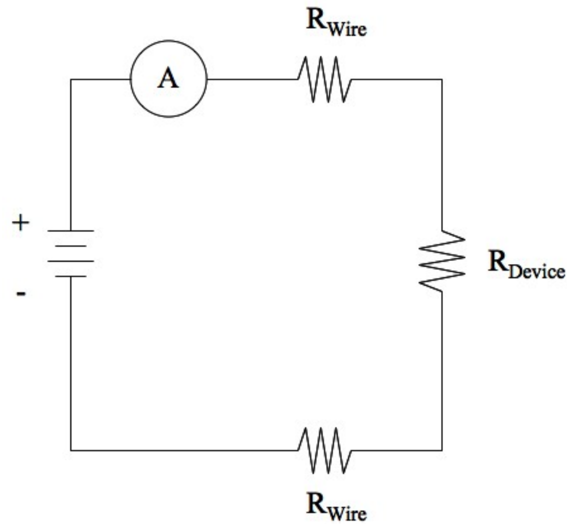

Figure 38: Two-terminal connection made to device having resistance $R=R_{Device}$.

In order to ameliorate the above-mentioned condition, both an ammeter and a voltmeter can be used as illustrated in Figure 39.

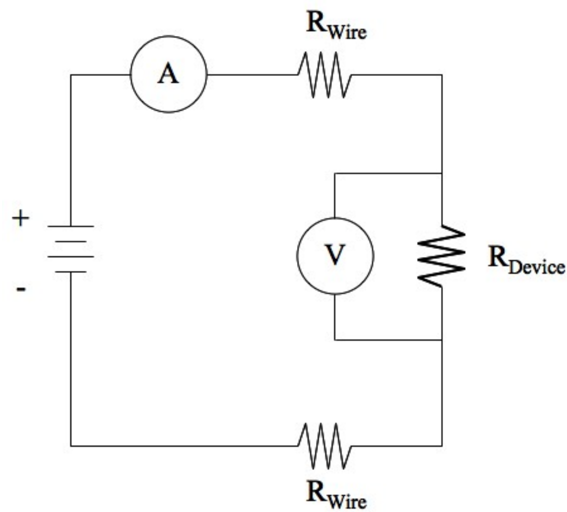

Figure 39: Use of both an ammeter and a voltmeter with a two-terminal connection made to device having resistance $R=R_{Device}$.

By applying Ohm's Law to the circuit illustrated in Figure 39, the resistance $R=R_{Device}$, is given by

$$R_{Device} = \frac{V}{A} \qquad \text{Equation 43}$$

where V is the voltmeter indication, and A is the ammeter indication. This kind of measurement is more accurate, as only the voltage across the device having resistance $R=R_{Device}$ (and not across the entire circuit) is being considered. Yet again, the wire resistance, $R=R_{Wire}$, can affect the current flowing through the device being tested, as the former is an element of a series circuit. In order remove the measuring error introduced by the wire resistance, $R=R_{Wire}$, a four-terminal connection (Kelvin sense) to the device having resistance $R=R_{Device}$ can be made as illustrated in Figure 40.

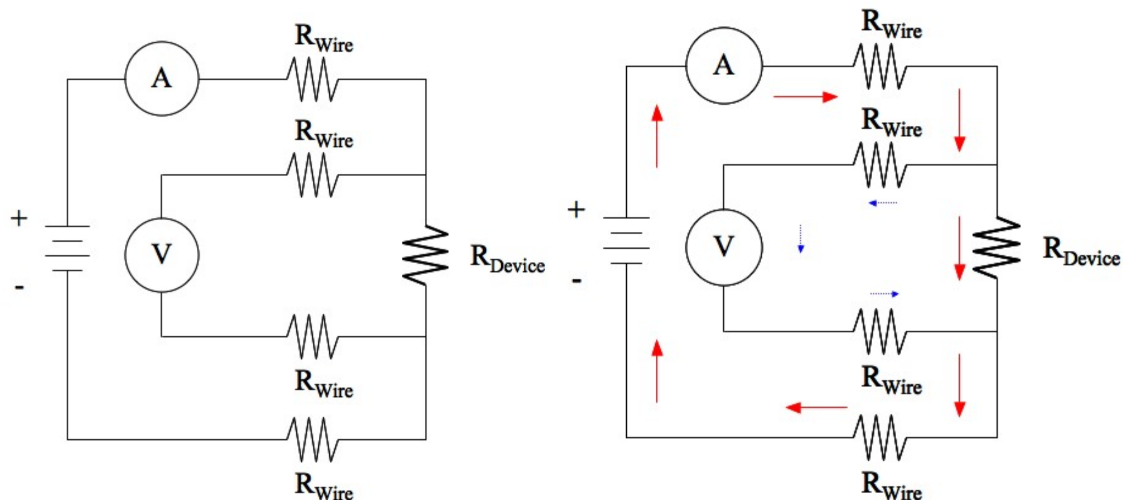

Figure 40: Use of both an ammeter and a voltmeter with a four-terminal connection made to device having resistance $R=R_{Device}$ (left). Circuit current flow diagram (right).

As shown in the circuit illustrated in Figure 40, the voltmeter and the ammeter are connected to the device with wires of similar length, and hence resistance R_{wire}. In this case the resistance $R=R_{Device}$, is still equal to the voltage across the device (voltmeter indication), and the current flowing in circuit (ammeter indication); nonetheless, this kind of measurement is more accurate and precise, as any voltage drop across the current

carrying wires (a negligible current flows in the wires that connect the voltmeter to the device) will not be measured by the voltmeter, and hence will not be factored in the calculation of the resistance $R=R_{Device}$.

The four-terminal sensing method is often combined with special probes, which are normally called Kelvin clips, or Kelvin probes. Such items may come in different shapes and design, but their fundamental concept, which is illustrated in Figure 41, is based on a 4-wire/4 –lead cable connected to two probes.

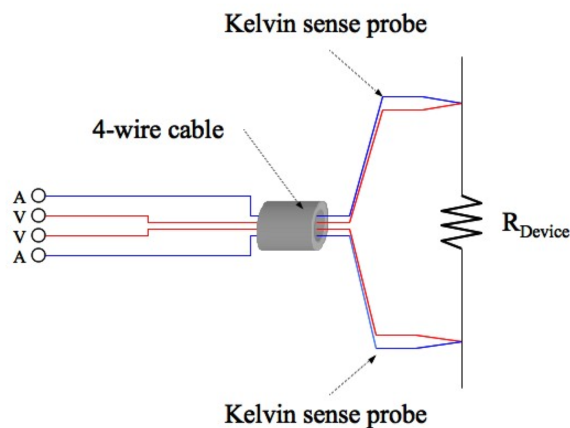

Figure 41: Conceptual schematics of Kelvin probes connected to a sample.

Kelvin sense probes as the one conceptualized in Figure 41 are often connected as close as possible to the probe needles of an IV curve tracer when it is necessary to investigate the nature of a given, unpackaged electronic device on wafer. A Tektronix 370B programmable curve tracer, which is capable of taking Kelvin sense measurements, was used to test some of the metal-semiconductor-metal (MSM) test structures on wafer. Such device, and its Kelvin sense connections are depicted in Figure 42.

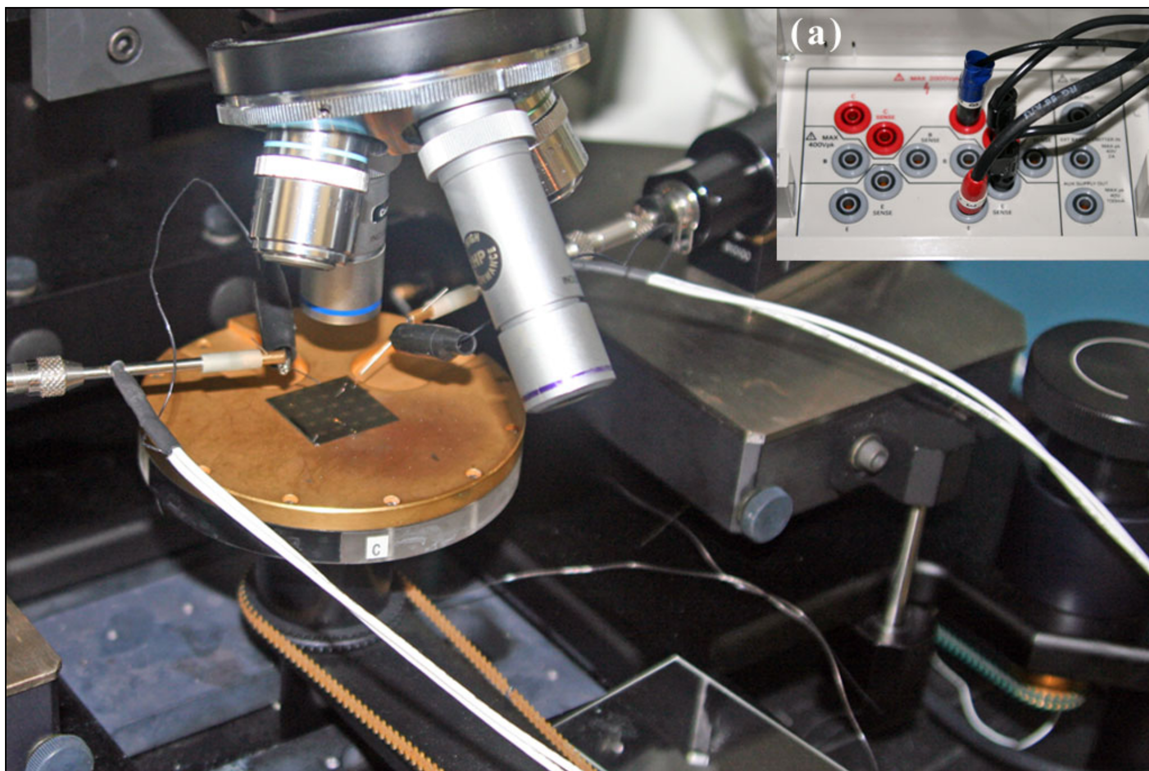

Figure 42: Test setup showing a detail of the probe station equipped with a Kelvin sense probe, and (a) the connection made to the Tektronix 370B to perform Kelvin sense measurements.

CHAPTER 5: PROCEDURE

In this chapter, procedures pertaining to the setup, alignment and fine-tuning of the LaserVision Optical Parametric Oscillator / Optical Parametric Amplifier (OPO/OPA), and its use in the Near IR, Intermediate IR, and Mid IR ranges will be described.

5.1. LaserVision OPO/OPA System Alignment

In this section, the procedure to achieve a successful alignment of LaserVision OPO/OPA system with the Nd:YAG 1024 nm laser source (YAG).

5.1.1. LaserVision OPO/OPA System Components

In order to achieve a successful infrared (IR) pumping of test structures, it is necessary that the LaserVision Optical Parametric Oscillator / Optical Parametric Amplifier (OPO/OPA) system is aligned with the Nd:YAG 1024 nm laser source (YAG). In the case of a faulty alignment, the OPO/OPA system will not be able to tune the YAG into a continuously tunable IR source, and two distinct cases may occur: 1) No IR power output will be detected, or very little power output will be available over a very narrow wavelength range. In any case, serious damage can occur to the optical element of the OPO/OPA system, and a realignment procedure must be completed. For the sake of the reader's comprehension, a photo-diagram illustrating the optical components of the OPO/OPA system is available in Figure 43, and a list of the afore-mentioned components is available in Table 2.

Table 2: Optical components of the OPO/OPA system.

OPO/OPA Optical Component # (as indicated in Figure 43)	Description
1	Beam Expander
2	Kinematic Mirror
3	Attenuator - OPO
4	Kinematic Mirror
5	Beam Dump
6	Kinematic Mirror – OPO Cavity L
7	Kinematic Mirror
8	Static Mirror
9	Kinematic Mirror – OPO Cavity R
10	Attenuator - OPA
11	Kinematic Mirror
12	Beam Dump
13	Si Polarizer
14	Beam Dump
15	Kinematic Mirror - OPA
16	Static Mirror - OPA
17	Polarizer
18	Iris
19	OPA Crystals (Left to Right: #3, #4, #5, and #6)
20	OPO Crystals (Left to Right: #1, and #2)

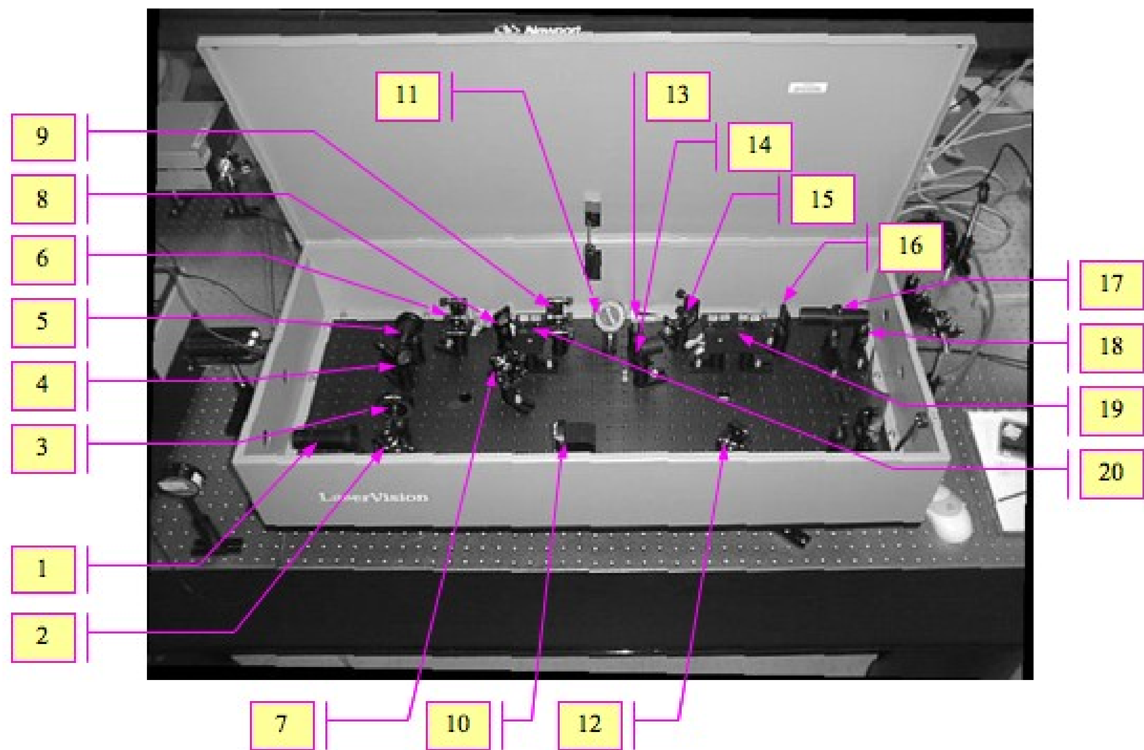

Figure 43: A photo-diagram illustrating the optical components of the OPO/OPA system.

5.1.2. Coarse Alignment of the Nd:YAG Laser and OPO/OPA System

Reduce the power output of the YAG to 200 mJ by decreasing the magnitude of the delay of the capacitor bank CB630C, and place an adjustable iris at the input of the OPO/OPA system to reduce the size of the input laser beam to a minimum as shown in Figure 44. Reducing the power output of the YAG will greatly decrease the possibility of having optical components damaged or the edges of the KTO and KTA crystals chipped, while reducing the size of the input laser beam will allow a better tracking of the former. Next remove the Si polarizer #13, the polarizer #17, and the adjustable iris #18.

Figure 44: Delay adjustment knob of the YAG’s capacitor bank CB 630C (right), and the adjustable iris placed at the input of the OPO/OPA system to reduce the size of the laser beam (left).

Next turn the OPO and OPA attenuators (#3 and #10) to 0° degrees so that the laser beam will not propagate beyond the Beam Expander (#1), and the kinematic mirror #2, and then coarsely align the YAG and the OPO/OPA system so that the YAG laser beam will go through the beam expander and hit the center of the kinematic mirror #2. Check the reflection of the laser beam on the back of the adjustable iris at the input of the OPO/OPA, and make sure that the laser beam traces itself back; in other words, the laser beam must follow the same path in both the forward and backward direction. If the laser beam traces itself back, a green laser beam spot will be visible on the back of the adjustable iris, as shown in Figure 45.

Once the coarse alignment the YAG and the OPO/OPA system has been accomplished, turn the attenuator #3 to 20° degrees (the laser beam power will be attenuated ~ 50%) so that the laser beam will propagate through the optical components of the OPO/OPA system. Make sure that the laser beam is propagating through the OPO crystals (#1, and #2).

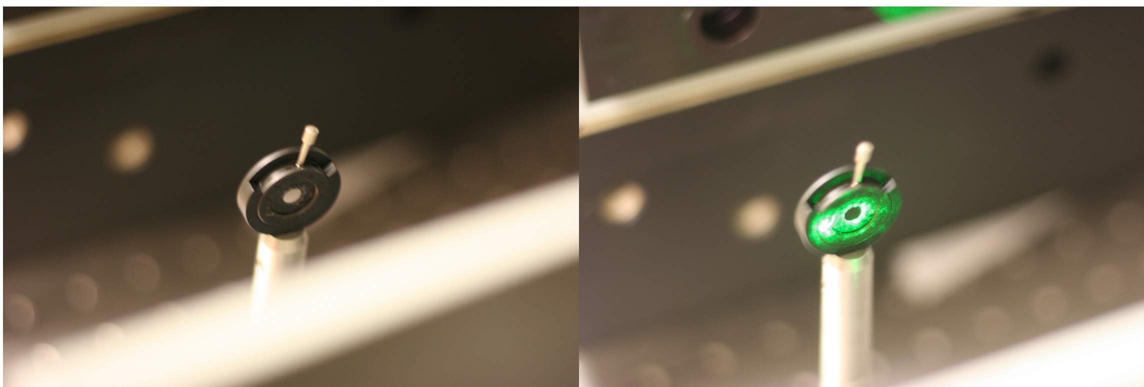

Figure 45: Adjustable iris placed at the input of the OPO/OPA system (left), and green laser beam spot on the back of the adjustable iris caused by the laser beam tracking itself back (right).

5.1.3. Fine Alignment of the Nd:YAG Laser and OPO/OPA System

Select the “Near Infrared” range (LaserVision software) as shown in Figure 46, and

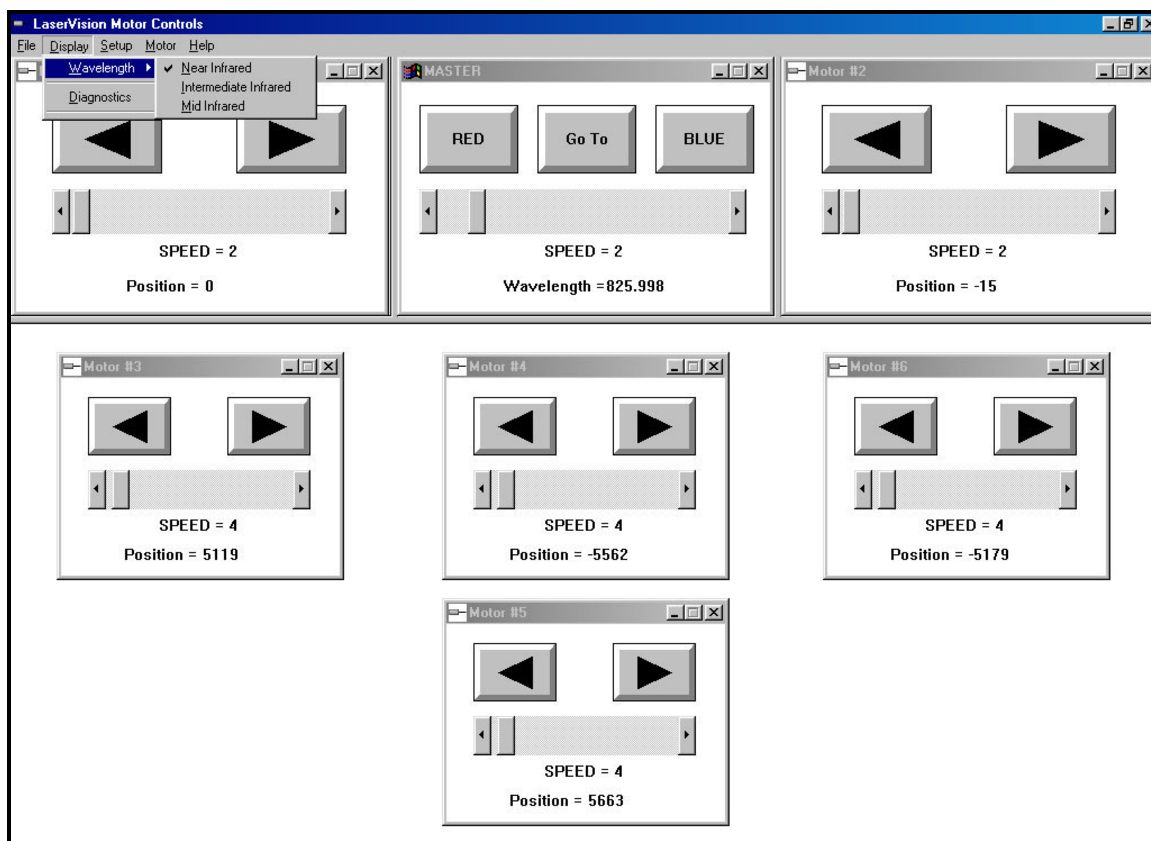

Figure 46: LaserVision Motor Control software showing the settings for Near Infrared.

then set the OPO/OPA to 825.998 nm as show in Figure 47.

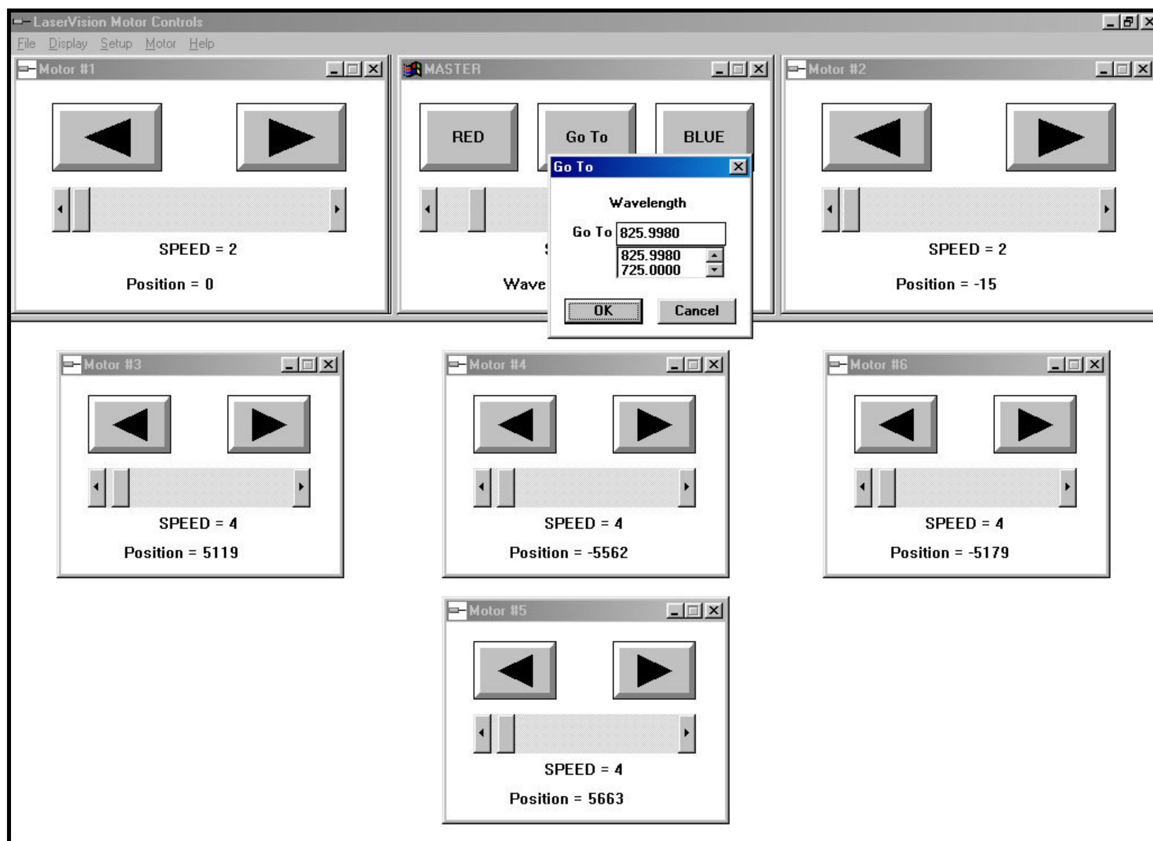

Figure 47: How to set the OPO/OPA system to 825.998 nm

Place a perforated card between the kinematic mirrors #4 and #7, which will allow the observation the laser beam reflection from the OPO crystals #1, and #2 (Figure 48).

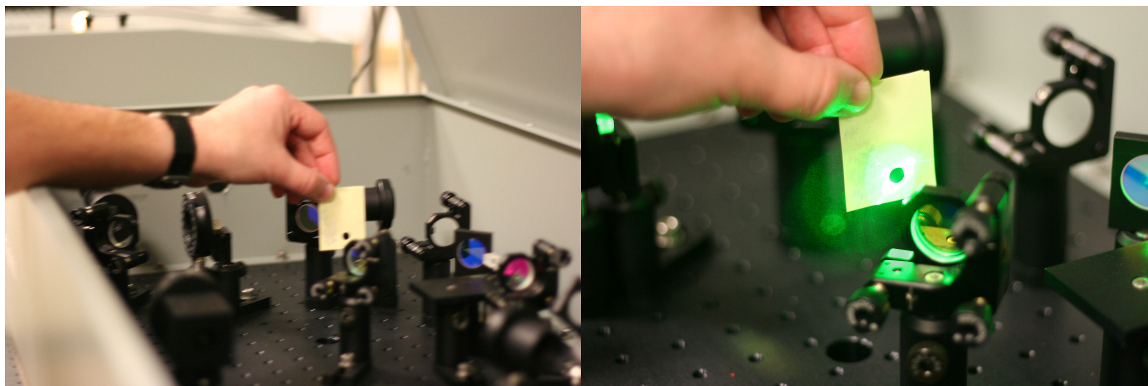

Figure 48: Perforated card used to observe the reflection of the OPO crystals.

The YAG laser beam will be reflected by the OPO crystals, and two distinct, bright spots will be visible on the back of the perforated card, as shown in Figure 49.

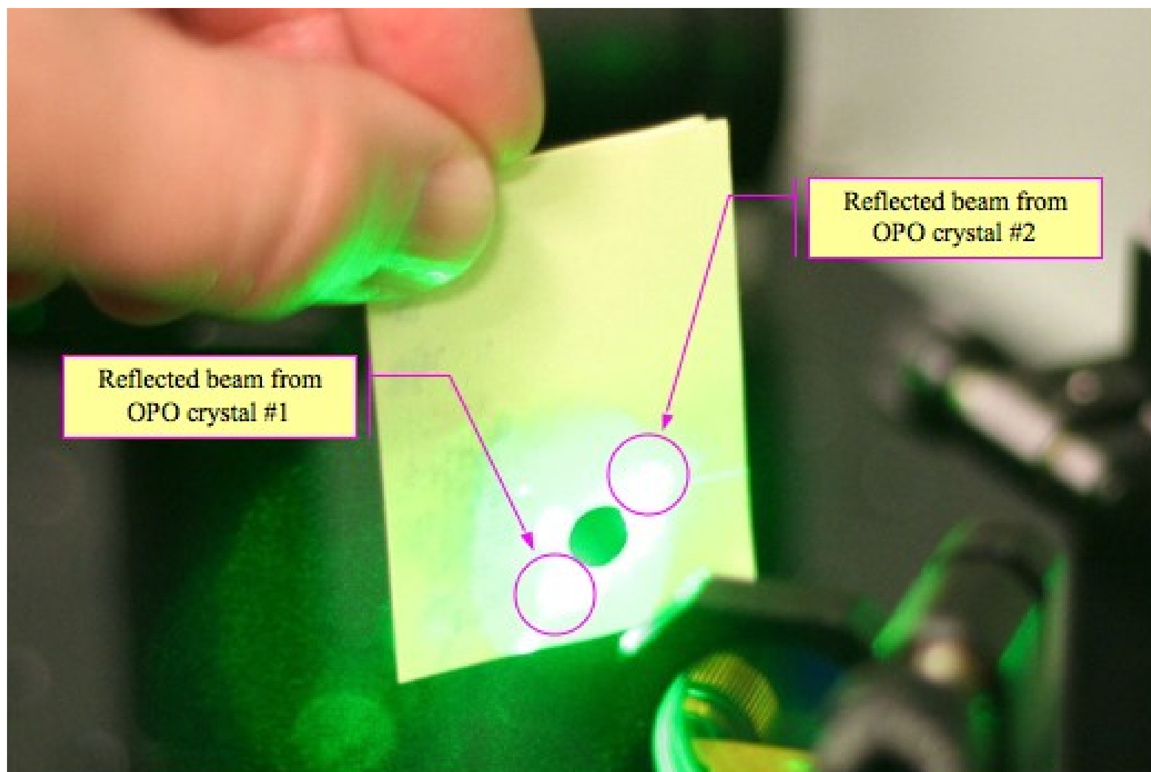

Figure 49: Two bright spot on the perforated card, which are generated by the reflection of the YAG laser beam by the OPO crystals.

By using the LaserVision Motor Control software, individually adjust the position of motors #1, and #2 until normal reflection is achieved; *id est*, when the two bright spots are vertically aligned. While adjusting the position of the above-mentioned motors (rotating clockwise, or counter clockwise), the bright spots will sweep horizontally, and normal reflection will be achieved when the two spots lie on the same vertical "imaginary" line that crosses the hole of the perforated card, as shown in Figure 50.

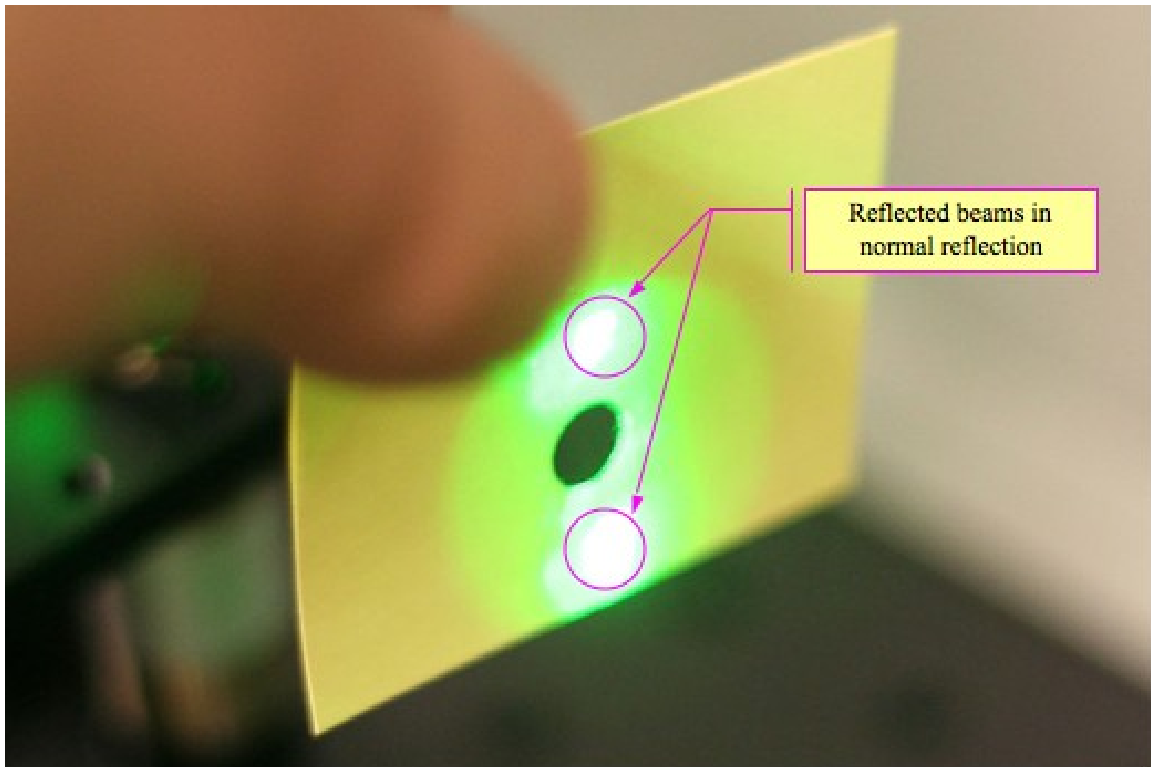

Figure 50: Normal reflection of the OPO crystals #1, and #2,

Once the normal reflection condition has been achieved, motors #1, and #2 will also physically be in the so-called “zero position”. When visually inspecting the OPO crystals, they will appear to be aligned along a line. Such a status must be matched by the software “zero position”, and this can be accomplished again by using the LaserVision Motor Control software. As shown in Figure 51, from the main menu of the LaserVision Motor Control software, select “Setup” and then “Motor #1”. This will allow controlling the status of motor #1 in a direct fashion.

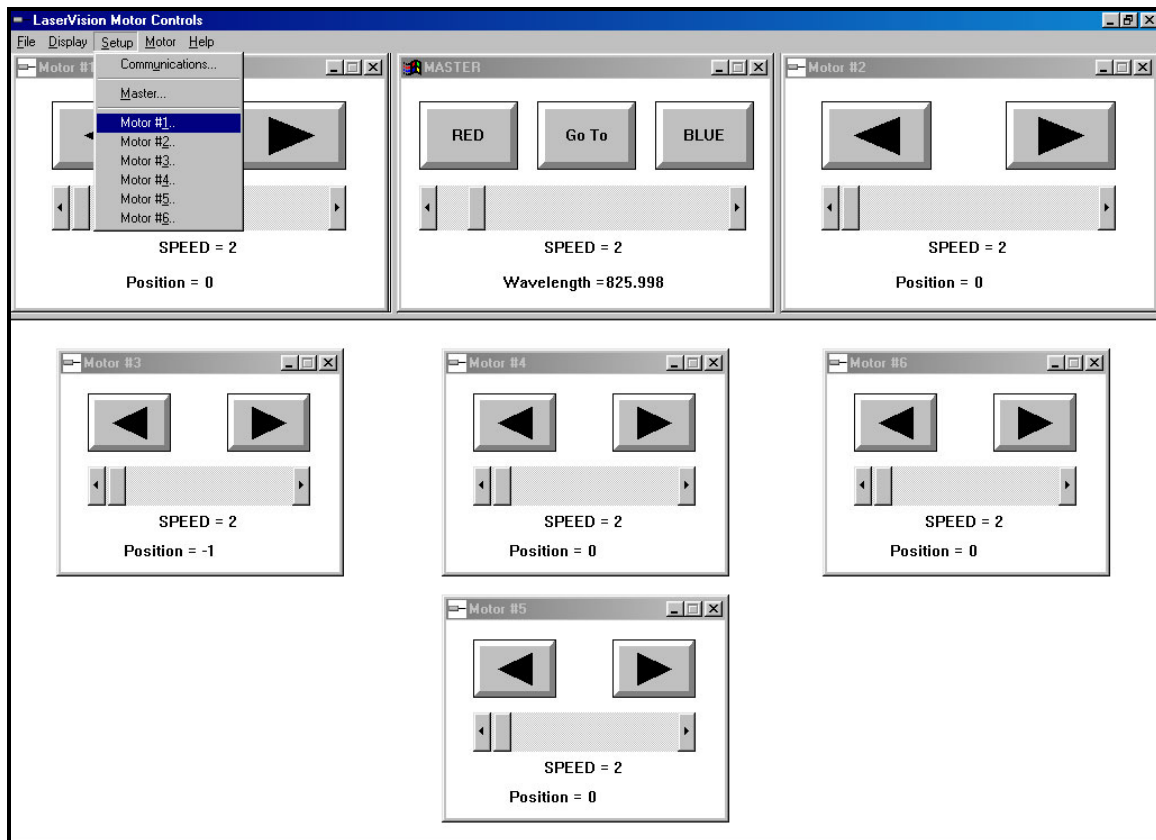

Figure 51: Direct control of motor #1 by using the LaserVision Motor Control software.

Once the direct control of the status of motor #1 has been achieved through the main menu of the LaserVision Motor Control software, the Motor Control menu will be displayed as shown in Figure 52; select the box titled “Position” and manually insert the value “0”. Having completed this task, the software “zero position” of motor #1 will be set to zero. Repeat the same procedure to gain direct control of the status of motor #2, and set its software “zero position”.

After both motors #1, and #2 have reached the physical and software “zero position” remove the kinematic mirror – OPO cavity R (#9) and replace it with a perforated card, which will allow the observation the laser beam reflection from the OPA

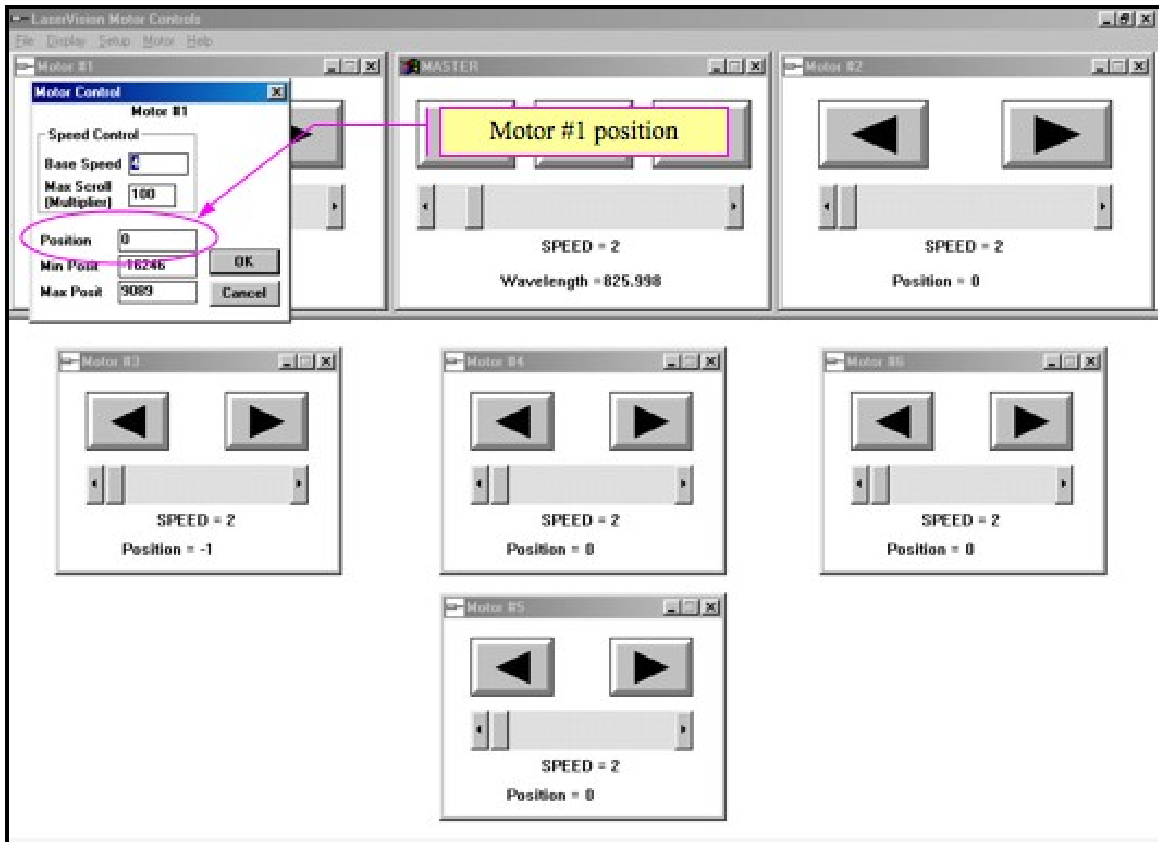

Figure 52: Motor Control menu windows displaying the motor control parameters.

crystals #3, #4, #5, and #6, as shown in Figure 53.

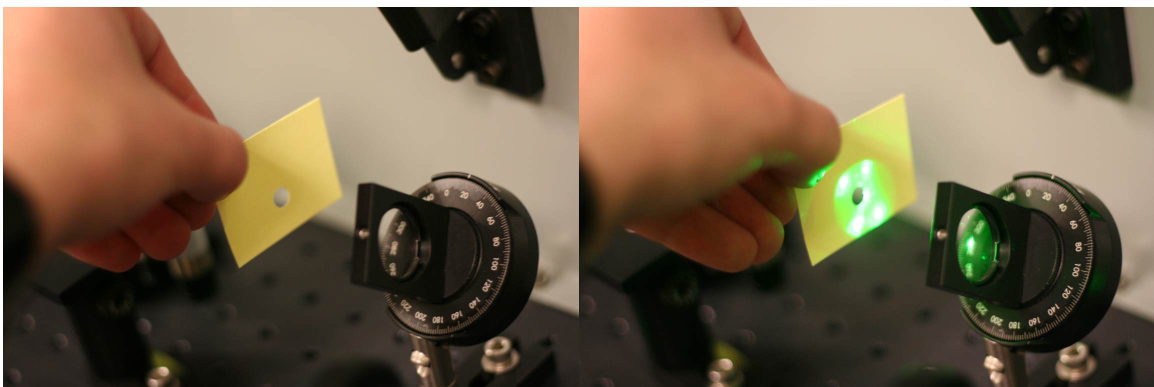

Figure 53: Perforated card replacing the Kinematic Mirror – OPO Cavity R (#9) (Left), and the four bright spots indicating the reflection of the OPA crystals #3, #4, #5, and #6 (right).

By using the LaserVision Motor Control software, individually adjust the position of motors #3, #4, #5, and #6 until normal reflection is achieved; *id est*, when the four bright spots shown in Figure 53 are vertically aligned. While adjusting the position of the above-mentioned motors (rotating clockwise, or counter clockwise), the bright spots will sweep horizontally, and normal reflection will be achieved when the four spots lie on the corners of an imaginary square as shown in Figure 54.

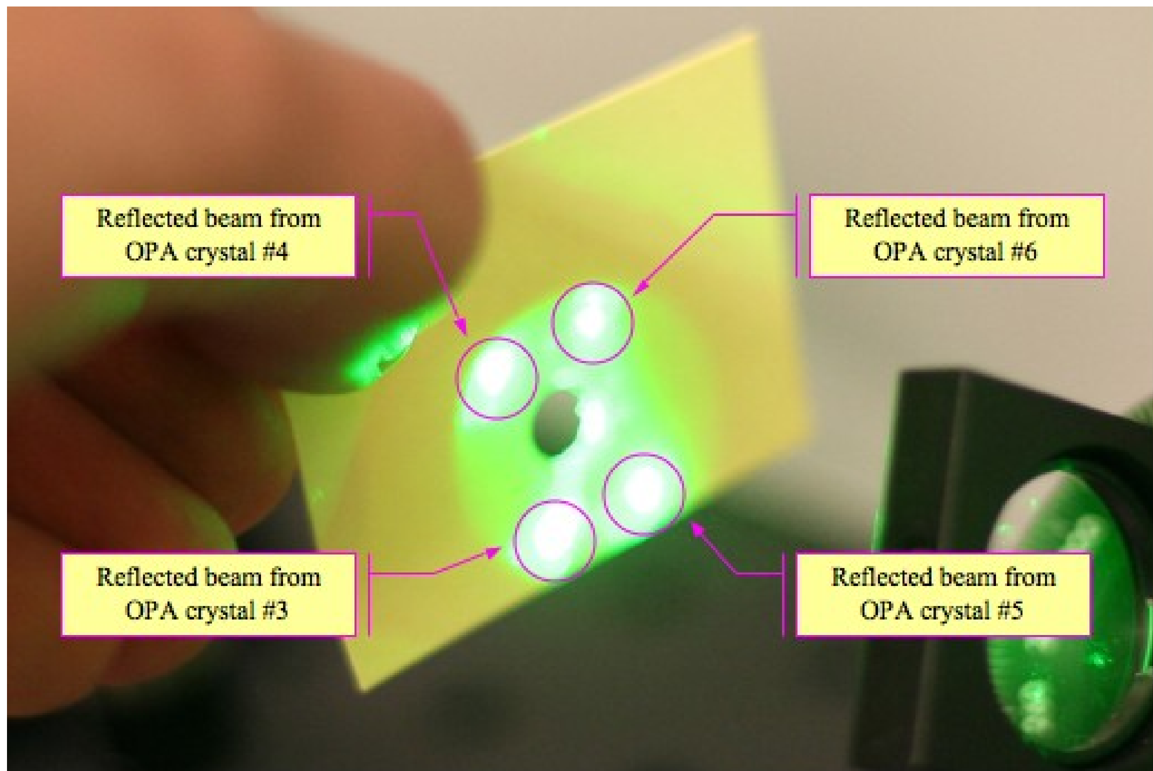

Figure 54: Normal reflection of the OPA crystals #3, #4, #5, and #6.

Once the normal reflection condition has been achieved, motors #3, #4, #5 and #6 will also physically be in the so-called "zero position". When visually inspecting the OPA crystals, they will appear to be aligned along a line. The physical "zero position" must be matched by the software "zero position", and this can be accomplished again by using the LaserVision Motor Control software as specified earlier.

After the physical and software "zero positions" have been set, put the Kinematic Mirror – OPO Cavity R (#9) back in place, and verify that the YAG laser beam is still tracking itself back properly, and entering the OPO crystals in the center. In order to verify that the YAG laser beam is tracking itself back properly, check the reflection of the laser beam onto the back of the adjustable iris at the input of the OPO/OPA. It is very likely that the YAG laser beam will not track itself properly, and in this case a distinct green light spot will be positioned to the right of the back of the iris, as shown in Figure 55. In Figure 55, it is also visible a bright light spot to the left of the back of the iris, and the position of such a light spot cannot be controlled; in other words, the presence of such light spot is permanent and normal.

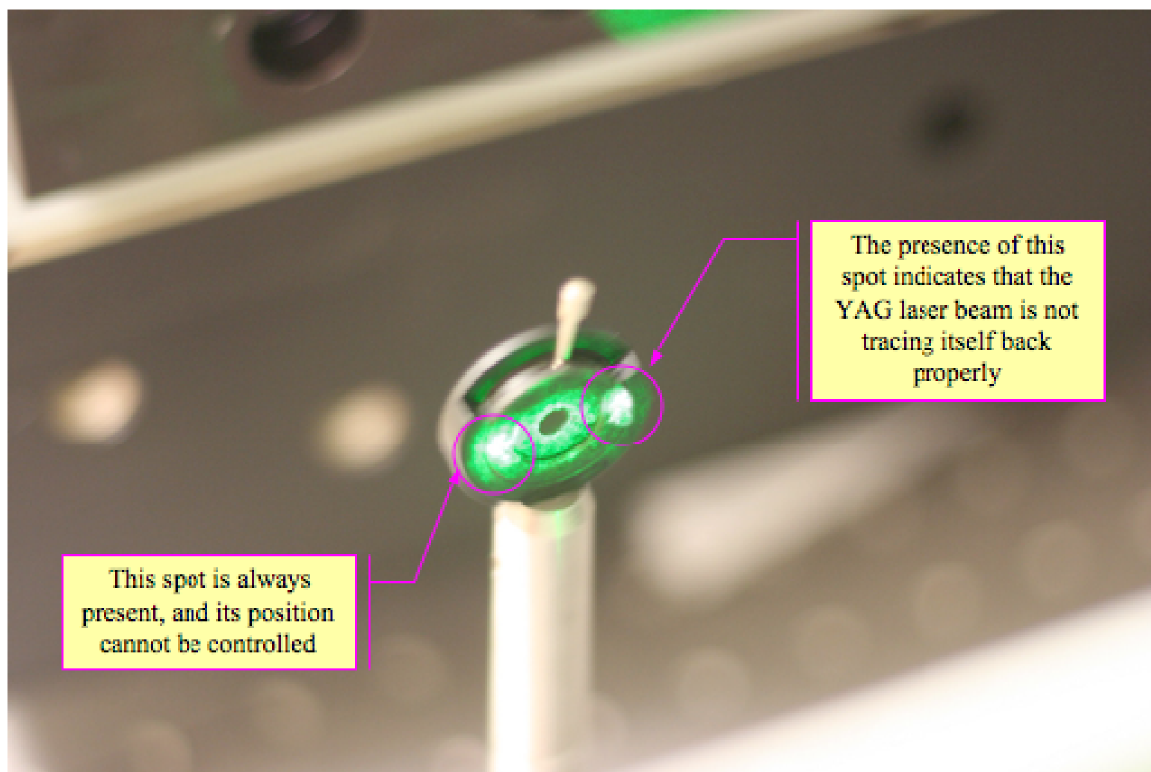

Figure 55: The reflection of the YAG laser beam on the back of the adjustable iris placed at the input of the OPO/OPA. The presence of the bright light spot to the right of the iris indicates that the laser beam is not tracing itself back properly, and that the position of the Kinematic Mirror – OPO Cavity R (#9) must be adjusted.

In order to have the YAG laser beam track itself back properly, it is necessary to adjust the position of the Kinematic Mirror – OPO Cavity R (#9) by using its three micropositioners. While adjusting the position of such mirror, the position of the bright light spot on the back of the iris will also change its position, as shown in Figure 56; the goal is to adjust the position of the mirror so that the bright light spot will be positioned in the center of the iris.

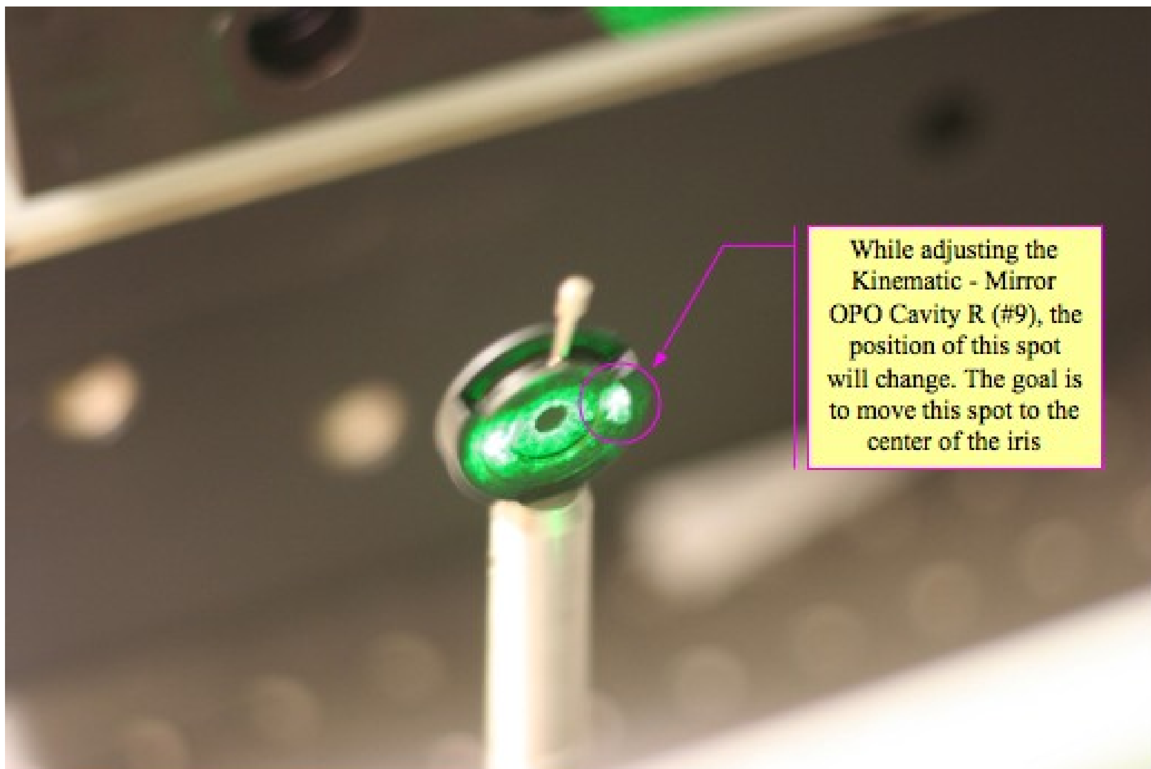

Figure 56: While adjusting the position of the Kinematic Mirror – OPO Cavity R (#9), the position of the bright light spot to the right of the iris will change position.

When the bright light spot is positioned in the center of the iris, as shown in Figure 57 the YAG laser beam is tracing itself back properly. Nonetheless, place a perforated card between the kinematic mirrors #4 and #7, and make sure that the reflection of the OPO crystals #1, and #2 is still normal (Figure 50).

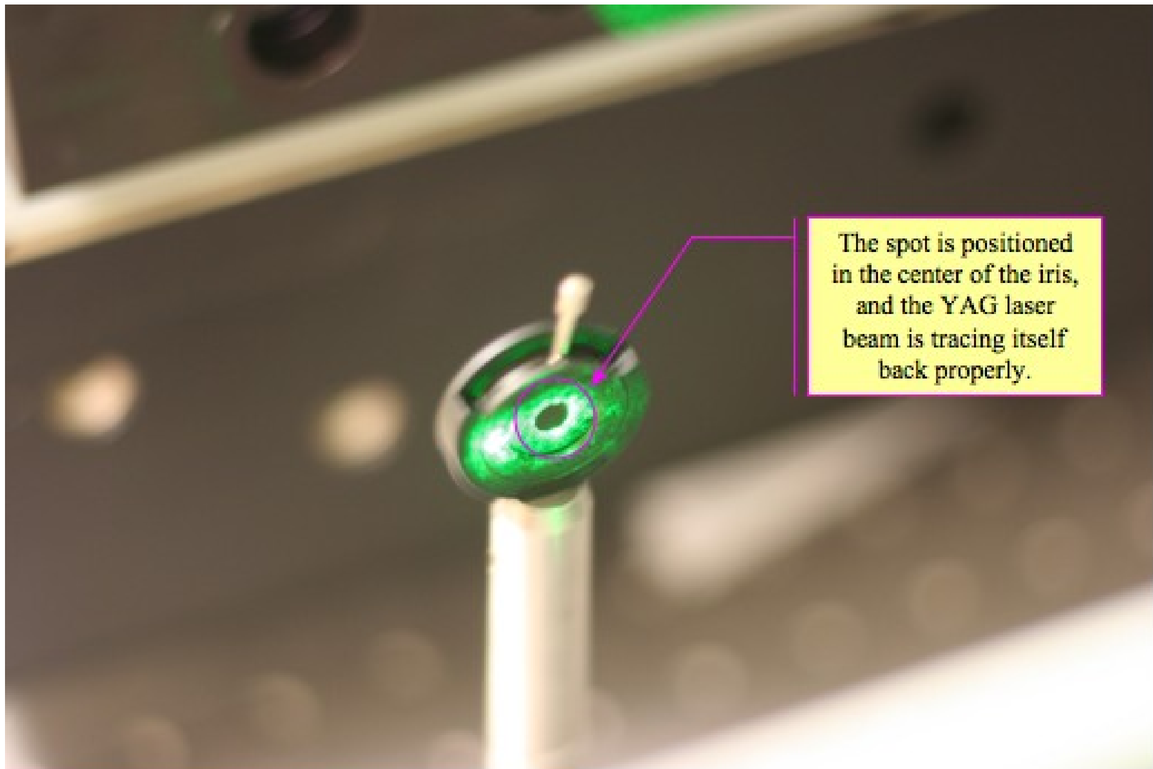

Figure 57: When the position of the Kinematic Mirror – OPO Cavity R (#9) is correct, the YAG laser beam traces itself back, and the "mobile" bright light spot will be positioned in the center of the iris.

Next, it is necessary to make sure that the YAG laser beam is entering the OPO crystals in the center. Cover the kinematic mirror #7 with a piece of optical lens paper, and place a card behind the OPO crystals as shown in Figure 58.

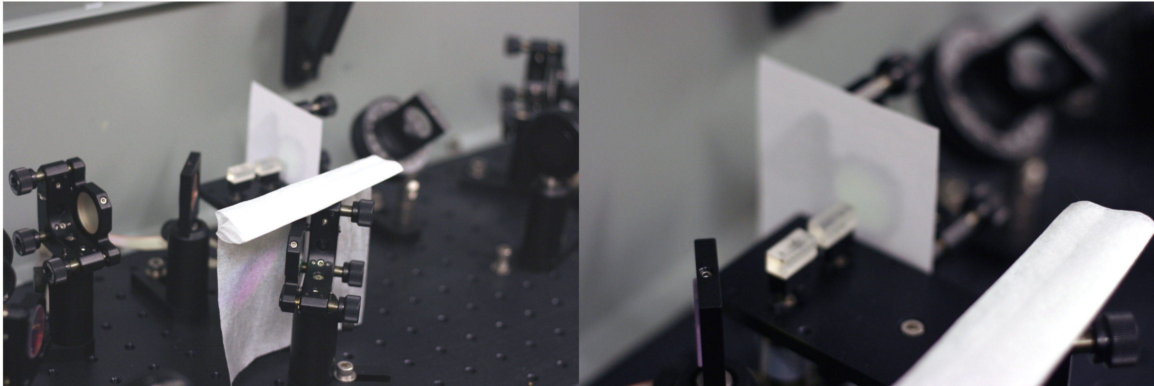

Figure 58: Optical lens paper covering the kinematic mirror #7 (left), and card placed behind the OPO crystals (right).

The purpose of covering the kinematic mirror #7 with a piece of optical lens paper is to scatter the YAG laser beam, and have the former project a silhouette of the OPO crystals onto the card placed behind them as shown in Figure 59.

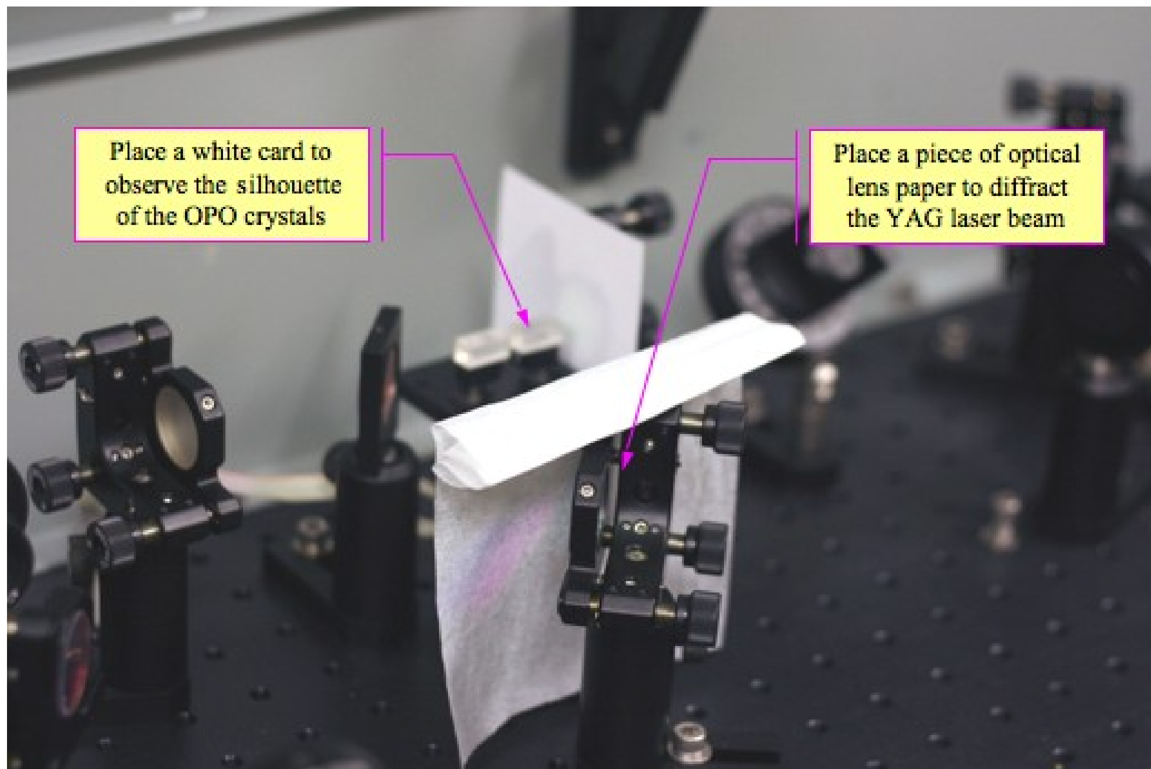

Figure 59: Kinematic mirror #7 masked with a piece of optical lens paper to diffract the YAG laser beam, and project a silhouette of the OPO crystals onto the card placed behind them.

As shown in Figure 60, the YAG laser beam will be diffracted by optical lens paper placed on the kinematic mirror #7, and the diffracted light will flood the OPO crystals; some of the light will propagate through the crystals themselves, and some of the light will propagate along the crystals instead. The propagation of the light through the OPO crystals will generate the projection shown in Figure 60. Adjust the position of kinematic mirror #7 to center the YAG laser beam. Having reached this point, it is necessary to verify –once again, that the YAG laser beam is still tracking itself back properly; thus, check the reflection of the laser beam onto the back of the adjustable iris at the input of the OPO/OPA, as shown in Figure 55, Figure 56, and Figure 57. As described earlier in

this section, use the kinematic mirror #9 to correct the propagation of the YAG laser beam through the OPO crystals.

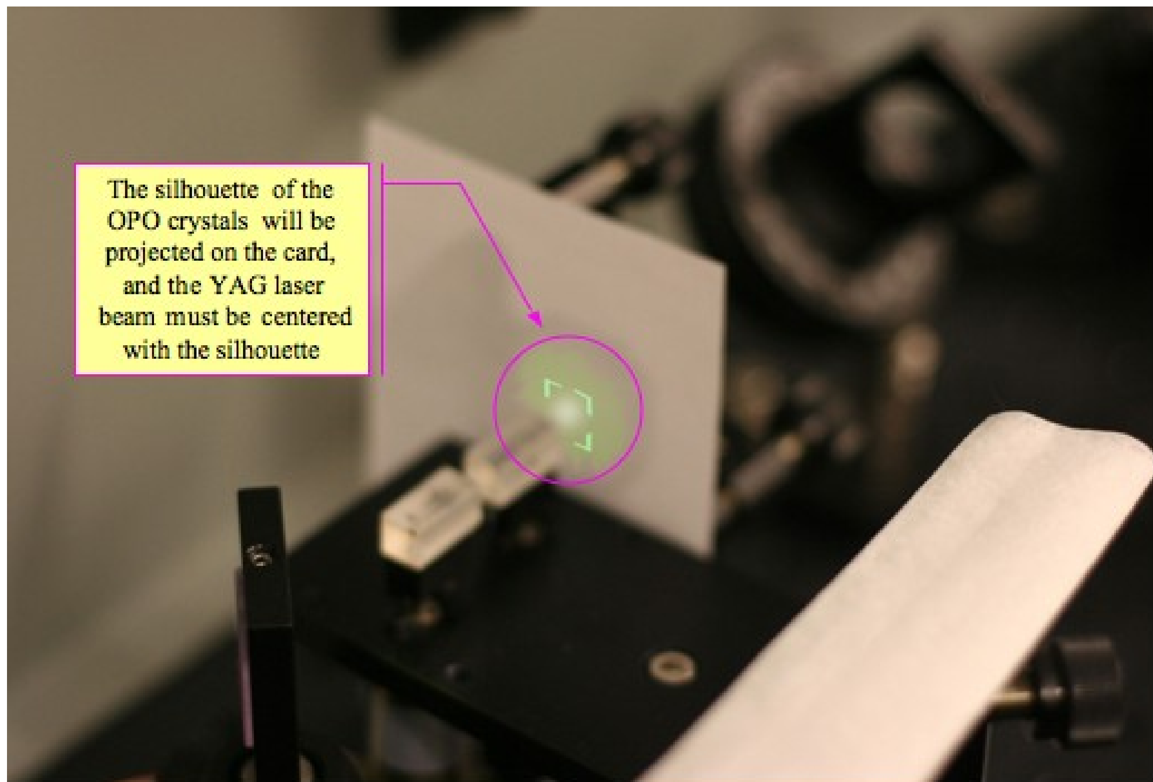

Figure 60: The silhouette of the OPO crystals projected onto a card.

Next, use the LaserVision Motor Control software to position the motors #3, #4, #5, and #6 as specified in Table 3. Such values have been calibrated ad-hoc for each of the OPA crystals by Dean R. Guyer, Ph.D. of LaserVision; they are specific values to be used only with this OPO/OPA system. Also, it is necessary to verify that the laser beam is propagating correctly through the OPA crystals (in the center) by monitoring the output of the OPO/OPA system with an IR detecting card. If no IR beam is detected at the output of the OPO/OPA system it is very likely that the laser beam is not propagating correctly thought the OPA crystals. Use the kinematic mirror #7 to adjust the propagation

of the laser beam through the OPA crystal; nonetheless, keep in mind that it will be necessary to repeat the fine alignment of the YAG laser and the OPO/OPA system.

Table 3: Optical components of the OPO/OPA system.

OPA crystal motor #	Position
3	5310
4	-4578
5	5715
6	-5073

Next, the turn the OPO and OPA attenuators (#3 and #10) to 45° degrees so that the YAG laser beam will propagate beyond the beam expander (#1), and the kinematic mirror #2, through the OPO and OPA crystals with full power. Also, remove the adjustable iris at the input of the OPO/OPA system so that the YAG laser beam will not be obstructed. Increase the power output of the YAG back to 500 mJ by increasing the magnitude of the delay of the capacitor bank CB630C. Using a power meter, measure the power at the end of the OPO crystals, and using LaserVision Motor Control software adjust the position of motor #2 to maximize power level (the optimal power level should be > 15 mJ). Next, place the power meter at the output of the OPO/OPA system, and by using the LaserVision Motor Control software adjust the position of motor #3, #4, #5, and #6 (not more than 500 counts per motor, in each direction) to maximize power output. Finally, place the adjustable iris #18 back in place, and adjust their position as necessary to obtain maximum output of the OPO/OPA. Note that the Si polarizer #13, and the polarizer #17 are not used when the OPO/OPA system is set in the “Near Infrared” range, as shown in Figure 46.

5.1.4. LaserVision OPO/OPA System Use in the Near Infrared Range

In order to use the OPO/OPA system in the Near Infrared range, it is necessary to modify its hardware configuration. Select the proper range by using the LaserVision Motor Control software as shown in Figure 61. Remove the silicon polarizer (#13), and the polarizer #17.

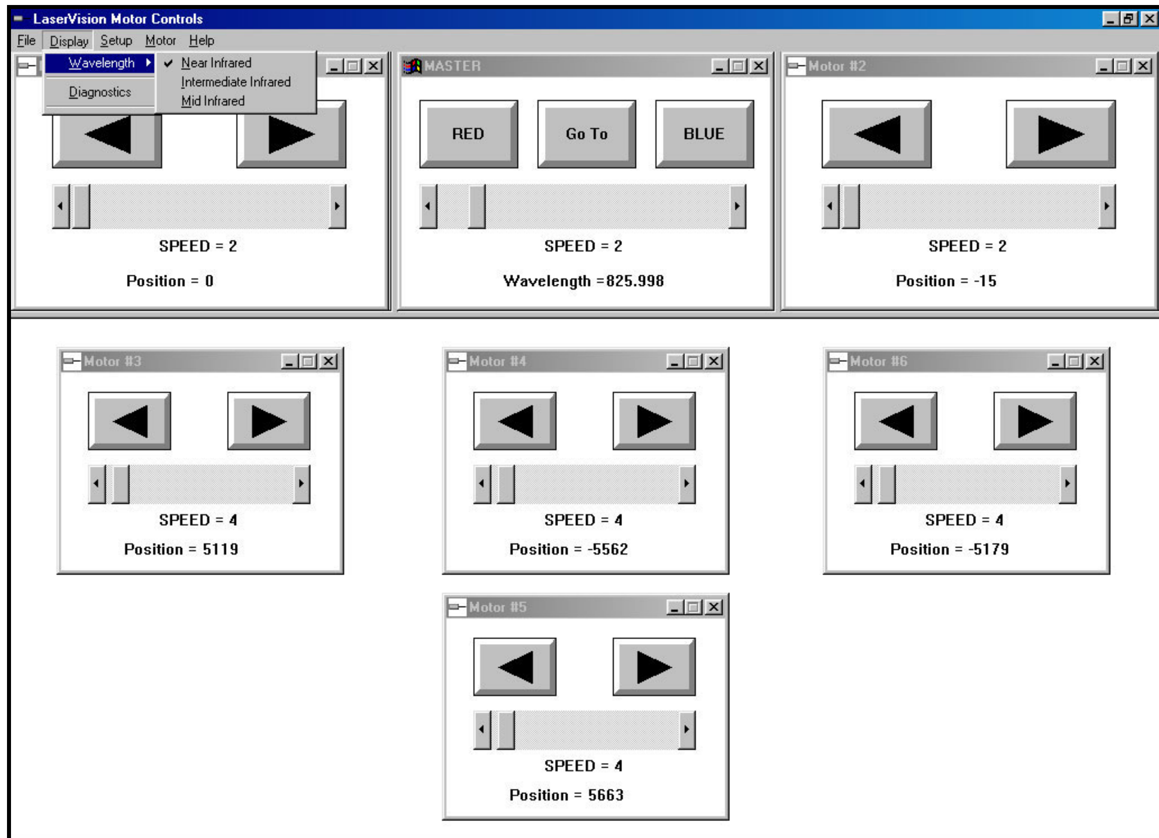

Figure 61: Selection of the Near Infrared range of the OPO/OPA system by using the LaserVision Motor Control software.

The power output spectrum of the OPO/OPA system, which was set to be used in the Near Infrared range, was made available as Figure 62. Note that such power output spectrum was obtained with no germanium crystal filter placed at the output of the OPO/OPA system.

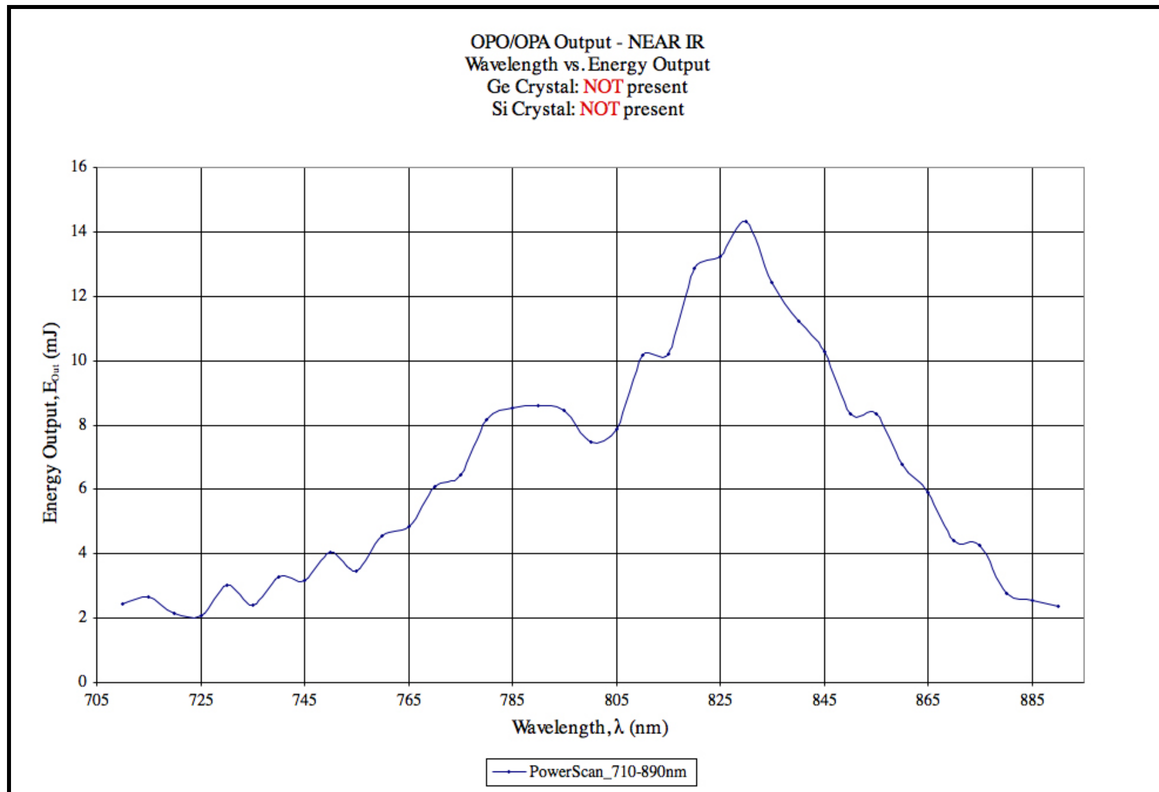

Figure 62: The power output spectrum of the OPO/OPA system, which was set to be used in the Near Infrared range. Note that such power output spectrum was obtained with no germanium crystal filter placed at the output of the OPO/OPA system.

5.1.5. LaserVision OPO/OPA System Use in the Intermediate Infrared Range

In order to use the OPO/OPA system in the Intermediate Infrared range, it is necessary to modify its hardware configuration. Select the proper range by using the LaserVision Motor Control software as shown in Figure 63.

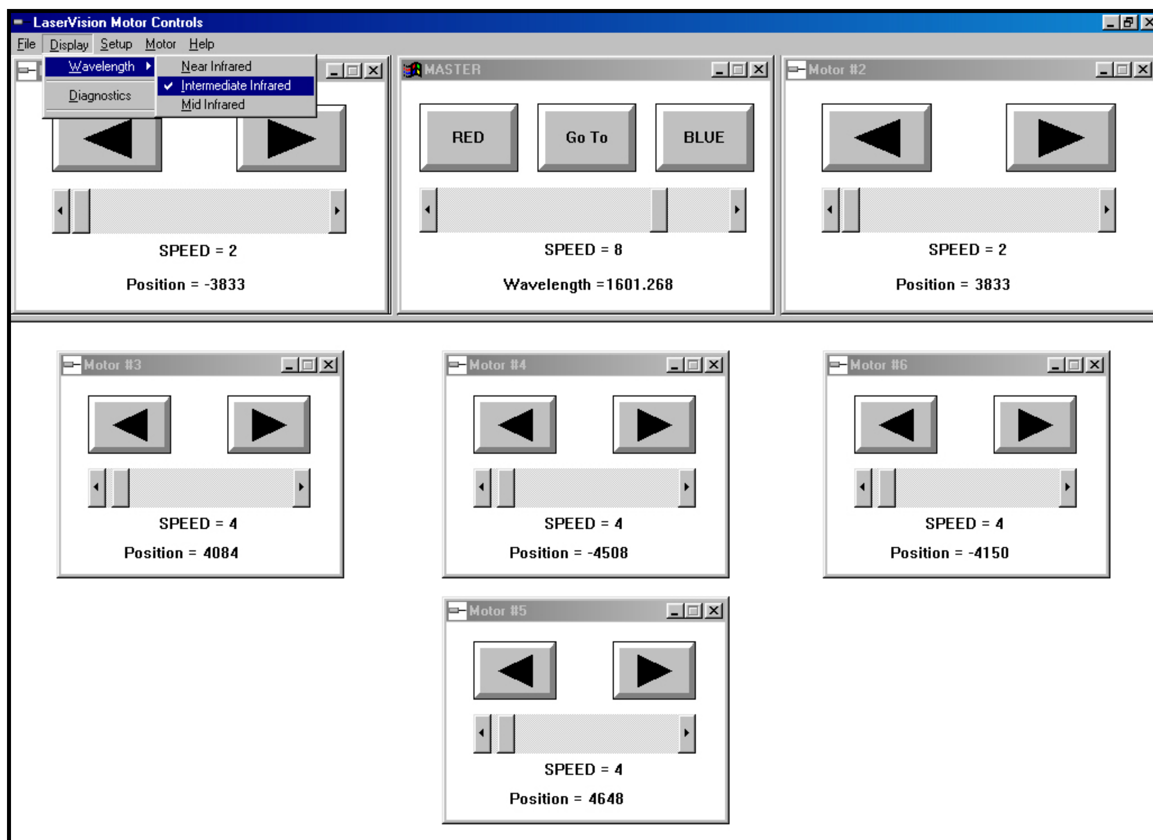

Figure 63: Selection of the Intermediate Infrared range of the OPO/OPA system by using the LaserVision Motor Control software.

Remove the silicon polarizer (#13), and turn the polarizer #17 until its core is positioned like a letter “U”, as shown in Figure 64.

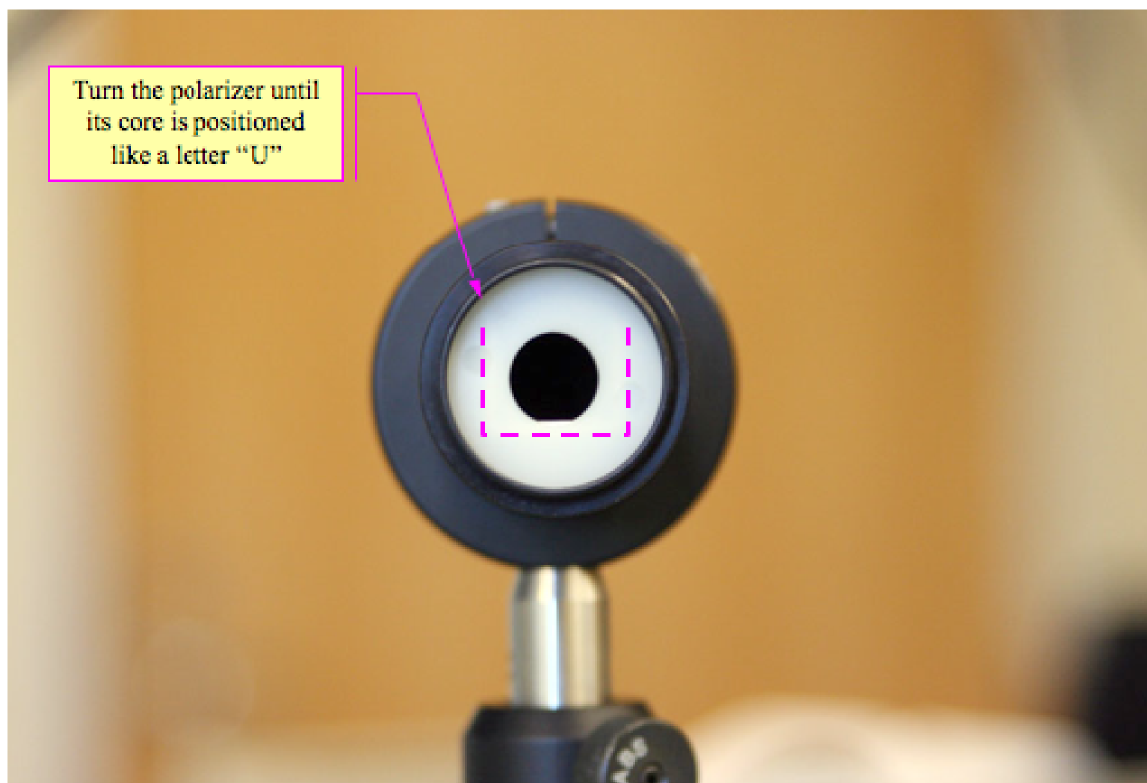

Figure 64: Core of the polarizer #17 positioned like a letter “U”.

The power output spectrum of the OPO/OPA system, which was set to be used in the Intermediate Infrared range, was made available as Figure 65. Note that such power output spectrum was obtained with no germanium crystal filter placed at the output of the OPO/OPA system.

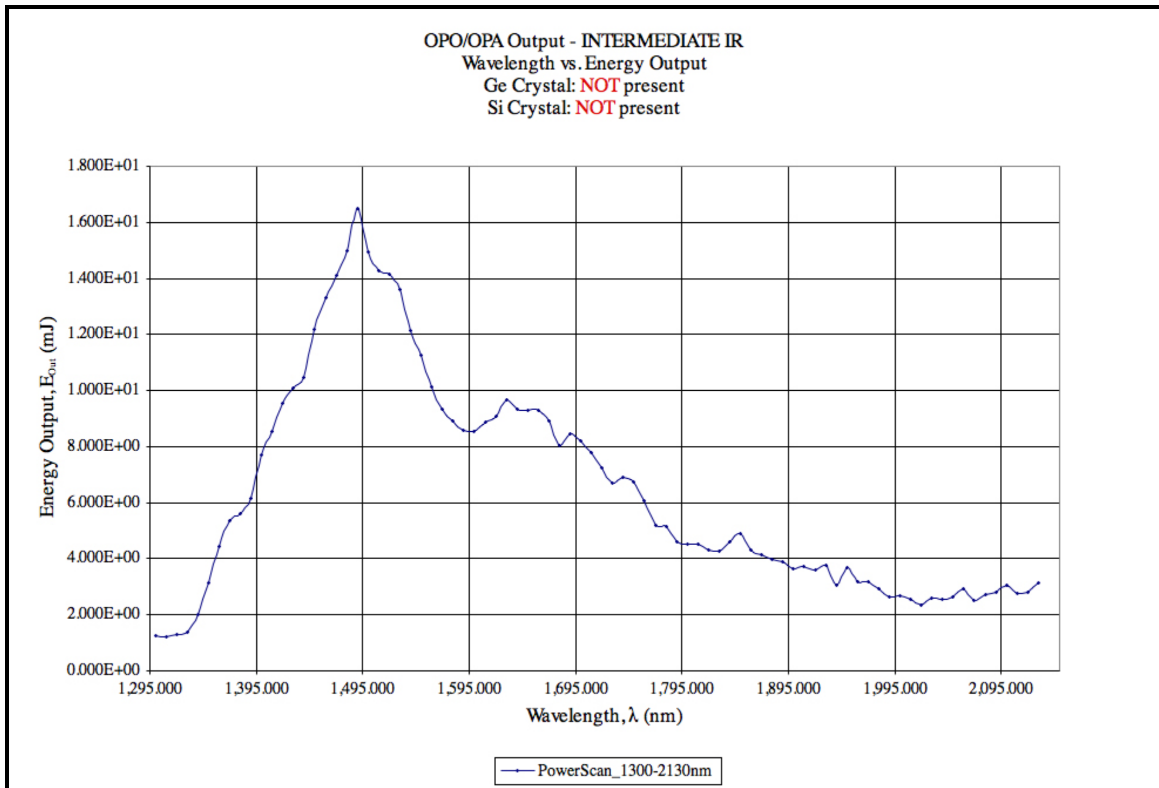

Figure 65: The power output spectrum of the OPO/OPA system, which was set to be used in the Intermediate Infrared range. Note that such power output spectrum was obtained with no germanium crystal filter placed at the output of the OPO/OPA system

5.1.6. LaserVision OPO/OPA System Use in the Mid Infrared Range

In order to use the OPO/OPA system in the Mid Infrared range, it is necessary to modify its hardware configuration. Select the proper range by using the LaserVision Motor Control software as shown in Figure 66.

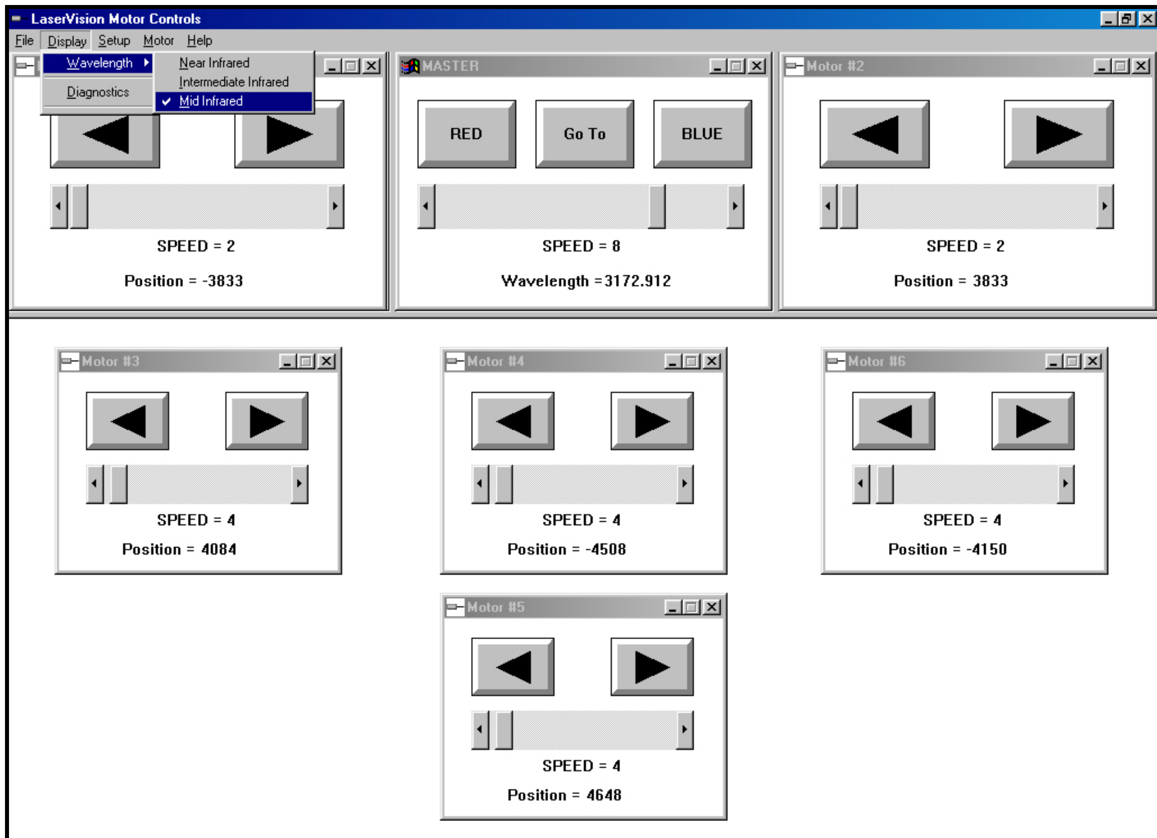

Figure 66: Selection of the Mid Infrared range of the OPO/OPA system by using the LaserVision Motor Control software.

Put the silicon polarizer (#13) back in place, and turn the polarizer #17 until its core is positioned liked a letter “C”, as show in Figure 67. The power output spectrum of the OPO/OPA system set to be used in the Mid Infrared range was made available as Figure 68.

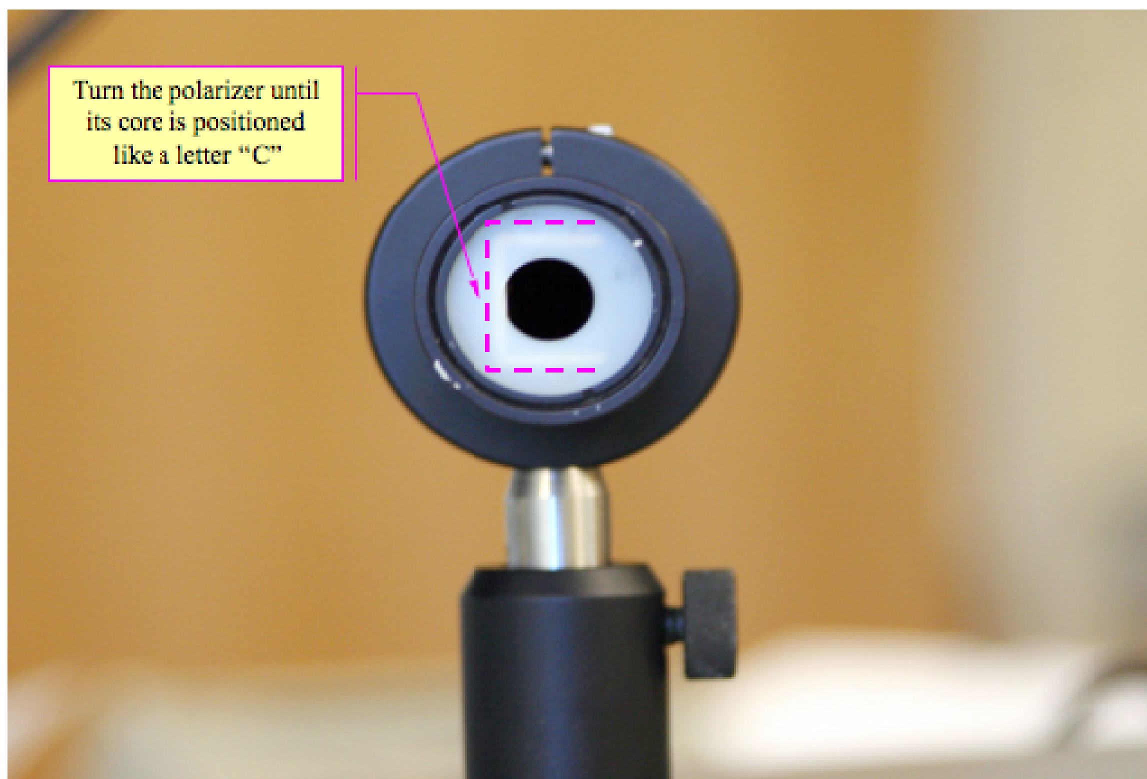

Figure 67: Core of the polarizer #17 positioned like a letter “C”.

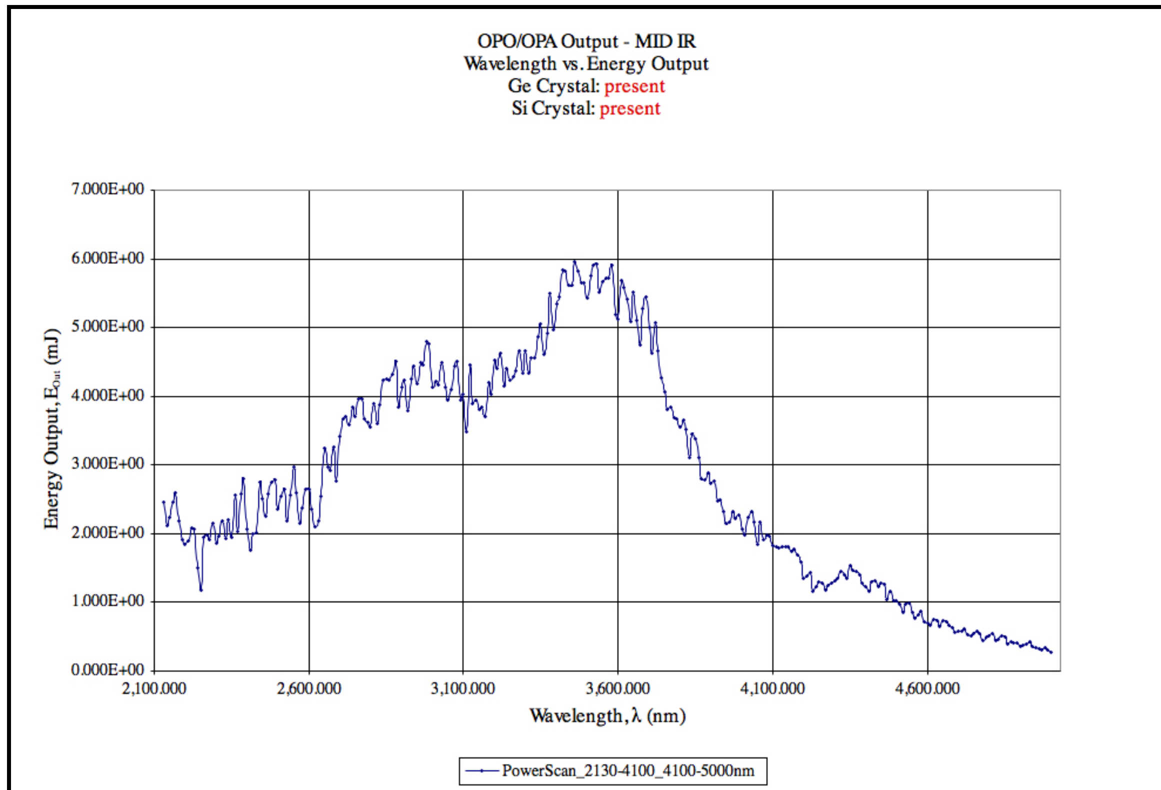

Figure 68: The power output spectrum of the OPO/OPA system, which was set to be used in the Mid Infrared range. Note that such power output spectrum was obtained with a germanium crystal filter placed at the output of the OPO/OPA system.

5.2. Tooling factor determination of the Kurt J. Lesker PDV 75 Deposition System for the deposition of Au, and Ni thin films

In this work, a Kurt J. Lesker PVD 75 Deposition System (Lesker PVD 75) was used to deposit metal thin films on Mg-doped GaN, and Mg-doped $Al_xGa_{1-x}N$. The Lesker PVD 75 available in the clean room, in Grigg Hall, at UNC Charlotte, has the capacity to process samples as small as 5 mm^2, three 100 mm wafers, or a single 150, 200, or 300 mm wafer. The deposition of thin films of metals is achieved either via thermal, or electron-beam (e-beam) evaporation. In the case of thermal evaporation, a filament heats the crucible that holds the source material, and it is hence useful for the evaporation of

low evaporation point sources and elements, or elements such as Al, and Sn that tend to form alloys and “wet” crucibles, or Fe, whose evaporation by means of e-beam is characterized by turbulent convention in the melt pool that leads to undesirable heat losses. In the case of e-beam evaporation, a source is heated and boiled off by an electron current that is attracted to the crucible by a high voltage, and whose trajectory is controlled by a magnetic field. E-beam evaporation is a preferred method for the evaporation and deposition of high melting point elements such as Au, and Ni.

As shown in Figure 69, the physical location of the crystal oscillator deposition monitor (crystal oscillator) differs from the physical location of the sample onto the sample holder; thus, the thickness of the thin films deposited on the sample and the crystal oscillator are different.

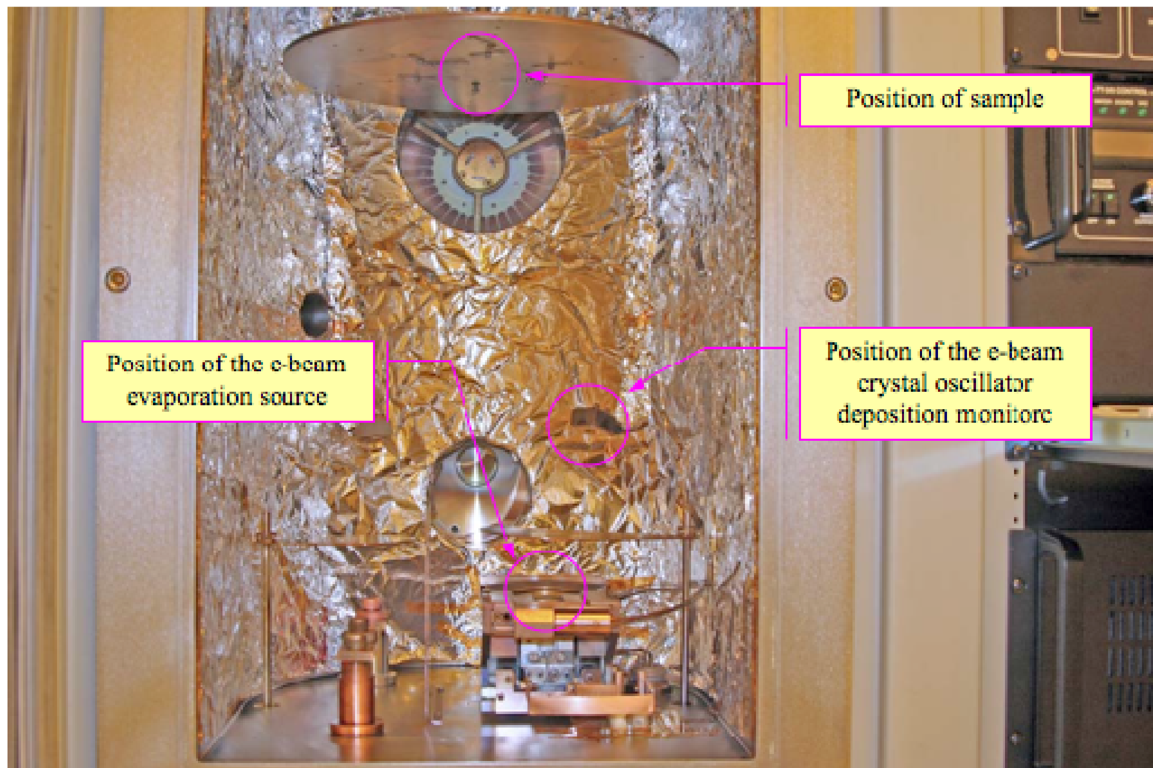

Figure 69: Interior of the D-chamber of the Kurt J. Lesker PVD 75 Deposition System used in this work. Note the different locations of crystal oscillator, and the sample.

Since the crystal oscillator is placed much closer to the location of the e-beam evaporation source, as shown in Figure 70, the thickness of the thin film deposited onto the crystal oscillator will be larger than the thickness of the thin film actually deposited onto the sample.

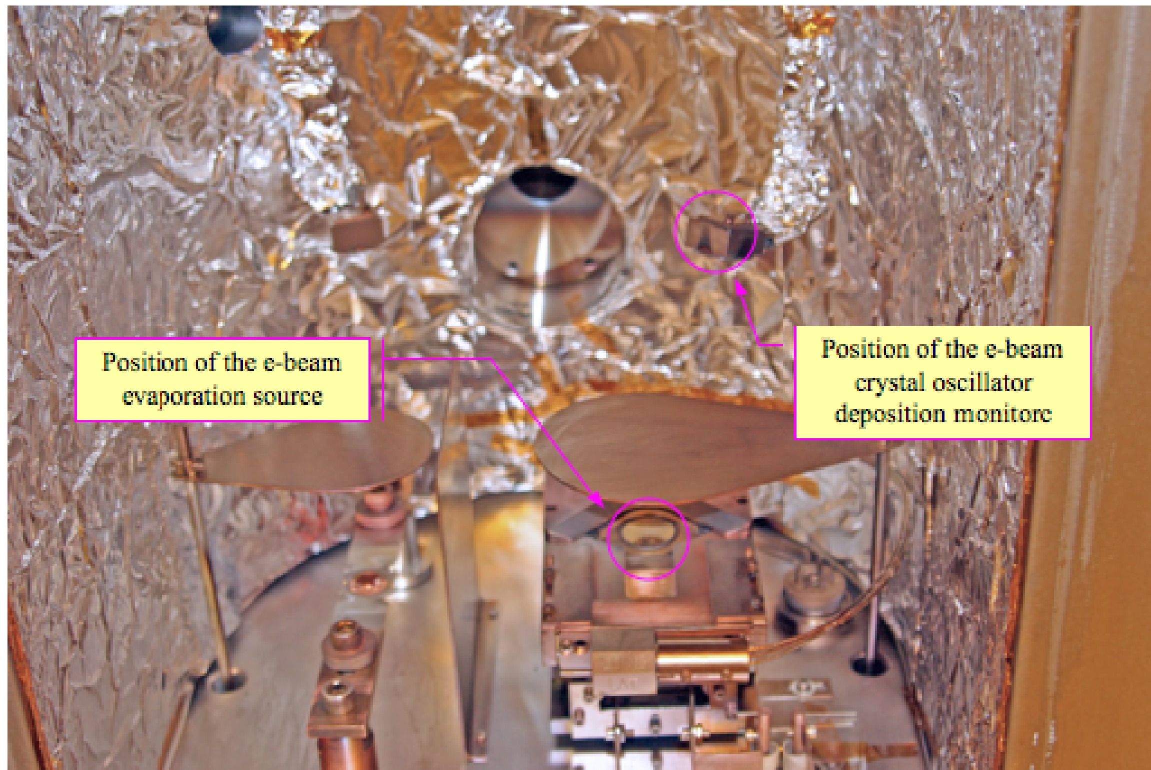

Figure 70: Interior close-up of the D-chamber of the Kurt J. Lesker PVD 75 Deposition System used in this work. Note the location of the crystal oscillator with respect to the position of the e-beam evaporation source.

Hence, it is necessary to determine the tooling factor, which is defined as the ratio between the film thicknesses on the sample and the crystal oscillator, and it is given by

$$F = \frac{T_m}{T_i} \qquad \text{Equation 44}$$

where F is the tooling factor, T_m is the actual thickness of the thin film of metal deposited onto the sample, and T_i is the thickness of the thin film of metal as deposited onto and

measured by the crystal oscillator. A tooling factor of 1.0 implies that the sample and the crystal oscillator received the same deposit thickness; a tooling factor larger than 1.0 implies that the sample received a thicker deposit than the crystal oscillator does, whereas a tooling factor smaller than 1.0 implies that the sample receives a thinner deposit than the sensor did.

In order to determine the value of the tooling factor with a given evaporation source, trial deposition of metals must be conducted onto masked samples, featured with sharp steps created by means of lift-off, and the actual thickness of the former determined by a precision measurement tool. In this work, the thicknesses of the trial deposition steps were determined with an error margin of 1 nm with the aid of a Taylor-Hobson TalyStep profilometer (courtesy of the Center for Precision Metrology at UNC Charlotte).

5.2.1. Preparation of masked samples for metal deposition trials with the Kurt J. Lesker PDV 75 Deposition System

Samples having a dimension of 1 in^2 were obtained by dicing 4-inch Si (111) wafers, stripped of native oxide with a 20 minute bath in buffer oxide etch (BOE), and rinsed in cascading de-ionized water (DI-H_20) for 20 minutes. The samples were then subjected to a surface cleaning treatment according to the following procedure:

1) Clean glassware and metal tweezers:
    a. Sonication with Naugra sonicator (power level 9) in Acetone for 2 minutes at a temperature of 35 °C.
    b. Sonication with Naugra sonicator (power level 9) in Methanol for 2 minutes at a temperature of 35 °C.

c. Rinse under DI-H_20 stream (18 MΩ), and then rinse in cascading DI-H_20 (18 MΩ) for 5 minutes, and dry samples with N_2.

2) Clean samples:

a. Sonication with Naugra sonicator (power level 9), face up in Acetone for 5 minutes at a temperature of 35 °C.

b. Sonication with Naugra sonicator (power level 9), face up in Methanol for 2 minutes at a temperature of 35 °C.

c. Rinse DI-H_20 stream (18 MΩ), and then rinse in cascading DI-H_20 (18 MΩ) for 15 minutes, and dry samples with N_2.

5.2.1.1.Masking and Patterning

The 1-in^2 Si (111) test structures were spin-coated with a ~ 1.5 m thick layer of Microposit 1813 positive photoresist (photoresist), then patterned using an LED mask, whose details are shown in Figure 71, and an ultraviolet (UV) photolithographic process controlled by a Quintel Q 4000-6 1:1 contact mask alignment system.

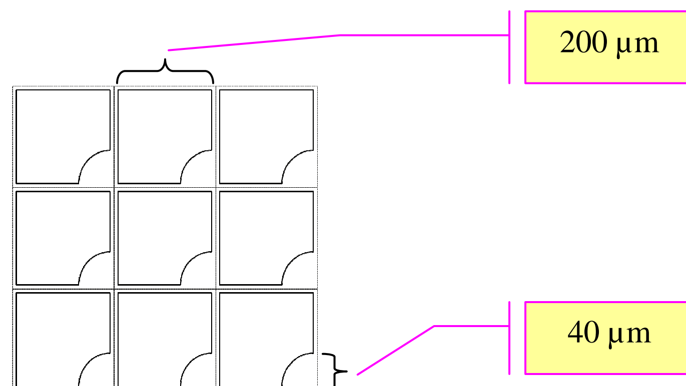

Figure 71: Detail of the LED mask used to pattern 1-in^2 Si (111) test structures.

Patterns were finally developed with Microposit 354 positive photoresist developer (developer) according to the following procedure:

1) Spin-coat Microposit 1813 positive photoresist using a Brewer Science Cee 200 High Speed Spin Processor with the following parameters:
    a. 3000 RPM spin rate
    b. 70 second spin time frame.
2) Soft-bake photoresist-covered sample on a quartz disk placed on a hot plate at a temperature of 115 °C for 70 seconds.
3) Align mask to photoresist-covered samples using a Quintel Q 4000-6 1:1 contact mask alignment system, and expose photoresist to UV lamp with a total UV dose of 120 mJ/cm^2.
4) Develop photoresist using 100 ml solution prepared with Microposit 354 positive photoresist developer, and DI-H_20 (18 MΩ) with a 1:1 ratio for 70 seconds.
5) Rinse under DI-H2O stream (18 MΩ), and then rinse in cascading DI-H_20 (18 MΩ) for 5 minutes, and dry samples with N_2.

5.2.1.2. Au film deposition, and determination of relative tooling factor

Masked and patterned test structures were used for the deposition of Au thin films with an increasing thickness as indicated in Table 4, which also indicates the value for the pressure in the D-chamber of the Lesker PVD 75 as measured at the beginning and the end of the Au thin film deposition, and the value for the thickness of each of the as-deposited Au thin films as determined by the crystal oscillator “Sigma 242”.

Table 4: Au deposition of Si (111): D-chamber pressure settings, and Au thin film thickness as measured by the crystal oscillator deposition monitor (Sigma 242).

Sample Number	Sample ID	D-Chamber Pressure $P_{Chamber}$ (torr)		Sigma 242 Thickness (KÅ)
		Beginning	End	
1	AuSi100	$1.40x10^{-7}$	$2.70x10^{-7}$	0.561
2	AuSi200	$1.40x10^{-7}$	$1.80x10^{-6}$	1.113
3	AuSi400	$1.70x10^{-7}$	$2.40x10^{-6}$	2.240
4	AuSi800	$8.10x10^{-8}$	$2.10x10^{-7}$	4.456

The thicknesses of each of the Au thin films deposited on Si (111) were determined with the aid of a TalyStep profilometer with a +/- 1 nm precision, and data was used in Table 5 to determine the tooling factor of the Lesker PVD 75.

Table 5: Au thin film deposition on Si (111): determination of the tooling factor of the Lesker PVD 75.

Sample Number	Sample ID	Au Thin Film Thickness (nm)		Stdev	Tooling Factor
		Sigma 242	TalyStep		
1	AuSi100	56.1	3.428	0.117	6.111%
2	AuSi200	111.3	10.670	2.352	9.587%
3	AuSi400	224.0	23.798	3.583	10.624%
4	AuSi800	445.6	52.083	2.982	11.688%

Figure 72 shows the graph of the thicknesses of the Au thin film deposited on Si (111) as measured by the crystal oscillator (Sigma 242) and the TalyStep profilometer, and the tooling factor as a function of Au thin film thickness.

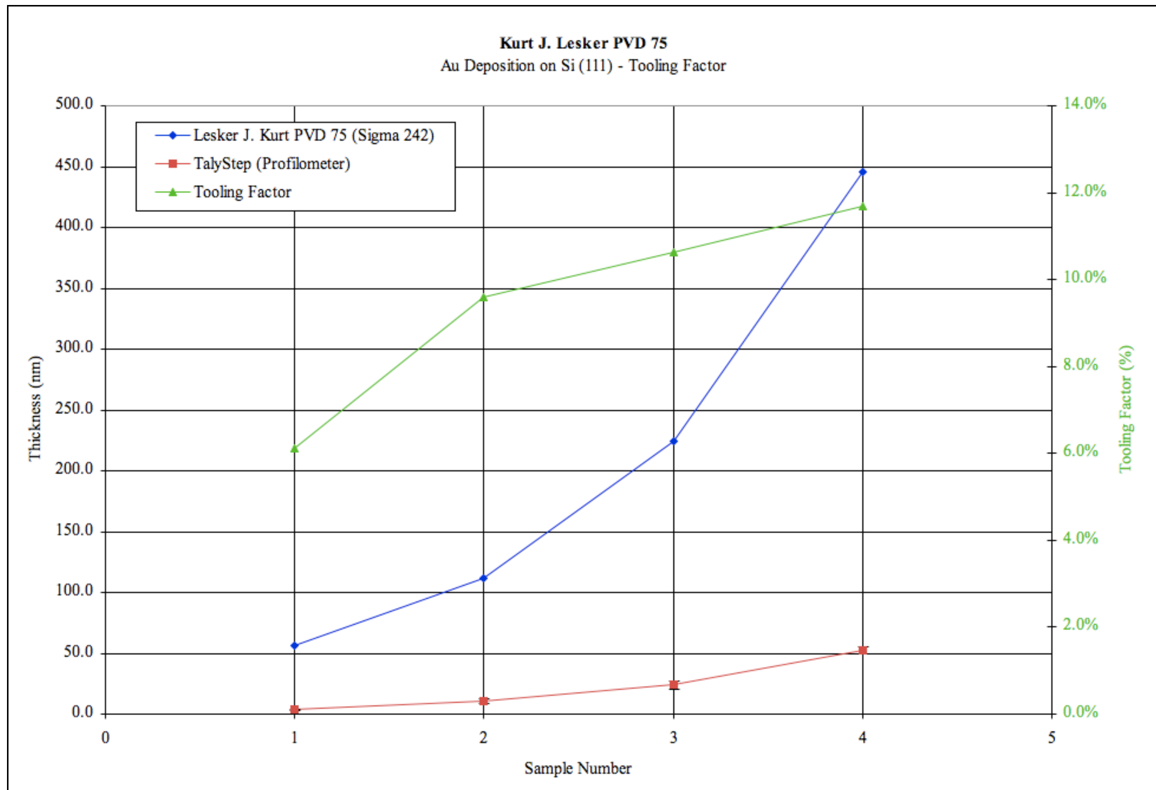

Figure 72: Thicknesses of Au thin film deposited on Si (111), as measured by the crystal oscillator deposition monitor (Sigma 242) and the TalyStep profilometer, and the determined tooling factor.

5.2.1.3. Ni film deposition, and determination of relative tooling factor

Masked and patterned test structures were used for the deposition of Ni thin films with an increasing thickness as indicated in Table 6, which also indicates the value for the pressure in the D-chamber of the Lesker PVD 75 as measured at the beginning and the end of the Au thin film deposition, and the value for the thickness of each of the as-deposited Au thin films as determined by the crystal oscillator "Sigma 242".

Table 6: Ni deposition of Si (111): D-chamber pressure settings, and Ni thin film thickness as measured by the crystal oscillator deposition monitor (Sigma 242).

Sample Number	Sample ID	D-Chamber Pressure $P_{Chamber}$ (torr)		Sigma 242 Thickness (KÅ)
		Beginning	End	
1	NiSi100	$1.70x10^{-7}$	$1.60x10^{-6}$	0.560
2	NiSi200	$1.30x10^{-7}$	$2.00x10^{-6}$	1.119
3	NiSi400	$1.60x10^{-7}$	$2.30x10^{-6}$	2.229
4	NiSi800	$2.00x10^{-7}$	$8.10x10^{-6}$	4.446

The thickness of each of the Au thin films deposited on Si (111) were determined with the aid of a TalyStep profilometer with a +/- 1 nm precision, and data was used in Table 7 to determined the tooling factor of the Lesker PVD 75.

Table 7: Ni thin film deposition on Si (111): determination of the tooling factor of the Lesker PVD 75.

Sample Number	Sample ID	Au Thin Film Thickness (nm)		Stdev	Tooling Factor
		Sigma 242	TalyStep		
1	NiSi100	56.0	11.714	1.458	20.918%
2	NiSi200	111.9	18.582	2.579	16.606%
3	NiSi400	222.9	33.259	2.729	14.921%
4	NiSi800	444.6	68.035	3.195	15.302%

Figure 73 shows the graph of the thicknesses of the Ni thin film deposited on Si (111) as measured by the crystal oscillator (Sigma 242) and the TalyStep profilometer, and the tooling factor as a function of Au thin film thickness.

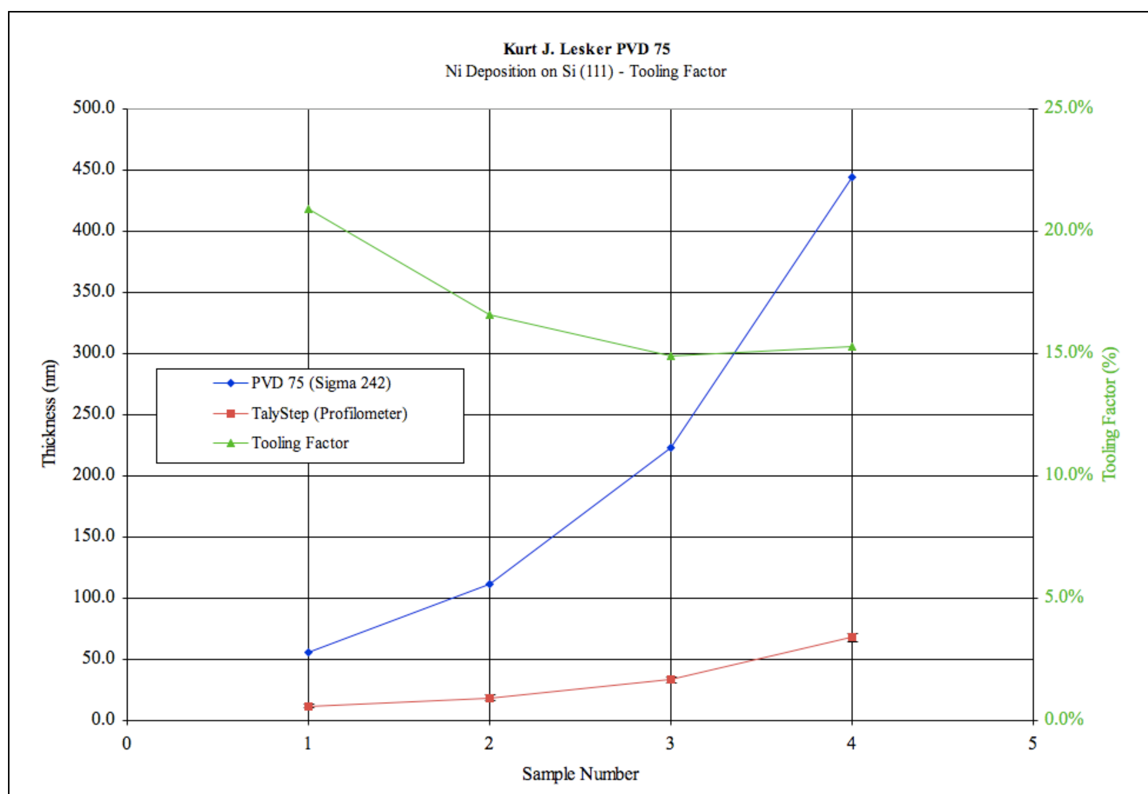

Figure 73: Thicknesses of Ni thin film deposited on Si (111), as measured by the crystal oscillator deposition monitor (Sigma 242) and the TalyStep profilometer, and the determined tooling factor.

5.2.1.4. Metal Lift-off Patterning

By using a metal lift-off patterning technique, the photoresist under the blanketed metal thin film is removed with solvent, taking the metal thin film with it, and leaving the areas of the metal thin film that was deposited onto the surface of the Si (111) sample. The metal lift-off patterning procedure is the following:

1) Clean glassware and metal tweezers:

    a. Sonication with Naugra sonicator (power level 9), in Acetone for 2 minutes at a temperature of 35 °C.

b. Sonication with Naugra sonicator (power level 9), in Methanol for 2 minutes at a temperature of 35 °C.

c. Rinse DI-H_20 stream (18 MΩ), then rinse in cascading DI-H_20 (18 MΩ) for 5 minutes, and dry samples with N_2.

2) Sonicate samples:

a. Sonication with Naugra sonicator (power level 3), face up in Acetone for 2 minutes at a temperature of 35 °C.

b. Rinse DI-H_20 stream (18 MΩ), then rinse in cascading DI-H_20 (18 MΩ) for 2 minutes, and dry samples with N_2.

Figure 74 shows the result of a successfully conducted lift-off patterning of a test structure consisting of a patterned Au thin film on Si (111); moreover, a control structure consisting of a patterned Ni thin film on Si (111) used to validate the lift-off process for the fabrication of the kind of metal semiconductor metal (MSM) structure used in this work is shown.

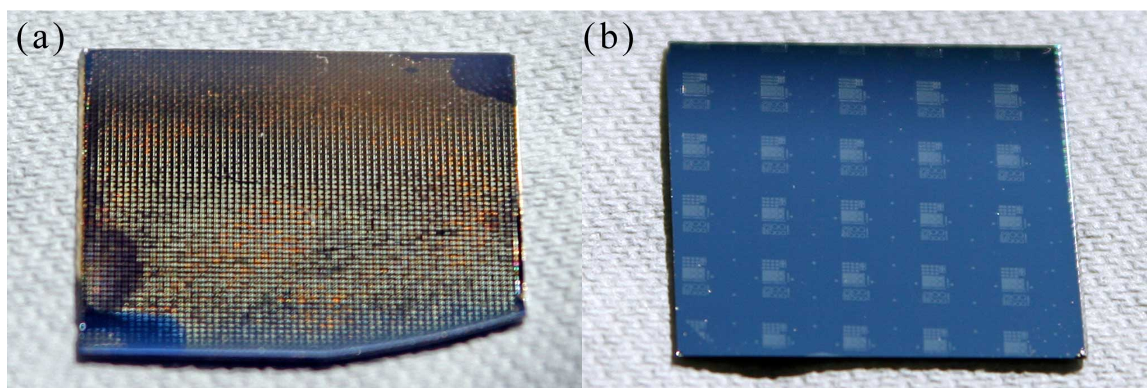

Figure 74: (a) Test structure consisting of a patterned Au thin film on Si (111), and (b) a control structure used to validate the lift-off process used to fabricate the kind of metal semiconductor metal (MSM) structure used in this work.

5.3. Fabrication of Ni-Au Ohmic contacts to Mg:doped GaN and $Al_xGa_{1-x}N$

Ni-Au Ohmic contacts to samples of Mg-doped GaN and $Al_xGa_{1-x}N$ having a dimension up to 1 cm^2 were fabricated using the following procedure:

1) Clean glassware and metal tweezers:
    a. Sonication with Naugra sonicator (power level 9) in Acetone for 5 minutes at a temperature of 35 °C.
    b. Sonication with Naugra sonicator (power level 9) in Methanol for 5 minutes at a temperature of 35 °C.
    c. Rinse under DI-H_20 stream (18 MΩ), and then rinse in cascading DI-H_20 (18 MΩ) for 20 minutes, and dry samples with N_2.
2) Clean samples:
    a. Sonication with Naugra sonicator (power level 9), face up in Acetone for 5 minutes at a temperature of 35 °C.
    b. Sonication with Naugra sonicator (power level 9), face up in Methanol for 2 minutes at a temperature of 35 °C.
    c. Rinse under DI-H_20 stream (18 MΩ), and then rinse in cascading DI-H_20 (18 MΩ) for 20 minutes, and dry samples with N_2.
3) Mask and pattern samples:
    a. Spin-coat with a ~1.5 μm thick layer of Microposit 1813 positive photoresist (photoresist) by using a Brewer Science Cee 200 High Speed Spin Processor with the following parameters:
        i. 3000 RPM spin rate.
        ii. 70 second spin time frame.

b. Soft-bake photoresist-covered sample on a quartz disk placed on a hot plate at a temperature of 115 °C for 70 seconds.

c. Align MSM/CTLM mask to photoresist-covered samples using a Quintel Q 4000-6 1:1 contact mask alignment system, and expose photoresist to UV lamp with a total UV dose of 120 mJ/cm^2.

d. Develop photoresist using 100 ml solution prepared with Microposit 354 positive photoresist developer, and DI-$H_2$0 (18 MΩ) with a 1:1 ratio for 70 seconds.

e. Rinse under DI-H_2O (18 MΩ) stream, and then rinse in cascading DI-$H_2$0 (18 MΩ) for 5 minutes, and dry samples with N_2.

f. Descum in oxygen plasma for 20 seconds at 50W.

g. Dip in solution of 37% HCl + 63% DI-$H_2$0 (18 MΩ) for 5 minutes, rinse under DI-H_2O (18 MΩ) stream, then rinse in cascading DI-$H_2$0 (18 MΩ) for 5 minutes, and dry samples with N_2, and place the sample(s) under vacuum in the D-chamber of the Lesker PVD 75.

4) Ni deposition on patterned samples:

a. Begin the deposition of 100 Å of Ni when the pressure is a D-chamber of the Lesker PVD 75 is below 2.0×10^{-7} torr. Use the following recipe from the recipe database of the Lekser PVD 75:

i. EB_Recipe_TP_Stokes_Ni_100A.

1. The sequence of commands included in the recipe "EB_Recipe_TP_Stokes_Ni_100A" is shown in Figure 75.

Order	Equipment	Equipment Ref	Operation	Value
1	Recipe	Set Abort Recipe	Abort Deposition	
2	Power Supply	Cru Pos 1	Turn_Off/Closed/Closing	
3	Power Supply	Cru Pos 2	Turn_Off/Closed/Closing	
4	Power Supply	Cru Pos 3	Turn_Off/Closed/Closing	
5	Power Supply	Cru Pos 4	Turn_Off/Closed/Closing	
6	Recipe	Dwell	5 Seconds	
7	Gauge	Wide Range Gauge PC	Check Pressure <= n.nn	.000009
8	Motors	Platen Motor On	Turn_On/Open/Opening	
9	Recipe	Dwell	5 Seconds	
10	Motors	Platen Motor Jog Velocity SP	Set Value = n.nn	10
11	Motors	Platen Motor Go Continuous +	Turn_On/Open/Opening	
12	Motors	Platen Motor Velocity	Check Value > n.nn	9
13	Sigma	Sigma Shutter Deposit Mapping 1	Set Value = n.nn	16
14	Recipe	Dwell	5 Seconds	
15	Recipe	Pause	"Informative Message"	Select Proper Sweep for Nickel
16	Power Supply	Cru Pos 3	Turn_On/Open/Opening	
17	Inputs	Crucible In Position 3	Check_On/Open/Opening	
18	Power Supply	EB Off	Turn_Off/Closed/Closing	
19	Power Supply	EB On	Turn_On/Open/Opening	
20	Power Supply	Ebeam Cutback	Check_Off/Closed/Closing	
21	Sigma	Sigma Control Request	Set Value = n.nn	Stokes_Ni_100A
22	Sigma	Sigma Start Process	Turn_On/Open/Opening	
23	Sigma	Sigma Process Stopped	Check_On/Open/Opening	
24	Power Supply	Power Supply1 Output Setpoint	Set Value = n.nn	0
25	Power Supply	EB On	Turn_Off/Closed/Closing	
26	Power Supply	EB Off	Turn_On/Open/Opening	
27	Power Supply	Cru Pos 3	Turn_Off/Closed/Closing	
32	Motors	Platen Motor Go Continuous +	Turn_Off/Closed/Closing	
33	Recipe	Dwell	N Seconds (n or HH:MM:SS)	10:00
34	Recipe	Pause	"Informative Message"	Wait Time for System to Cool

Figure 75: The sequence of commands included in the recipe used to deposit a 100 Å thick Ni film (EB_Recipe_TP_Stokes_Ni_100A).

b. The process called by the recipe “EB_Recipe_TP_Stokes_Ni_100A” is named “Stokes_Ni_100A”, and its details are shown in Figure 76:

i. The deposition rate (SetPt) is set to 0.5 Å/s.

ii. The final thickness of the Ni film to be deposited is set to 0.478 K Å, based on the relative tooling factor shown in Figure 73.

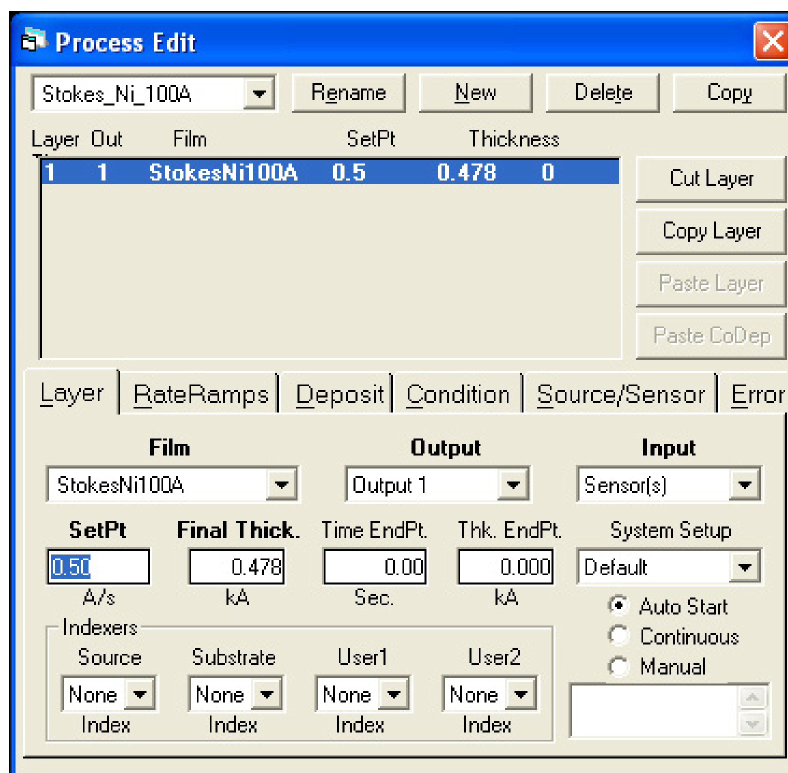

Figure 76: Screen shot showing the details of the process “Stokes_Ni_100A”, which is called by the recipe “EB_Recipe_TP_Stokes_Ni_100A”. Note the deposition rate (SetPt) which is set at 0.5 Å /s, and the final thickness of the Ni film to be deposited, which is set to 0.478 kÅ, based on the tooling factor of the Lesker PVD 75 for Ni deposition.

iii. The details of the film recipe (StokesNi100A) called by the process named “Stokes_Ni_100A” are shown in Figure 77:

1. PID controller settings.
2. E-beam power pre-deposition, and post-deposition conditions.
3. Metal source, and max e-beam power allocated.
4. Error controls.

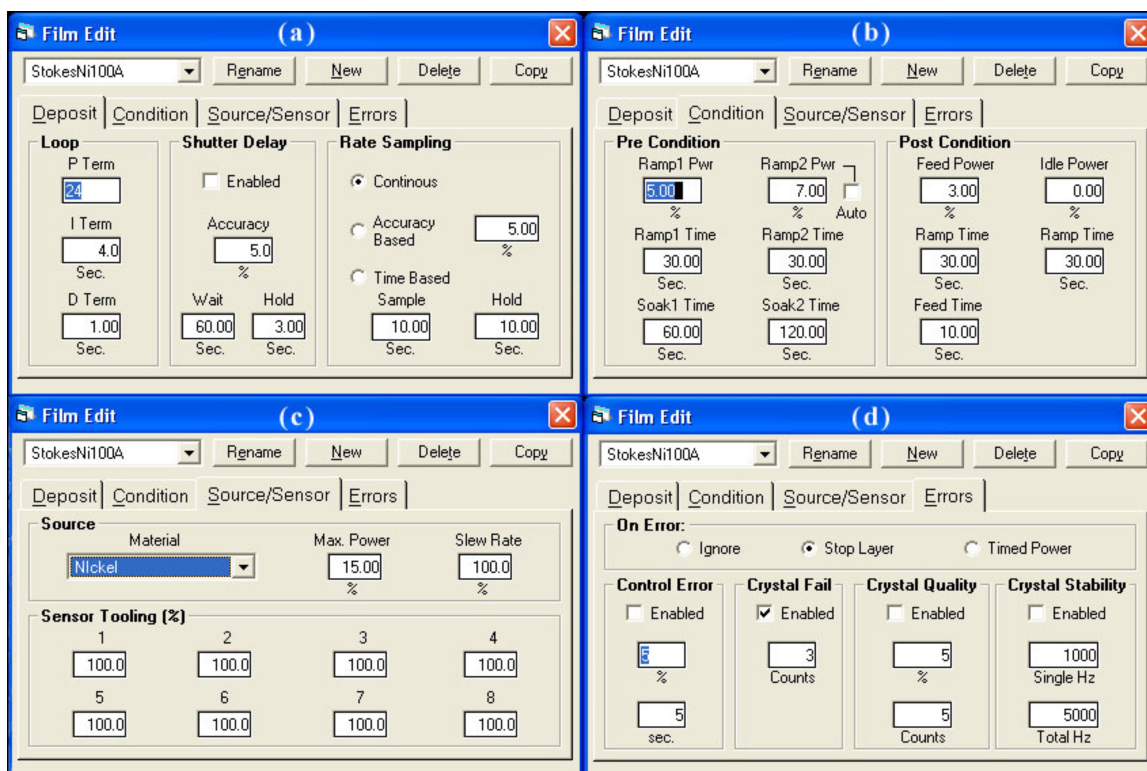

Figure 77: Screen shot showing the details of the film recipe (StokesNi100A) called by the process named “Stokes_Ni_100A”. (a) PID controller settings, (b) e-beam power pre-deposition, and post-deposition settings, (c) metal source, and max e-beam power allocated, and (d) error controls.

5) Au deposition on patterned samples:

   a. Following the deposition of 100 Å, begin the deposition of 100 Å of Au when the pressure is a D-chamber of the Lesker PVD 75 is below 2.0×10^{-7} torr. Use the following recipe from the recipe database of the Lekser PVD 75:

      i. EB_Recipe_TP_Stokes_Au_100A.

         1. The sequence of commands included in the recipe “EB_Recipe_TP_Stokes_Au_100A” is shown in Figure 78.

Order	Equipment	Equipment Ref	Operation	Value
1	Recipe	Set Abort Recipe	Abort Deposition	
2	Power Supply	Cru Pos 1	Turn_Off/Closed/Closing	
3	Power Supply	Cru Pos 2	Turn_Off/Closed/Closing	
4	Power Supply	Cru Pos 3	Turn_Off/Closed/Closing	
5	Power Supply	Cru Pos 4	Turn_Off/Closed/Closing	
6	Recipe	Dwell	5 Seconds	
7	Gauge	Wide Range Gauge PC	Check Pressure <= n.nn	.000009
8	Motors	Platen Motor On	Turn_On/Open/Opening	
9	Recipe	Dwell	5 Seconds	
10	Motors	Platen Motor Jog Velocity SP	Set Value = n.nn	10
11	Motors	Platen Motor Go Continuous +	Turn_On/Open/Opening	
12	Motors	Platen Motor Velocity	Check Value > n.nn	9
13	Sigma	Sigma Shutter Deposit Mapping 1	Set Value = n.nn	16
14	Recipe	Dwell	5 Seconds	
15	Recipe	Pause	"Informative Message"	Select Proper Sweep for Gold
16	Power Supply	Cru Pos 4	Turn_On/Open/Opening	
17	Inputs	Crucible In Position 4	Check_On/Open/Opening	
18	Power Supply	EB Off	Turn_Off/Closed/Closing	
19	Power Supply	EB On	Turn_On/Open/Opening	
20	Power Supply	Ebeam Cutback	Check_Off/Closed/Closing	
21	Sigma	Sigma Control Request	Set Value = n.nn	Stokes_Au_100A
22	Sigma	Sigma Start Process	Turn_On/Open/Opening	
23	Sigma	Sigma Process Stopped	Check_On/Open/Opening	
24	Power Supply	Power Supply1 Output Setpoint	Set Value = n.nn	0
25	Power Supply	EB On	Turn_Off/Closed/Closing	
26	Power Supply	EB Off	Turn_On/Open/Opening	
27	Power Supply	Cru Pos 4	Turn_Off/Closed/Closing	
32	Motors	Platen Motor Go Continuous +	Turn_Off/Closed/Closing	
33	Recipe	Dwell	N Seconds (n or HH:MM:SS)	10:00
34	Recipe	Pause	"Informative Message"	Wait Time for System to Cool

Figure 78: The sequence of commands included in the recipe used to deposit a 100 Å thick Au film (EB_Recipe_TP_Stokes_Au100A).

b. The process called by the recipe "EB_Recipe_TP_Stokes_Au_100A" is named "Stokes_au_100A", and its details are shown in Figure 79:

   i. The deposition rate (SetPt) is set to 1 Å/s.

   ii. The final thickness of the Ni film to be deposited is set to 1.636 K Å, based on the relative tooling factor shown in Figure 72:

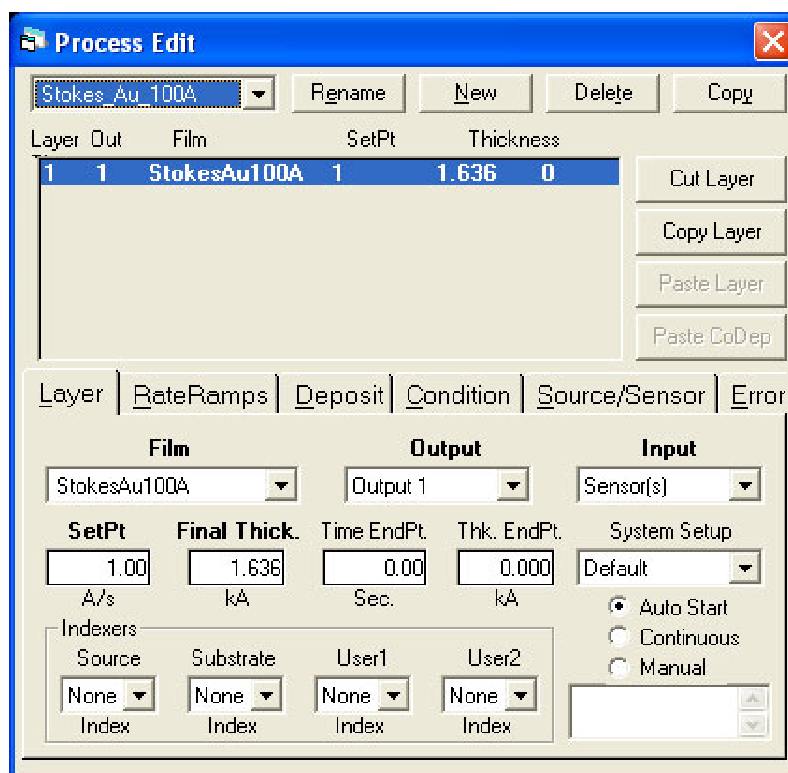

Figure 79: Screen shot showing the details of the process "Stokes_Au_100A", which is called by the recipe "EB_Recipe_TP_Stokes_Au_100A". Note the deposition rate (SetPt) which is set at 1 Å /s, and the final thickness of the Ni film to be deposited, which is set to 1.636 kÅ, based on the tooling factor of the Lesker PVD 75 for Au deposition.

iii. The details of the film recipe (StokesAu100A) called by the process named "Stokes_Au_100A" are shown in Figure 80:

1. PID controller settings.
2. E-beam power pre-deposition, and post-deposition conditions.
3. Metal source, and max e-beam power allocated.
4. Error controls.

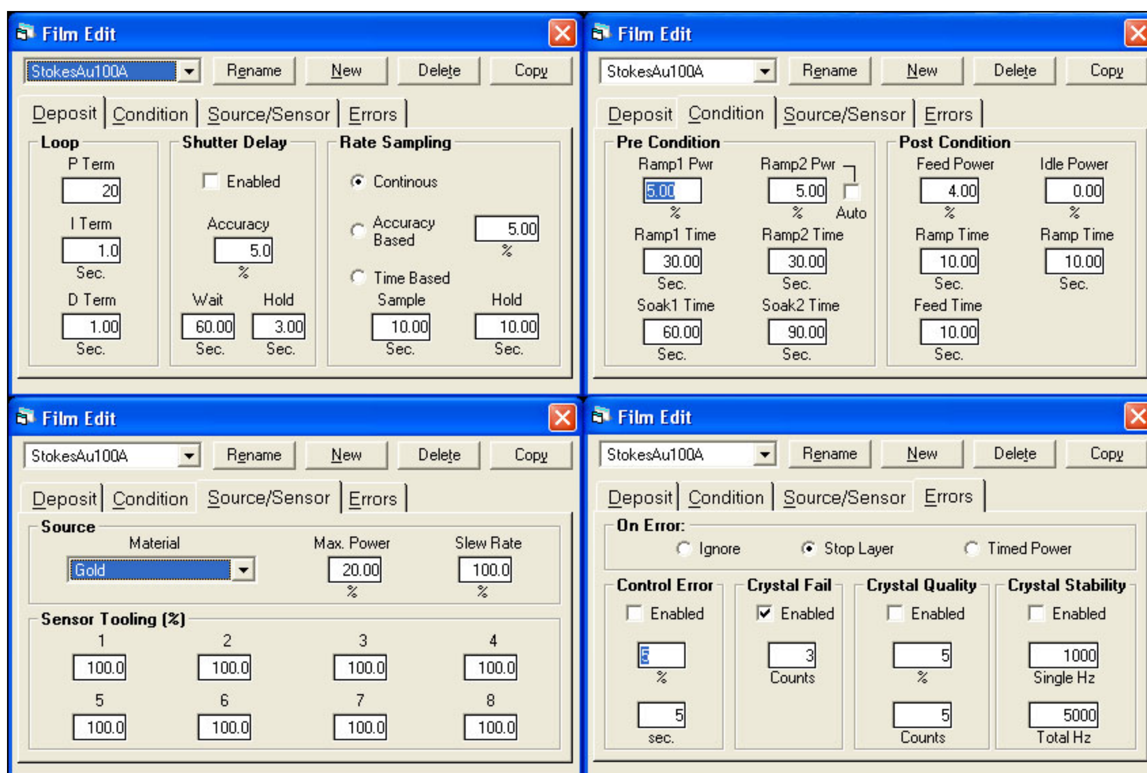

Figure 80: Screen shot showing the details of the film recipe (StokesAu100A) called by the process named “Stokes_Au_100A”. (a) PID controller settings, (b) e-beam power pre-deposition, and post-deposition settings, (c) metal source, and max e-beam power allocated, and (d) error controls.

6) Ni-Au Lift-off patterning:

   a. Clean glassware and metal tweezers:

      i. Sonication with Naugra sonicator (power level 9), in Acetone for 2 minutes at a temperature of 35 °C.

      ii. Sonication with Naugra sonicator (power level 9), in Methanol for 2 minutes at a temperature of 35 °C.

      iii. Rinse under DI-$H_2$0 (18 M water stream, and then rinse in cascading DI-$H_2$0 for 5 minutes, and dry samples with N_2.

   b. Sonicate samples:

i. Sonication with Naugra sonicator (power level 3), face up in Acetone for 2 minutes at a temperature of 35 °C.

ii. Rinse under DI-H_20 stream (18 MΩ) then rinse in cascading DI-H_20 (18 MΩ) for 2 minutes, and dry samples with N_2.

7) Ni-Au Anneal:

a. Anneal in (80% N_2 + 20% O_2) environment, at a temperature of 650 °C for 10 minutes by means of Surface Science Integration (SSI) Solaris 150 rapid thermal processing system:

i. The sequence of commands included in the recipe "GaN_650_N2O2" used in this work is shown in Figure 81.

Step#	Operation	Control Temp	Ramp Rate/Step Time	REM/Intensity	Control Device	Nitrogen	Ar/Oxygen	D Value	P Value	I Value	URLP	UFLP	LLP
1	Purge	0.0	90.0	0.0	Tracy TC	6.4	1.6	0.0	0.0	0.0	0.0	0.0	0.0
2	Ramp Up	650.0	25.0	40.0	Tracy TC	6.4	1.6	0.0	2.0	0.0	100.0	100.0	100.0
3	Hold	650.0	600.0	6.7	Tracy TC	6.4	1.6	0.0	60.0	20.0	100.0	100.0	100.0
4	Ramp Down	100.0	50.0	0.0	Tracy TC	6.4	1.6	0.0	0.0	0.0	0.0	0.0	0.0
5	Finish	100.0	10.0	0.0	Tracy TC	6.4	1.6	0.0	0.0	0.0	0.0	0.0	0.0

Figure 81: The sequence of commands included in the recipe used to anneal Ni-Au contacts to Mg-doped GaN, and $Al_xGa_{1-x}N$ (GaN_650_N2O2).

ii. Figure 82 shows a screen shot of the "Solaris RTP Process Page" with the details of the anneal process used in this work to obtain Ohmic contacts to Mg-doped GaN and $Al_xGa_{1-x}N$.

1. Recipe, and Calibration files.
2. Over-temperature Setpoint, Power Limit, and Power Limit Time.
3. Purge Mass Flow Controller (MFC) set point, Learn Mode, and Thermocouple (TC) selection.

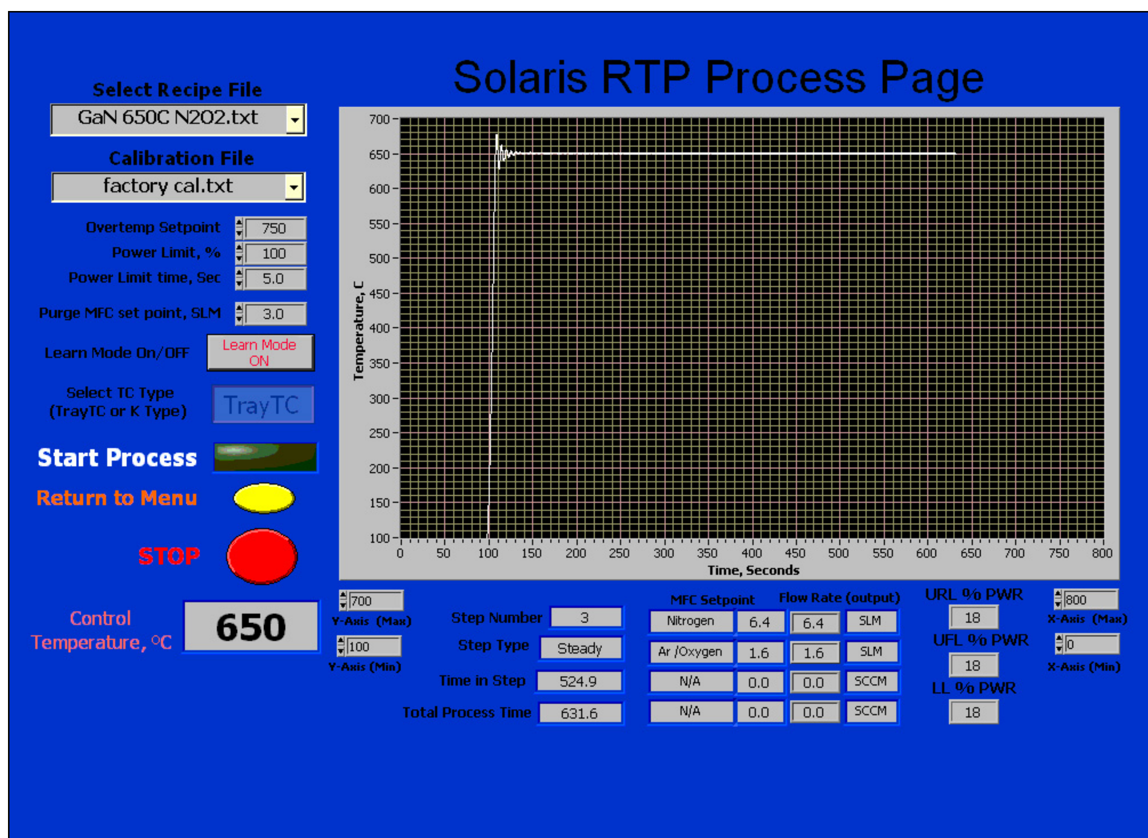

Figure 82: A screen shot of the “Solaris RTP Process Page” with the details of the anneal process used in this work to obtain Ohmic contacts to Mg-doped GaN and $Al_xGa_{1-x}N$.

iii. The temperature profile of the anneal process used in this work to obtain Ohmic contacts to Mg-doped GaN and $Al_xGa_{1-x}N$ is shown in Figure 83.

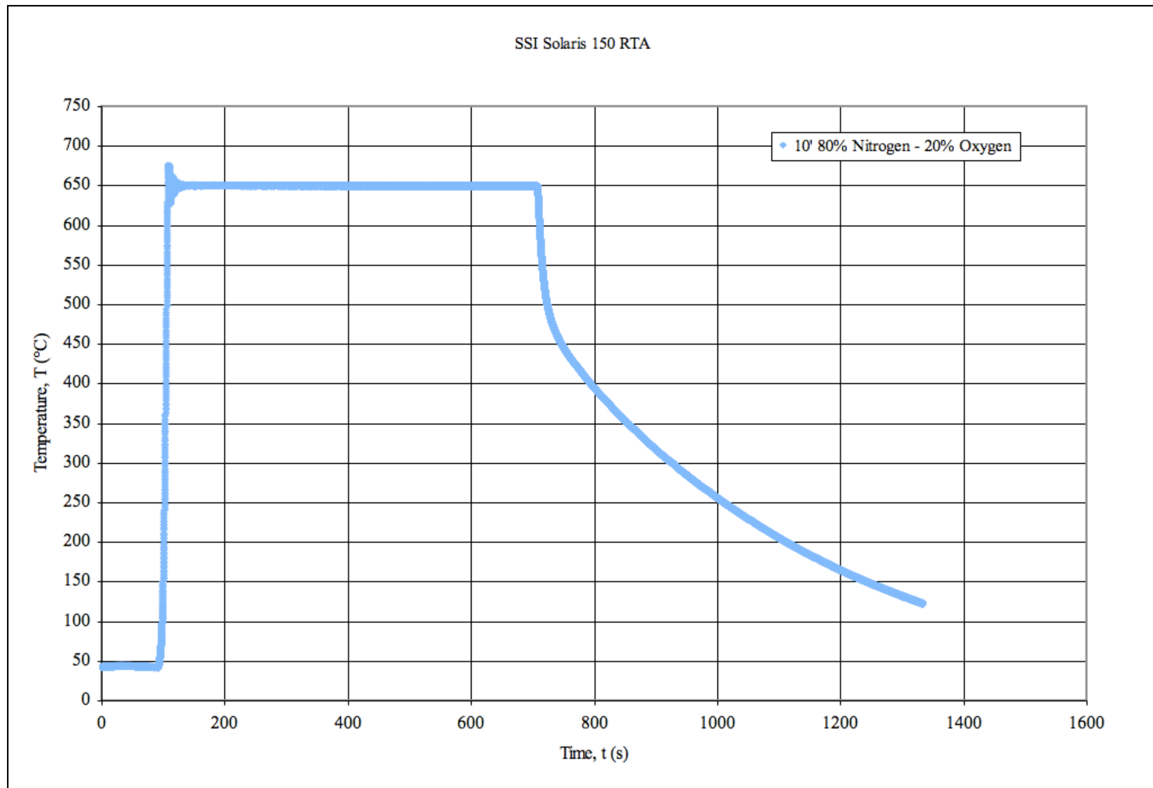

Figure 83: Temperature profile of the anneal process used in this work to obtain Ohmic contacts to Mg-doped GaN and $Al_xGa_{1-x}N$.

Figure 84 shows a set of micrographs of test structures, consisting of Ohmic Ni-Au contacts (MSM test structures) fabricated onto Mg-doped $Al_{0.37}Ga_{0.63}N$ (PARC), that were used in this work. Moreover, Figure 84 documents the three crucial steps of the fabrication process, and the effect of anneal on the contact morphology: 1) patterning by means of photolithography, 2) metallization, and 3) anneal.

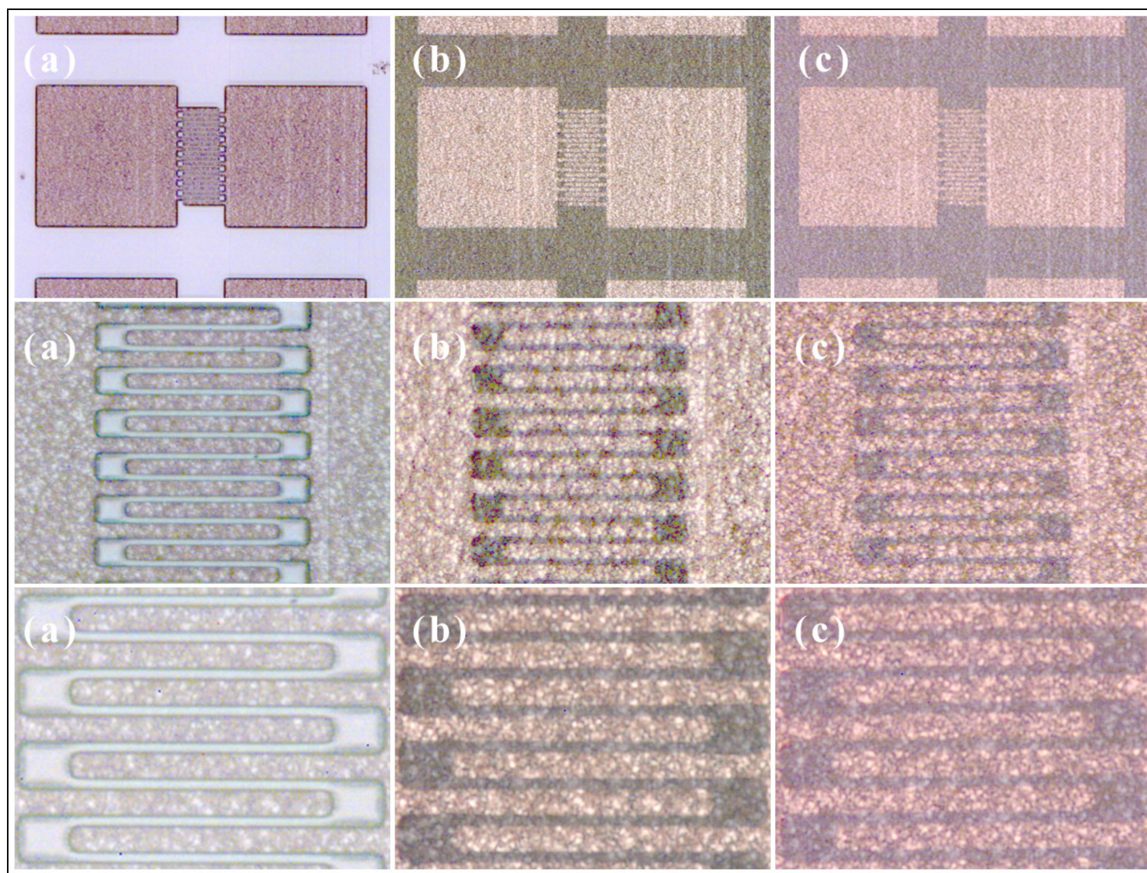

Figure 84: Ohmic Ni-Au MSM test structure fabricated on Mg-doped $Al_{0.37}Ga_{0.63}N$ (PARC): (a) patterning by means of photolithography, (b) Ni-Au metallization, and (c) Ni-Au MSM test structure annealed for 10 minutes at 650 °C in a (80% N_2 / 20% O_2) environment.

Figure 85 shows a graph of the I-V characteristic curves determined by probing Ni-Au CTLM control structures, with a gap spacing varying from 5 μm to 45 μm, fabricated in parallel with the Ni-Au MSM test structures shown in Figure 84. Such I-V characteristic curves were determined both before and after the anneal process.

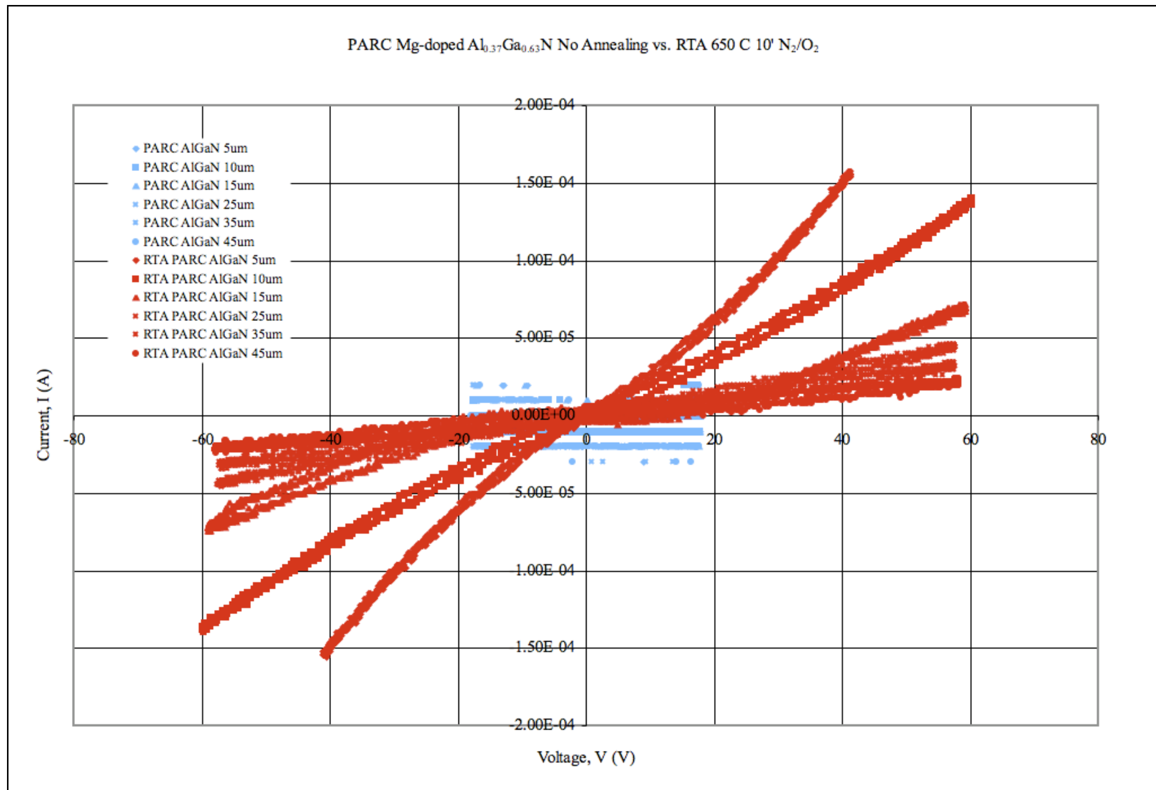

Figure 85: I-V characteristic curves determined by probing Ni-Au CTLM control structures having a gap spacing varying from 5 µm to 45 µm, fabricated on Mg-doped $Al_{0.37}Ga_{0.63}N$ before and after the anneal process. These Ni-Au CTLM control structures were fabricated in parallel with the Ni-Au MSM test structures shown in Figure 84.

Figure 86 shows a set of micrographs of test structures, consisting of Ohmic Ni-Au contacts (MSM test structures) fabricated onto Mg-doped GaN (TDI), that were used in this work. Moreover, Figure 86 documents the three crucial steps of the fabrication process, and the effect of anneal on the contact morphology: 1) patterning by means of photolithography, 2) metallization, and 3) anneal.

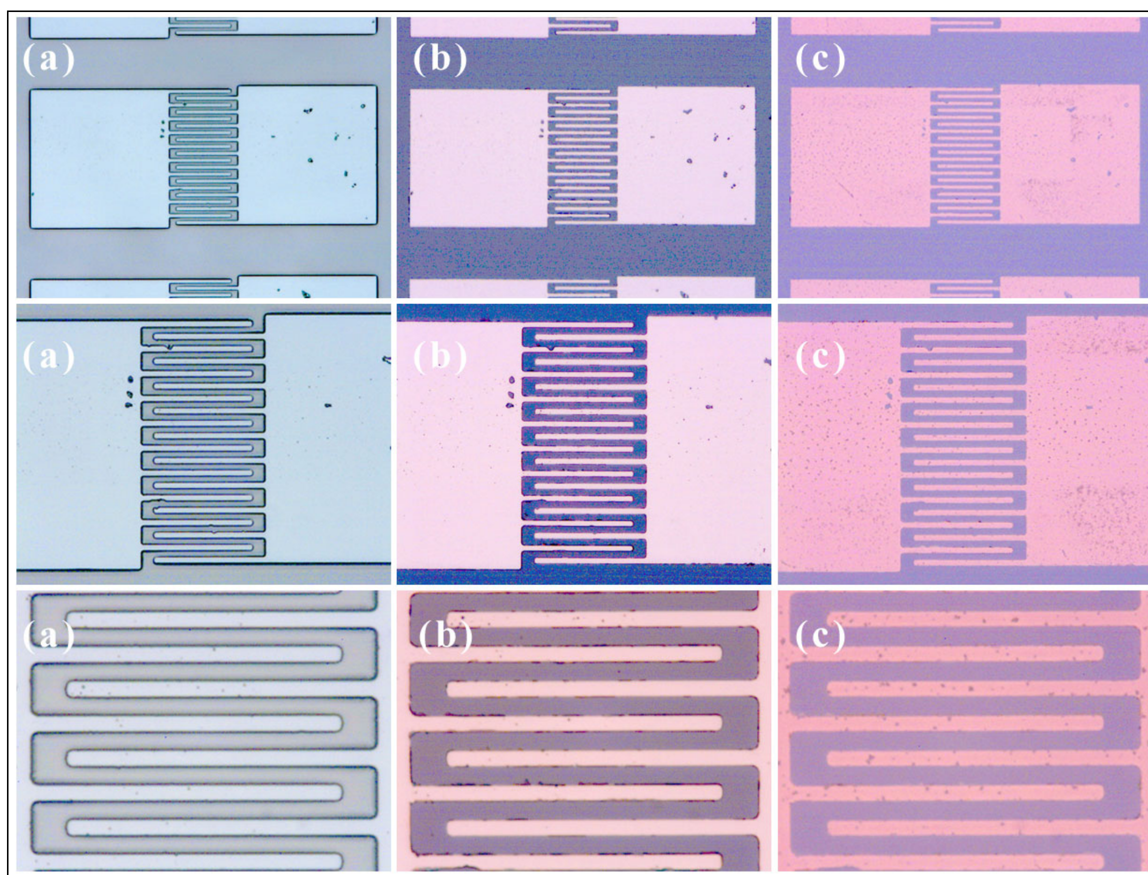

Figure 86: Ohmic Ni-Au MSM test structure fabricated on Mg-doped GaN (TDI): (a) patterning by means of photolithography, (b) Ni-Au metallization, and (c) Ni-Au MSM test structure annealed for 10 minutes at 650 °C in a (80% N_2 / 20% O_2) environment.

Figure 87 shows a graph of the I-V characteristic curves determined by probing Ni-Au CTLM control structures, with a gap spacing varying from 5 μm to 45 μm, fabricated in parallel with the Ni-Au MSM test structures shown in Figure 86. Such I-V characteristic curves were determined both before and after the anneal process.

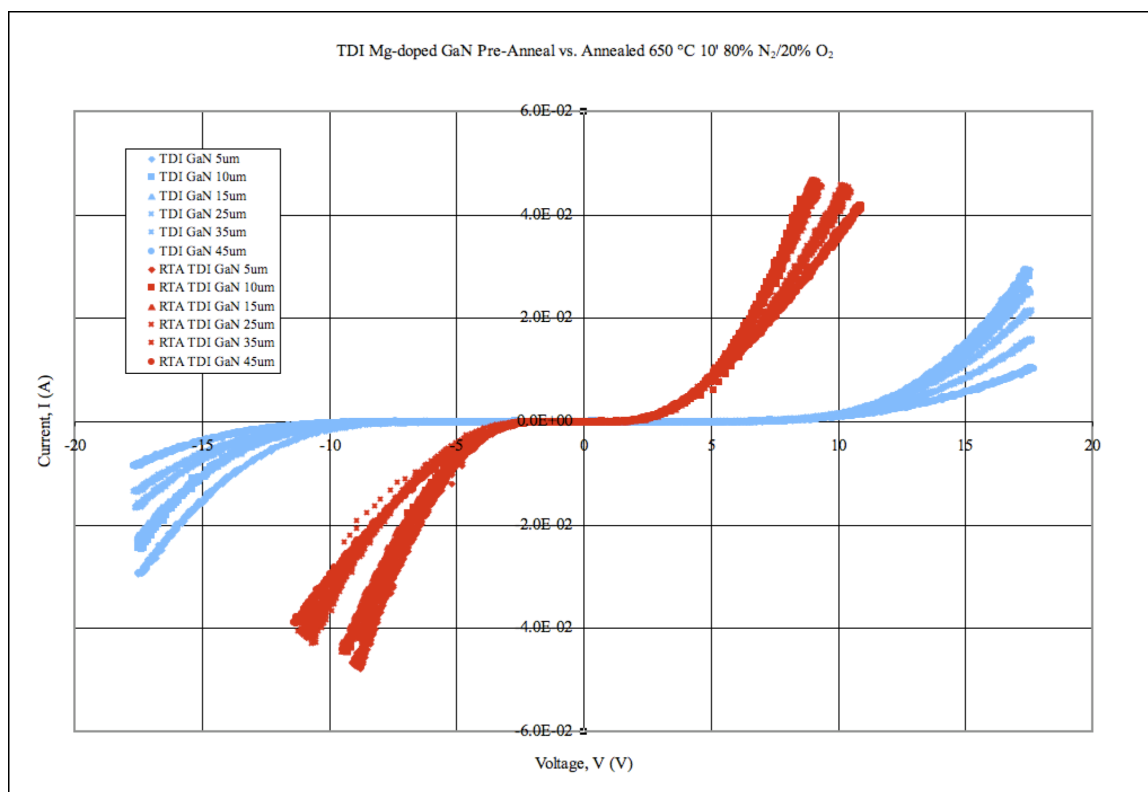

Figure 87: I-V characteristic curves determined by probing Ni-Au CTLM control structures having a gap spacing varying from 5 µm to 45 µm, fabricated on Mg-doped GaN (TDI), before and after the anneal process. These Ni-Au CTLM control structures were fabricated in parallel with the Ni-Au MSM test structures shown in Figure 86.

8) Packaging:

Upon the successful fabrication of Ohmic contacts to Mg-doped GaN and $Al_xGa_{1-x}N$, samples were secured onto TO5 headers, and wire bonded as shown in Figure 88. The T05 header was chosen because it could be easily accommodated within the cavity of a heat sink, and also because it allowed a safe, and rapid exchange of the various test structures during the experiment. In addition, the T05 header and the heat sink were mounted on a micro positioner, and this configuration allowed the maximization of the signal with respect to the relative position of the test structure and the OPO/OPA beam (Figure 89).

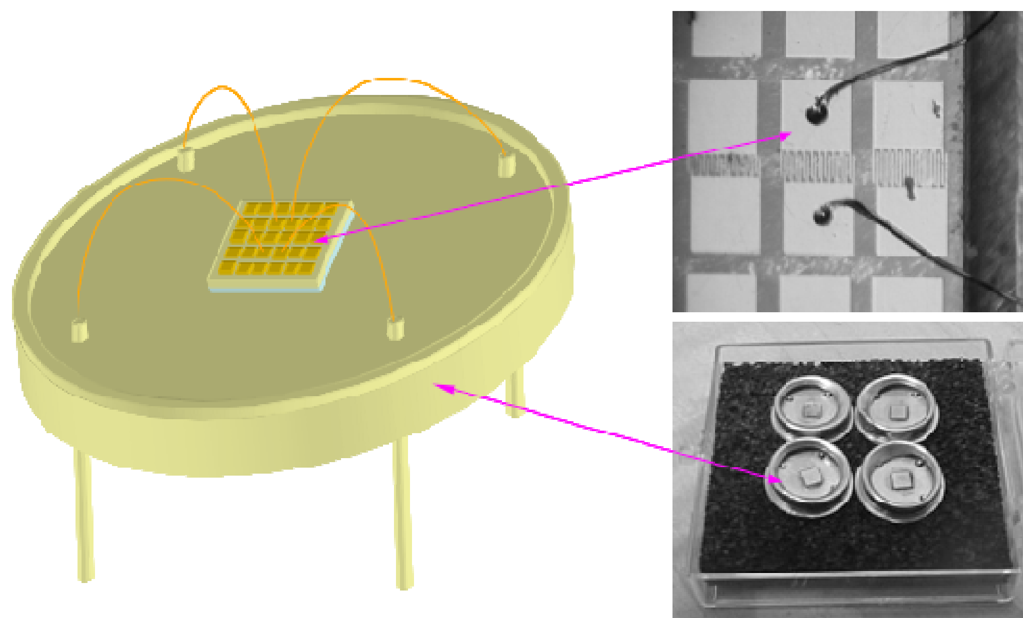

Figure 88: Diagram schematics showing a packaged test structure used in this work.

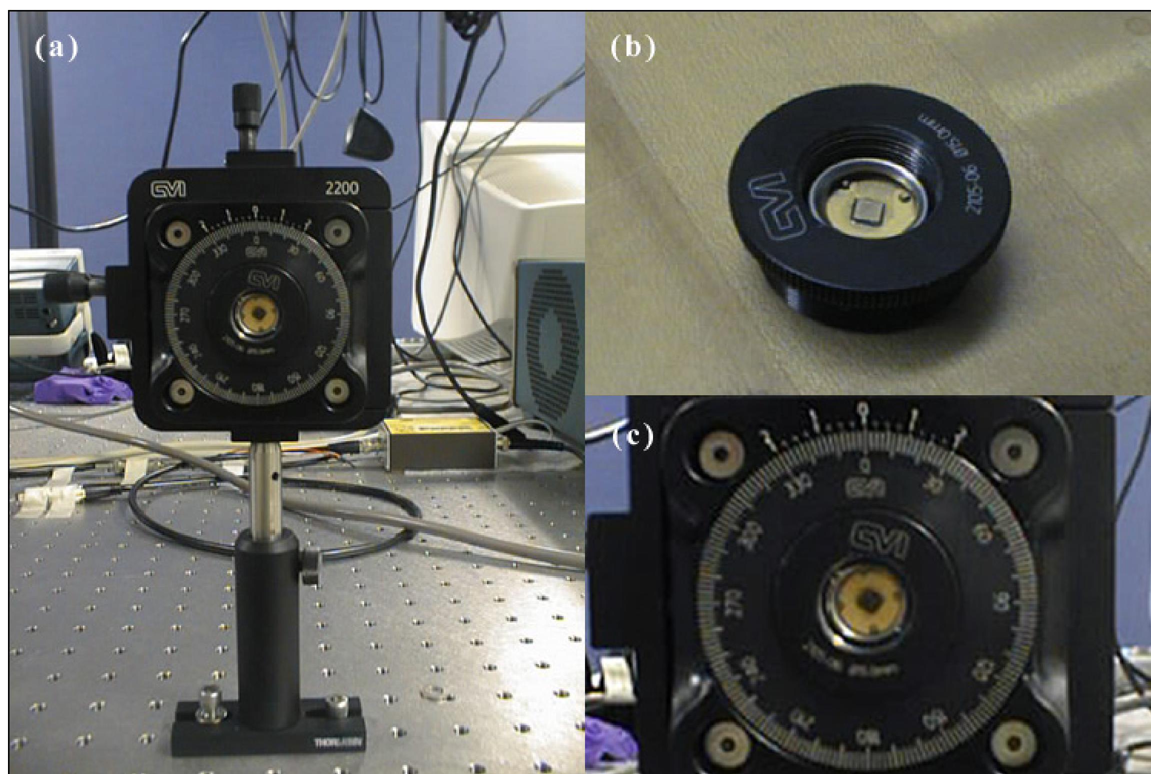

Figure 89: (a) Packaged test structure accommodated in the cavity of a micro positioning optical mount, (b) (c) and details of the cavity.

5.4. Test Bed Setup

The investigation of the Mg-doped GaN and $Al_xGa_{1-x}N$ test structures was carried out with the unique testing system illustrated by the schematics shown in Figure 90.

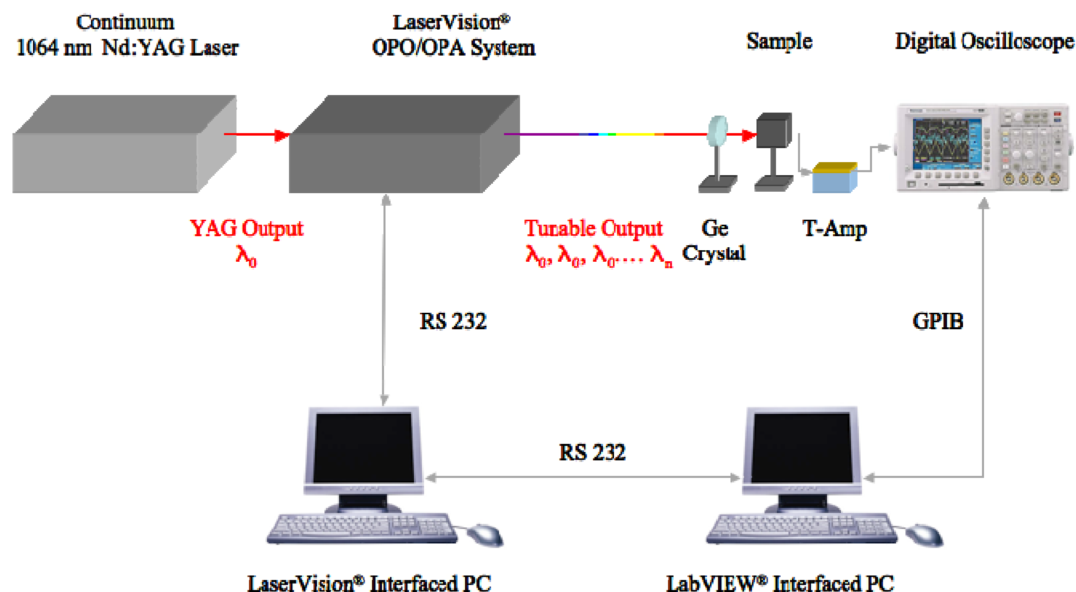

Figure 90: Schematic diagram of the testing system used to investigate the Mg-doped GaN $Al_xGa_{1-x}N$ test structures.

A Q-switched Nd:YAG laser (Powerlite® 8000, Continuum, Santa Clara, CA) operating at 1064 nm, and generating 3 ns pulses was used to pump an Optical Parametric Oscillator/Optical Parametric Amplifier (OPO/OPA) system (LaserVision, Bellevue, WA) as shown in Figure 91. The pulse energy output of the Nd:YAG laser, was maintained at a constant value of 500 mJ. The OPO/OPA, controlled by LaserVision software, converted the fundamental wavelength of the Nd:YAG laser into a continuously tunable infrared wavelength by means of non-linear parametric processes. And in our experiments, the output wavelength of the OPO/OPA was systematically tuned with constant wavelength increments in the Near Infrared range 710 nm to 890 nm (1.75 eV to

1.40 eV), Intermediate Infrared range 1300 nm to 2120 nm (950 meV to 585 meV), and Mid Infrared range 2150 nm to 5000 nm (577 meV to 248 meV). A wafer of electronic grade crystalline Ge crystal (1" in diameter) was used to block any accidental output of visible radiation coming from Q-switched Nd:YAG, when the OPO/OPA was systematically tuned in the Near Infrared range.

Figure 91: (a) Q-switched Nd:YAG laser (Powerlite® 8000, Continuum) used to pump an (b) Optical Parametric Oscillator/Optical Parametric Amplifier (OPO/OPA) system (LaserVision, Bellevue, WA), whose details are shown in (c) and (d).

Transient photocurrent was collected and converted to a transient voltage signal by a 10 kHz – 5 MHz transimpedence amplifier (Puppy PreAmp®, Electrosolutions, Flemington, NJ). During each single test, the power irradiating the test structures was determined with an infrared pulse energy meter (Orion PE25Sh Pyroelectric Detector, Ophir Optronics,

MA) and the relative data were collected with the aid of the digital oscilloscope above mentioned. An instrument control computer program (LabVIEW®, National Instruments, Austin, TX) was specifically written to interface with both the LaserVision software and the digital oscilloscope (Model 3054B, Tektronix, Beaverton, OR) , and also to download the data from the oscilloscope to a personal computer. RS232, and GPIB connections were used to interface the digital oscilloscope and a personal computer.

When conducting temperature dependant Infrared photocurrent spectroscopy, packaged samples were accommodated within the cavity of a cryogenic cold finger (Cryogenic Control Systems, Rancho Santa Fe, CA) controlled by a temperature controller (Cryo-con 32, Cryogenic Control Systems, Rancho Santa Fe, CA), as shown in Figure 92. Typical temperature dependant Infrared photocurrent spectroscopy was conducted in the temperature range 77 °K to 300 °K.

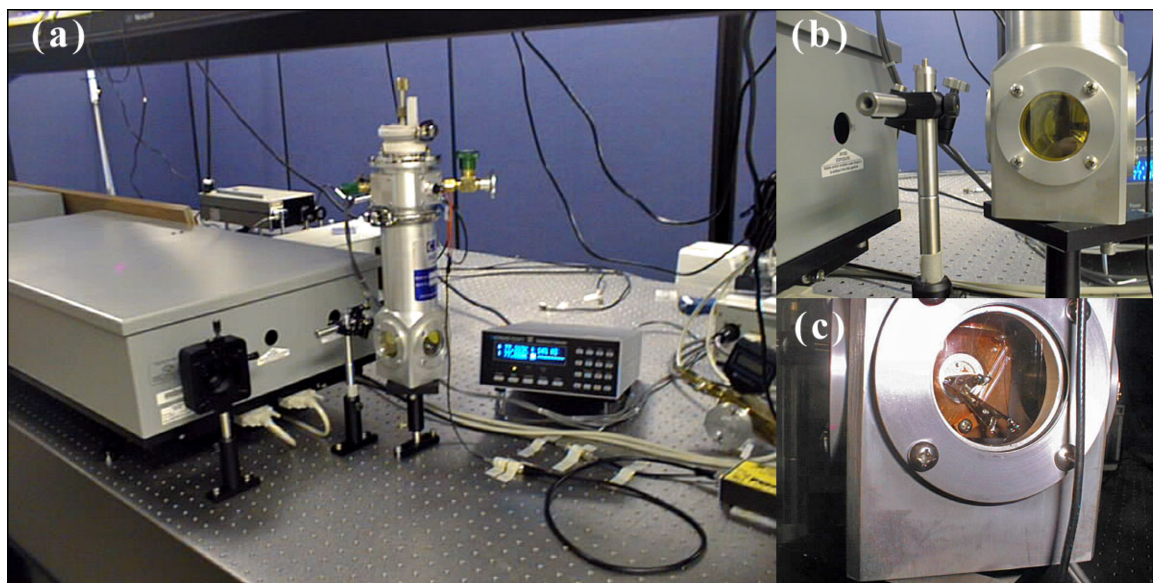

Figure 92: (a) Cryogenic cold finger and relative temperature controller used to conduct temperature dependant Infrared photocurrent spectroscopy in this work. Details of the cold finger cavity are shown in (b) and (c).

For the investigation of the effects on forward current and light output from commercial ultraviolet III-nitride LEDs, under IR stimulation provided by the YAG pumped OPO/OPA system, the test bed set shown in Figure 90 was modified as shown in Figure 93.

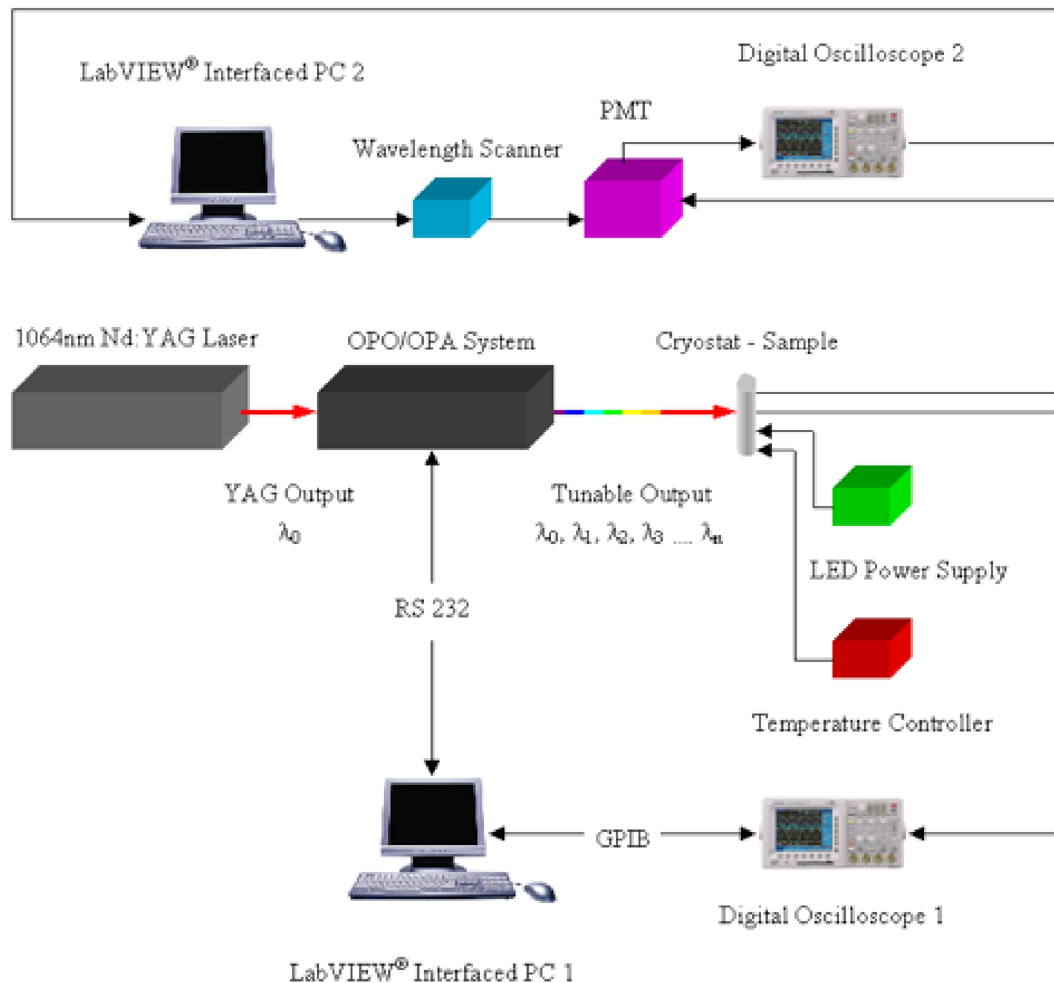

Figure 93: Schematic diagram of the testing system used to investigate from commercial ultraviolet III-nitride LEDs, under IR stimulation provided by the YAG pumped OPO/OPA system.

Commercial UV LED dice (365 nm – Nitride Semiconductors Co., LTD Japan) were secured onto T018 headers, and wire bonded as shown in Figure 94.

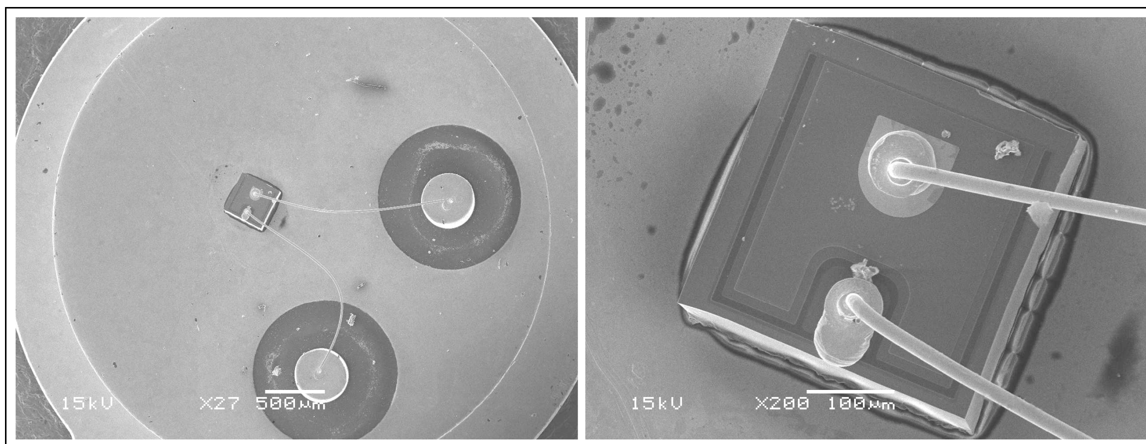

Figure 94: Details of the UV LED packaging**.**

Packaged UV LEDs were positively biased with a constant positive voltage, and systematically excited with IR radiation in the Mid IR range (2150 nm to 5000 nm). During each single test, the power irradiating the test structures was determined with an infrared pulse energy meter (Orion PE25Sh Pyroelectric Detector, Ophir Optronics, MA) and the relative data was collected with the aid of a digital oscilloscope (Model TDS 524A, Tektronix, Beaverton, OR). An instrument control computer program (LabVIEW®, National Instruments, Austin, TX) was specifically written to interface with the LaserVision software, the photo multiplier tube (Model SpectraPro 275, Acton Research Corporation, Princeton Instruments, Trenton, NJ), and the stepping motor wavelength scan controller (Model SpectraDrive, Acton Research Corporation, Princeton Instruments, Trenton, NJ) to a personal computer. RS232, and GPIB connections were used to interface the digital oscilloscope and a personal computer.

When conducting temperature dependant Infrared photocurrent spectroscopy, packaged samples were accommodated within the cavity of a cryogenic cold finger (Cryogenic Control Systems, Rancho Santa Fe, CA) controlled by a temperature

controller (Cryo-con 32, Cryogenic Control Systems, Rancho Santa Fe, CA), as shown in Figure 92.

5.5. Origin of Mg-doped GaN, and Mg-doped $Al_xGa_{1-x}N$ samples

A set of III-nitride films were grown by Honeywell via MOCVD (Honeywell Labs, Minneapolis, MN), on an AlN buffer layer (0.05 µm thick), on c-plane sapphire; three kinds of films were provided: Mg-doped GaN (3.5 µm thick), Mg-doped $Al_{020}Ga_{0.80}N$ (3.6 µm thick), and Mg-doped $Al_{0.52}Ga_{0.48}N$ (0.71 µm thick). Film thickness was determined by a Perkin Elmer Lambda 19 spectrophotometer. Annealing of the III-nitride films was conducted at 900 °C for two minutes. Sheet resistance, mobility and carrier concentration were determined with a Leihighton non-contact resistivity system, and an in-house built Hall system respectively. Mg-doped $Al_{0.20}Ga_{0.80}N$ and Mg-doped $Al_{0.51}Ga_{0.48}N$ films resulted to be highly resistive, while Mg-doped GaN was determined to have R_s=10.9 KOhm/cm^2, mobility = 11 cm^2/V-s, and a carrier concentration of 1.60x10^{17} cm-3. Lesker PVD 75.

Highly resistive samples of Mg-doped $Al_{0.42}Ga_{0.58}N$ (200 nm thick) grown by MOCVD on freestanding c-plane AlN substrate (epitaxy run CIS 0314 of 06/24/08), Mg-doped $Al_{0.15}Ga_{0.85}N$ grown on AlN buffer/c-plane sapphire substrate, and Mg-doped $Al_{0.35}Ga_{0.65}N$ (980 nm thick) MOCVD grown (PARC B3566) on commercial AlGaN template (TDI HVPE-grown 2 µn u-GaN on c-plane sapphire) were made available by Crystal IS (Crystal IS, Green Island, NY), Epitex (EpiTEX Advanced Materials and Devices, University of Texas at Austin), and PARC (Xerox Palo Alto Research Center, Palo Alto, CA), respectively. Additional samples of Mg-doped GaN grown on c-plane

sapphire were provided by ATMI (ATMI, Danbury, CT) and TDI (Technologies and Devices International, Inc., Silver Spring, MD).

5.5.1. IV Characterization of Mg-doped GaN, and Mg-doped $Al_xGa_{1-x}N$ test structures

IV characterization of Mg-doped GaN, and Mg-doped $Al_xGa_{1-x}N$ test structures is listed in Table 8.

Table 8: IV Characterization of Mg-doped GaN, and Mg-doped $Al_xGa_{1-x}N$ test structures.

Figure	Test Structure
Figure 95	Honeywell Mg-doped $Al_{0.52}Ga_{0.48}N$ [4a]
Figure 96	Honeywell Mg-doped $Al_{0.52}Ga_{0.48}N$ [1]
Figure 97	Honeywell Mg-doped $Al_{0.52}Ga_{0.48}N$ [3]
Figure 98	Honeywell Mg-doped $Al_{0.52}Ga_{0.48}N$ [6]
Figure 99	Crystal IS Mg-doped $Al_{0.42}Ga_{0.58}N$ [1]
Figure 100	Crystal IS Mg-doped $Al_{0.42}Ga_{0.58}N$ [2]
Figure 101	Honeywell Mg-doped $Al_{0.20}Ga_{0.80}N$ [3]
Figure 102	Honeywell Mg-doped $Al_{0.20}Ga_{0.80}N$ [4]
Figure 103	Epitex Mg-doped $Al_{0.15}Ga_{0.85}N$ [2]
Figure 104	Epitex Mg-doped $Al_{0.15}Ga_{0.85}N$ [3]
Figure 105	Honeywell Mg-doped GaN [1]
Figure 106	Honeywell Mg-doped GaN [6]
Figure 107	ATMI Mg-doped GaN [1]
Figure 108	ATMI Mg-doped GaN [7]
Figure 109	TDI Mg-doped GaN [1]
Figure 110	TDI Mg-doped GaN [2]

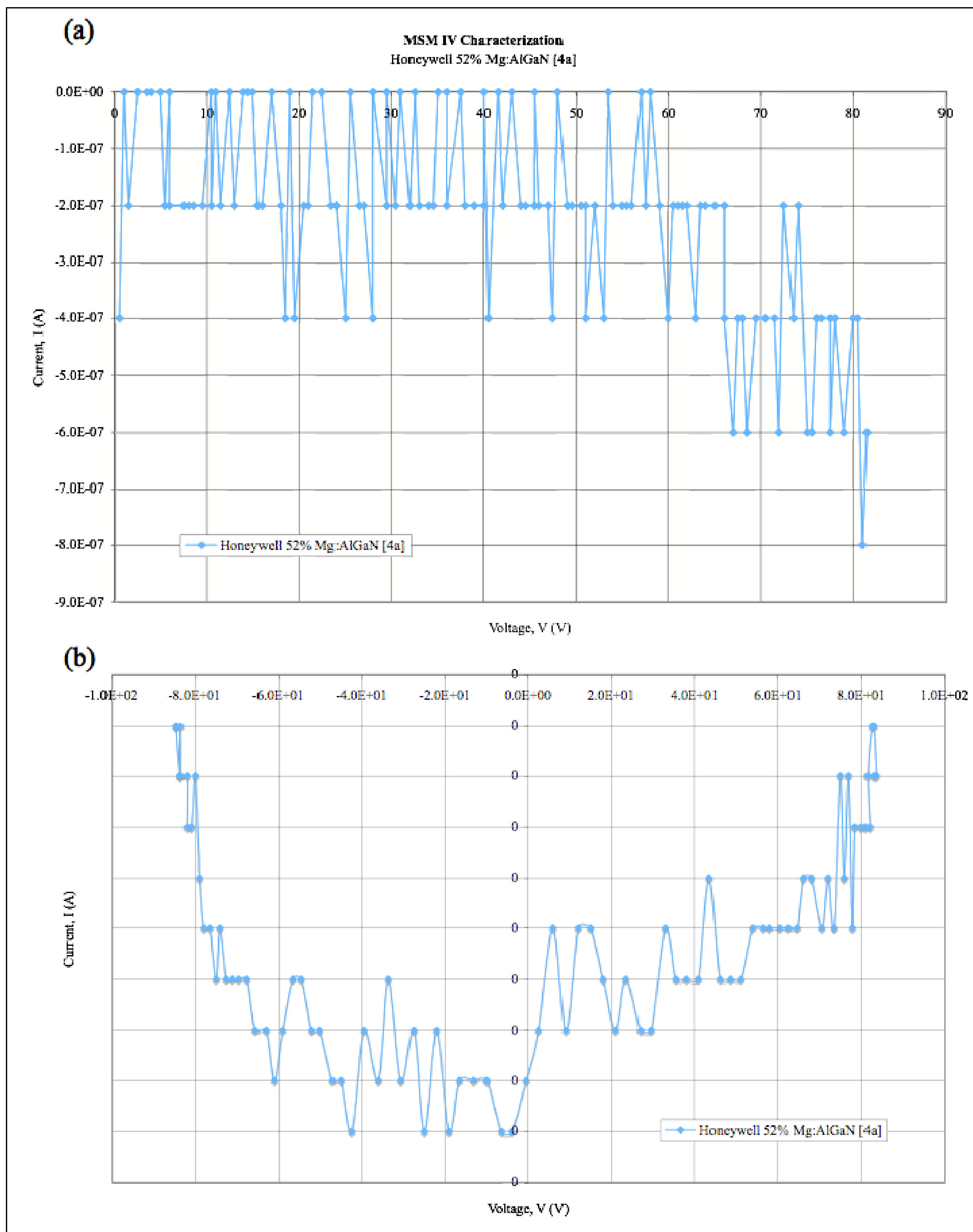

Figure 95: IV Characterization of test structure [4a] fabricated on Honeywell Mg-doped $Al_{0.52}Ga_{0.48}N$.

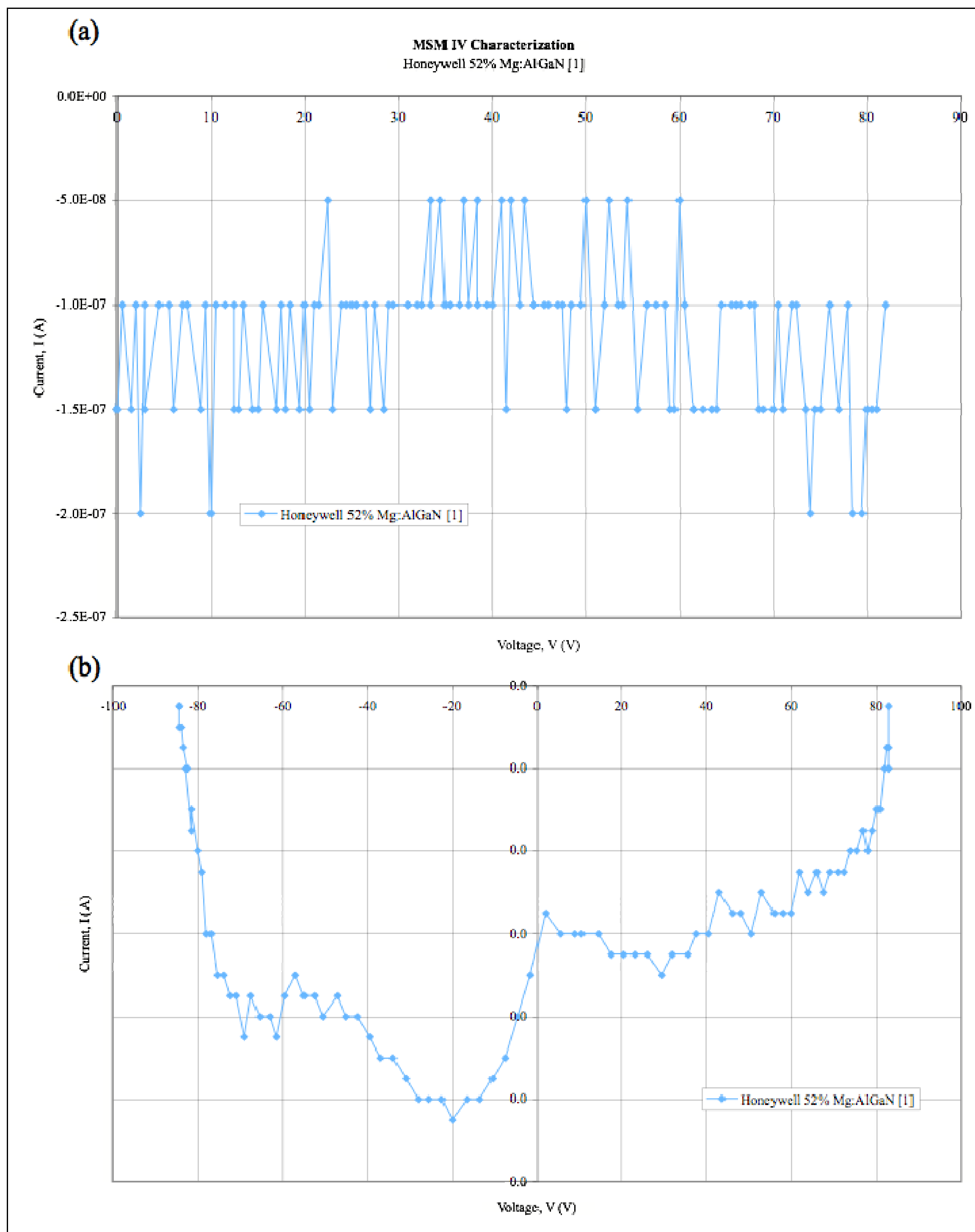

Figure 96: IV Characterization of test structure [1] fabricated on Honeywell Mg-doped $Al_{0.52}Ga_{0.48}N$.

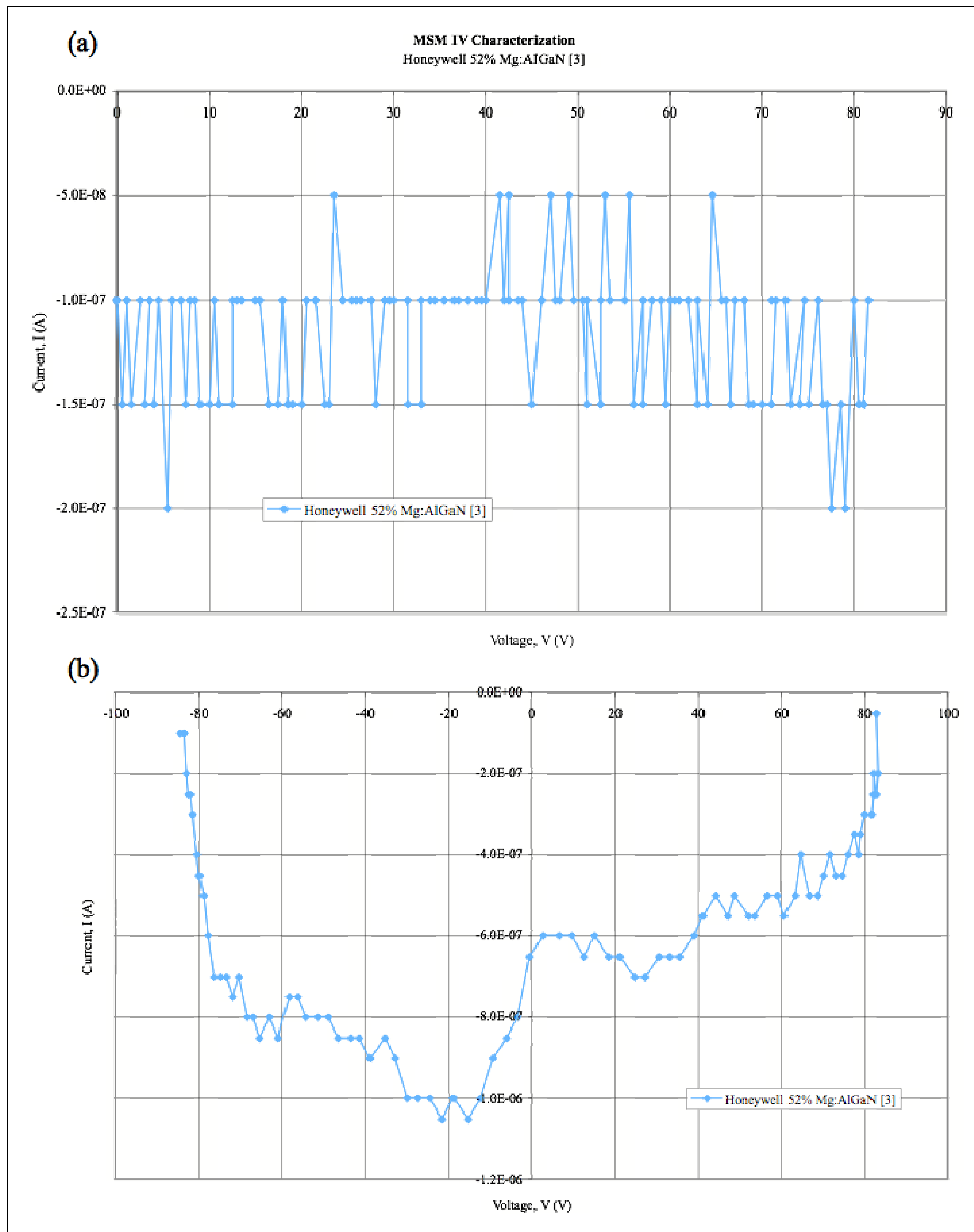

Figure 97: IV Characterization of test structure [3] fabricated on Honeywell Mg-doped $Al_{0.52}Ga_{0.48}N$.

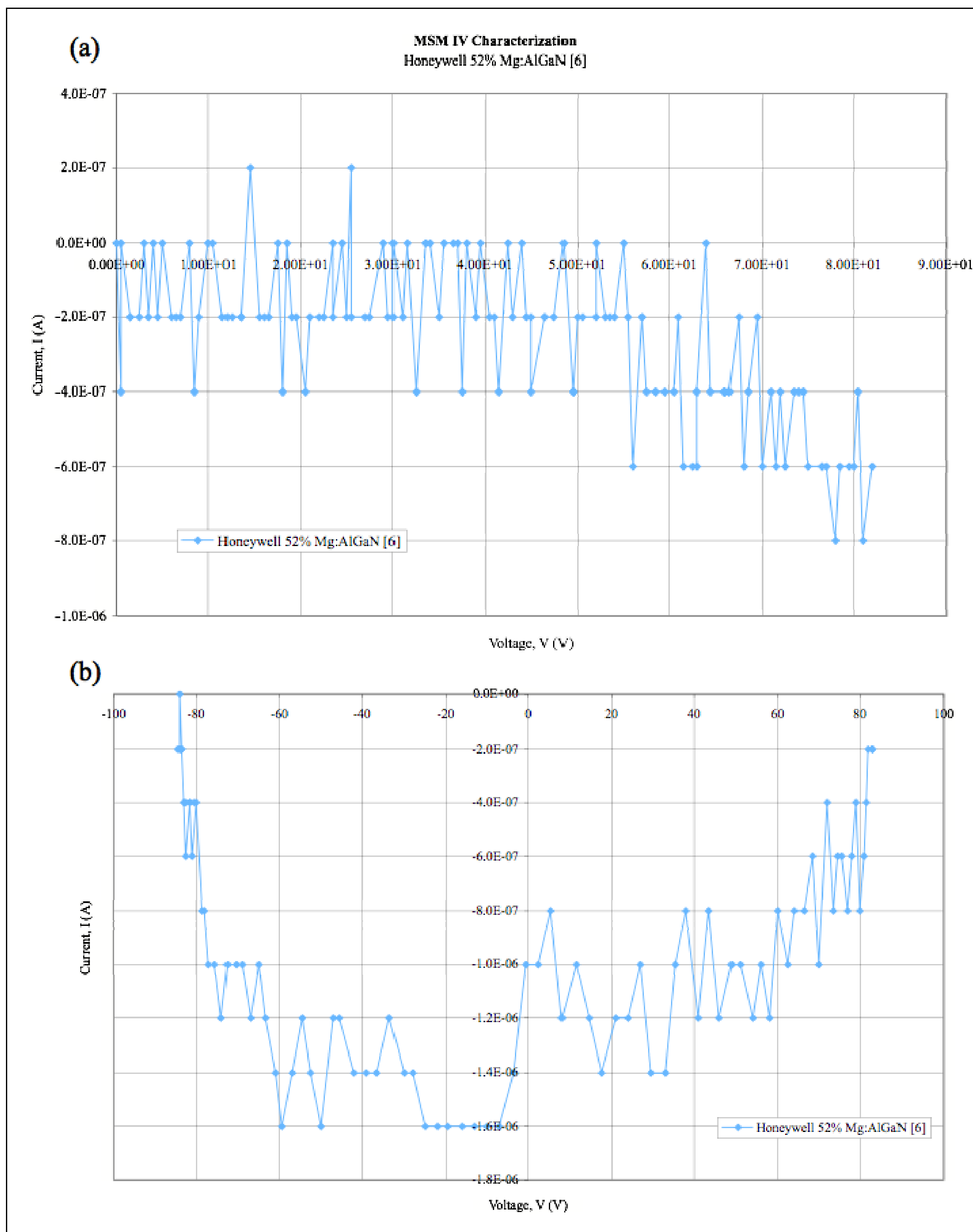

Figure 98: IV Characterization of test structure [6] fabricated on Honeywell Mg-doped $Al_{0.52}Ga_{0.48}N$.

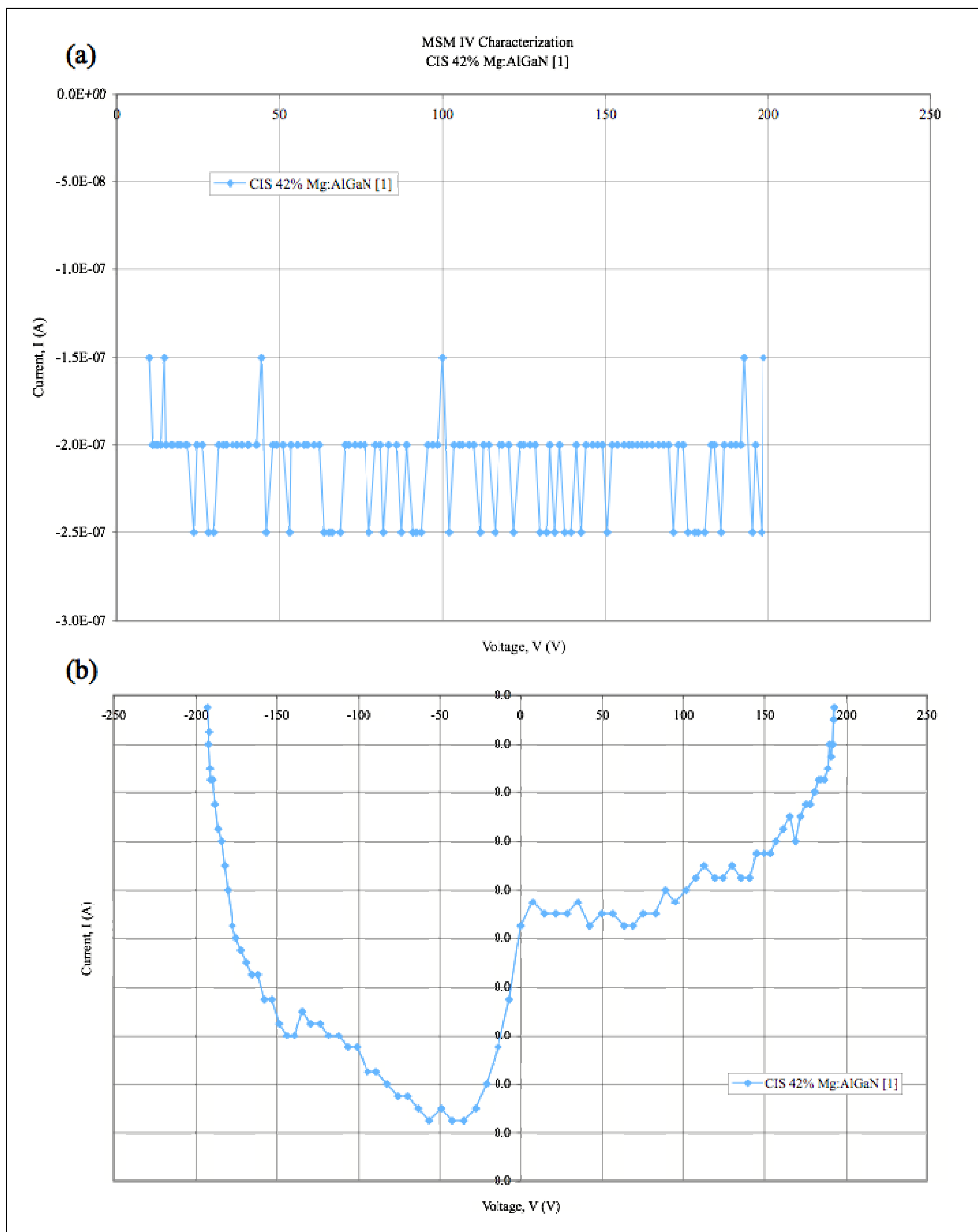

Figure 99: IV Characterization of test structure [1] fabricated on Crystal IS D151X Mg-doped $Al_{0.42}Ga_{0.58}N$.

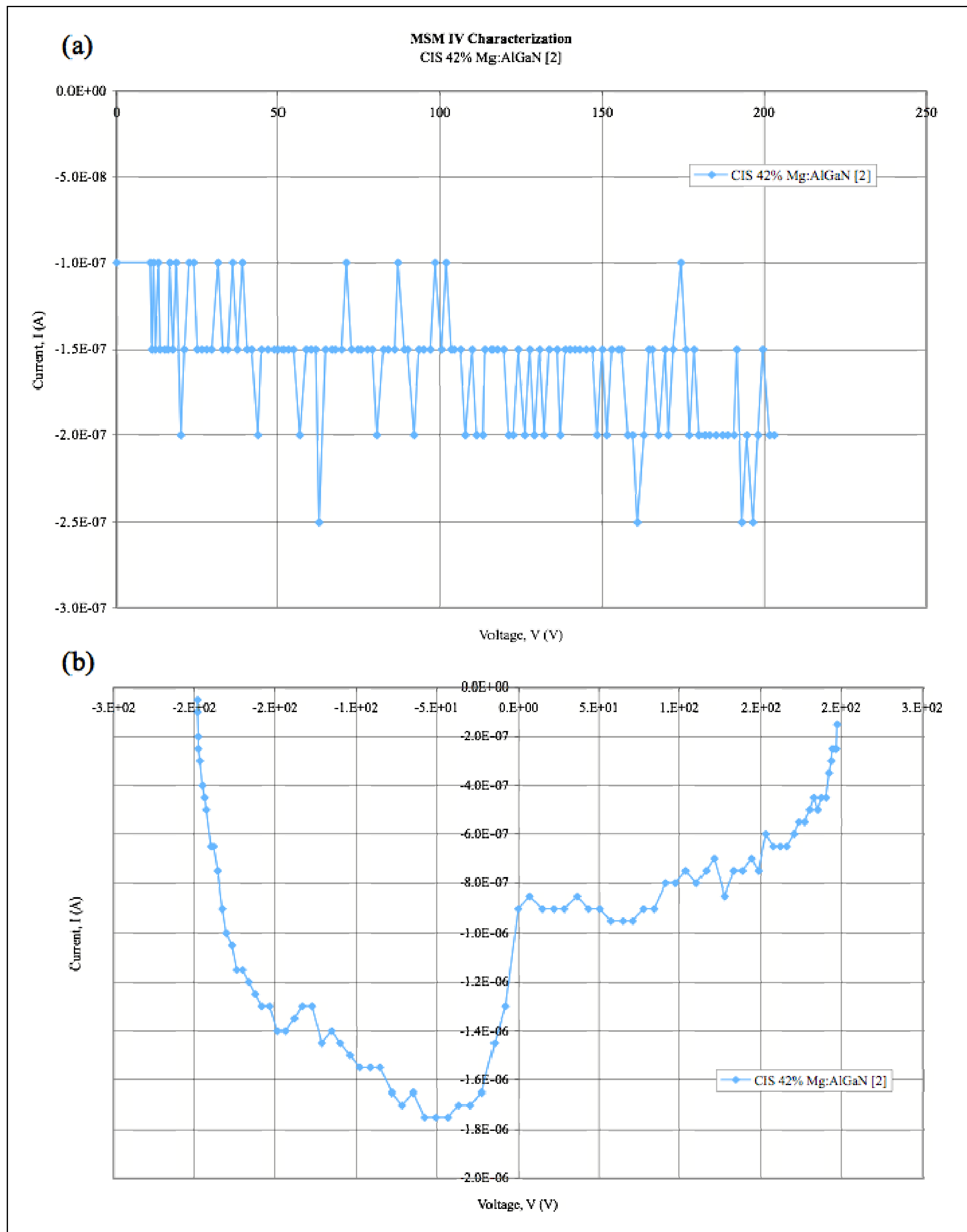

Figure 100: IV Characterization of test structure [2] fabricated on Crystal IS D151X Mg-doped $Al_{0.42}Ga_{0.58}N$.

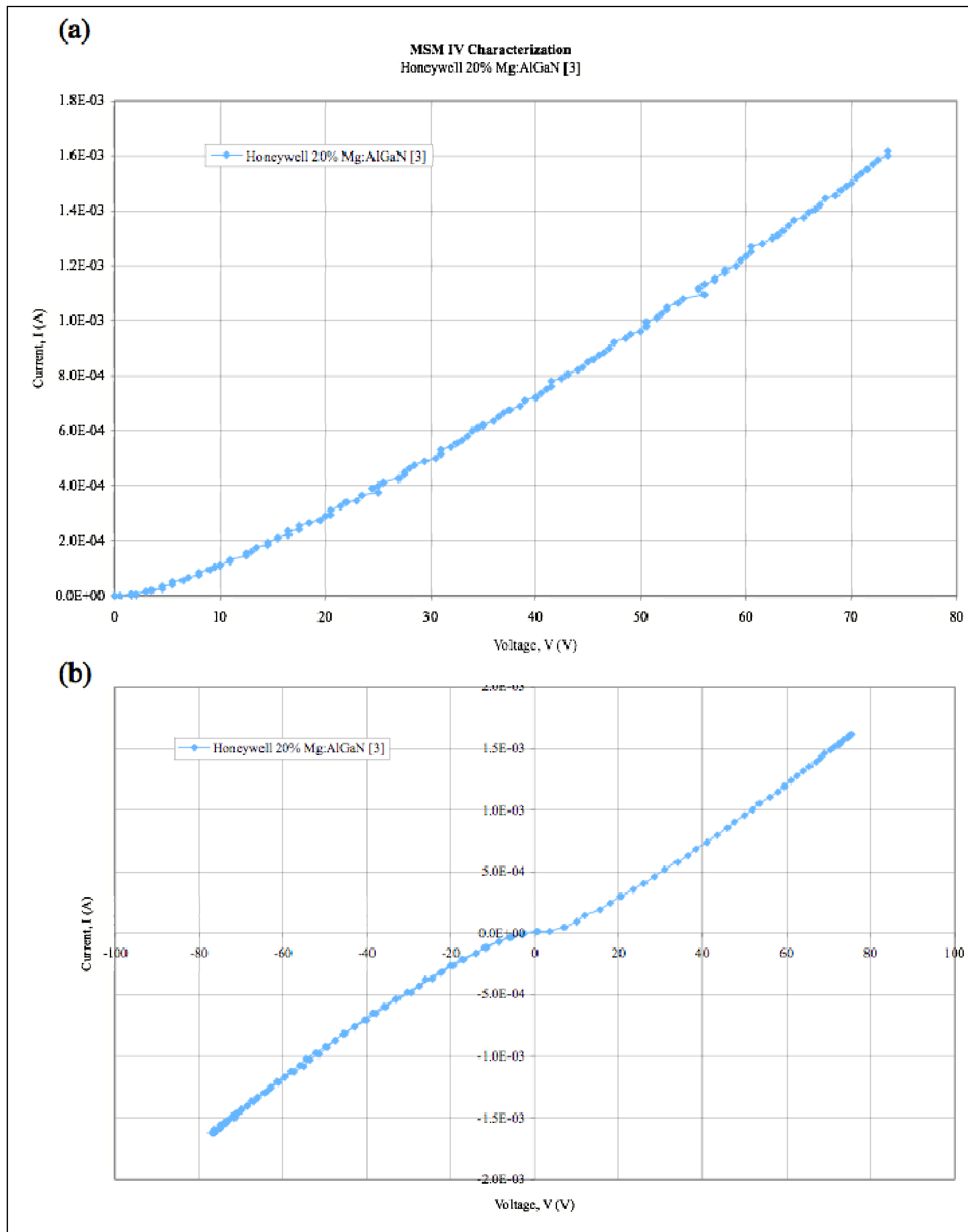

Figure 101: IV Characterization of test structure [3] fabricated on Honeywell Mg-doped $Al_{0.20}Ga_{0.80}N$.

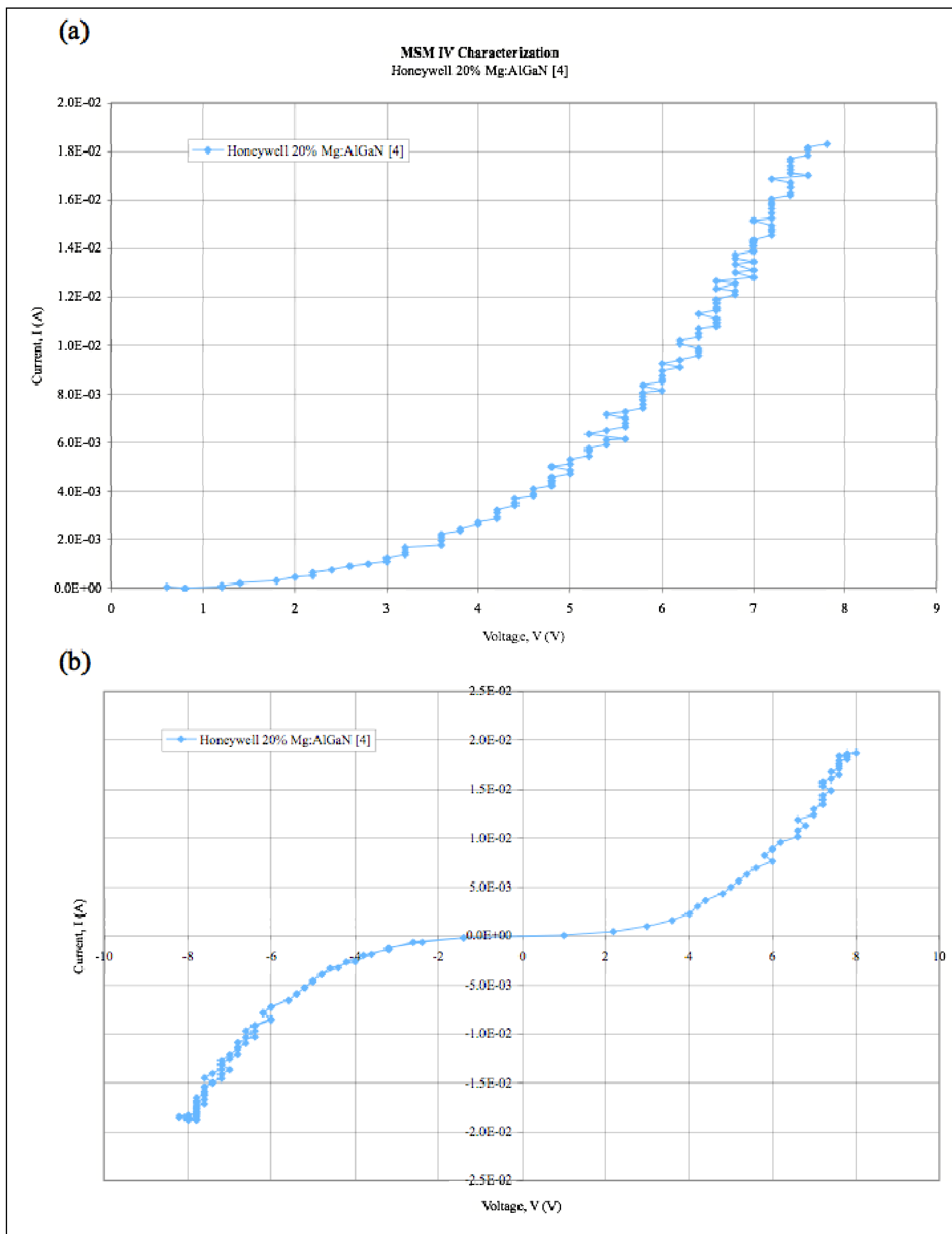

Figure 102: IV Characterization of test structure [4] fabricated on Honeywell Mg-doped $Al_{0.20}Ga_{0.80}N$.

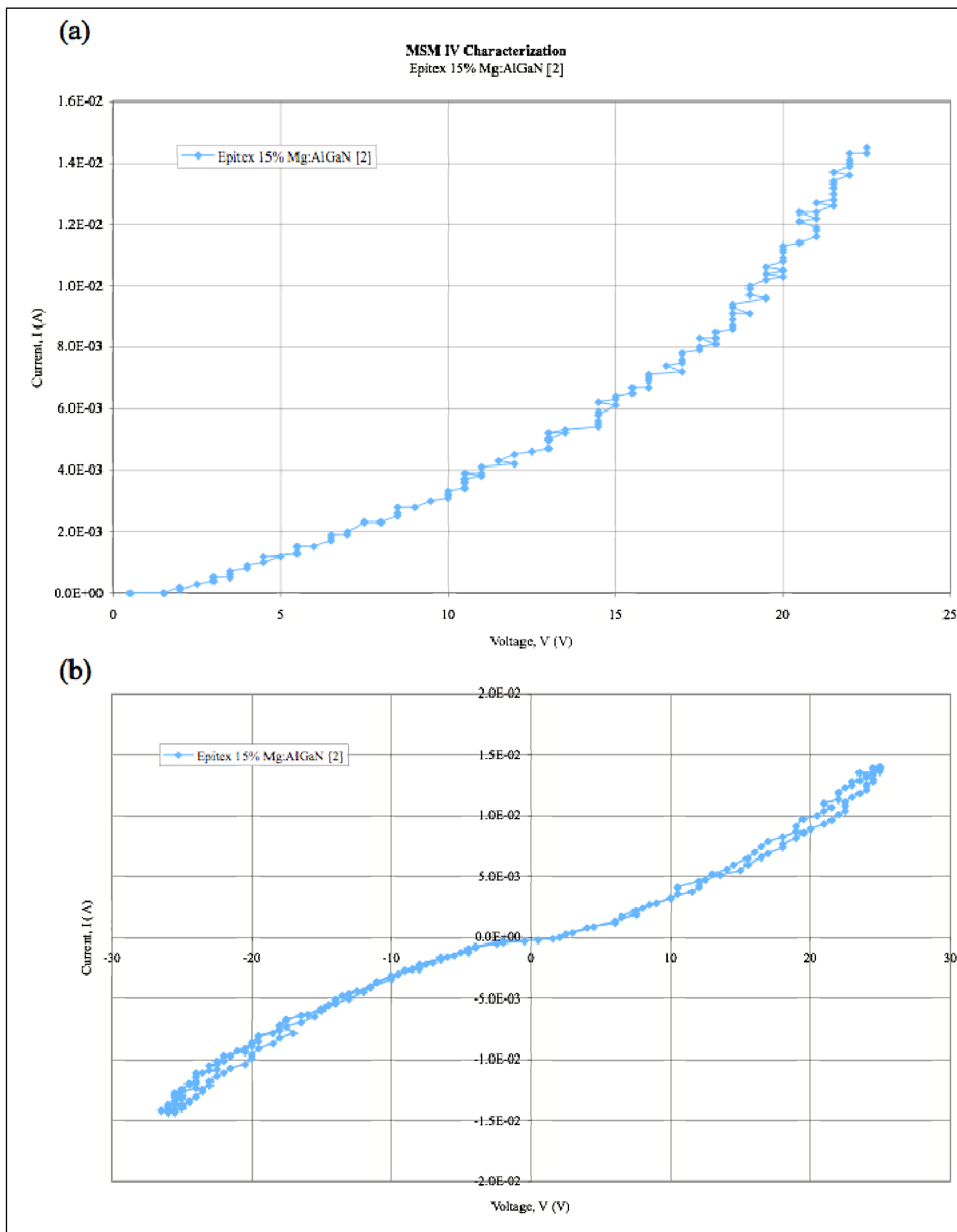

Figure 103: IV Characterization of test structure [2] fabricated on Epitex Mg-doped $Al_{0.15}Ga_{0.85}N$.

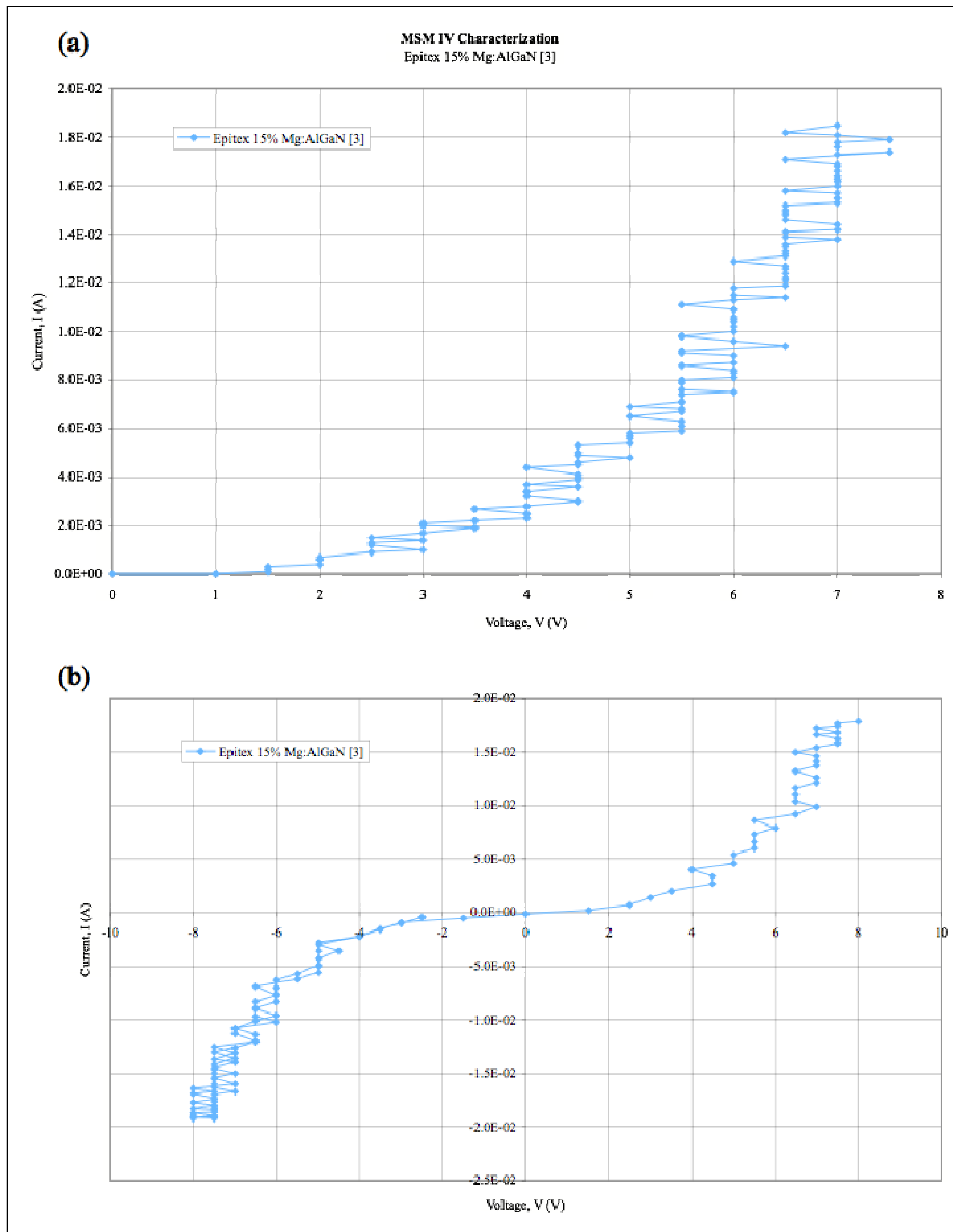

Figure 104: IV Characterization of test structure [3] fabricated on Epitex Mg-doped $Al_{0.15}Ga_{0.85}N$.

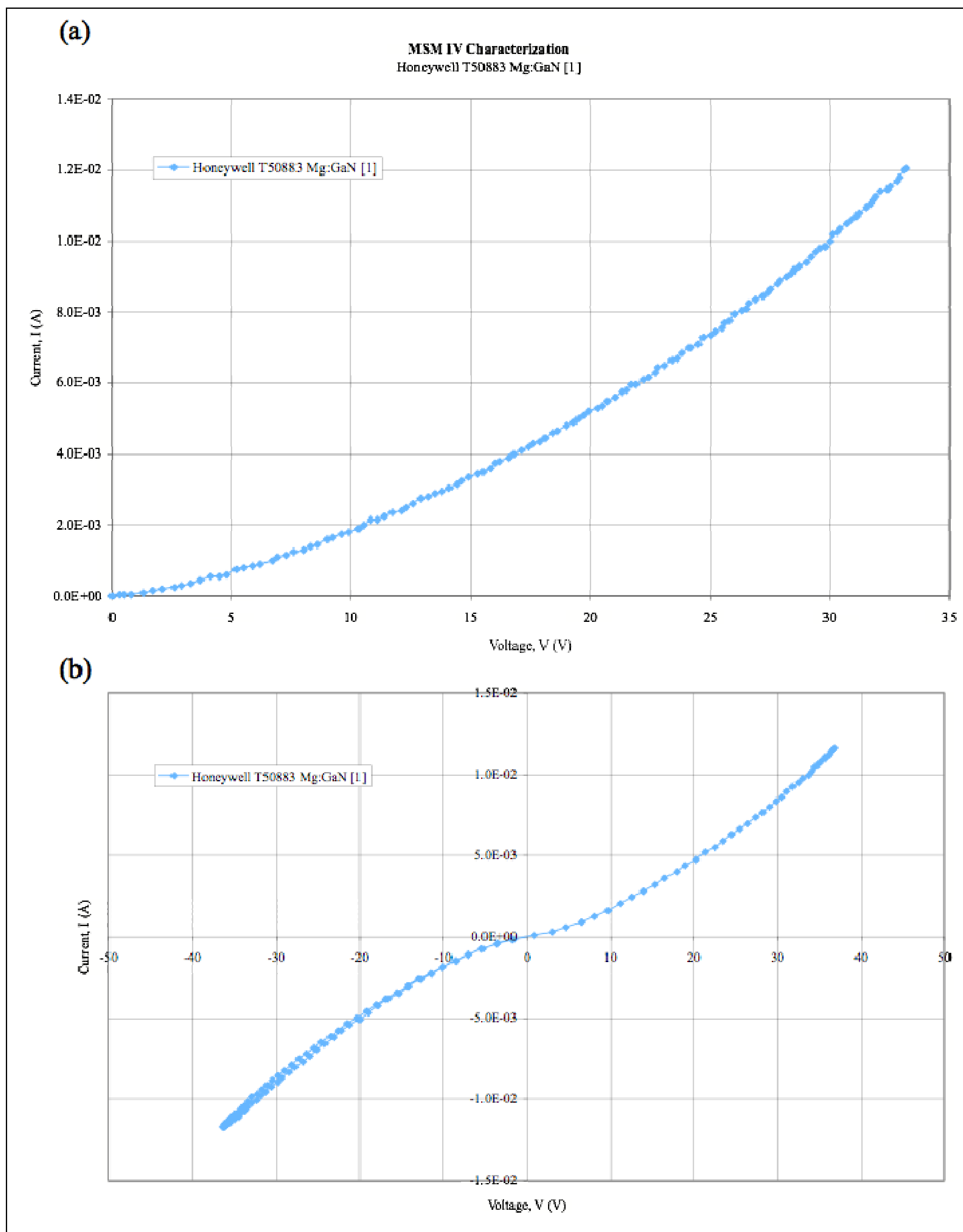

Figure 105: IV Characterization of test structure [1] fabricated on Honeywell Mg-doped GaN.

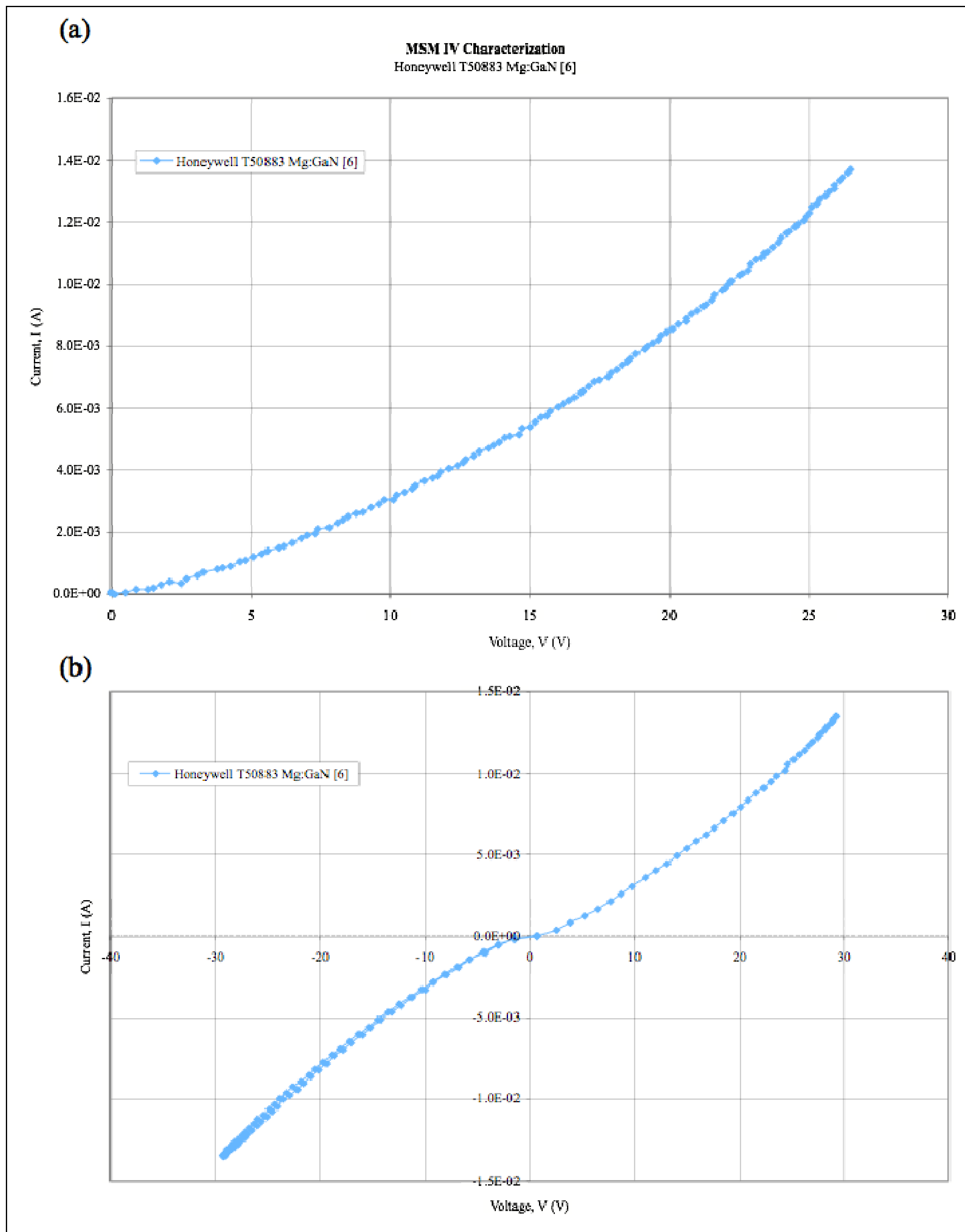

Figure 106: IV Characterization of test structure [6] fabricated on Honeywell Mg-doped GaN.

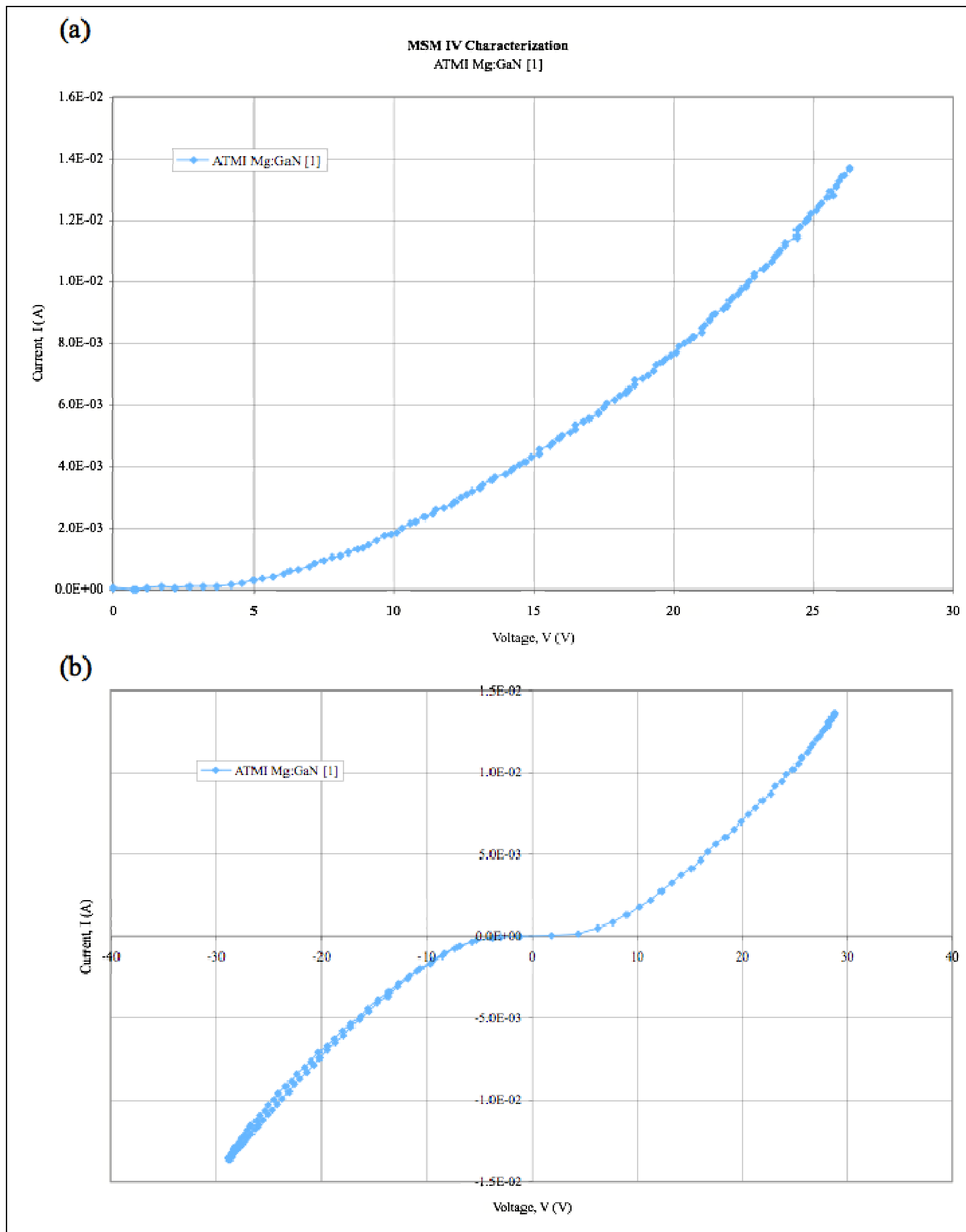

Figure 107: IV Characterization of test structure [1] fabricated on ATMI Mg-doped GaN.

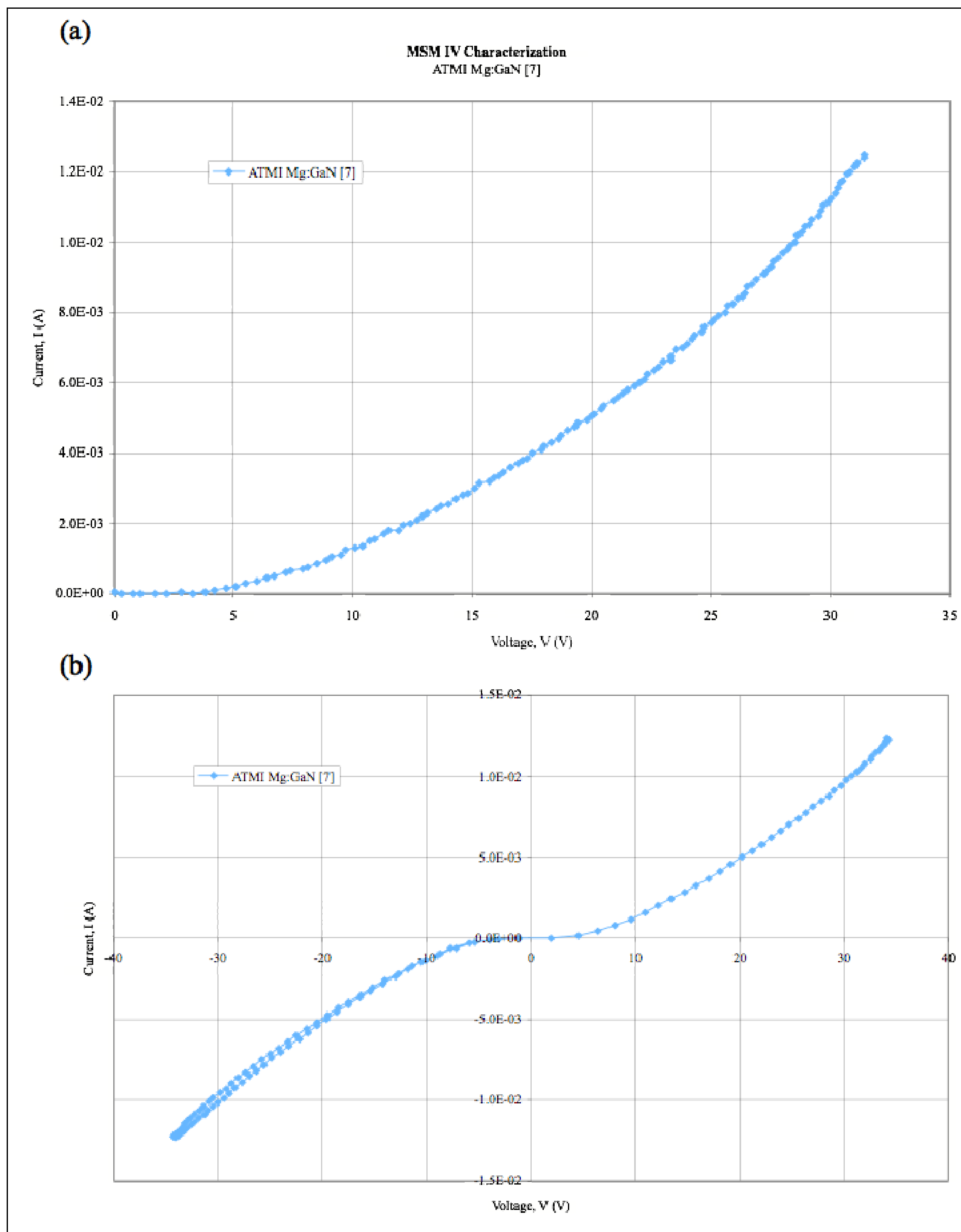

Figure 108: IV Characterization of test structure [7] fabricated on ATMI Mg-doped GaN.

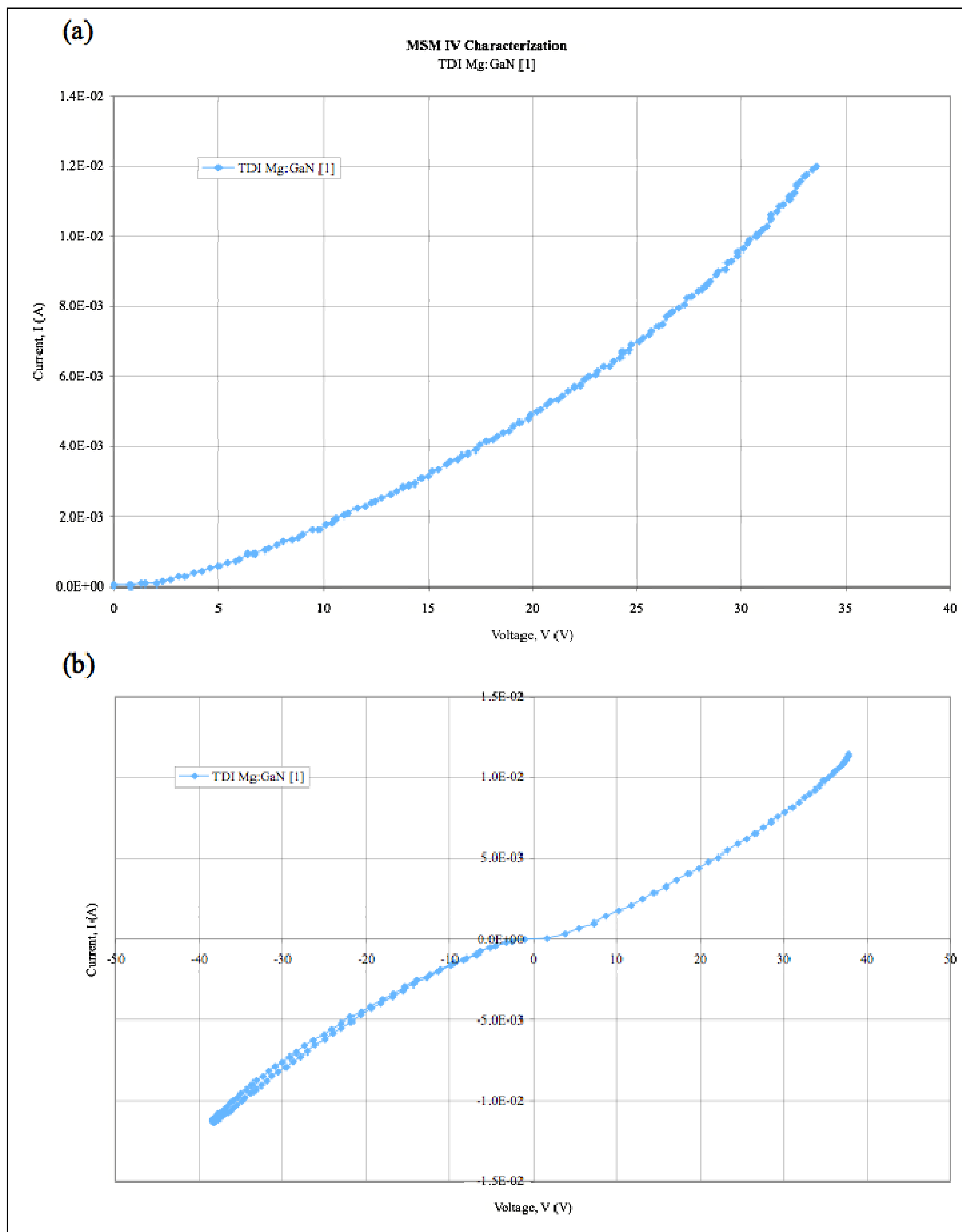

Figure 109: IV Characterization of test structure [1] fabricated on TDI Mg-doped GaN.

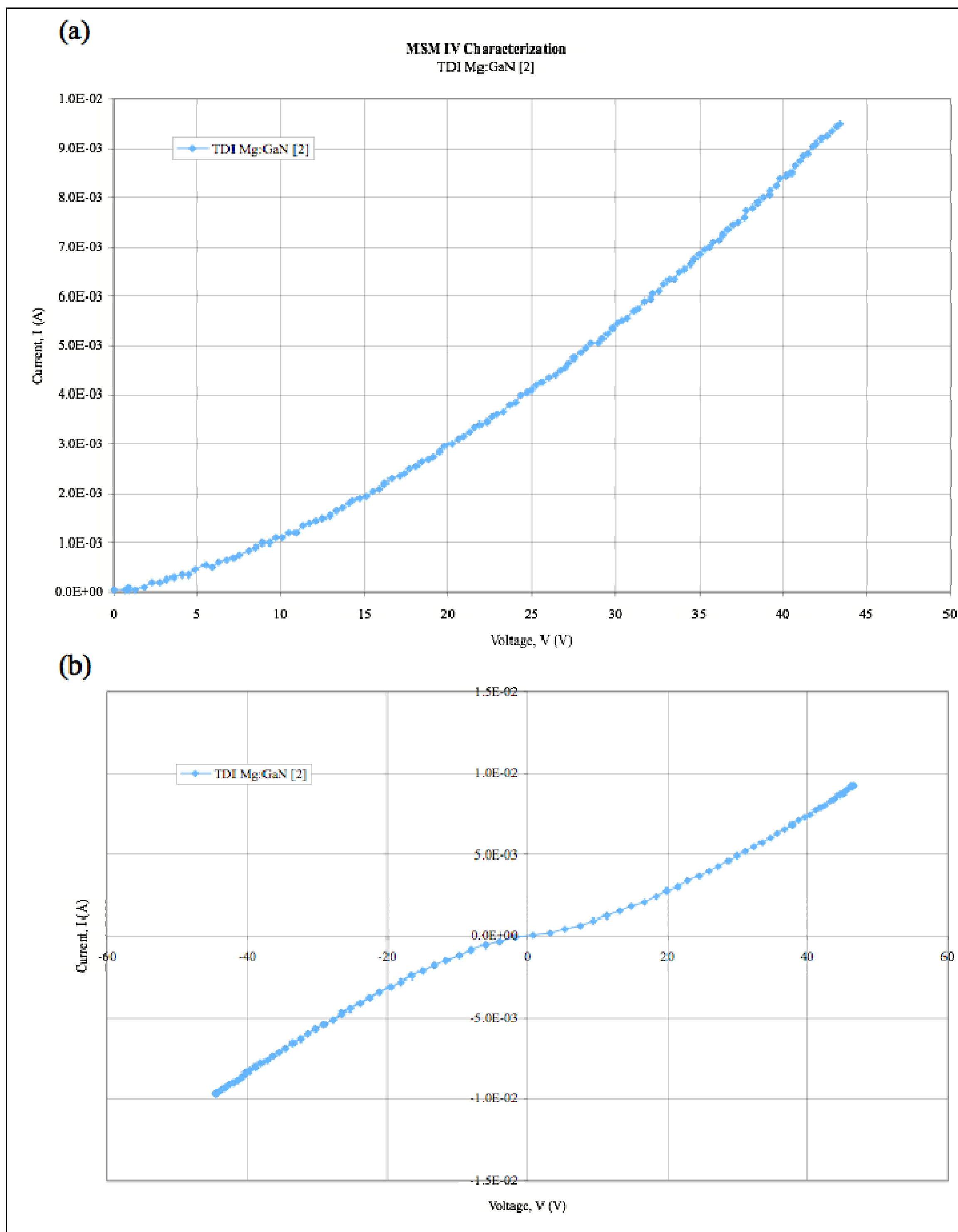

Figure 110: IV Characterization of test structure [2] fabricated on TDI Mg-doped GaN.

CHAPTER 6: RESULTS

In this chapter, infrared photocurrent spectra are presented from a variety of GaN and $Al_xGa_{1-x}N$ test structures, and the effects on forward current and light output from commercial ultraviolet III-nitride LEDs under IR irradiation are reported.

6.1. Infrared Photocurrent Spectra from Mg-doped $Al_{0.52}Ga_{0.48}N$ Test Structures

Figure 111 shows the high resolution plot (0.5 nm step) of the IR photocurrent response of a Ni/Au MSM test structure (MSM 4a) fabricated on Honeywell, Mg-doped $Al_{0.52}Ga_{0.48}N$ ("normalized" for each wavelength by the pulse energy at that wavelength), and the optical power output available for IR optical pumping provided by the OPO/OPA system in the Intermediate IR range (1350 nm to 1800 nm). A peak in the IR photocurrent response is observed at ~1450 nm (~855 meV), which is independent of the peak of the OPO/OPA system's power output located at ~1520 nm (~816 meV).

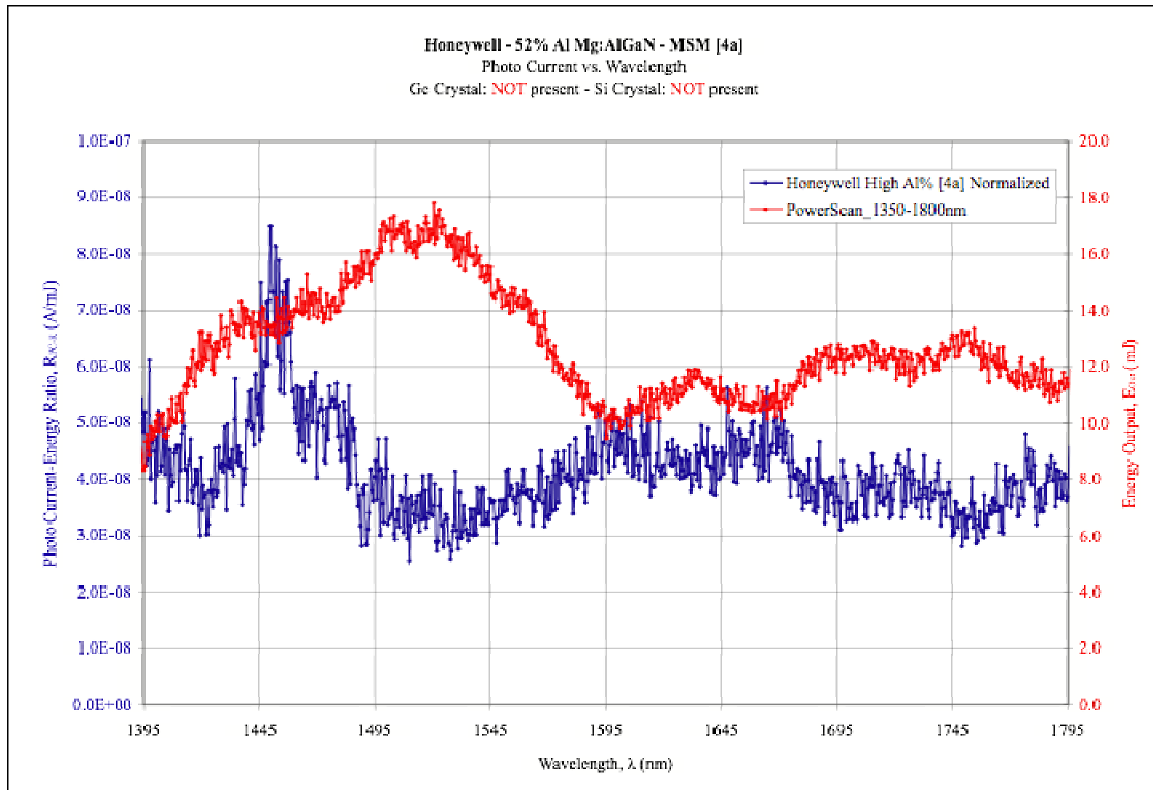

Figure 111: High resolution (0.5 nm step) plot of the IR photocurrent response of a Ni/Au MSM test structure (MSM 4a) fabricated on Honeywell, Mg-doped $Al_{0.52}Ga_{0.48}N$ ("normalized" for each wavelength by the pulse energy at that wavelength), and the optical power output available for IR optical pumping provided by the OPO/OPA system in the Intermediate IR range (1350 nm to 1800 nm). A peak in the IR photocurrent response is observed at ~1450 nm (~855 meV), which is independent of the peak of the OPO/OPA system's power output located at ~1520 nm (~816 meV).

Figure 112 shows the "raw" (not "normalized") high resolution plot (0.5 nm step) of the IR photocurrent response of a Ni/Au MSM test structure fabricated on Honeywell, Mg-doped $Al_{0.52}Ga_{0.48}N$, and the optical power output available for IR optical pumping provided by the OPO/OPA system in the Intermediate IR range (1350 nm to 1800 nm).

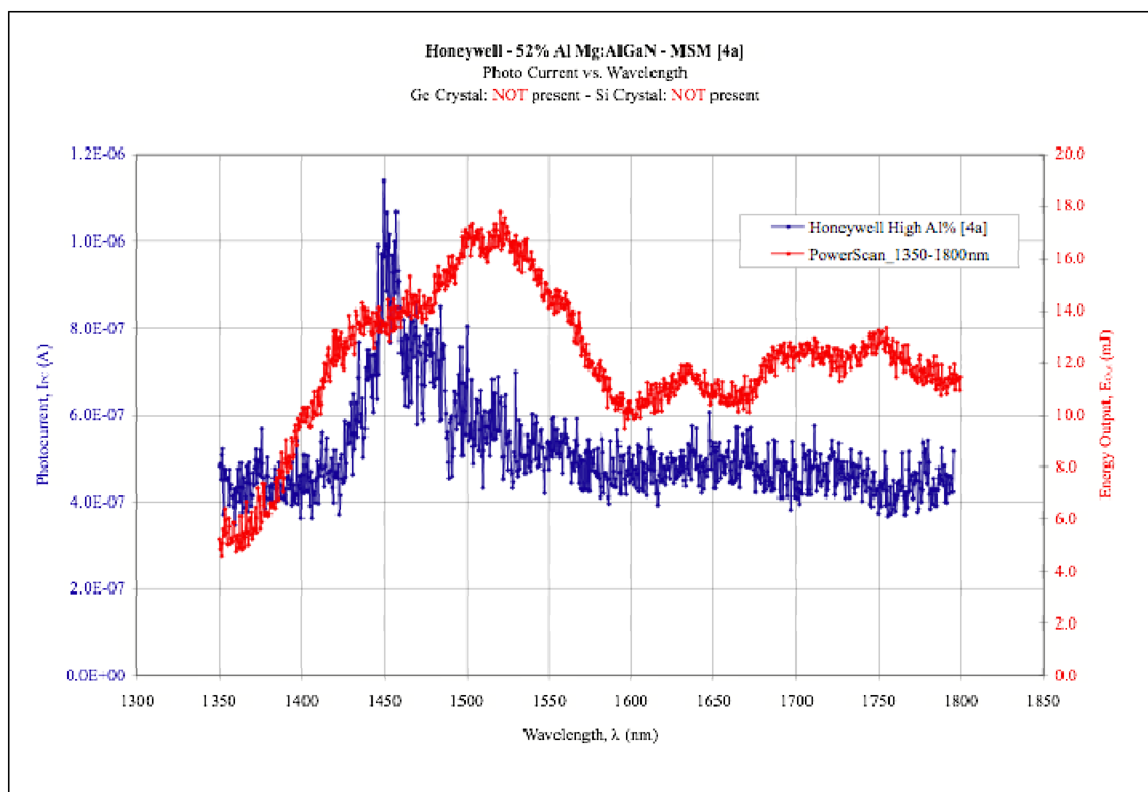

Figure 112: High resolution (0.5 nm step) plot of the “raw” (not “normalized”) IR photocurrent response of a Ni/Au MSM test structure (MSM 4a) fabricated on Honeywell, Mg-doped $Al_{0.52}Ga_{0.48}N$, and the optical power output available for IR optical pumping provided by the OPO/OPA system in the Intermediate IR range (1350 nm to 1800 nm).

Figure 113 shows the high-resolution plot (0.5 nm step) of the IR photocurrent response of a Ni/Au MSM test structure (MSM 4a) fabricated on Honeywell, Mg-doped $Al_{0.52}Ga_{0.48}N$ (“normalized” for each wavelength by the pulse energy at that wavelength) shown in Figure 111.

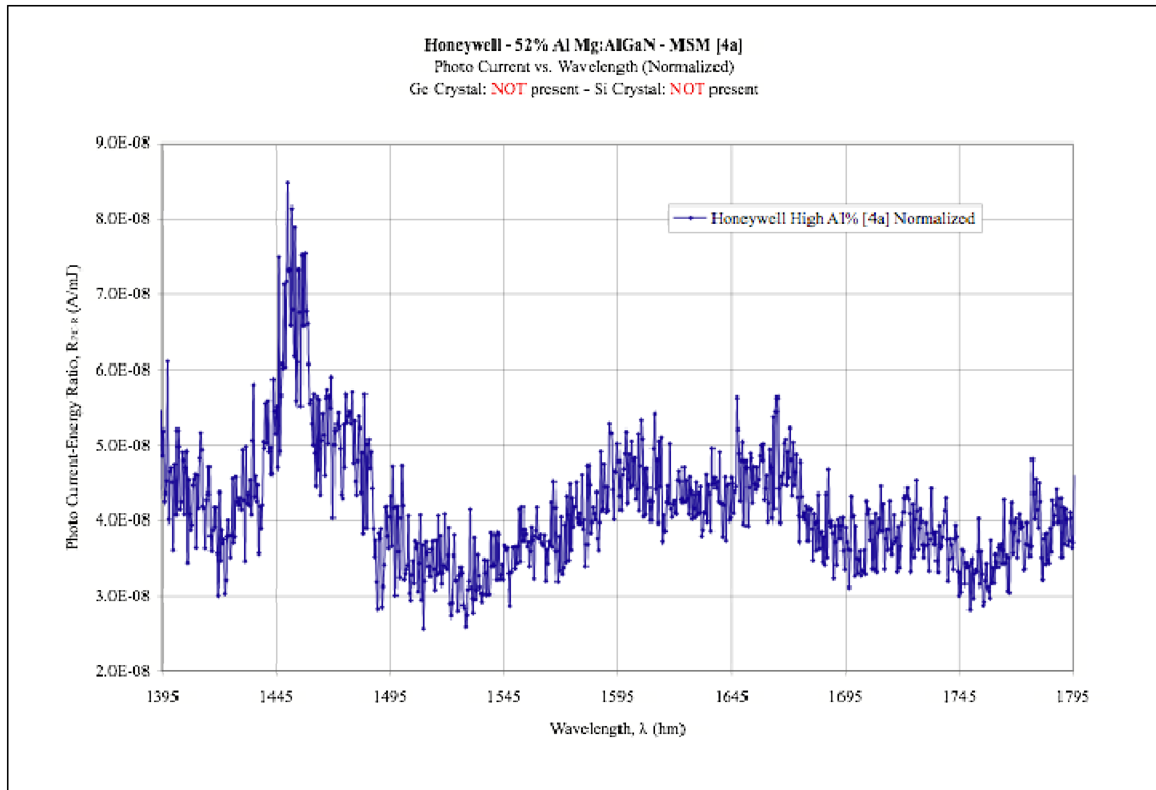

Figure 113: High-resolution plot (0.5 nm step) of the IR photocurrent response of a Ni/Au MSM test structure (MSM 4a) fabricated on Honeywell, Mg-doped $Al_{0.52}Ga_{0.48}N$ ("normalized" for each wavelength by the pulse energy at that wavelength) shown in Figure 111.

Figure 114 shows the curve fitting of the observed peak of the high-resolution plot (0.5 nm step) of the "normalized" IR photocurrent response of a Ni/Au MSM test structure (MSM 4a) fabricated on Honeywell, Mg-doped $Al_{0.52}Ga_{0.48}N$ shown in Figure 113.

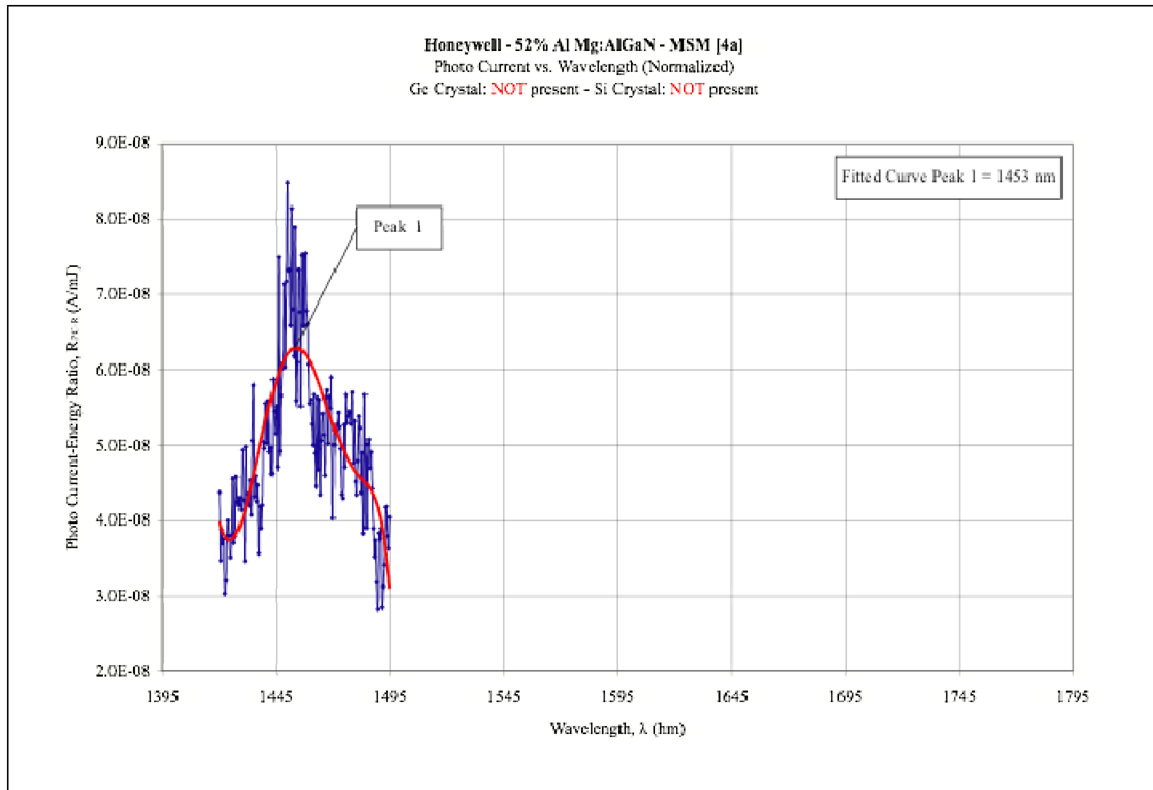

Figure 114: Curve fitting (polynomial) of the peak response observed in the high-resolution plot (0.5 nm step) shown in Figure 113.

Figure 115 shows the high-resolution plot (0.5 nm step) of the “raw” (not “normalized”) IR photocurrent response of a Ni/Au MSM test structure (MSM 4a) fabricated on Honeywell, Mg-doped $Al_{0.52}Ga_{0.48}N$ shown in Figure 112.

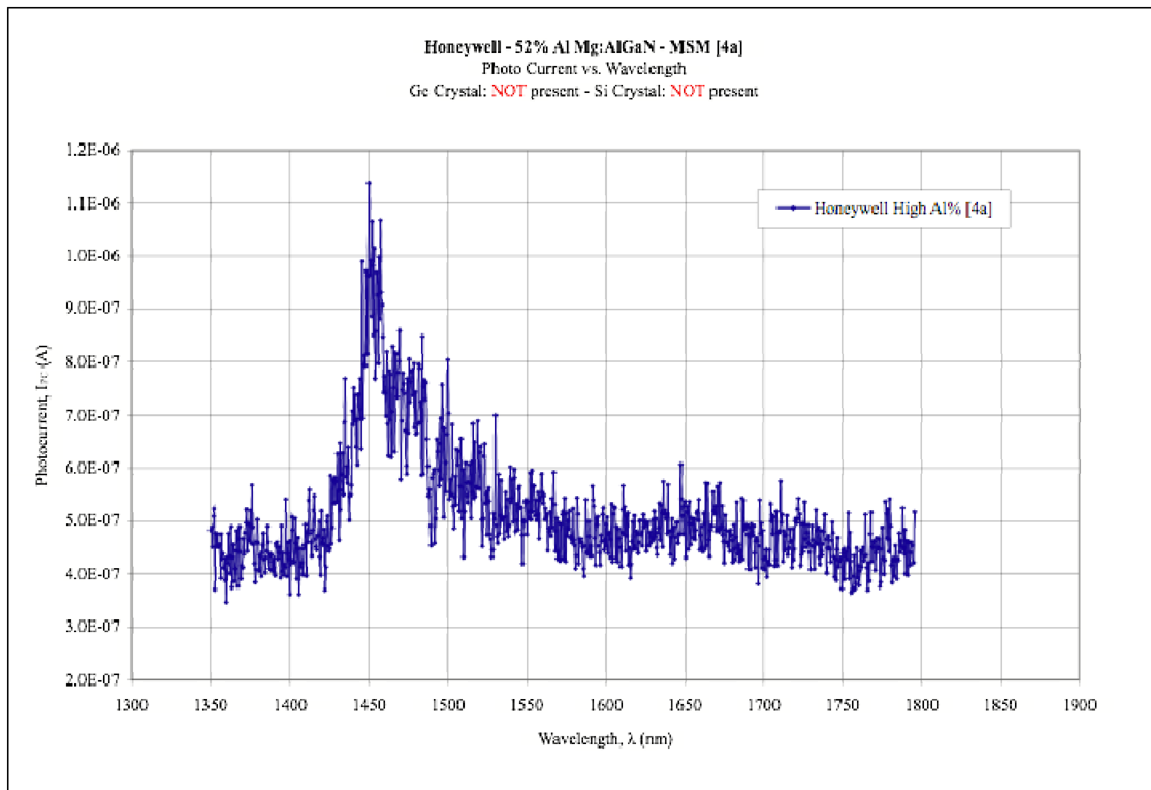

Figure 115: High-resolution plot (0.5 nm step) of the “raw” (not “normalized”) IR photocurrent response of a Ni/Au MSM test structure (MSM 4a) fabricated on Honeywell, Mg-doped $Al_{0.52}Ga_{0.48}N$ shown in Figure 112.

Figure 116 shows the plot (5 nm step) of the IR photocurrent response of other Ni/Au MSM test structures (MSM 1, 3, and 6) fabricated on Honeywell, Mg-doped $Al_{0.52}Ga_{0.48}N$ (“normalized” for each wavelength by the pulse energy at that wavelength), and the optical power output available for IR optical pumping provided by the OPO/OPA system in the Intermediate IR range (1350 nm to 2100 nm). Peaks in the IR photocurrent responses are observed at ~1430 nm (~867 meV), which are independent of the peak of the OPO/OPA system’s power output located at ~1520 nm (~816 meV).

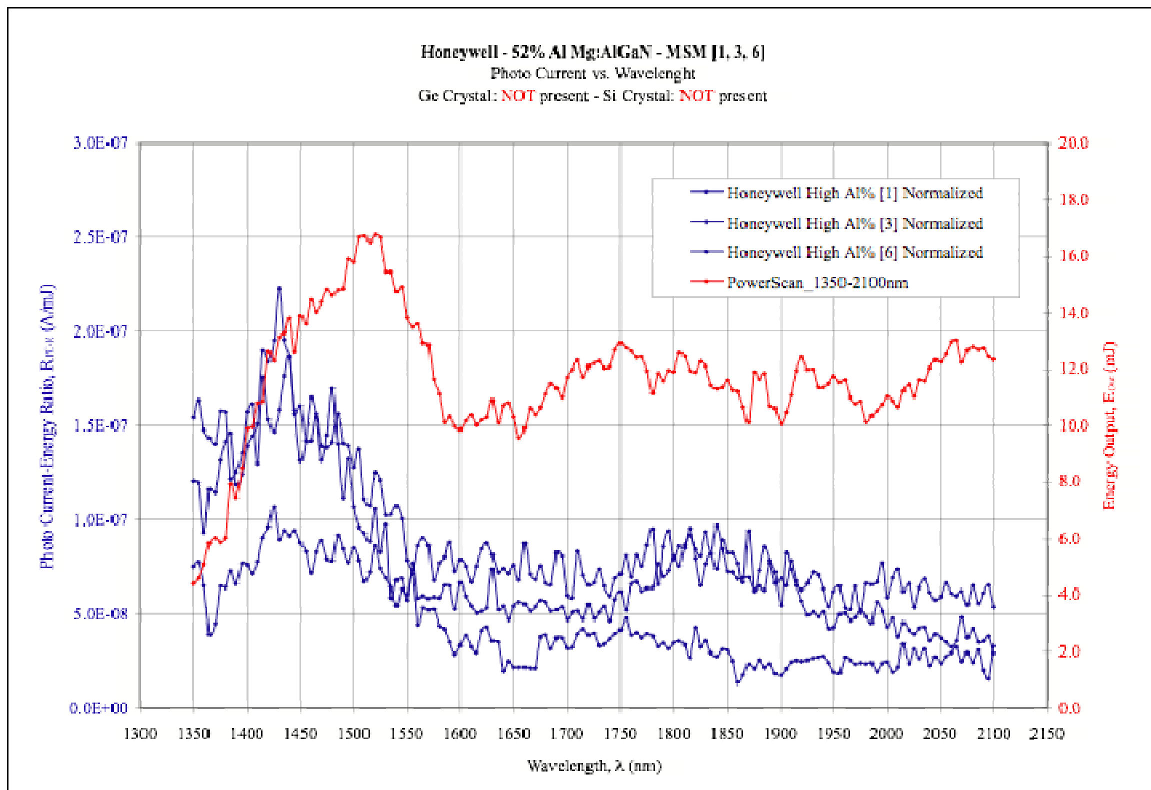

Figure 116: Plot (5 nm step) of the IR photocurrent response of other Ni/Au MSM test structures fabricated on Honeywell (MSM 1, 3, and 6), Mg-doped $Al_{0.52}Ga_{0.48}N$ ("normalized" for each wavelength by the pulse energy at that wavelength), and the optical power output available for IR optical pumping provided by the OPO/OPA system in the Intermediate IR range (1350 nm to 2100 nm). Peaks in the IR photocurrent responses are observed at ~1430 nm (~867 meV), which is independent of the peak of the OPO/OPA system's power output located at ~1520 nm (~816 meV).

Figure 118 shows the curve fitting of the observed peaks in the plot (5 nm step) of the "normalized" IR photocurrent response of test structure #1, #3, and #6 fabricated on Honeywell, Mg-doped $Al_{0.52}Ga_{0.48}N$ shown in shown in Figure 116.

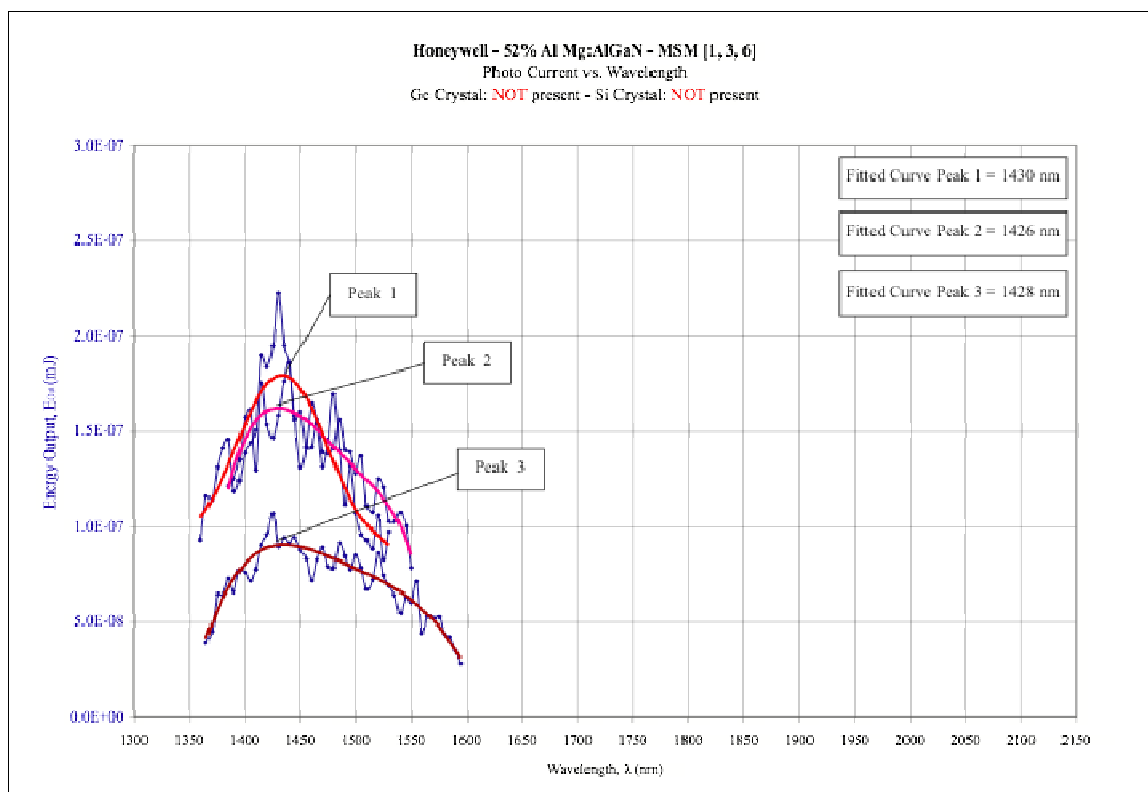

Figure 117: Curve fitting (polynomial) of the peak responses observed in the high-resolution plot (0.5 nm step) shown in Figure 116.

Figure 118 shows the plot (5 nm step) of the "raw" (not "normalized") IR photocurrent response of other Ni/Au MSM test structures (MSM 1, 3, and 6) fabricated on Honeywell, Mg-doped $Al_{0.52}Ga_{0.48}N$ shown in Figure 116.

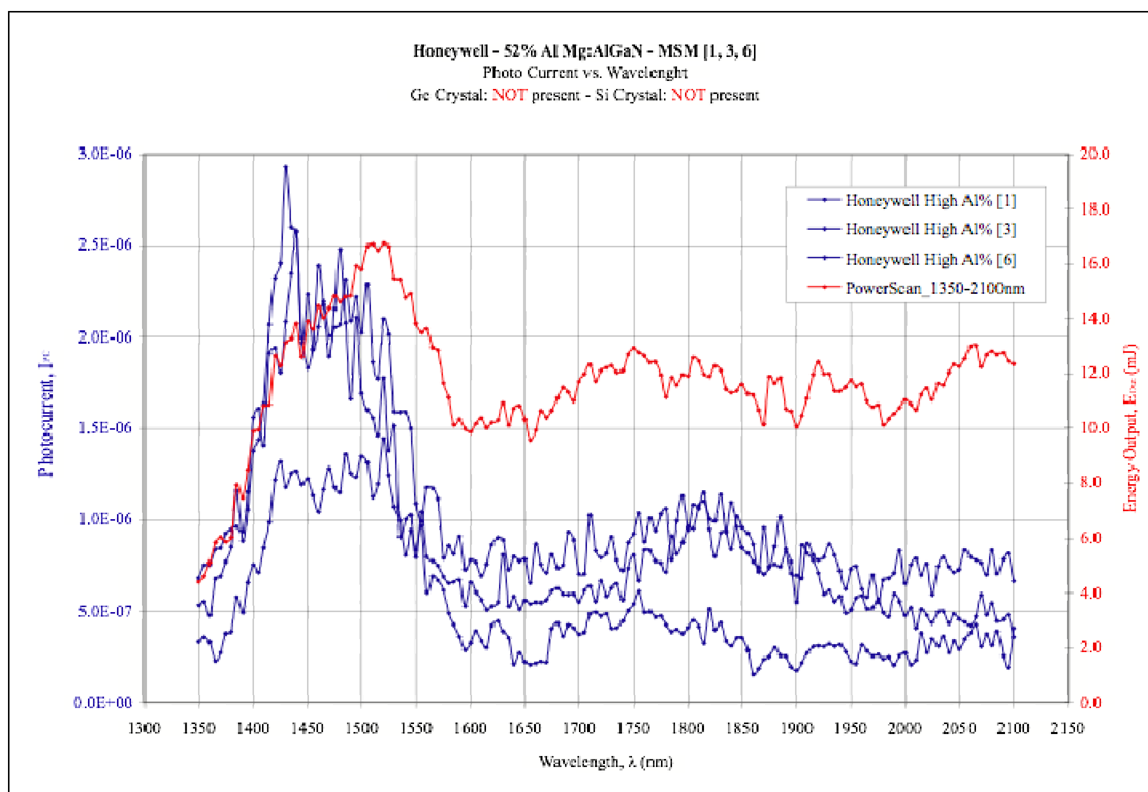

Figure 118: Plot (5 nm step) of the “raw” (not “normalized”) IR photocurrent response of other Ni/Au MSM test structures (MSM 1, 3, and 6) fabricated on Honeywell, Mg-doped $Al_{0.52}Ga_{0.48}N$ shown in Figure 116.

Figure 119 shows the plot (5 nm step) of the IR photocurrent response of Ni/Au MSM test structure #1 fabricated on Honeywell, Mg-doped $Al_{0.52}Ga_{0.48}N$ (“normalized” for each wavelength by the pulse energy at that wavelength), and the optical power output available for IR optical pumping provided by the OPO/OPA system in the Intermediate IR range (1350 nm to 2100 nm). Besides a peak in the IR photocurrent response observed at ~1430 nm (~867 meV), a plausible secondary peak is observed at ~1840 nm (~674 meV); both IR photocurrent response peaks are independent of the peak of the OPO/OPA system’s power output located at ~1520 nm (~816 meV).

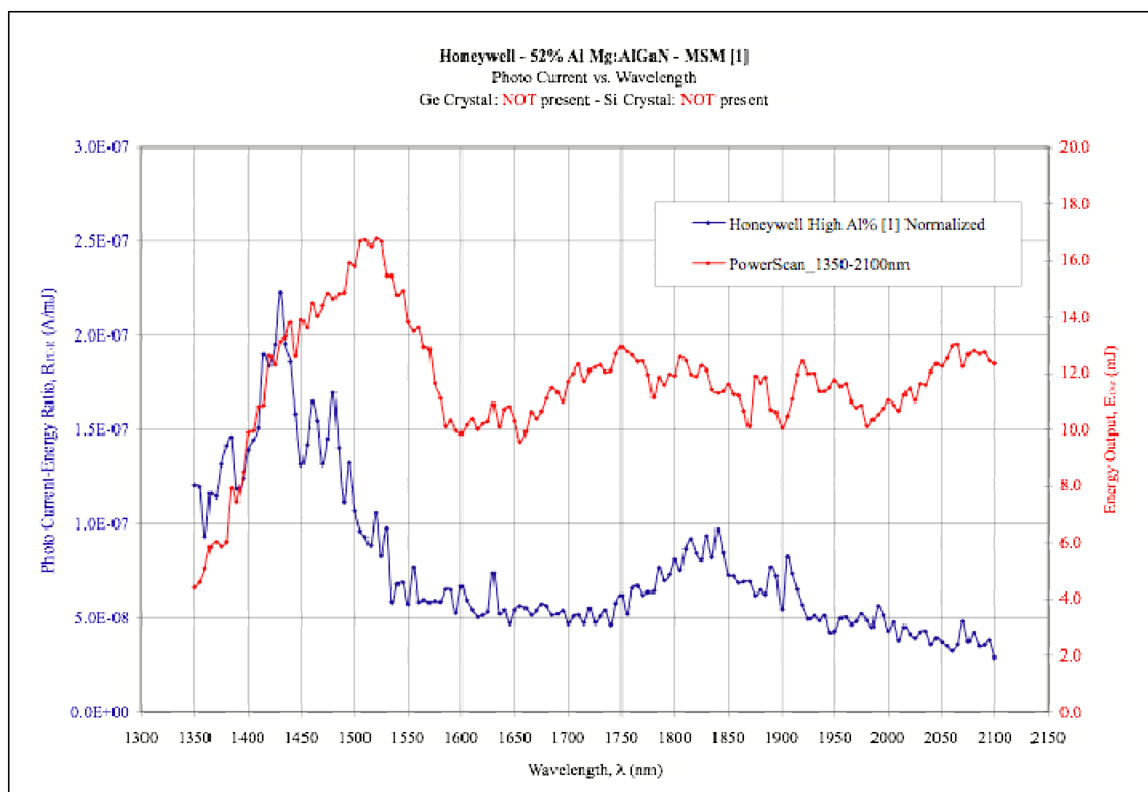

Figure 119: Plot (5 nm step) of the IR photocurrent response of Ni/Au MSM test structure #1 fabricated on Honeywell, Mg-doped $Al_{0.52}Ga_{0.48}N$ ("normalized" for each wavelength by the pulse energy at that wavelength), and the optical power output available for IR optical pumping provided by the OPO/OPA system in the Intermediate IR range (1350 nm to 2100 nm). Besides a peak in the IR photocurrent response observed at ~1430 nm (~867 meV), a plausible secondary peak is observed at ~1840 nm (~674 meV); both IR photocurrent response peaks are independent of the peak of the OPO/OPA system's power output located at ~1520 nm (~816 meV).

6.2. Infrared Photocurrent Spectra from Mg-doped $Al_{0.42}Ga_{0.58}N$ Test Structures

Figure 120 shows the high resolution plot (0.5 nm step) of the IR photocurrent response of test structure #1 fabricated on Crystal IS, Mg-doped $Al_{0.42}Ga_{0.58}N$ ("normalized" for each wavelength by the pulse energy at that wavelength), and the optical power output available for IR optical pumping provided by the OPO/OPA system in the Intermediate IR range (1350 nm to 2100 nm). A peak in the IR photocurrent

response is observed at ~1495 nm (~829 meV), which is independent of the peak of the OPO/OPA system's power output located at ~1525 nm (~813 meV).

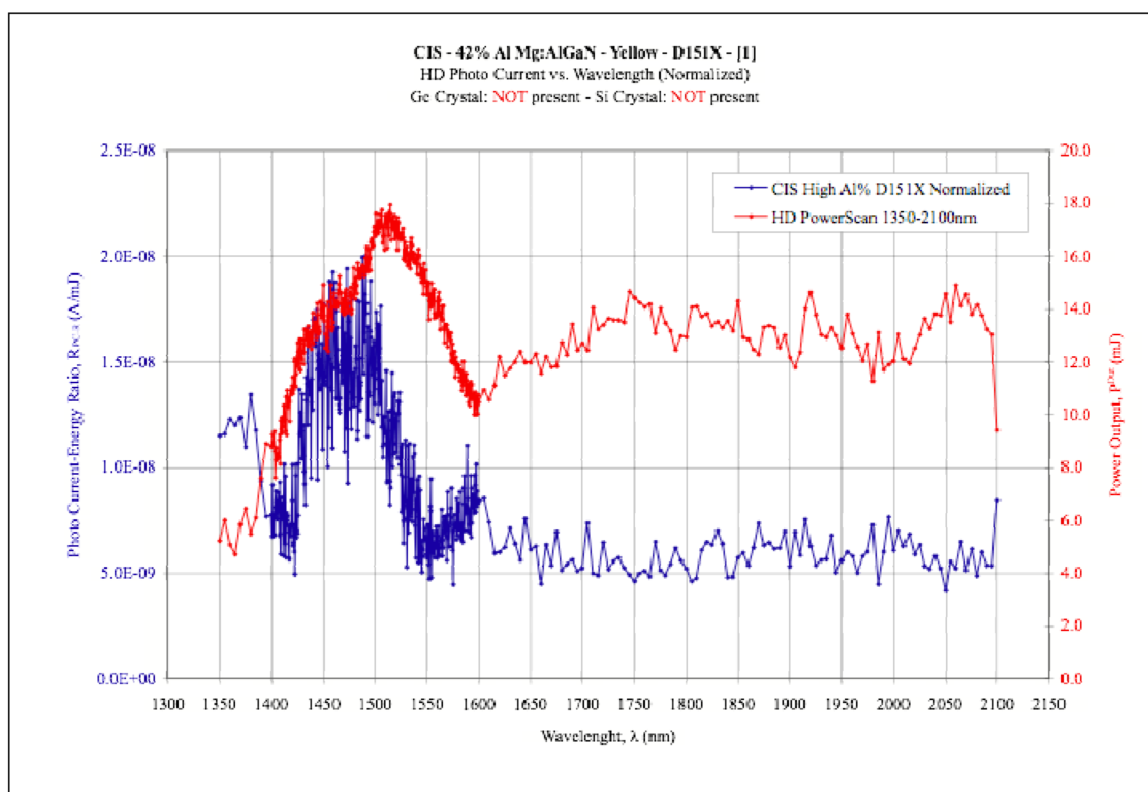

Figure 120: High resolution plot (0.5 nm step) of the IR photocurrent response of test structure #1 fabricated on Crystal IS, Mg-doped $Al_{0.42}Ga_{0.58}N$ ("normalized" for each wavelength by the pulse energy at that wavelength), and the optical power output available for IR optical pumping provided by the OPO/OPA system in the Intermediate IR range (1350 nm to 2100 nm). A peak in the IR photocurrent response is observed at ~1495 nm (~829 meV), which is independent of the peak of the OPO/OPA system's power output located at ~1525 nm (~813 meV).

Figure 121 shows the "raw" (not "normalized") high resolution plot (0.5 nm step) of the IR photocurrent response of test structure #1 fabricated on Crystal IS, Mg-doped $Al_{0.42}Ga_{0.58}N$, and the optical power output available for IR optical pumping provided by the OPO/OPA system in the Intermediate IR range (1350 nm to 2100 nm).

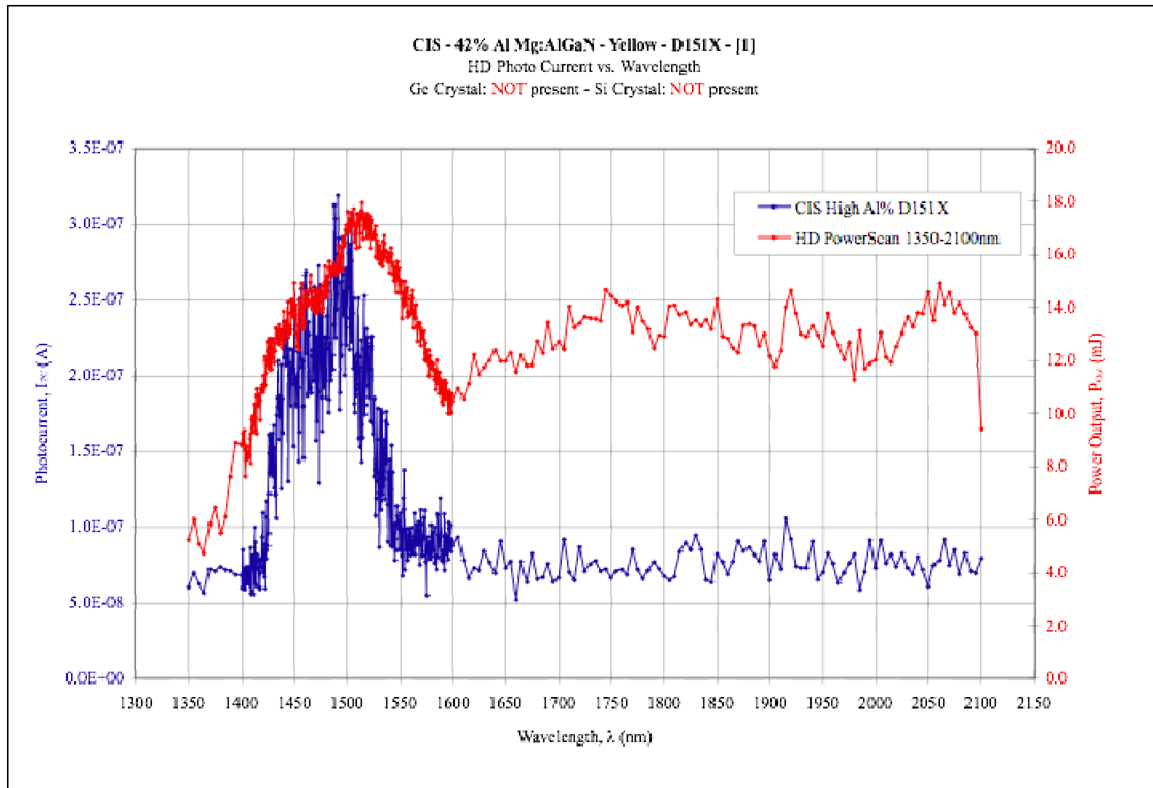

Figure 121: High-resolution plot (0.5 nm step) of the "raw" (not "normalized") IR photocurrent response of test structure #1 fabricated on Crystal IS, Mg-doped $Al_{0.42}Ga_{0.58}N$, and the optical power output available for IR optical pumping provided by the OPO/OPA system in the Intermediate IR range (1350 nm to 2100 nm).

Figure 122 shows the high-resolution plot (0.5 nm step) of the IR photocurrent response of test structure #1 fabricated on Crystal IS, Mg-doped $Al_{0.42}Ga_{0.58}N$, ("normalized" for each wavelength by the pulse energy at that wavelength) shown in Figure 120.

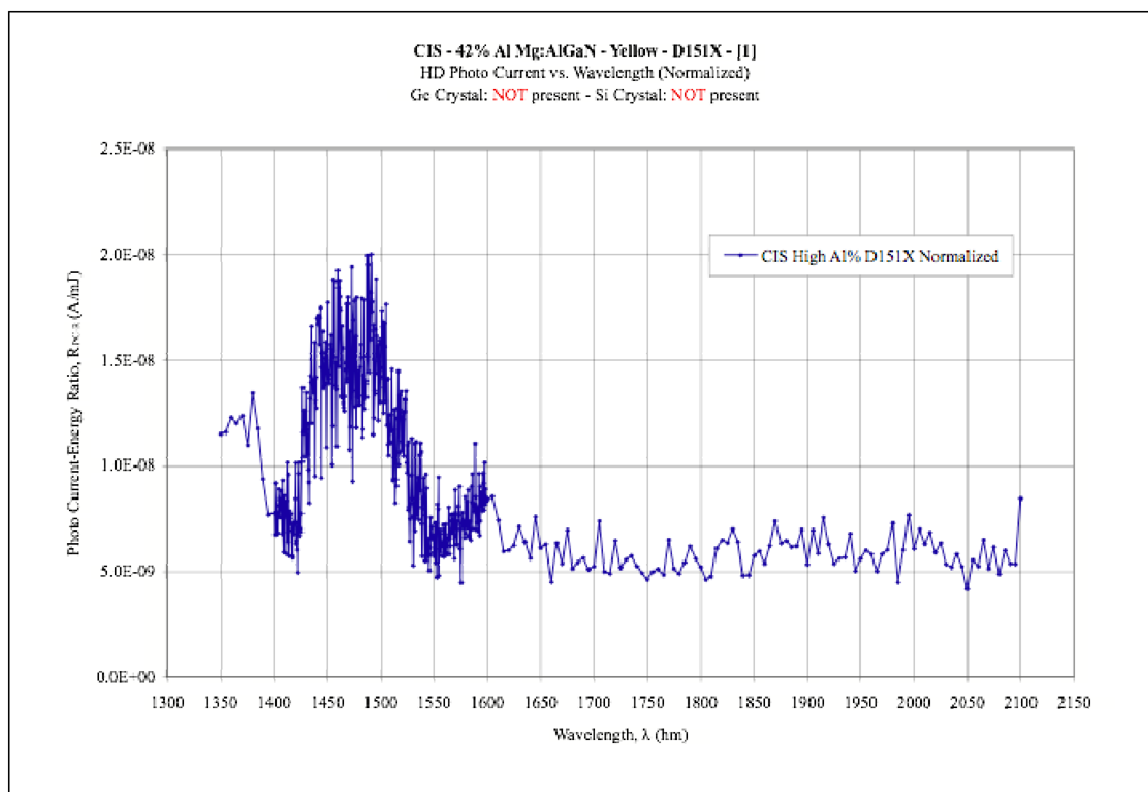

Figure 122: High-resolution plot (0.5 nm step) of the IR photocurrent response of test structure #1 fabricated on Crystal IS, Mg-doped $Al_{0.42}Ga_{0.58}N$ ("normalized" for each wavelength by the pulse energy at that wavelength).

Figure 123 shows curve fitting of the observed peak of the high-resolution plot (0.5 nm step) of the "normalized" IR photocurrent response of test structure #1 fabricated on Crystal IS, Mg-doped $Al_{0.42}Ga_{0.58}N$ shown in Figure 122.

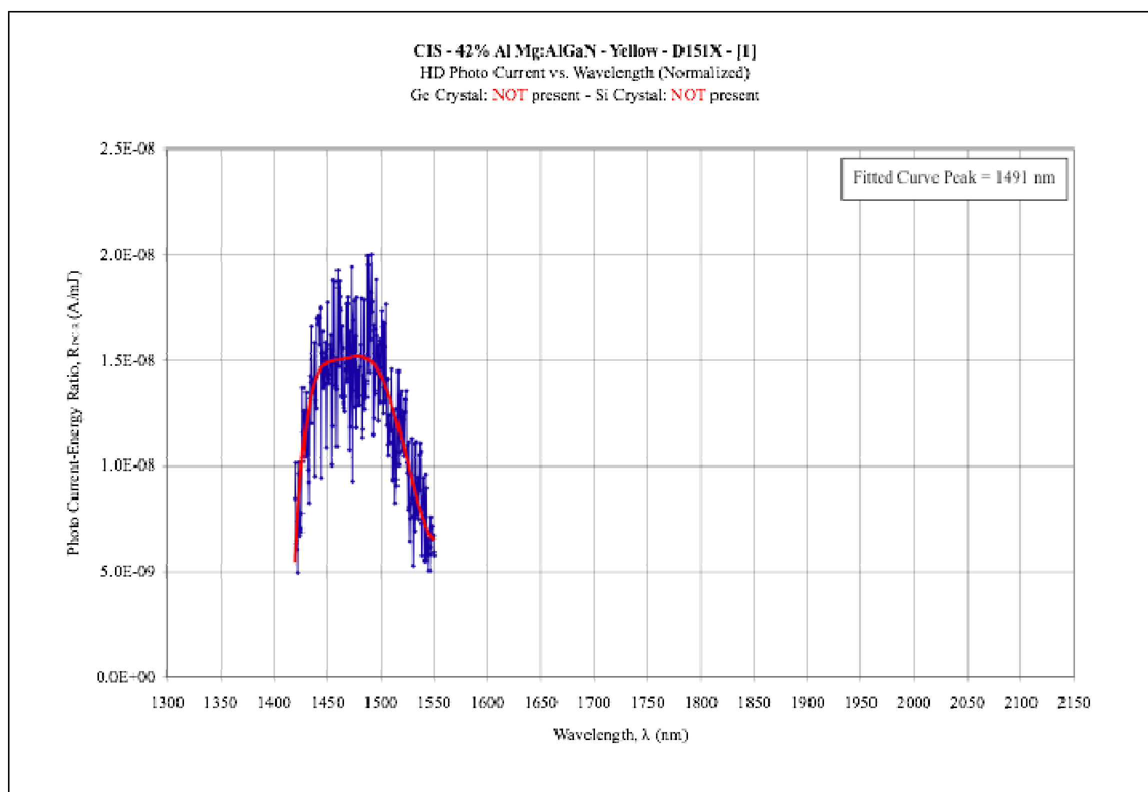

Figure 123: Curve fitting (polynomial) of the peak response observed in the high-resolution plot (0.5 nm step) shown in Figure 122.

Figure 124 shows the high-resolution plot (0.5 nm step) of the raw (not "normalized") IR photocurrent response of test structure #1 fabricated on Crystal IS, Mg-doped $Al_{0.42}Ga_{0.58}N$ shown in Figure 121.

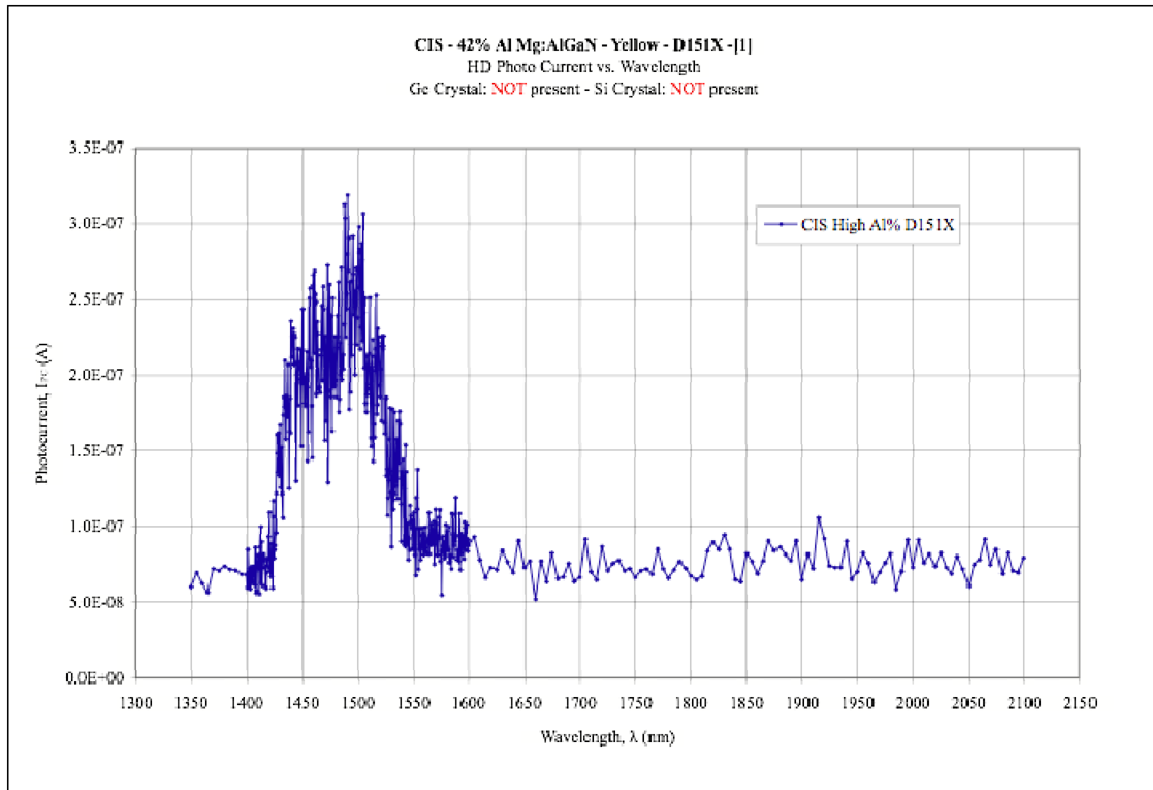

Figure 124: High-resolution plot (0.5 nm step) of the raw (not "normalized") IR photocurrent response of test structure #1 fabricated on Crystal IS, Mg-doped $Al_{0.42}Ga_{0.58}N$ shown in Figure 121.

Figure 125 shows the plot (5 nm step) of the IR photocurrent response of test structure #2 fabricated on Crystal IS, Mg-doped $Al_{0.42}Ga_{0.58}N$ ("normalized" for each wavelength by the pulse energy at that wavelength), and the optical power output available for IR optical pumping provided by the OPO/OPA system in the Intermediate IR range (1350 nm to 2100 nm). A peak in the IR photocurrent response is observed at ~1465 nm (~846 meV), which is independent of the peak of the OPO/OPA system's power output located at ~1525 nm (~813 meV).

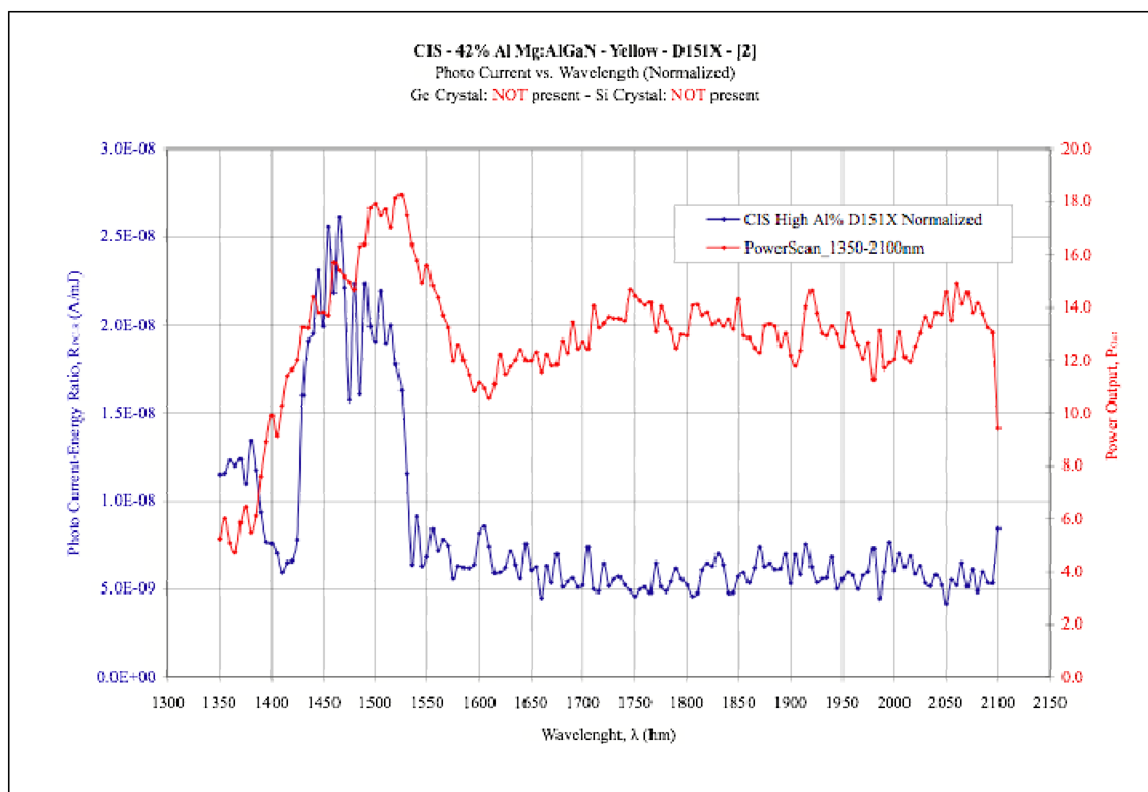

Figure 125: Plot (5 nm step) of the IR photocurrent response of test structure #2 fabricated on Crystal IS, Mg-doped $Al_{0.42}Ga_{0.58}N$ ("normalized" for each wavelength by the pulse energy at that wavelength), and the optical power output available for IR optical pumping provided by the OPO/OPA system in the Intermediate IR range (1350 nm to 2100 nm). A peak in the IR photocurrent response is observed at ~1465 nm (~846 meV), which is independent of the peak of the OPO/OPA system's power output located at ~1525 nm (~813 meV).

Figure 126 shows the "raw" (not "normalized") plot (5 nm step) of the IR photocurrent response of test structure #2 fabricated on Crystal IS, Mg-doped $Al_{0.42}Ga_{0.58}N$, and the optical power output available for IR optical pumping provided by the OPO/OPA system in the Intermediate IR range (1350 nm to 2100 nm).

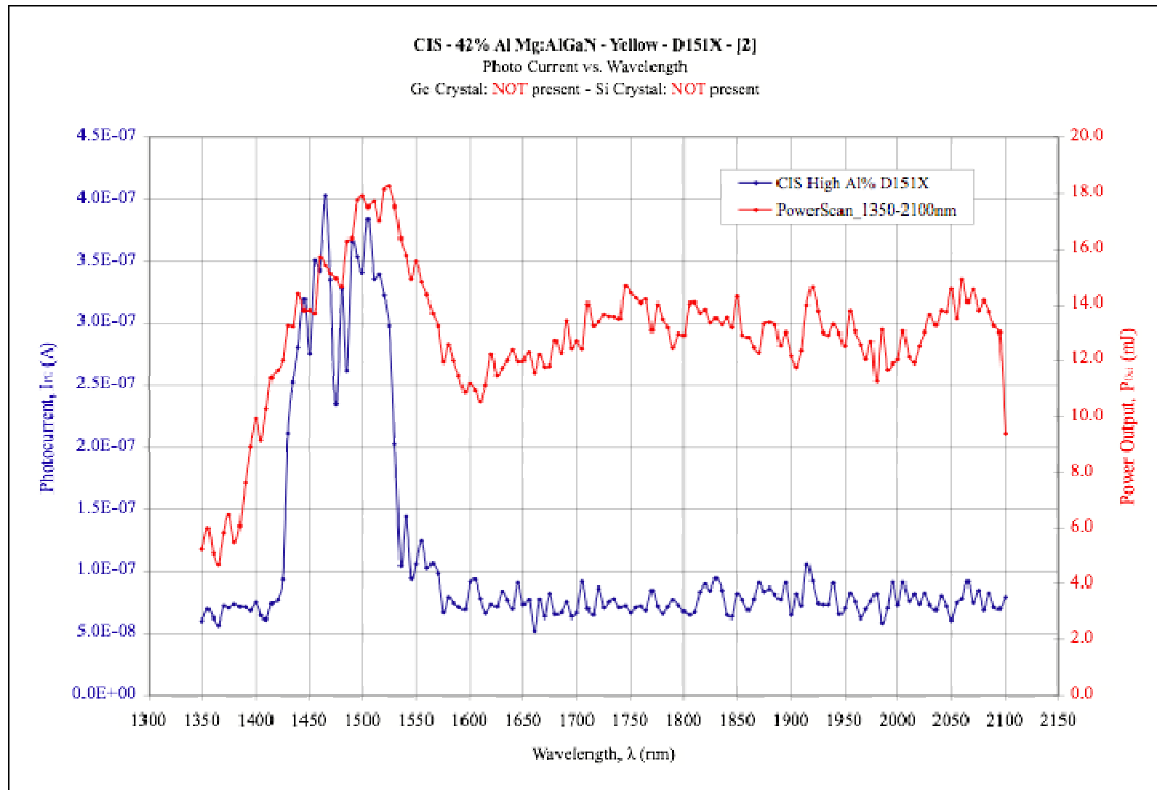

Figure 126: Plot (5 nm step) of the raw (not "normalized") IR photocurrent response of test structure #2 fabricated on Crystal IS, Mg-doped $Al_{0.42}Ga_{0.58}N$. A peak in the IR photocurrent response is observed at ~1465 nm (~846 meV), which is independent of the peak of the OPO/OPA system's power output located at ~1525 nm (~813 meV).

Figure 127 shows the plot (5 nm step) of the IR photocurrent response of test structure #2 fabricated on Crystal IS, Mg-doped $Al_{0.42}Ga_{0.58}N$, ("normalized" for each wavelength by the pulse energy at that wavelength) shown in Figure 125.

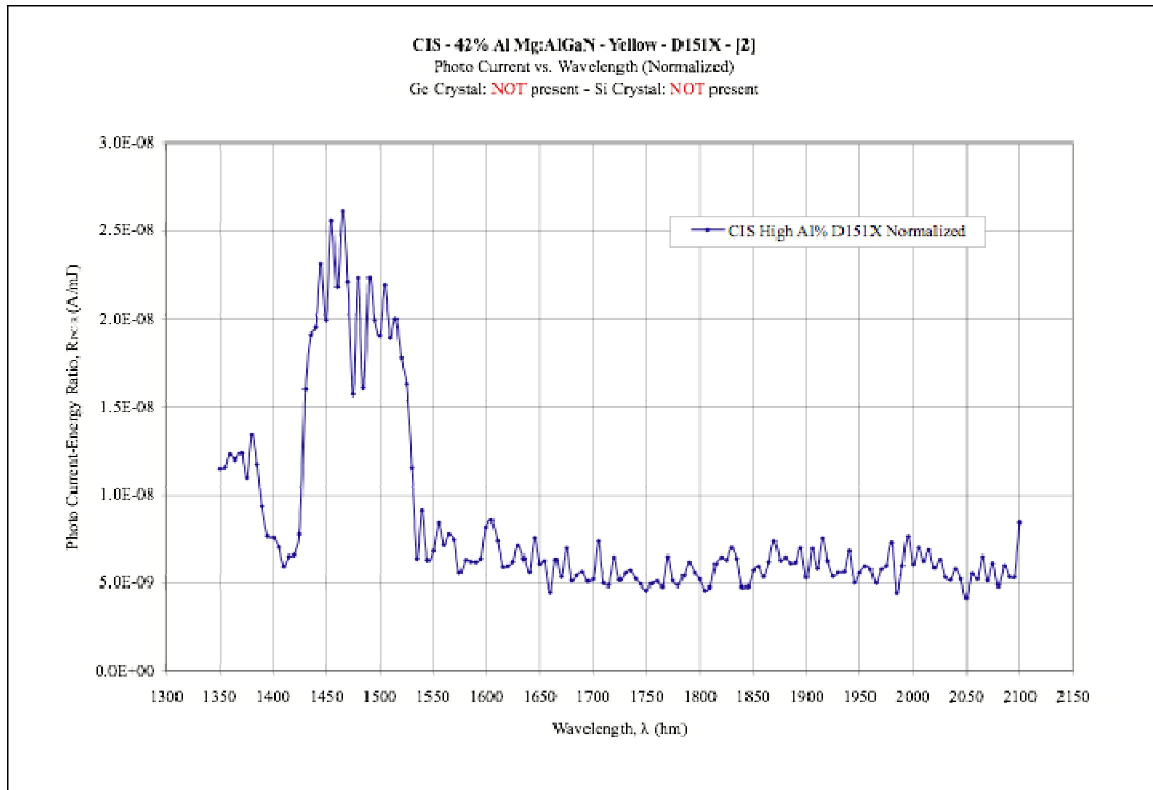

Figure 127: Plot (5 nm step) of the IR photocurrent response of test structure #2 fabricated on Crystal IS, Mg-doped $Al_{0.42}Ga_{0.58}N$ shown in Figure 125.

Figure 128 shows curve fitting of the observed peak of the high-resolution plot (5 nm step) of the "normalized" IR photocurrent response of test structure #2 fabricated on Crystal IS, Mg-doped $Al_{0.42}Ga_{0.58}N$ shown in Figure 127.

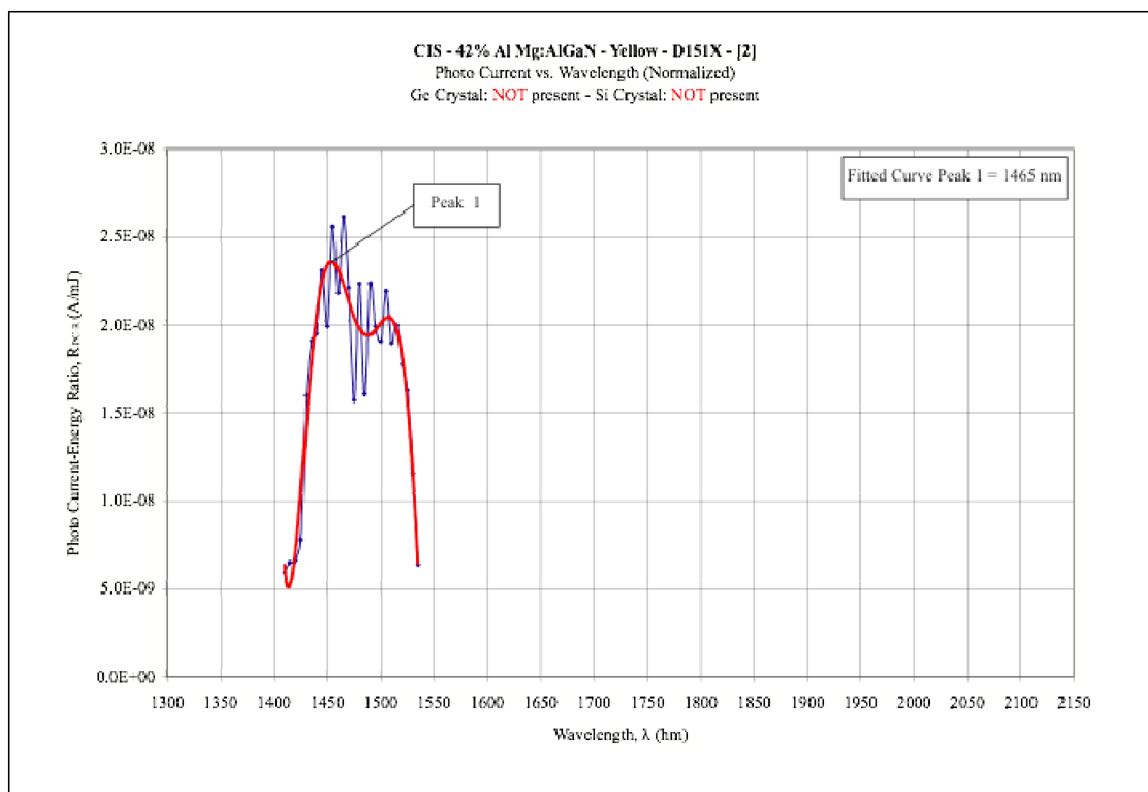

Figure 128: Curve fitting (polynomial) of the peak response observed in the plot (5 nm step) shown in Figure 127.

Figure 129 shows the plot (5 nm step) of the raw (not "normalized") IR photocurrent response of test structure #2 fabricated on Crystal IS, Mg-doped $Al_{0.42}Ga_{0.58}N$ shown in Figure 126.

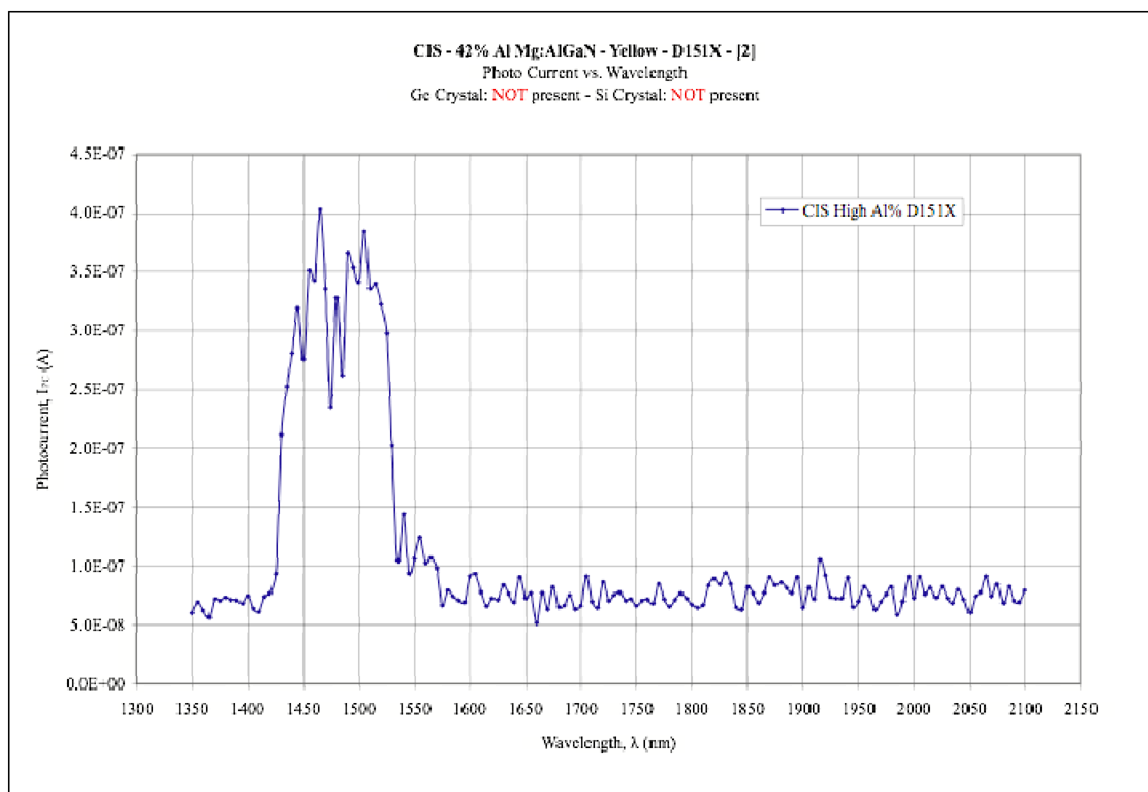

Figure 129: Plot (5 nm step) of the raw (not "normalized') IR photocurrent response of test structure #2 fabricated on Crystal IS, Mg-doped $Al_{0.42}Ga_{0.58}N$ shown in Figure 126.

6.3. Infrared Photocurrent Spectra from Mg-doped $Al_{0.20}Ga_{0.80}N$ Test Structures

Figure 130 shows the plot (5 nm step) of the IR photocurrent response of Ni/Au MSM test structure #4 fabricated on Honeywell, Mg-doped $Al_{0.20}Ga_{0.80}N$ ("normalized" for each wavelength by the pulse energy at that wavelength), and the optical power output available for IR optical pumping provided by the OPO/OPA system in the Mid IR range (2100 nm to 4000 nm). A peak in the IR photocurrent response is observed at ~2585 nm (~480 meV), which is independent of the peak of the OPO/OPA system's power output located at ~2200 nm (~564 meV).

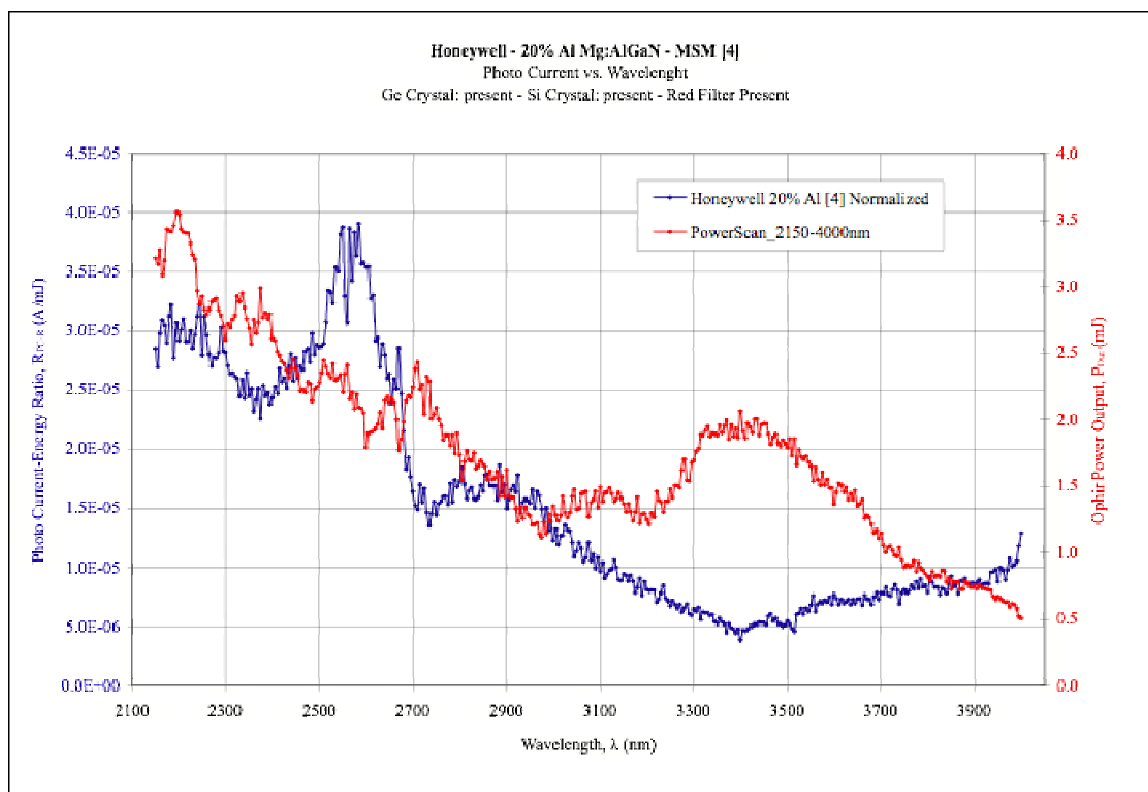

Figure 130: Plot (5 nm step) of the IR photocurrent response photocurrent response of Ni/Au MSM test structure #4 fabricated on Honeywell, Mg-doped $Al_{0.20}Ga_{0.80}N$ ("normalized" for each wavelength by the pulse energy at that wavelength), and the optical power output available for IR optical pumping provided by the OPO/OPA system in the Mid IR range (2100 nm to 4000 nm). A peak in the IR photocurrent response is observed at ~2585 nm (~480 meV), which is independent of the peak of the OPO/OPA system's power output located at ~2200 nm (~564 meV).

Figure 131 shows the "raw" (not "normalized") plot (5 nm step) of the IR photocurrent response Ni/Au MSM test structure #4 fabricated on Honeywell, Mg-doped $Al_{0.20}Ga_{0.80}N$, and the optical power output available for IR optical pumping provided by the OPO/OPA system in the Mid IR range (2100 nm to 4000 nm).

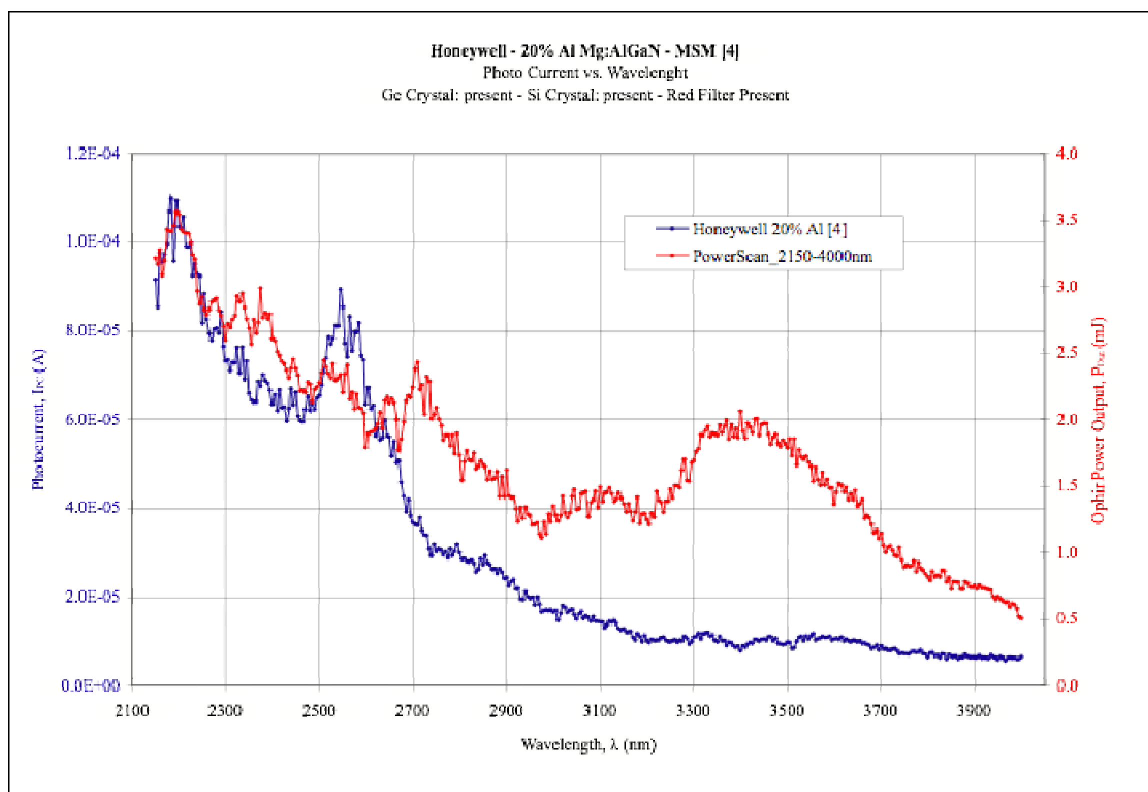

Figure 131: Plot (5 nm step) of the "raw" (not "normalized") IR photocurrent response Ni/Au MSM test structure #4 fabricated on Honeywell, Mg-doped $Al_{0.20}Ga_{0.80}N$, and the optical power output available for IR optical pumping provided by the OPO/OPA system in the Mid IR range (2100 nm to 4000 nm).

Figure 132 shows the plot (5 nm step) of the IR photocurrent response of Ni/Au MSM test structure #4 fabricated on Honeywell, Mg-doped $Al_{0.20}Ga_{0.80}N$ ("normalized" for each wavelength by the pulse energy at that wavelength) shown in Figure 130.

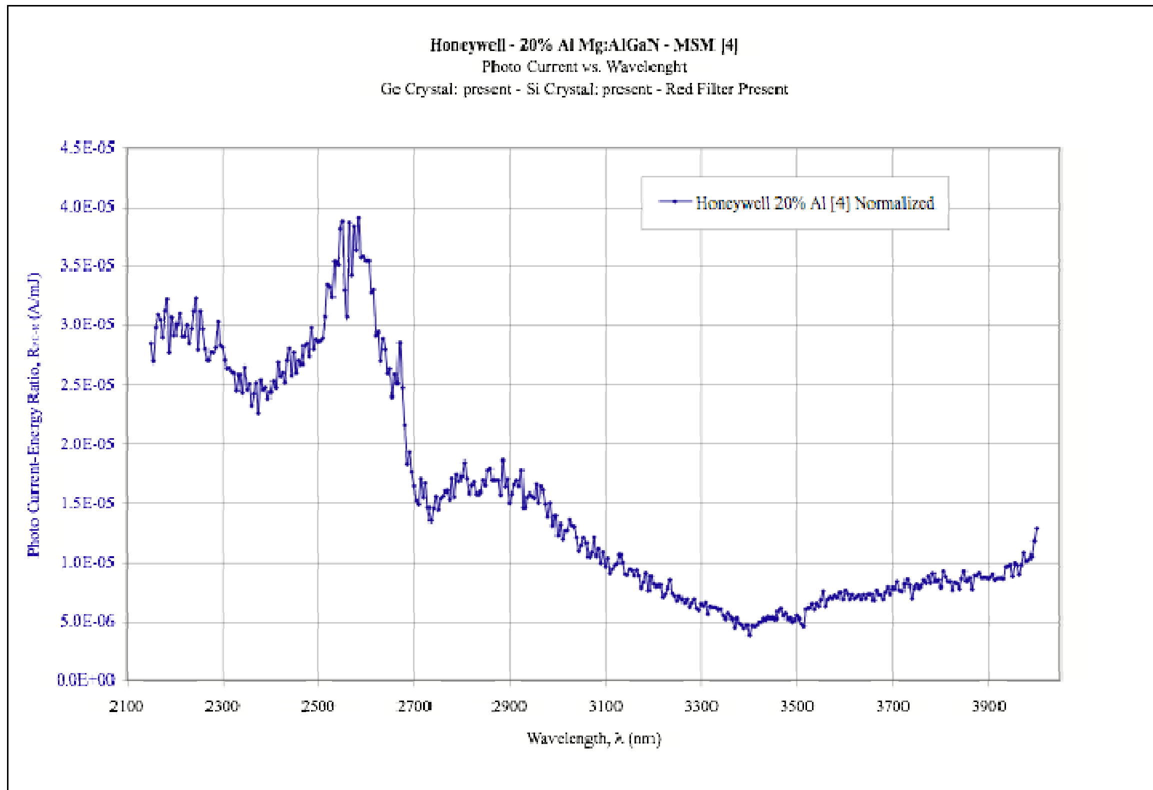

Figure 132: Plot (5 nm step) of the IR photocurrent response of Ni/Au MSM test structure #4 fabricated on Honeywell, Mg-doped $Al_{0.20}Ga_{0.80}N$ ("normalized" for each wavelength by the pulse energy at that wavelength) shown in Figure 130.

Figure 133 shows the curve fitting of the observed peak of the plot (5 nm step) of the "normalized" IR photocurrent response of test structure #4 fabricated on Honeywell, Mg-doped $Al_{0.20}Ga_{0.80}N$ shown in Figure 132.

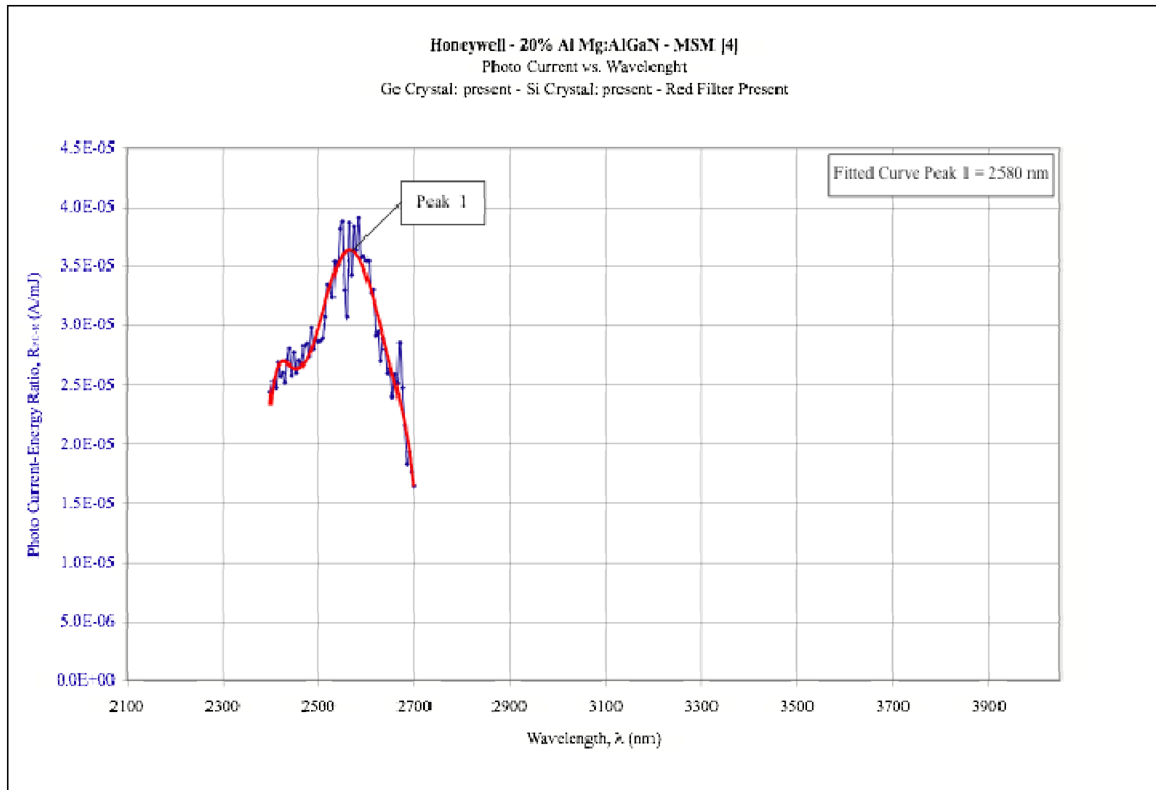

Figure 133: Curve fitting (polynomial) of the peak response observed in the plot (5 nm step) shown in Figure 132.

Figure 134 shows the plot (5 nm step) of the IR photocurrent response of Ni/Au MSM test structure #3 fabricated on Honeywell, Mg-doped $Al_{0.20}Ga_{0.80}N$ ("normalized" for each wavelength by the pulse energy at that wavelength), and the optical power output available for IR optical pumping provided by the OPO/OPA system in the Mid IR range (2100 nm to 4000 nm). A peak in the IR photocurrent response is observed at ~2525 nm (~491 meV), which is independent of the peak of the OPO/OPA system's power output located at ~2200 nm (~564 meV).

.

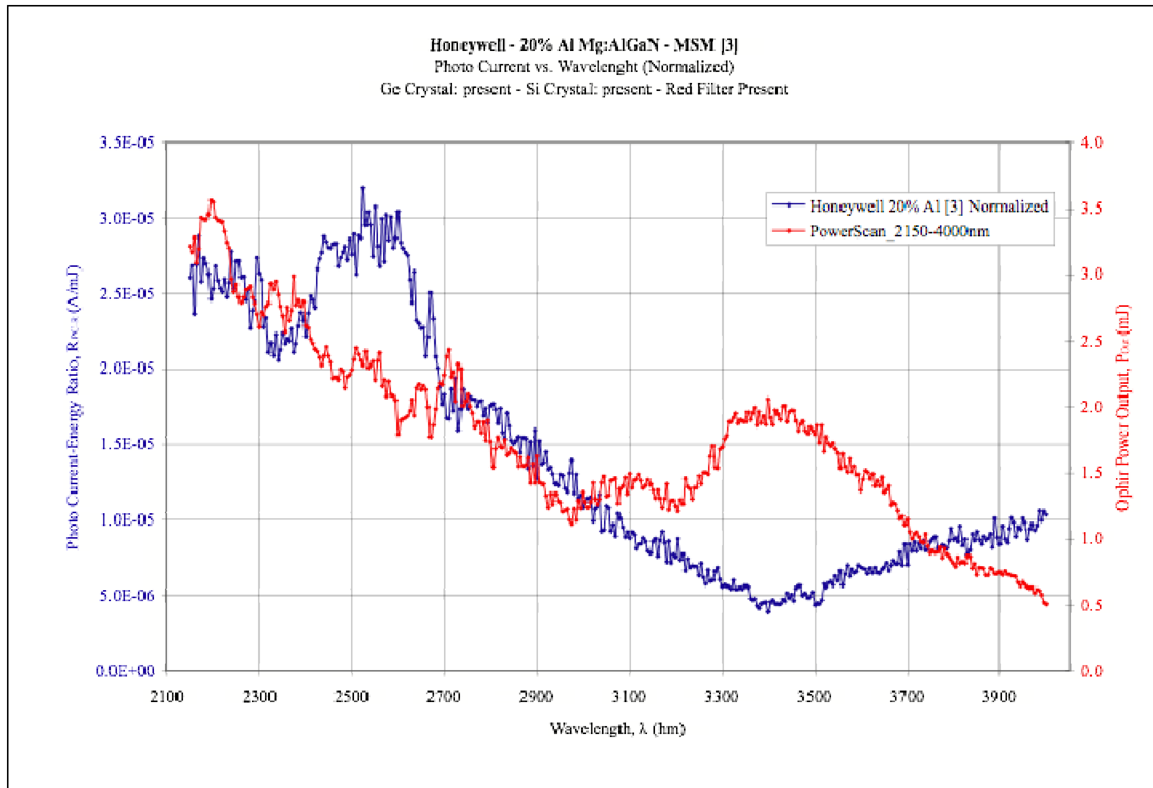

Figure 134: Plot (5 nm step) of the IR photocurrent response photocurrent response of Ni/Au MSM test structure #3 fabricated on Honeywell, Mg-doped $Al_{0.20}Ga_{0.80}N$ ("normalized" for each wavelength by the pulse energy at that wavelength), and the optical power output available for IR optical pumping provided by the OPO/OPA system in the Mid IR range (2100 nm to 4000 nm). A peak in the IR photocurrent response is observed at ~2525 nm (~491 meV), which is independent of the peak of the OPO/OPA system's power output located at ~2200 nm (~564 meV).

Figure 135 shows the "raw" (not "normalized") plot (5 nm step) of the IR photocurrent response Ni/Au MSM test structure #3 fabricated on Honeywell, Mg-doped $Al_{0.20}Ga_{0.80}N$, and the optical power output available for IR optical pumping provided by the OPO/OPA system in the Mid IR range (2100 nm to 4000 nm).

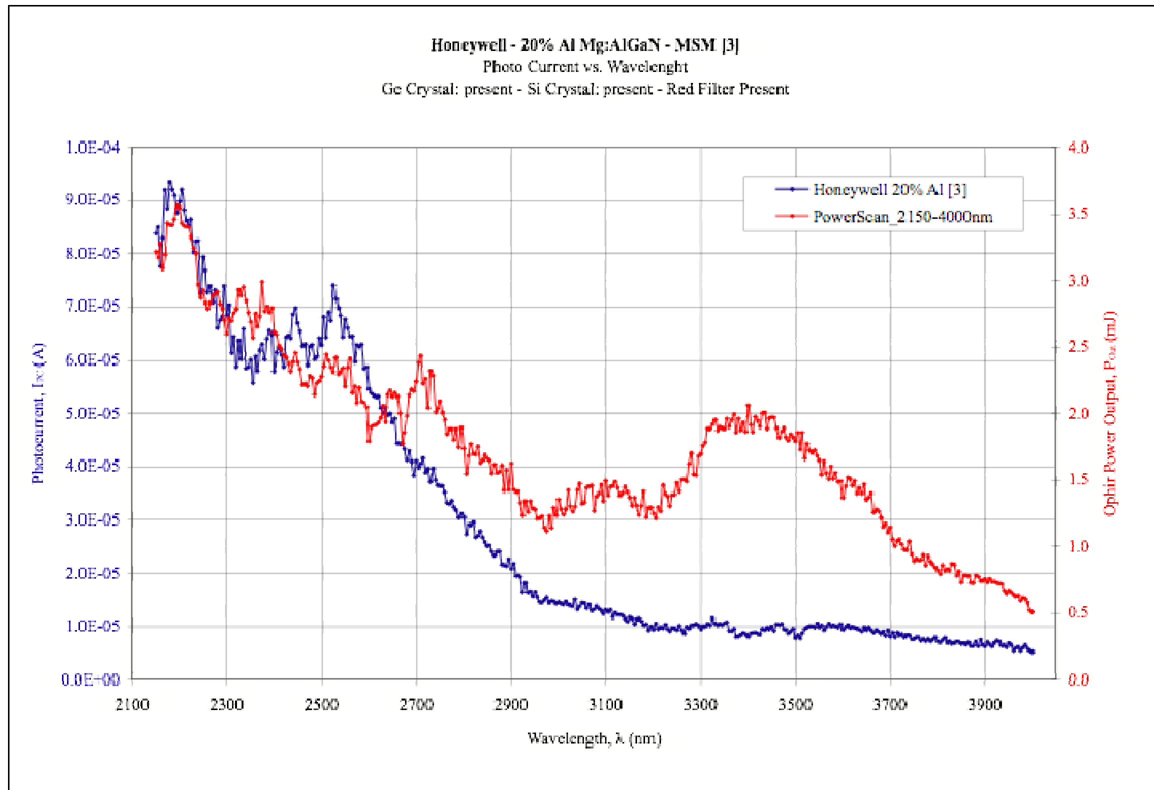

Figure 135: Plot (5 nm step) of the "raw" (not "normalized") IR photocurrent response Ni/Au MSM test structure #3 fabricated on Honeywell, Mg-doped $Al_{0.20}Ga_{0.80}N$, and the optical power output available for IR optical pumping provided by the OPO/OPA system in the Mid IR range (2100 nm to 4000 nm).

Figure 136 shows the plot (5 nm step) of the IR photocurrent response of Ni/Au MSM test structure #3 fabricated on Honeywell, Mg-doped $Al_{0.20}Ga_{0.80}N$ ("normalized" for each wavelength by the pulse energy at that wavelength) shown in Figure 134.

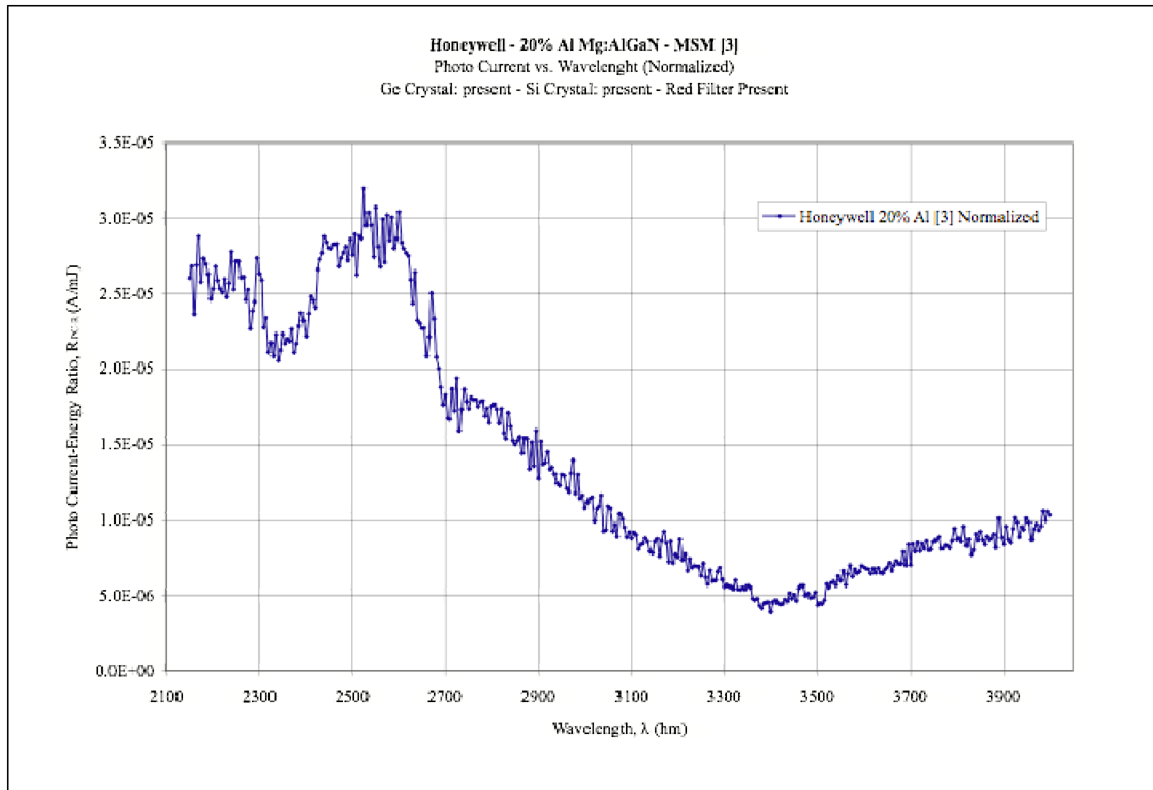

Figure 136: Plot (5 nm step) of the IR photocurrent response of Ni/Au MSM test structure #3 fabricated on Honeywell, Mg-doped $Al_{0.20}Ga_{0.80}N$ ("normalized" for each wavelength by the pulse energy at that wavelength) shown in Figure 134.

Figure 137 shows the curve fitting of the observed peak of the plot (5 nm step) of the "normalized" IR photocurrent response of test structure #3 fabricated on Honeywell, Mg-doped $Al_{0.20}Ga_{0.80}$ shown in Figure 136.

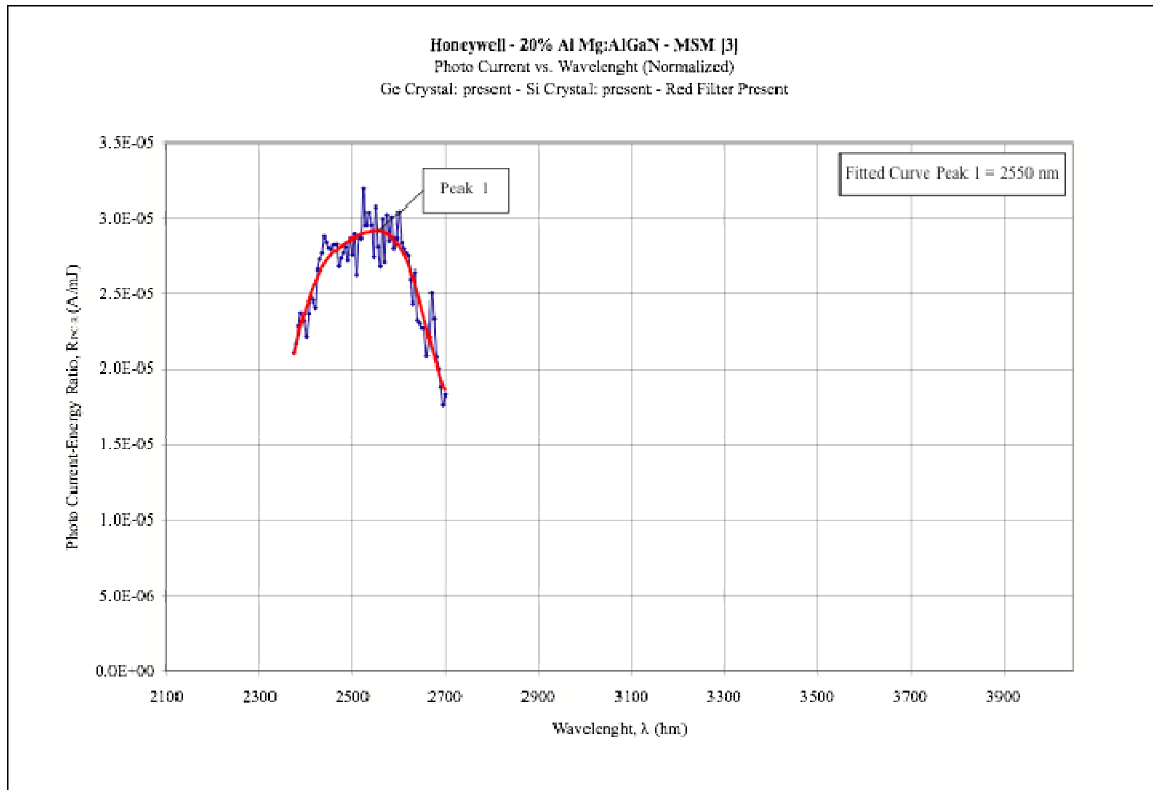

Figure 137: Curve fitting (polynomial) of the peak response observed in the plot (5 nm step) shown in Figure 136.

6.4. Infrared Photocurrent Spectra from Mg-doped $Al_{0.15}Ga_{0.85}N$ Test Structures

Figure 138 shows the plot (5 nm step) of the IR photocurrent response of Ni/Au MSM test structure #3 fabricated on Epitex, Mg-doped $Al_{0.15}Ga_{0.85}N$ ("normalized" for each wavelength by the pulse energy at that wavelength), and the optical power output available for IR optical pumping provided by the OPO/OPA system in the Mid IR range (2100 nm to 4000 nm). A peak in the IR photocurrent response is observed at ~2605 nm (~476 meV), which is independent of the peak of the OPO/OPA system's power output located at ~2200 nm (~564 meV).

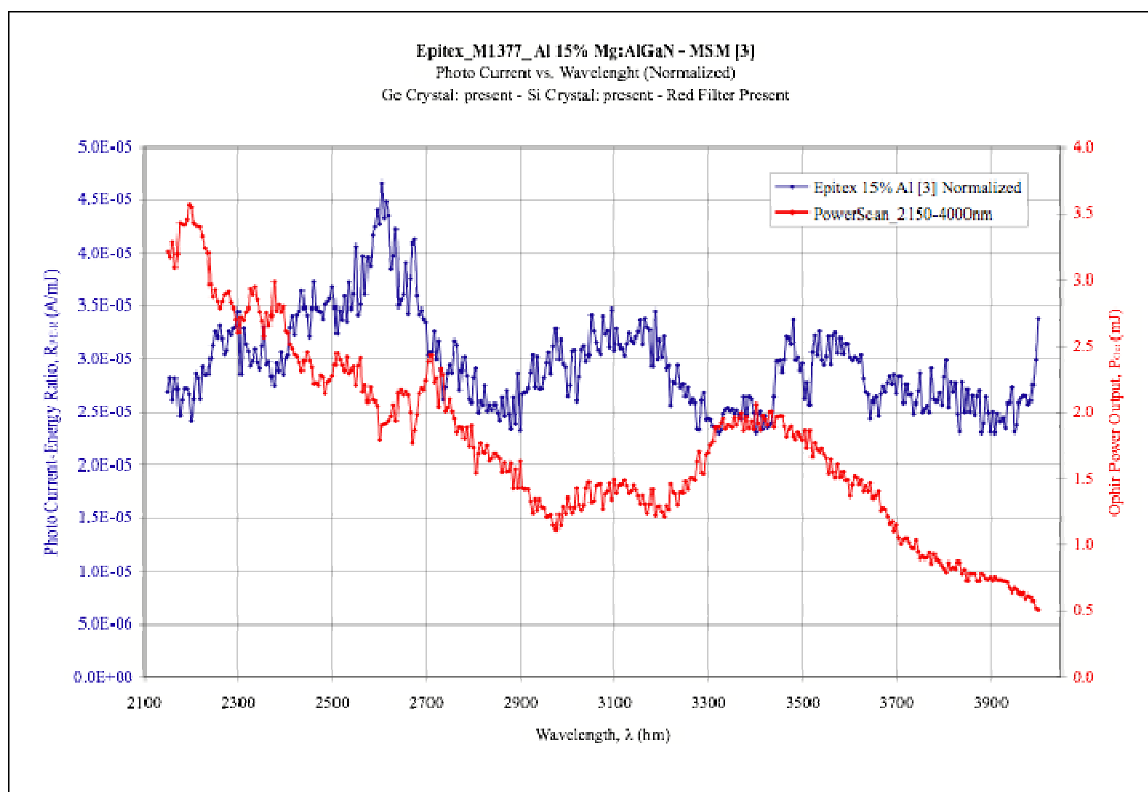

Figure 138: Plot (5 nm step) of the IR photocurrent response photocurrent response of Ni/Au MSM test structure #3 fabricated on Epitex, Mg-doped $Al_{0.15}Ga_{0.85}N$ ("normalized" for each wavelength by the pulse energy at that wavelength), and the optical power output available for IR optical pumping provided by the OPO/OPA system in the Mid IR range (2100 nm to 4000 nm). A peak in the IR photocurrent response is observed at ~2605 nm (~476 meV), which is independent of the peak of the OPO/OPA system's power output located at ~2200 nm (~564 meV).

Figure 139 shows the "raw" (not "normalized") plot (5 nm step) of the IR photocurrent response Ni/Au MSM test structure #3 fabricated on Epitex, Mg-doped $Al_{0.15}Ga_{0.85}N$, and the optical power output available for IR optical pumping provided by the OPO/OPA system in the Mid IR range (2100 nm to 4000 nm).

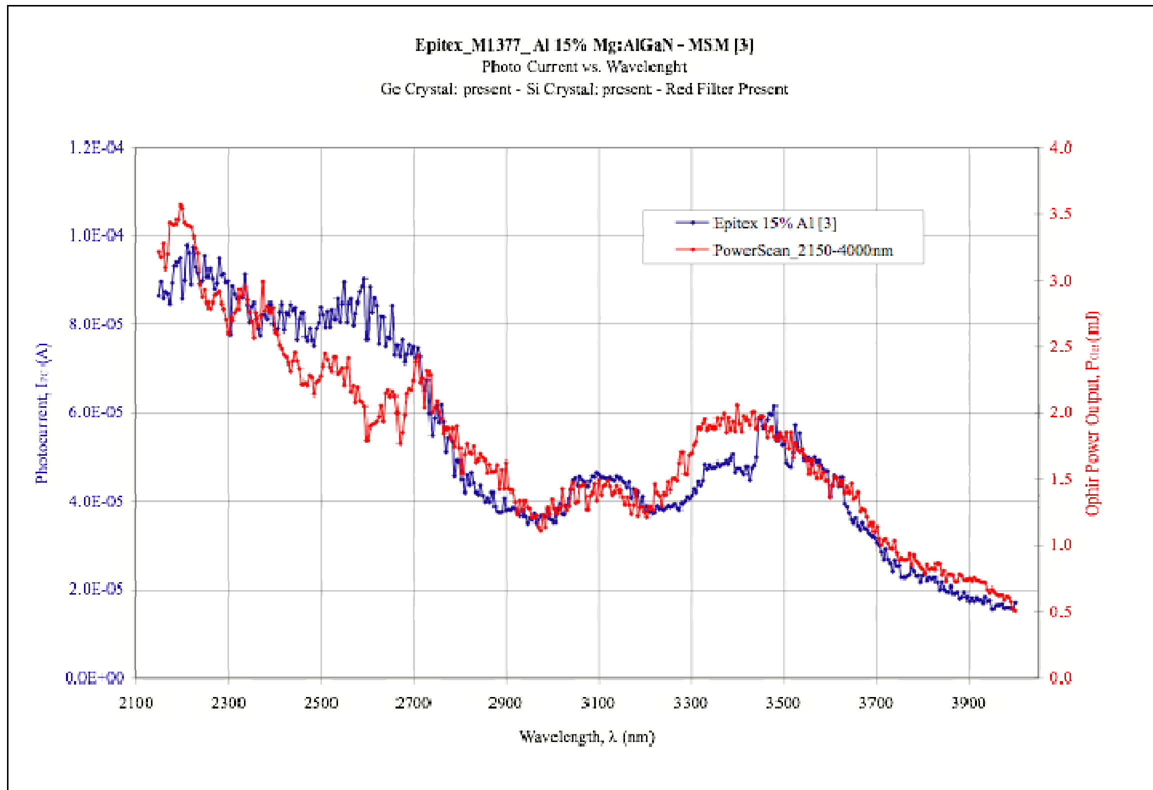

Figure 139: Plot (5 nm step) of the "raw" (not "normalized") IR photocurrent response Ni/Au MSM test structure #3 fabricated on Epitex, Mg-doped $Al_{0.15}Ga_{0.85}N$, and the optical power output available for IR optical pumping provided by the OPO/OPA system in the Mid IR range (2100 nm to 4000 nm).

Figure 140 shows the plot (5 nm step) of the IR photocurrent response of Ni/Au MSM test structure #3 fabricated on Epitex, Mg-doped $Al_{0.15}Ga_{0.85}N$ ("normalized" for each wavelength by the pulse energy at that wavelength) shown in Figure 138.

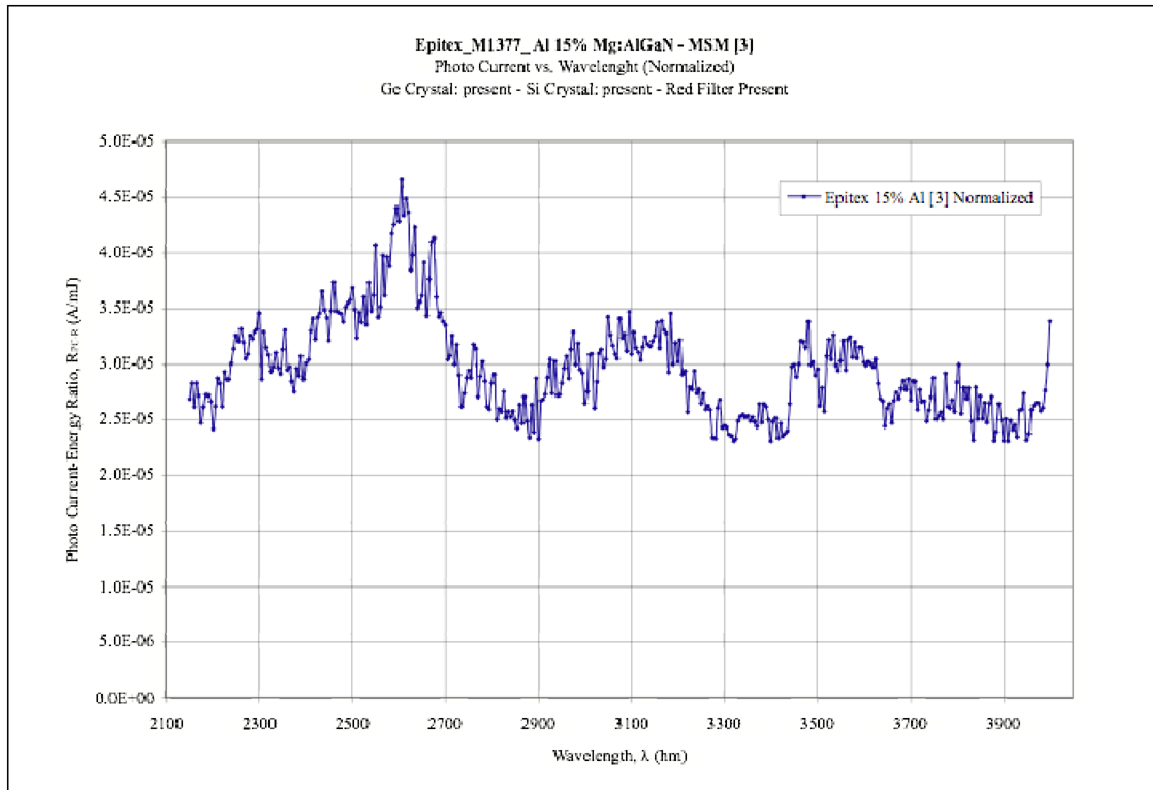

Figure 140: Plot (5nm step) of the IR photocurrent response of Ni/Au MSM test structure #3 fabricated on Epitex, Mg-doped $Al_{0.15}Ga_{0.85}N$ ("normalized" for each wavelength by the pulse energy at that wavelength) shown in Figure 138.

Figure 141 shows the curve fitting of the observed peak of the plot (5 nm step) of the "normalized" IR photocurrent response of test structure #3 fabricated on Epitex, Mg-doped $Al_{0.15}Ga_{0.85}N$ shown in Figure 140.

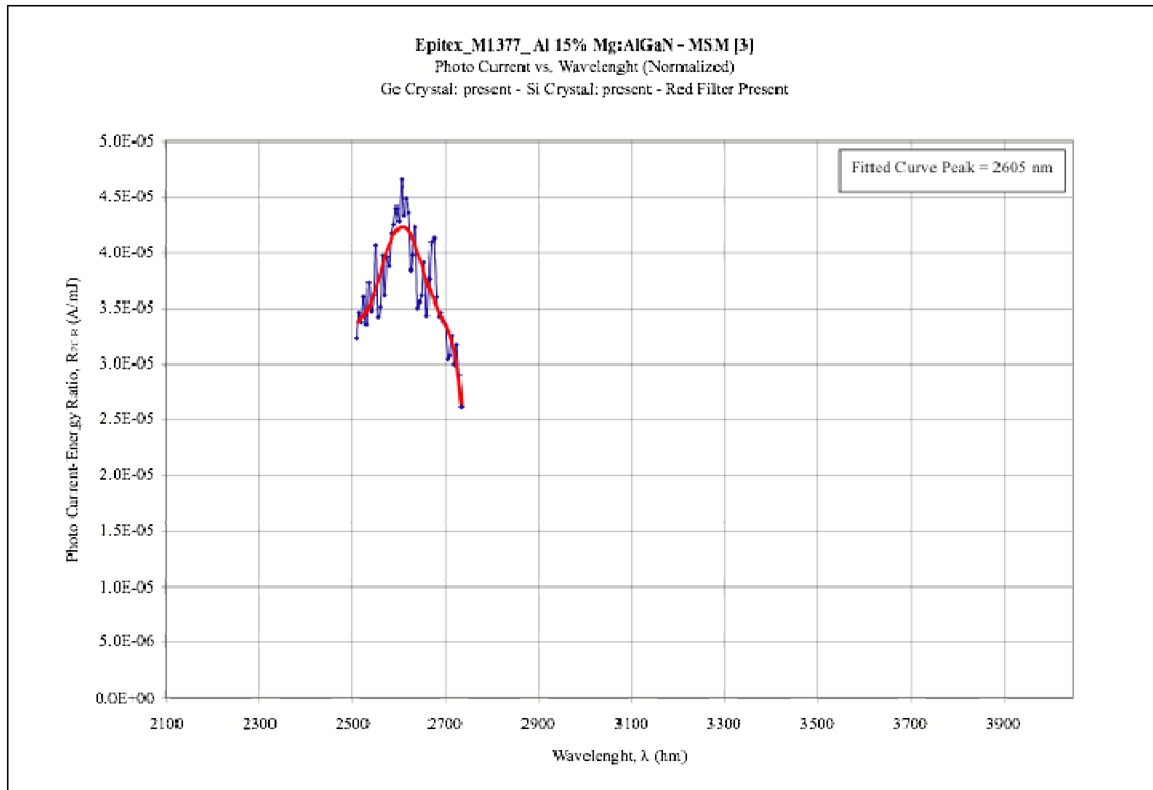

Figure 141: Curve fitting (polynomial) of the peak response observed in the plot (5 nm step) shown in Figure 140.

Figure 142 shows the plot (5 nm step) of the IR photocurrent response of Ni/Au MSM test structure #2 fabricated on Epitex, Mg-doped $Al_{0.15}Ga_{0.85}N$ ("normalized" for each wavelength by the pulse energy at that wavelength), and the optical power output available for IR optical pumping provided by the OPO/OPA system in the Mid IR range (2100 nm to 4000 nm). A peak in the IR photocurrent response is observed at ~2605 nm (~476 meV), which is independent of the peak of the OPO/OPA system's power output located at ~2200 nm (~564 meV).

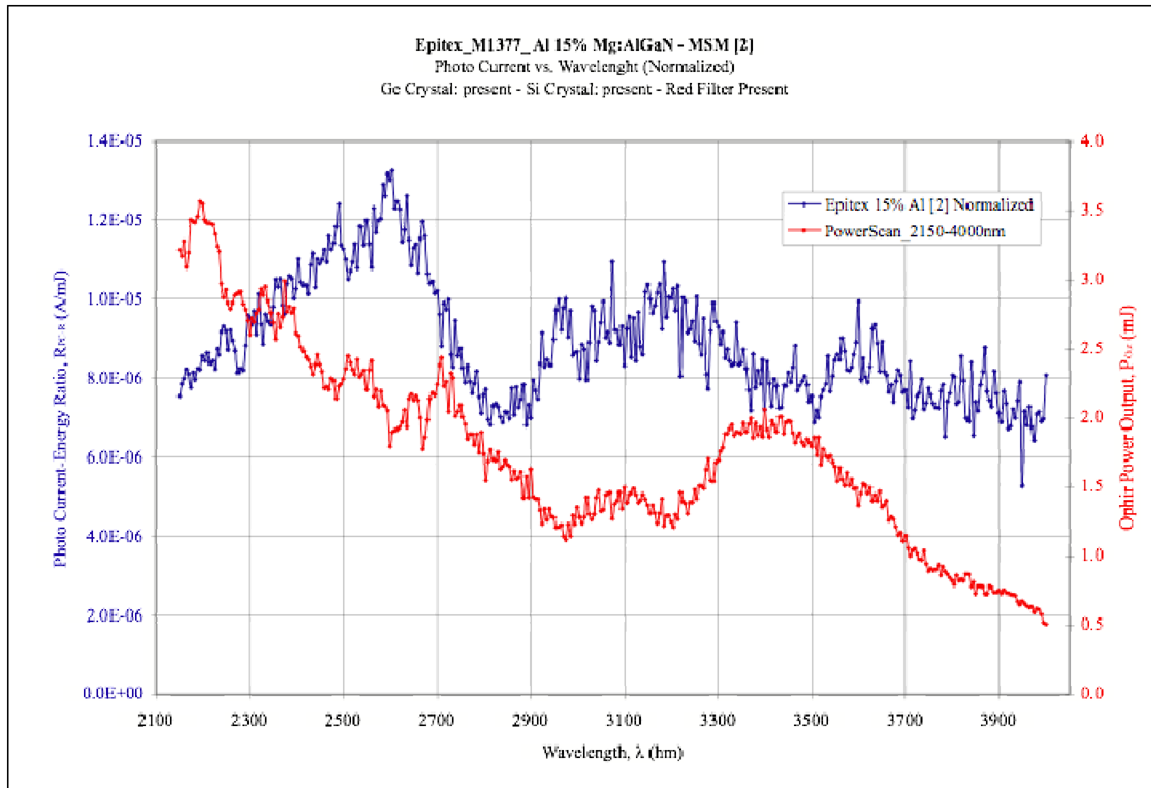

Figure 142: Plot (5 nm step) of the IR photocurrent response photocurrent response of Ni/Au MSM test structure #2 fabricated on Epitex, Mg-doped $Al_{0.15}Ga_{0.85}N$ ("normalized" for each wavelength by the pulse energy at that wavelength), and the optical power output available for IR optical pumping provided by the OPO/OPA system in the Mid IR range (2100 nm to 4000 nm). A peak in the IR photocurrent response is observed at ~2605 nm (~476 meV), which is independent of the peak of the OPO/OPA system's power output located at ~2200 nm (~564 meV).

Figure 143 shows the "raw" (not "normalized") plot (5 nm step) of the IR photocurrent response Ni/Au MSM test structure #2 fabricated on Epitex, Mg-doped $Al_{0.15}Ga_{0.85}N$, and the optical power output available for IR optical pumping provided by the OPO/OPA system in the Mid IR range (2100 nm to 4000 nm).

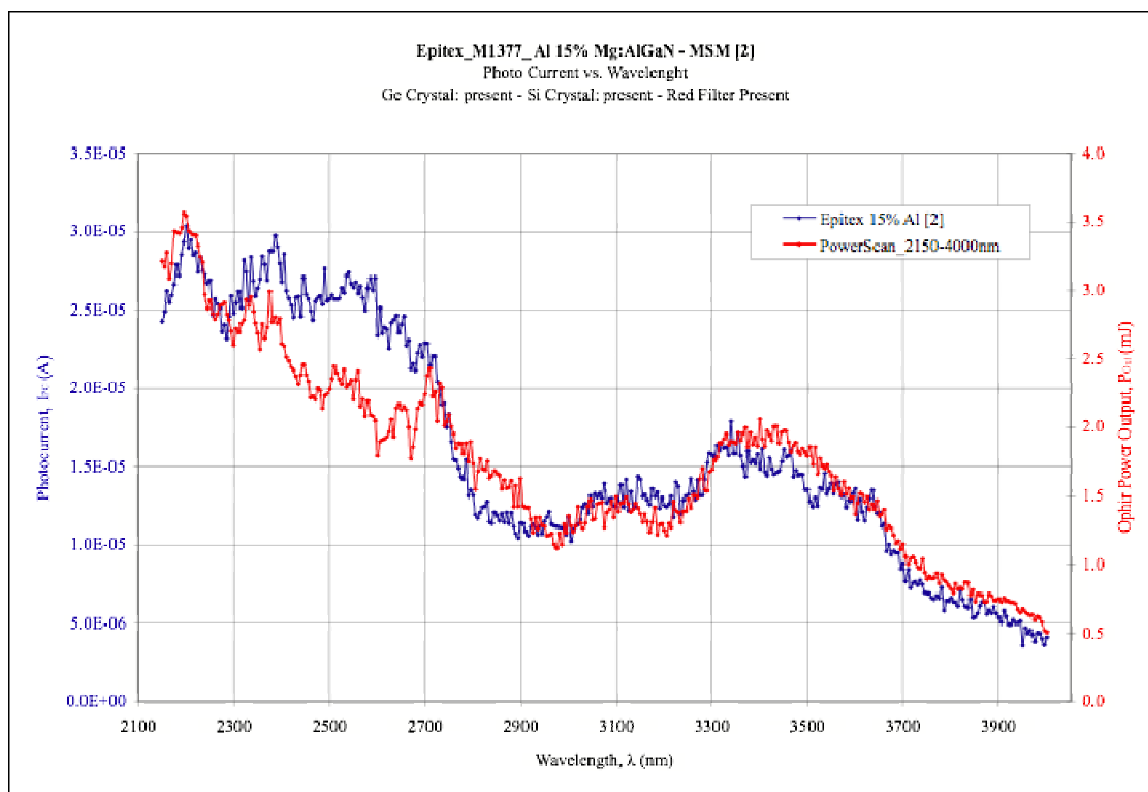

Figure 143: Plot (5 nm step) of the "raw" (not "normalized") IR photocurrent response Ni/Au MSM test structure #2 fabricated on Epitex, Mg-doped $Al_{0.15}Ga_{0.85}N$, and the optical power output available for IR optical pumping provided by the OPO/OPA system in the Mid IR range (2100 nm to 4000 nm).

Figure 144 shows the plot (5 nm step) of the IR photocurrent response of Ni/Au MSM test structure #2 fabricated on Epitex, Mg-doped $Al_{0.15}Ga_{0.85}N$ ("normalized" for each wavelength by the pulse energy at that wavelength) shown in Figure 142.

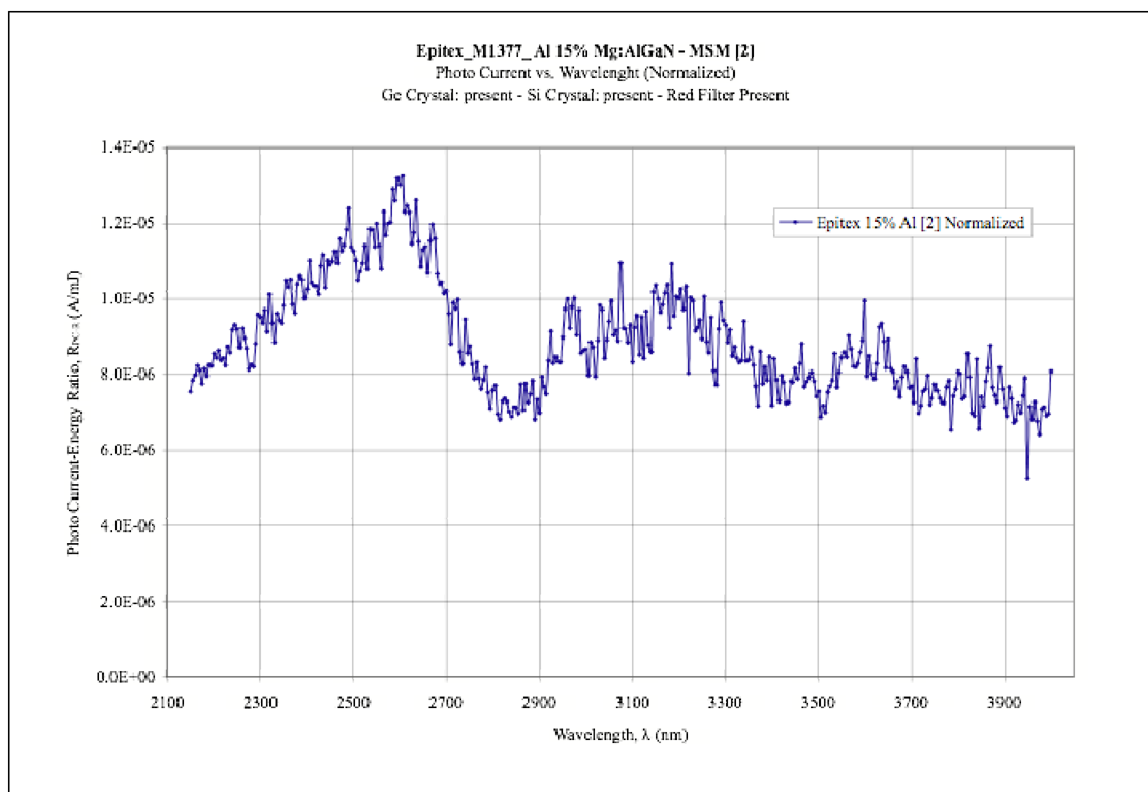

Figure 144: Plot (5nm step) of the IR photocurrent response of Ni/Au MSM test structure #2 fabricated on Epitex, Mg-doped $Al_{0.15}Ga_{0.85}N$ ("normalized" for each wavelength by the pulse energy at that wavelength) shown in Figure 142.

Figure 145 shows the curve fitting of the observed peak of the plot (5 nm step) of the "normalized" IR photocurrent response of test structure #2 fabricated on Epitex, Mg-doped $Al_{0.15}Ga_{0.85}N$ shown in Figure 144.

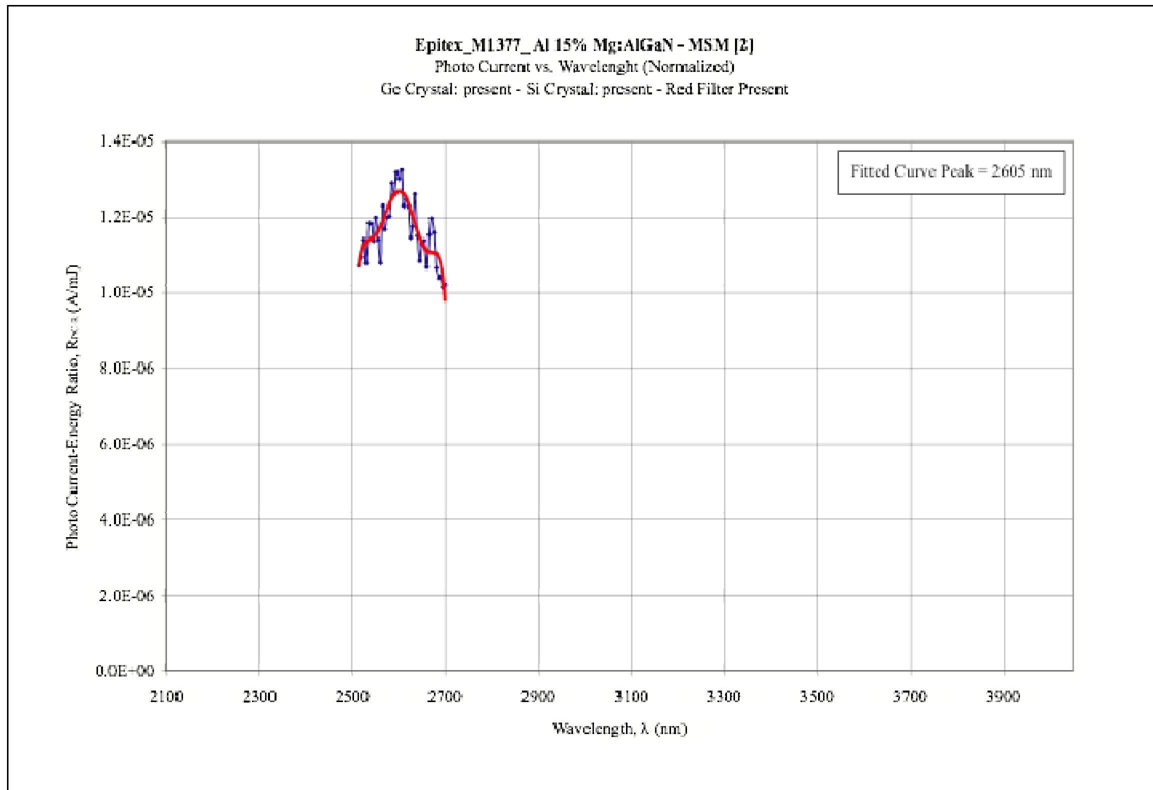

Figure 145: Curve fitting (polynomial) of the peak response observed in the plot (5 nm step) shown in Figure 144.

6.5. Infrared Photocurrent Spectra from Mg-doped GaN Test Structures

Figure 146 shows the plot (5 nm step) of the IR photocurrent response of Ni/Au MSM test structure #1 fabricated on Honeywell, Mg-doped GaN ("normalized" for each wavelength by the pulse energy at that wavelength), and the optical power output available for IR optical pumping provided by the OPO/OPA system in the Mid IR range (2100 nm to 4000 nm). A primary peak in the IR photocurrent response is observed at ~3150 nm (~394 meV), and a secondary peak is observed at ~2670 nm (~464 meV); both are independent of the peak of the OPO/OPA system's power output located at ~2200 nm (~564 meV).

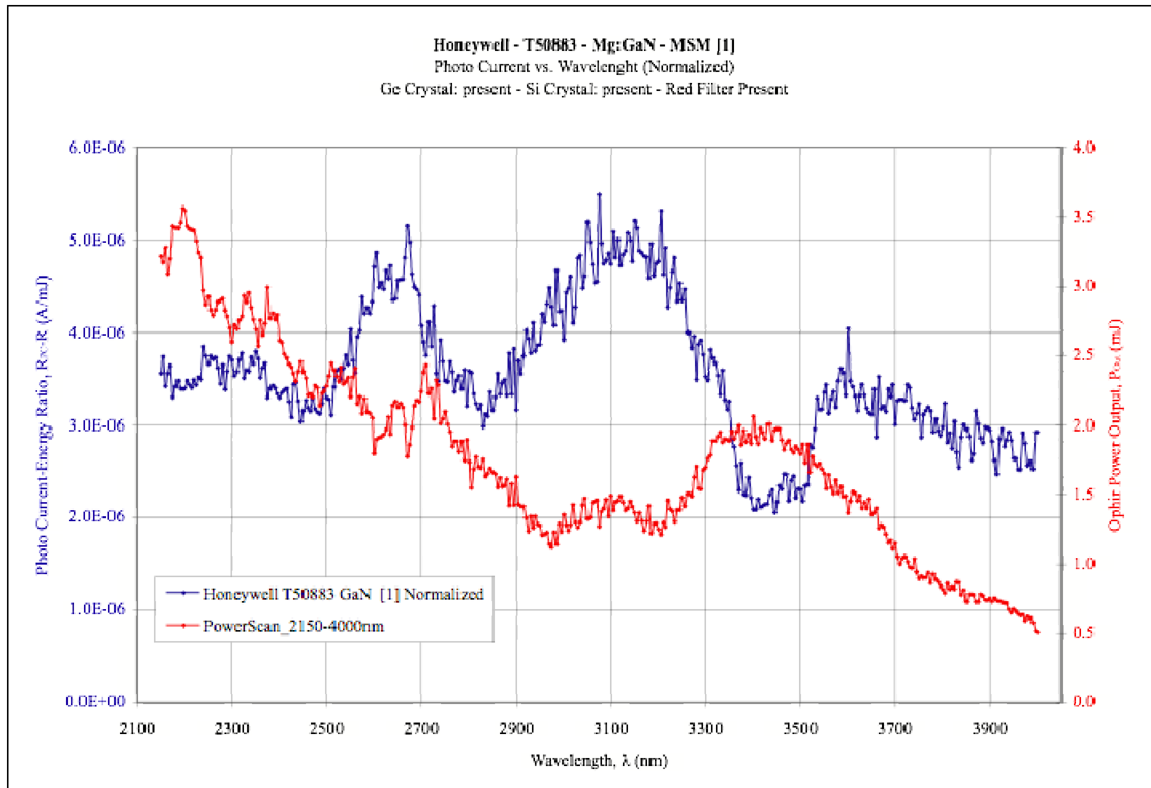

Figure 146: Plot (5 nm step) of the IR photocurrent response photocurrent response of Ni/Au MSM test structure #1 fabricated on Honeywell, Mg-doped GaN ("normalized" for each wavelength by the pulse energy at that wavelength), and the optical power output available for IR optical pumping provided by the OPO/OPA system in the Mid IR range (2100 nm to 4000 nm). A primary peak in the IR photocurrent response is observed at ~3150 nm (~394 meV), and a secondary peak is observed at ~2670 nm (~464 meV); both are independent of the peak of the OPO/OPA system's power output located at ~2200 nm (~564 meV).

Figure 147 shows the "raw" (not "normalized") plot (5 nm step) of the IR photocurrent response Ni/Au MSM test structure #1 fabricated on Honeywell, Mg-doped GaN, and the optical power output available for IR optical pumping provided by the OPO/OPA system in the Mid IR range (2100 nm to 4000 nm).

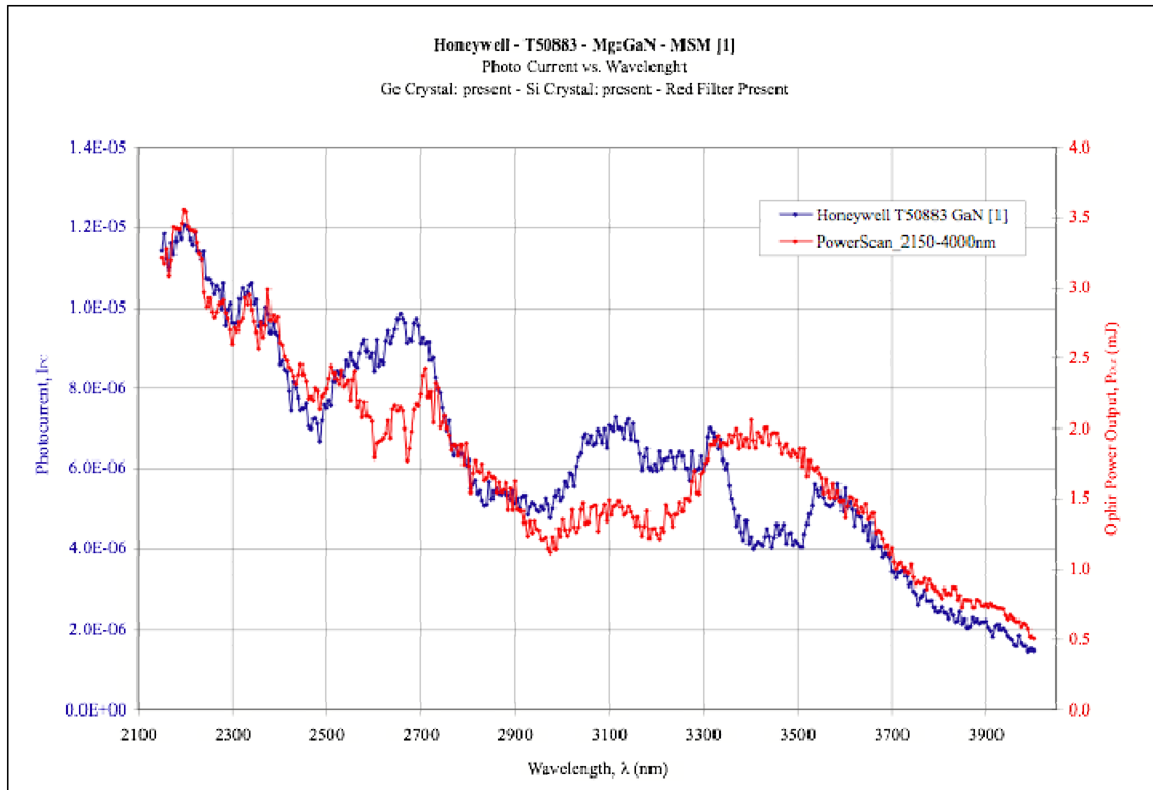

Figure 147: Plot (5 nm step) of the "raw" (not "normalized") IR photocurrent response Ni/Au MSM test structure #1 fabricated on Honeywell, Mg-doped GaN, and the optical power output available for IR optical pumping provided by the OPO/OPA system in the Mid IR range (2100 nm to 4000 nm).

Figure 148 shows the plot (5 nm step) of the IR photocurrent response of Ni/Au MSM test structure #1 fabricated on Honeywell, Mg-doped GaN ("normalized" for each wavelength by the pulse energy at that wavelength) shown in Figure 146

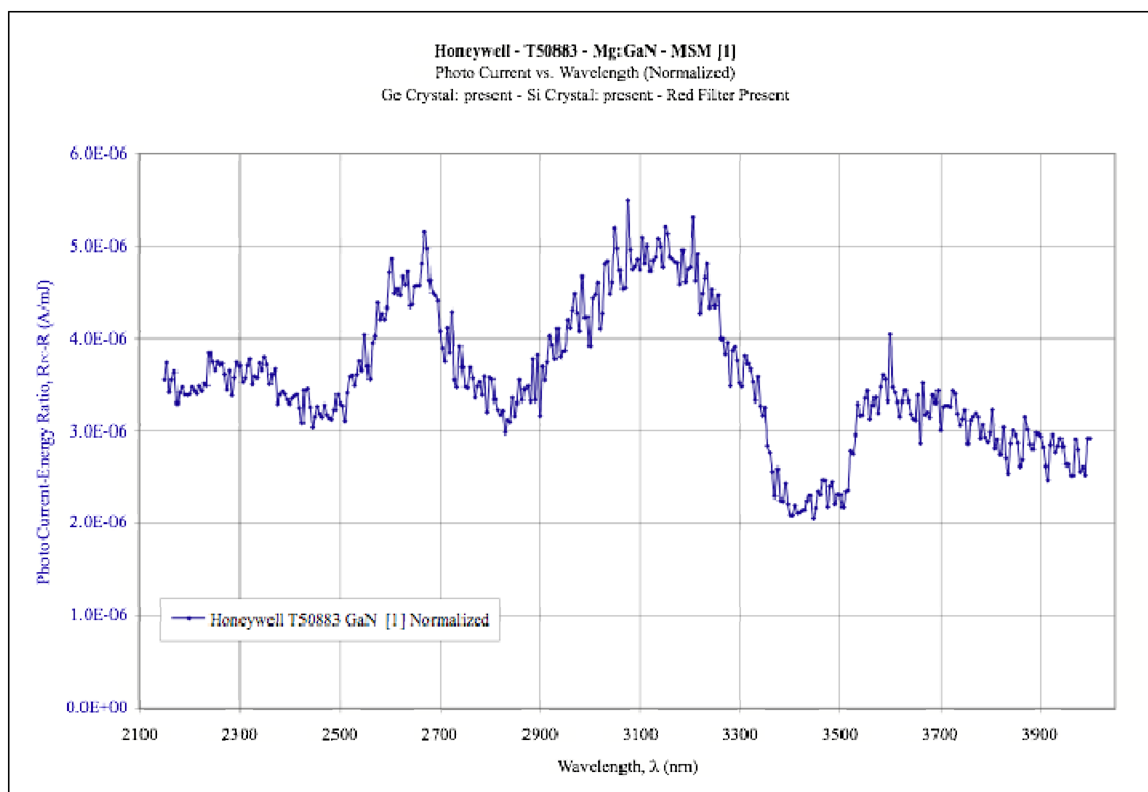

Figure 148: Plot (5nm step) of the IR photocurrent response of Ni/Au MSM test structure #1 fabricated on Honeywell, Mg-doped GaN ("normalized" for each wavelength by the pulse energy at that wavelength) shown in Figure 146.

Figure 149 shows the curve fitting of the observed peak of the plot (5 nm step) of the "normalized" IR photocurrent response of test structure #1 fabricated on Honeywell, Mg-doped GaN shown in Figure 148.

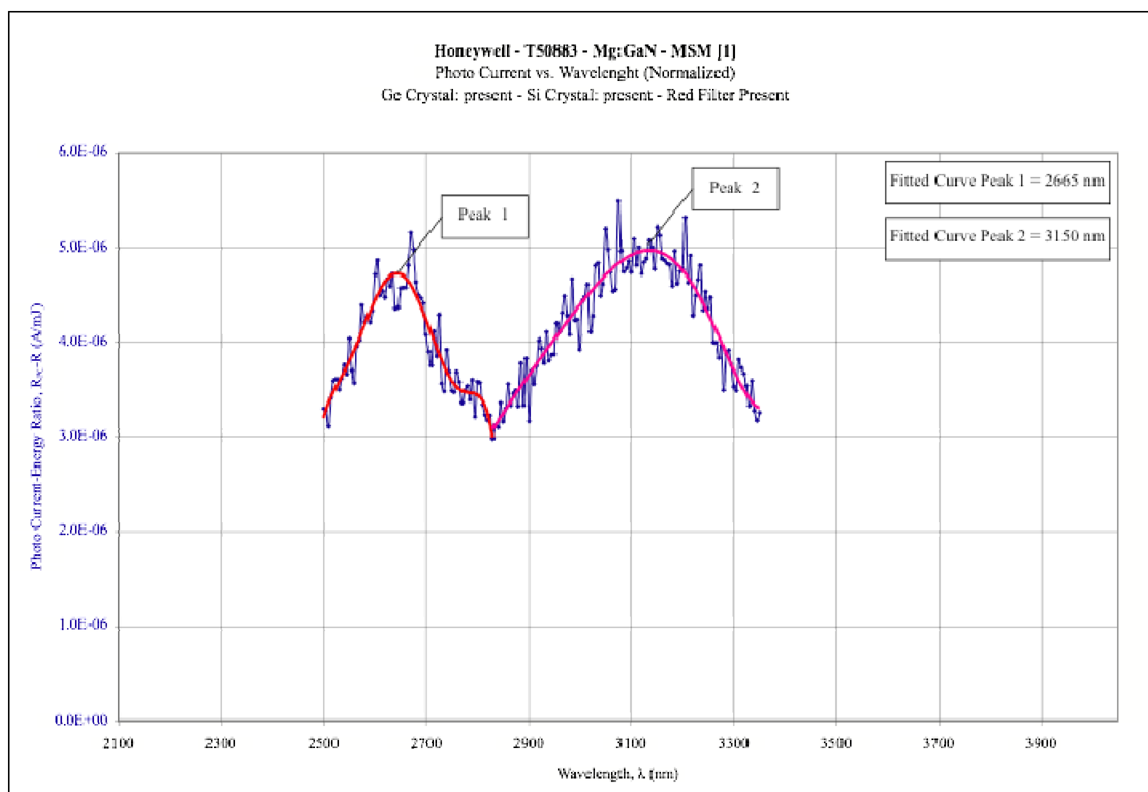

Figure 149: Curve fitting (polynomial) of the peak response observed in the plot (5 nm step) shown in Figure 148.

Figure 150 shows the plot (5 nm step) of the IR photocurrent response of Ni/Au MSM test structure #6 fabricated on Honeywell, Mg-doped GaN ("normalized" for each wavelength by the pulse energy at that wavelength), and the optical power output available for IR optical pumping provided by the OPO/OPA system in the Mid IR range (2100 nm to 4000 nm). A primary peak in the IR photocurrent response is observed at ~3050 nm (~407 meV), and a secondary peak is observed at ~2700 nm (~459 meV); both are independent of the peak of the OPO/OPA system's power output located at ~2200 nm (~564 meV).

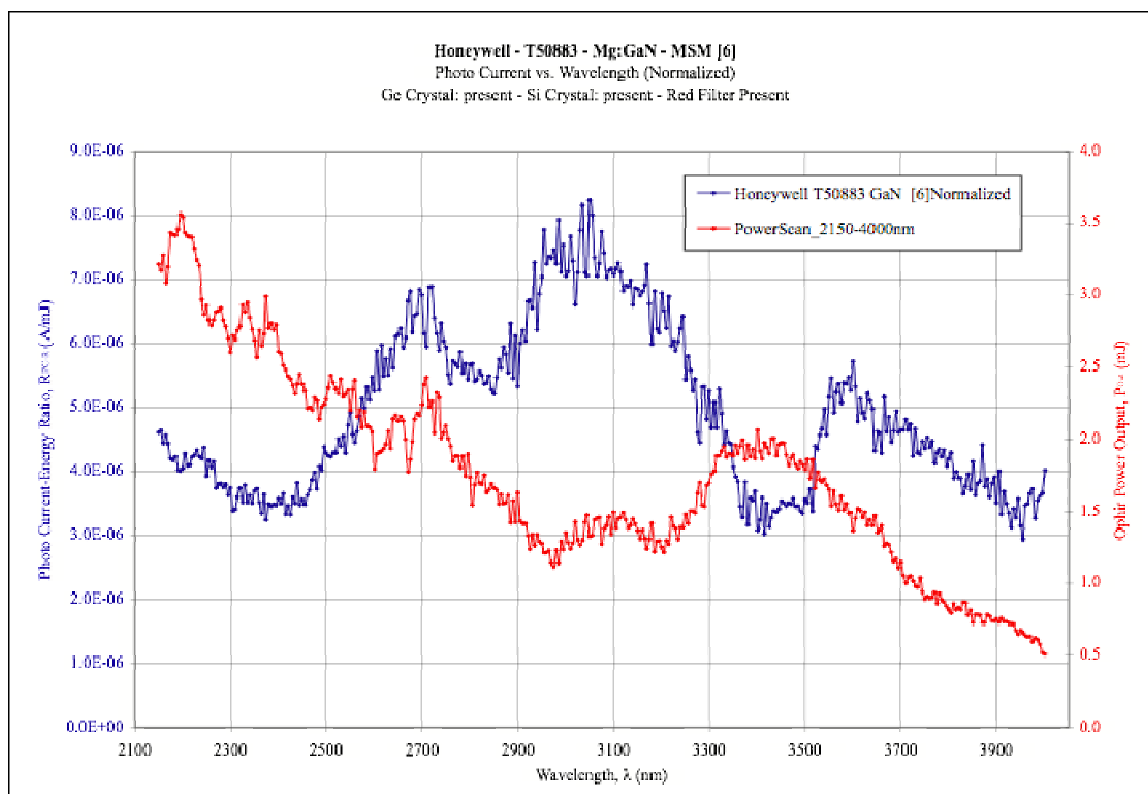

Figure 150: Plot (5 nm step) of the IR photocurrent response photocurrent response of Ni/Au MSM test structure #6 fabricated on Honeywell, Mg-doped GaN ("normalized" for each wavelength by the pulse energy at that wavelength), and the optical power output available for IR optical pumping provided by the OPO/OPA system in the Mid IR range (2100 nm to 4000 nm). A primary peak in the IR photocurrent response is observed at ~3050 nm (~407 meV), and a secondary peak is observed at ~2700 nm (~459 meV); both are independent of the peak of the OPO/OPA system's power output located at ~2200 nm (~564 meV).

Figure 151 shows the "raw" (not "normalized") plot (5 nm step) of the IR photocurrent response Ni/Au MSM test structure #6 fabricated on Honeywell, Mg-doped GaN, and the optical power output available for IR optical pumping provided by the OPO/OPA system in the Mid IR range (2100 nm to 4000 nm).

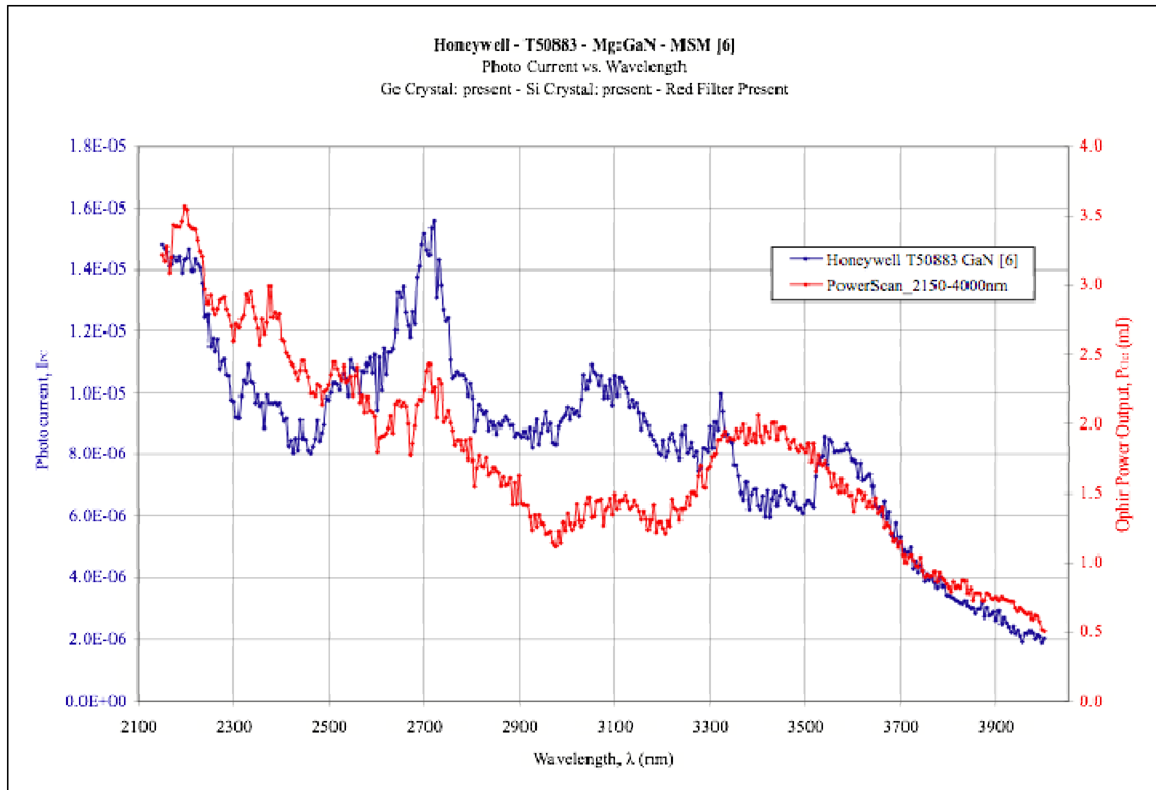

Figure 151: Plot (5 nm step) of the "raw" (not "normalized") IR photocurrent response Ni/Au MSM test structure #6 fabricated on Honeywell, Mg-doped GaN, and the optical power output available for IR optical pumping provided by the OPO/OPA system in the Mid IR range (2100 nm to 4000 nm).

Figure 152 shows the plot (5 nm step) of the IR photocurrent response of Ni/Au MSM test structure #6 fabricated on Honeywell, Mg-doped GaN ("normalized" for each wavelength by the pulse energy at that wavelength) shown in Figure 150.

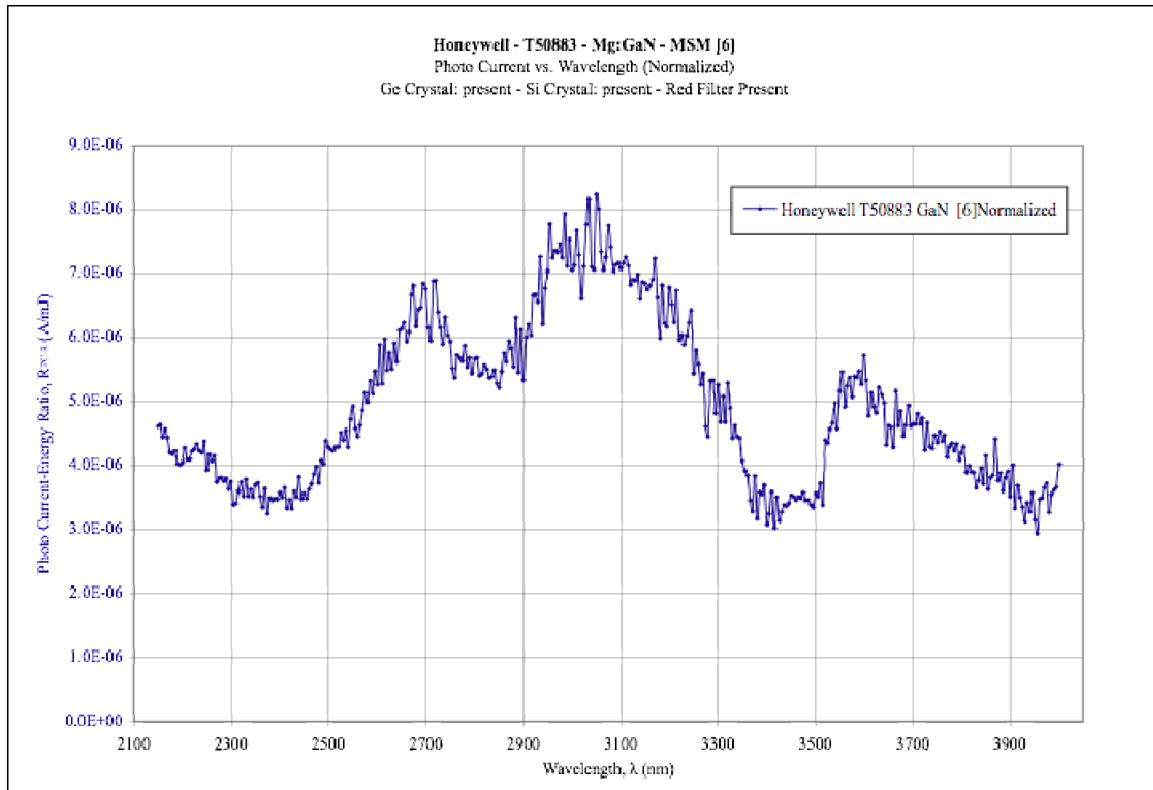

Figure 152: Plot (5nm step) of the IR photocurrent response of Ni/Au MSM test structure #6 fabricated on Honeywell, Mg-doped GaN ("normalized" for each wavelength by the pulse energy at that wavelength) shown in Figure 150.

Figure 154 shows the curve fitting of the observed peak of the plot (5 nm step) of the "normalized" IR photocurrent response of test structure #6 fabricated on Honeywell, Mg-doped GaN shown in Figure 152.

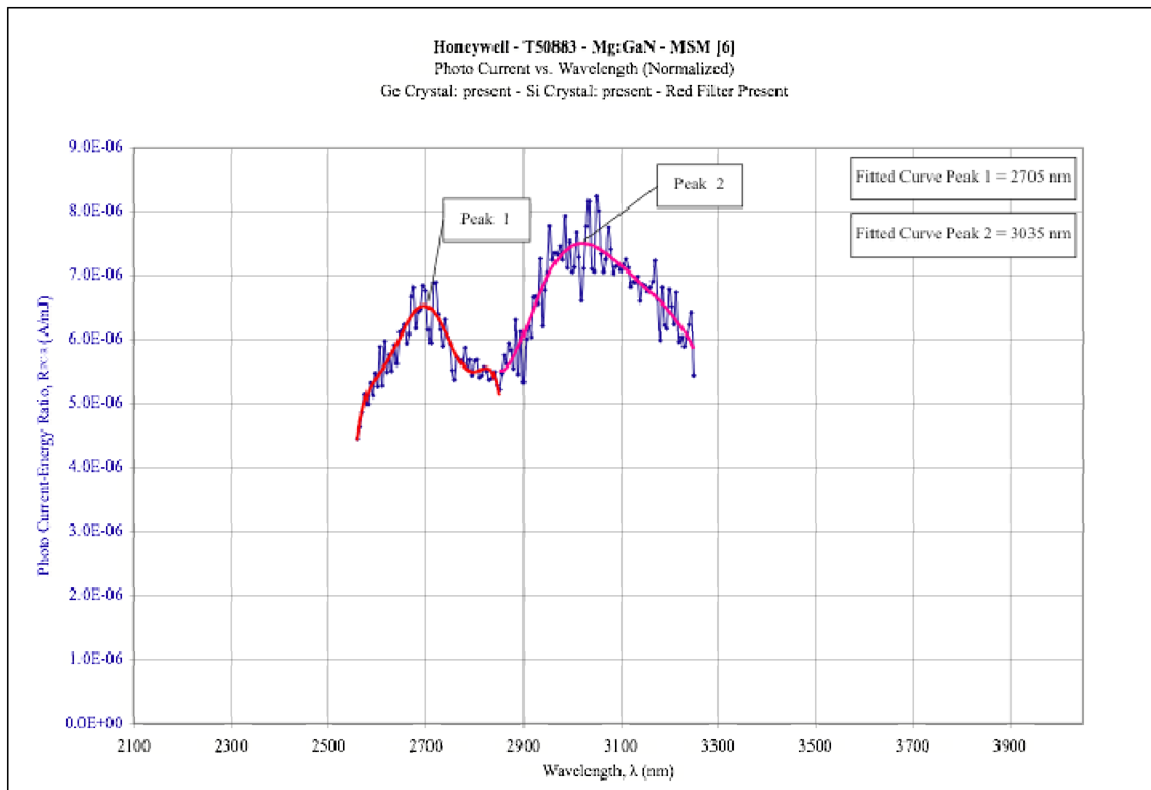

Figure 153: Curve fitting (polynomial) of the peak response observed in the high-resolution plot (5 nm step) shown in Figure 152.

Figure 154 shows the plot (5 nm step) of the IR photocurrent response of Ni/Au MSM test structure #7 fabricated on ATMI, Mg-doped GaN ("normalized" for each wavelength by the pulse energy at that wavelength), and the optical power output available for IR optical pumping provided by the OPO/OPA system in the Mid IR range (2100 nm to 4000 nm). A peak in the IR photocurrent response is observed at ~3170 nm (~391 meV), and a secondary peak is observed at ~2600 nm (~477 meV); both are independent of the peak of the OPO/OPA system's power output located at ~2200 nm (~564 meV).

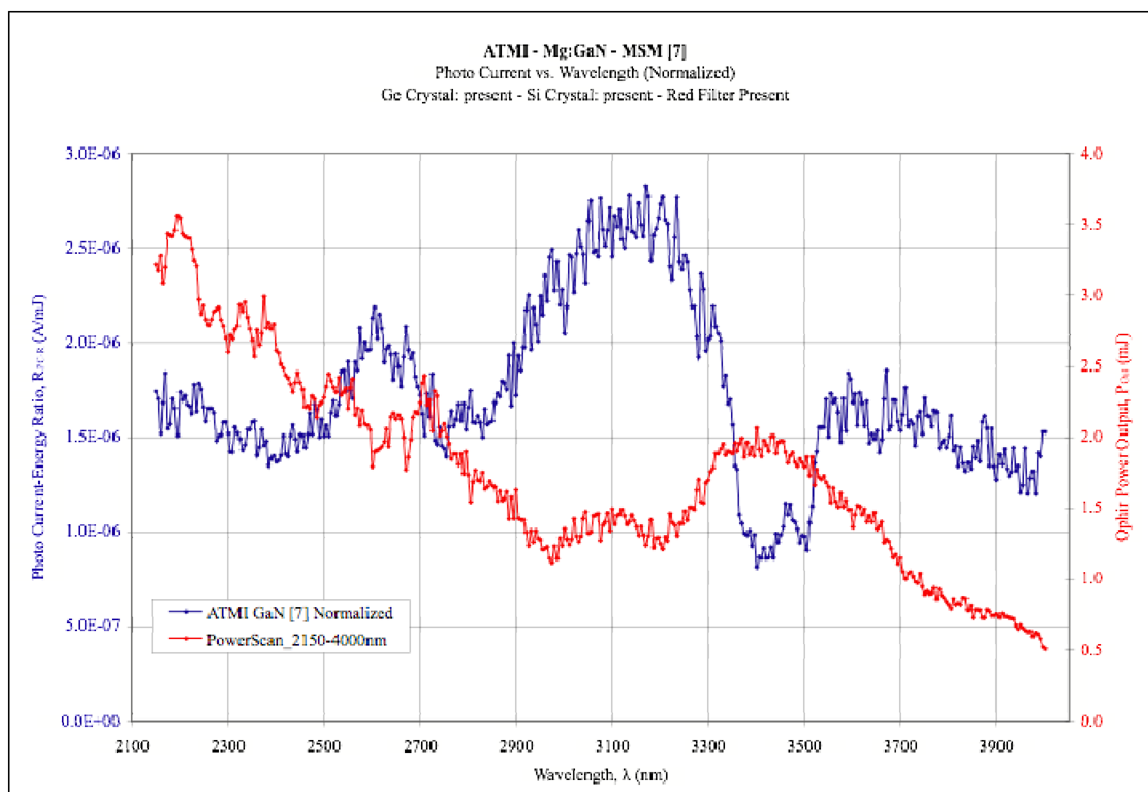

Figure 154: Plot (5 nm step) of the IR photocurrent response photocurrent response of Ni/Au MSM test structure #7 fabricated on ATMI, Mg-doped GaN ("normalized" for each wavelength by the pulse energy at that wavelength), and the optical power output available for IR optical pumping provided by the OPO/OPA system in the Mid IR range (2100 nm to 4000 nm). A peak in the IR photocurrent response is observed at ~3170 nm (~476 meV), and a second peak is observed at ~2600 nm (~477 meV); both are independent of the peak of the OPO/OPA system's power output located at 2200 nm (~564 meV).

Figure 155 shows the "raw" (not "normalized") plot (5 nm step) of the IR photocurrent response Ni/Au MSM test structure #7 fabricated on ATMI, Mg-doped GaN, and the optical power output available for IR optical pumping provided by the OPO/OPA system in the Mid IR range (2100 nm to 4000 nm).

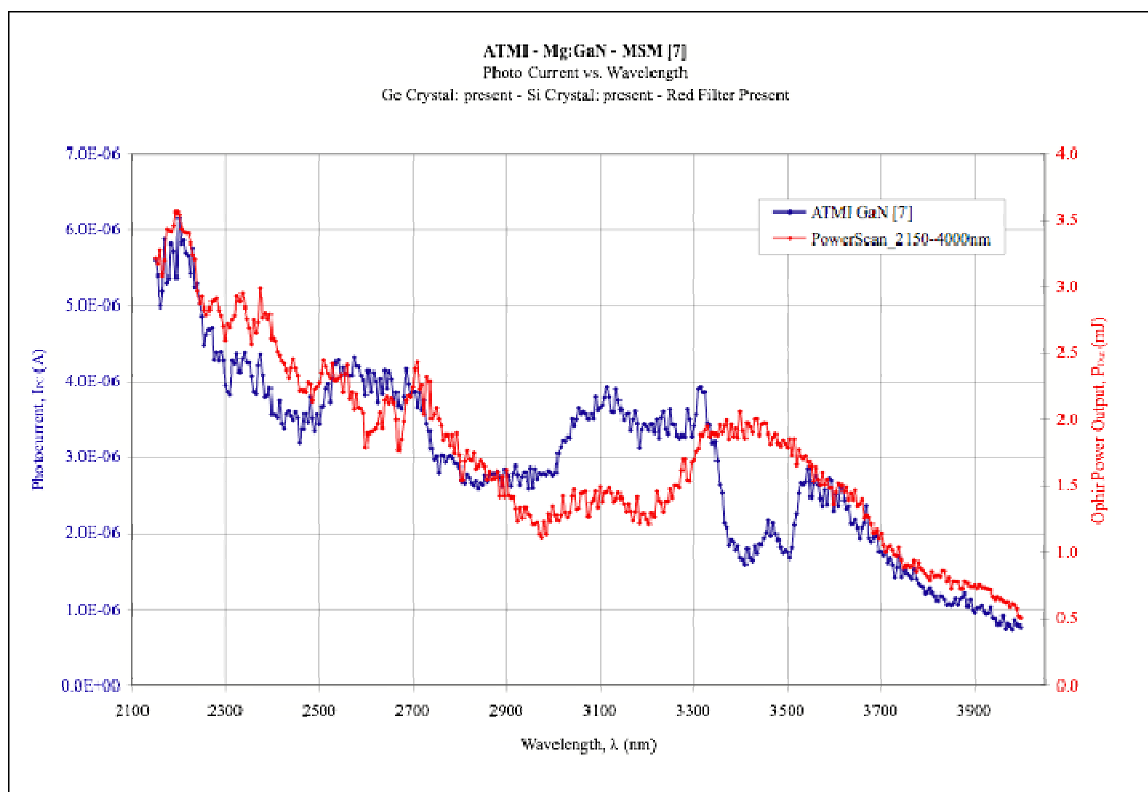

Figure 155: Plot (5 nm step) of the "raw" (not "normalized") IR photocurrent response Ni/Au MSM test structure #7 fabricated on ATMI, Mg-doped GaN, and the optical power output available for IR optical pumping provided by the OPO/OPA system in the Mid IR range (2100 nm to 4000 nm).

Figure 156 shows the plot (5 nm step) of the IR photocurrent response of Ni/Au MSM test structure #7 fabricated on ATMI, Mg-doped GaN ("normalized" for each wavelength by the pulse energy at that wavelength) shown in Figure 154.

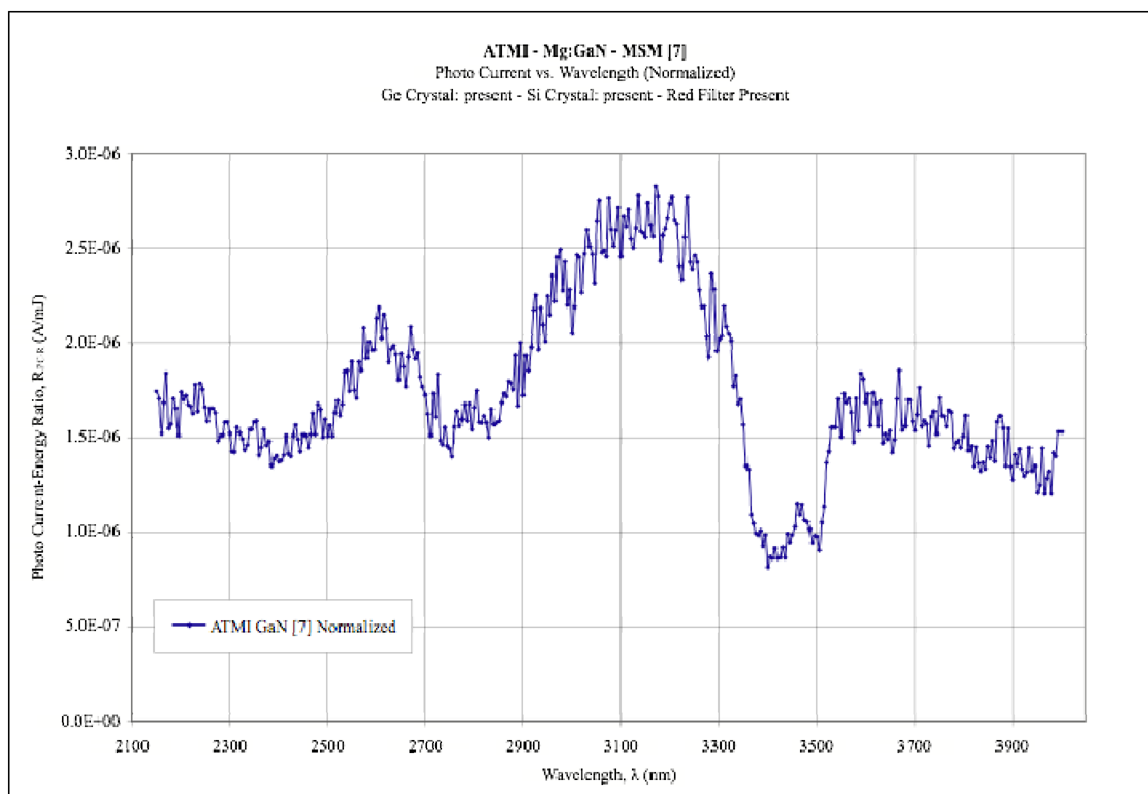

Figure 156: Plot (5nm step) of the IR photocurrent response of Ni/Au MSM test structure #2 fabricated on ATMI, Mg-doped GaN ("normalized" for each wavelength by the pulse energy at that wavelength) shown in Figure 154.

Figure 157 shows the curve fitting of the observed peak of the plot (5 nm step) of the "normalized" IR photocurrent response of test structure #7 fabricated on ATMI, Mg-doped GaN shown in Figure 156.

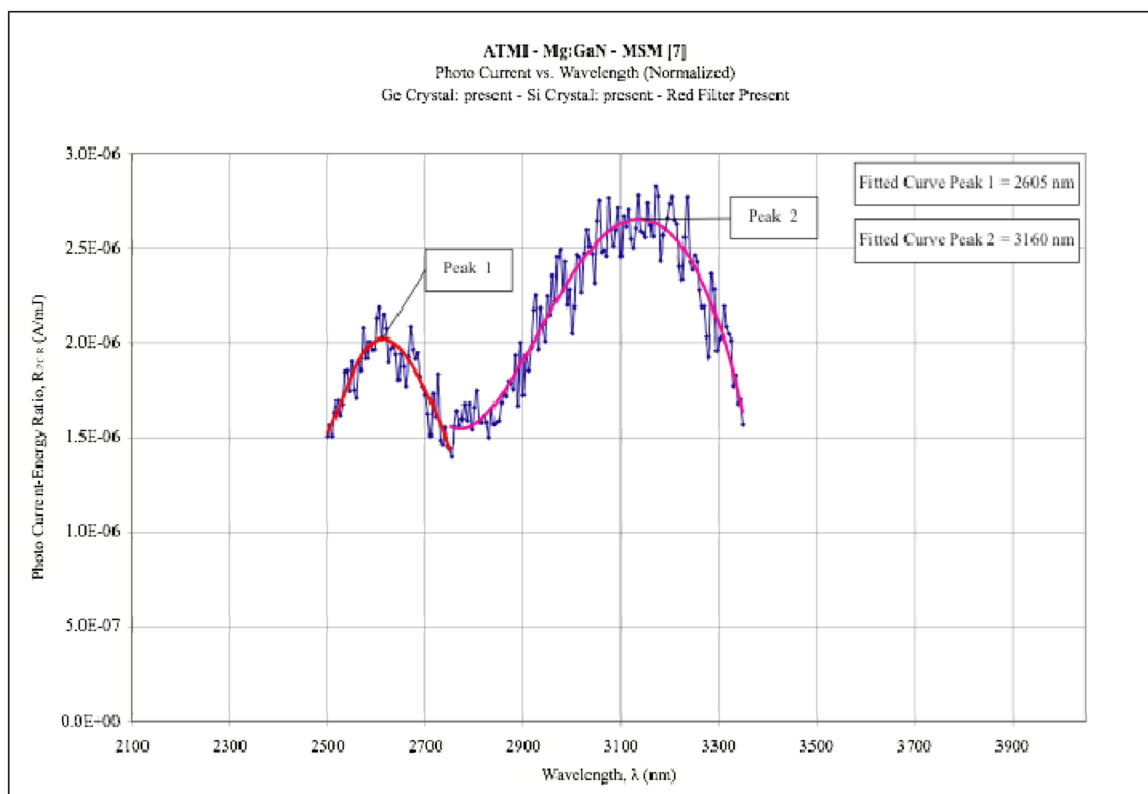

Figure 157: Curve fitting (polynomial) of the peak response observed in the high-resolution plot (5 nm step) shown in Figure 156.

Figure 158 shows the plot (5 nm step) of the IR photocurrent response of Ni/Au MSM test structure #1 fabricated on ATMI, Mg-doped GaN ("normalized" for each wavelength by the pulse energy at that wavelength), and the optical power output available for IR optical pumping provided by the OPO/OPA system in the Mid IR range (2100 nm to 4000 nm). A peak in the IR photocurrent response is observed at ~3075 nm (~403 meV), and a secondary peak is observed at ~2600 nm (~ 477meV); both are independent of the peak of the OPO/OPA system's power output located at ~2200 nm (~564 meV).

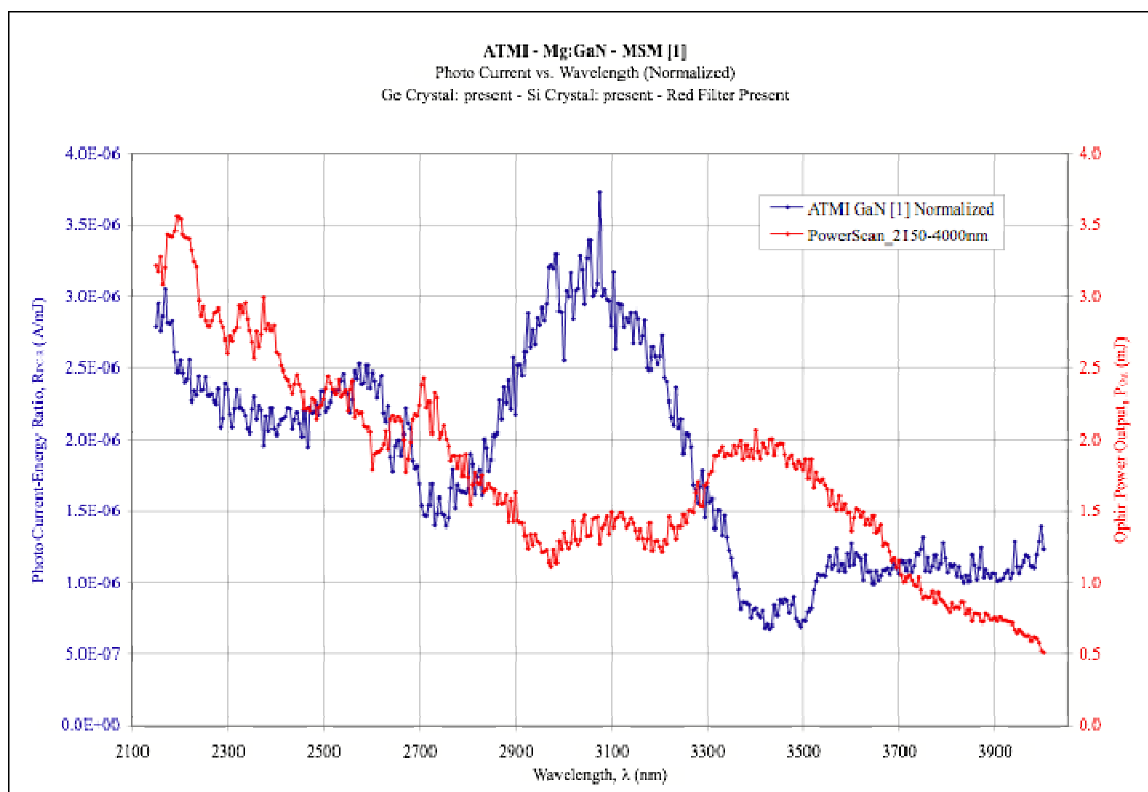

Figure 158: Plot (5 nm step) of the IR photocurrent response photocurrent response of Ni/Au MSM test structure #1 fabricated on ATMI, Mg-doped GaN ("normalized" for each wavelength by the pulse energy at that wavelength), and the optical power output available for IR optical pumping provided by the OPO/OPA system in the Mid IR range (2100 nm to 4000 nm). A peak in the IR photocurrent response is observed at ~3075 nm (~403 meV), and a secondary peak is observed at ~2600 nm (~477 meV); both are independent of the peak of the OPO/OPA system's power output located at ~2200 nm (~564 meV).

Figure 159 shows the "raw" (not "normalized") plot (5 nm step) of the IR photocurrent response Ni/Au MSM test structure #1 fabricated on ATMI, Mg-doped GaN, and the optical power output available for IR optical pumping provided by the OPO/OPA system in the Mid IR range (2100 nm to 4000 nm).

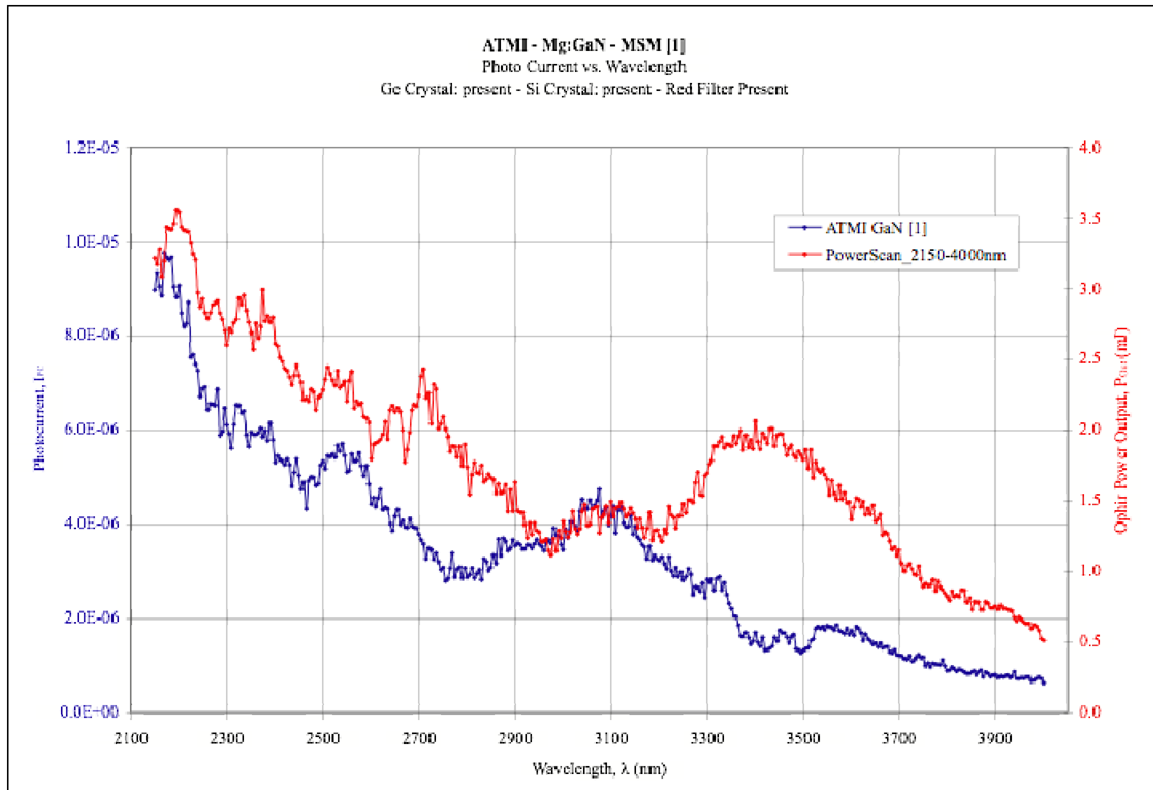

Figure 159: Plot (5 nm step) of the "raw" (not "normalized") IR photocurrent response Ni/Au MSM test structure #1 fabricated on ATMI, Mg-doped GaN, and the optical power output available for IR optical pumping provided by the OPO/OPA system in the Mid IR range (2100 nm to 4000 nm).

Figure 160 shows the plot (5 nm step) of the IR photocurrent response of Ni/Au MSM test structure #1 fabricated on ATMI, Mg-doped GaN ("normalized" for each wavelength by the pulse energy at that wavelength) shown in Figure 158.

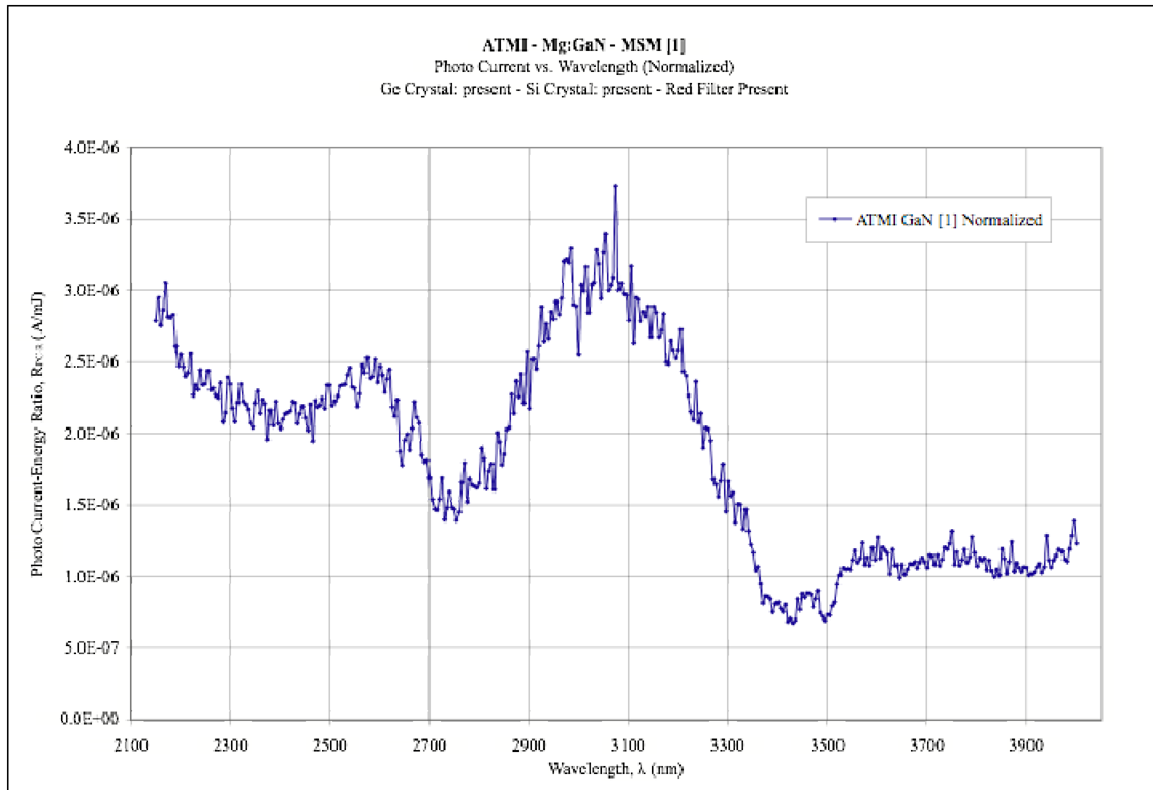

Figure 160: Plot (5 nm step) of the IR photocurrent response of Ni/Au MSM test structure #1 fabricated on ATMI, Mg-doped GaN ("normalized" for each wavelength by the pulse energy at that wavelength) shown Figure 158.

Figure 162 shows the curve fitting of the observed peak of the plot (5 nm step) of the "normalized" IR photocurrent response of test structure #7 fabricated on ATMI, Mg-doped GaN shown in Figure 160.

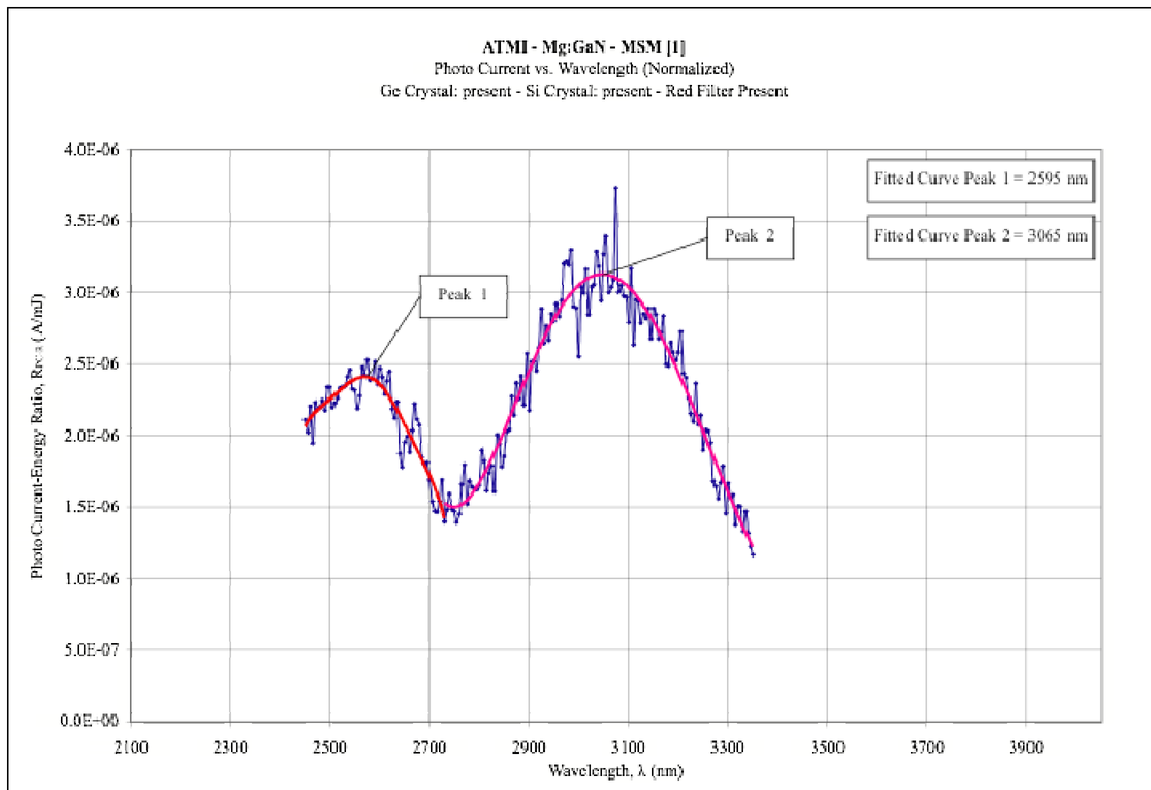

Figure 161: Curve fitting (polynomial) of the peak response observed in the high-resolution plot (5 nm step) shown in Figure 160.

Figure 162 shows the plot (5 nm step) of the IR photocurrent response of Ni/Au MSM test structure #1 fabricated on TDI, Mg-doped GaN ("normalized" for each wavelength by the pulse energy at that wavelength), and the optical power output available for IR optical pumping provided by the OPO/OPA system in the Mid IR range (2100 nm to 4000 nm). A peak in the IR photocurrent response is observed at ~3185 nm (~389 meV), and a secondary peak is observed at ~2600 nm (~477 meV); both are independent of the peak of the OPO/OPA system's power output located at ~2200 nm (~564 meV).

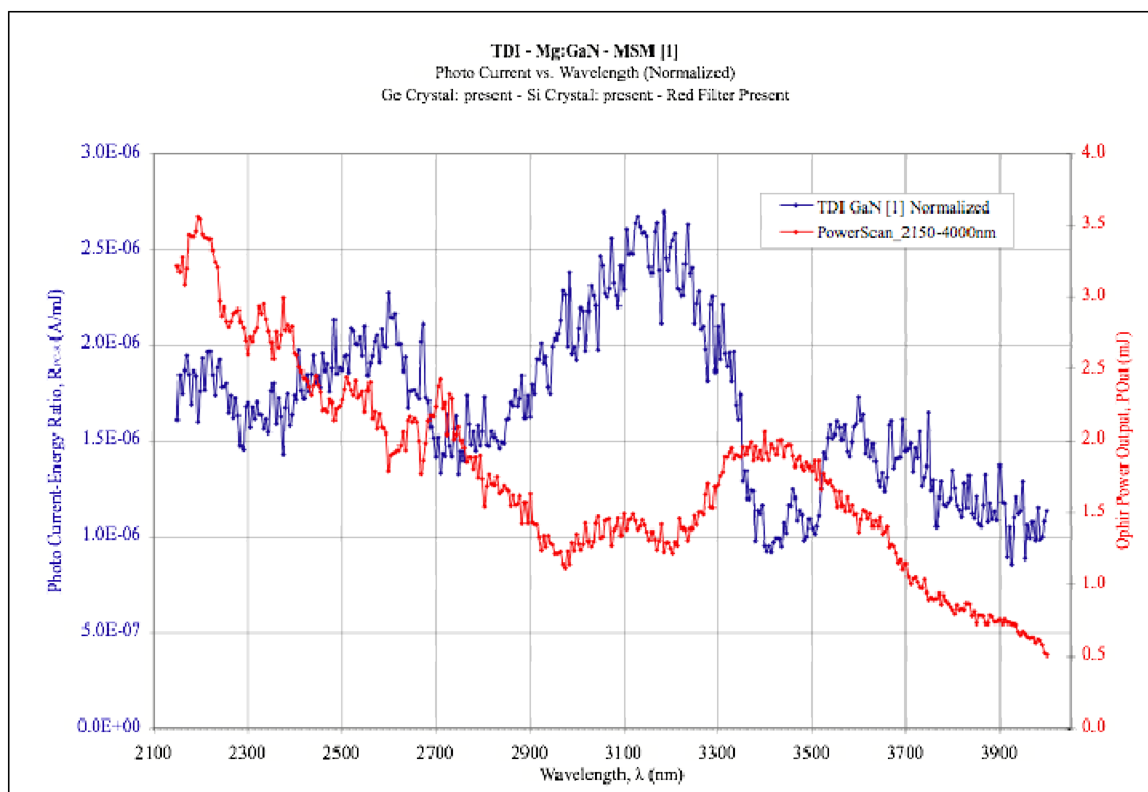

Figure 162: Plot (5 nm step) of the IR photocurrent response photocurrent response of Ni/Au MSM test structure #1 fabricated on TDI, Mg-doped GaN ("normalized" for each wavelength by the pulse energy at that wavelength), and the optical power output available for IR optical pumping provided by the OPO/OPA system in the Mid IR range (2100 nm to 4000 nm). A peak in the IR photocurrent response is observed at ~3185 nm (~389 meV), and a secondary peak is observed at ~2600 nm (~477 meV); both are independent of the peak of the OPO/OPA system's power output located at ~2200 nm (~564 meV).

Figure 163 shows the "raw" (not "normalized") plot (5 nm step) of the IR photocurrent response Ni/Au MSM test structure #1 fabricated on TDI, Mg-doped GaN, and the optical power output available for IR optical pumping provided by the OPO/OPA system in the Mid IR range (2100 nm to 4000 nm).

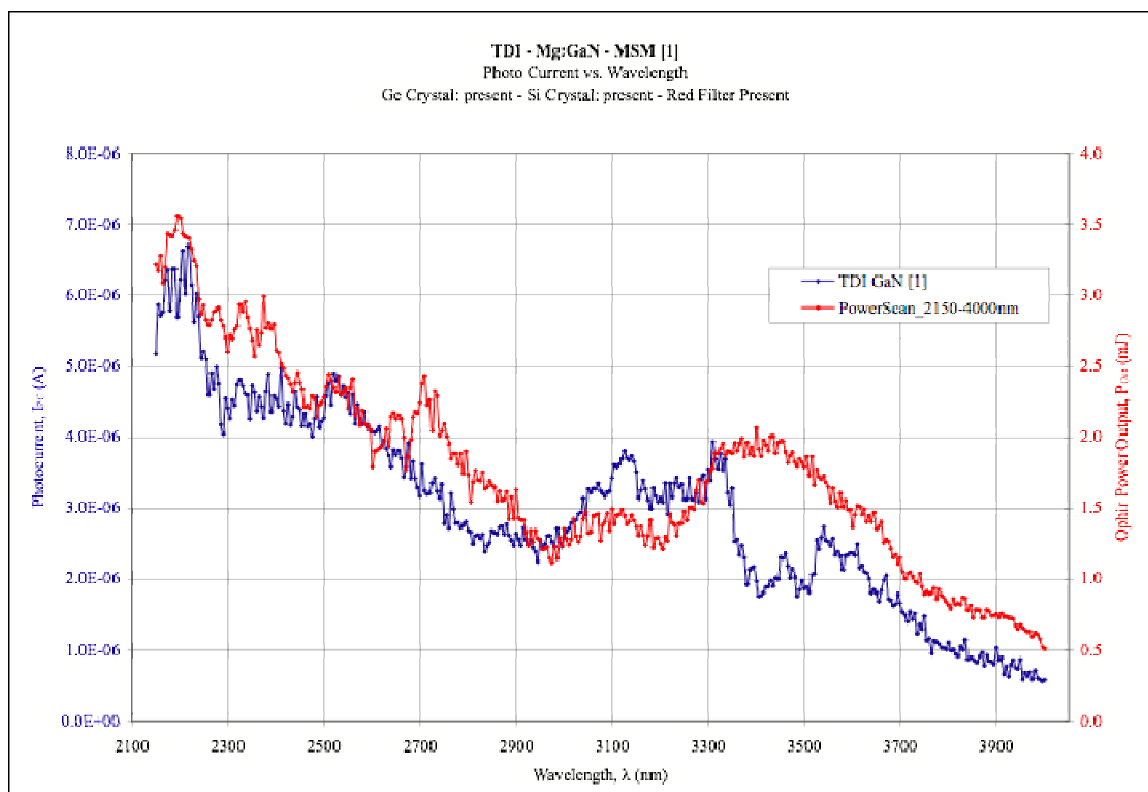

Figure 163: Plot (5 nm step) of the “raw” (not “normalized”) IR photocurrent response Ni/Au MSM test structure #1 fabricated on TDI, Mg-doped GaN, and the optical power output available for IR optical pumping provided by the OPO/OPA system in the Mid IR range (2100 nm to 4000 nm).

Figure 164 shows the plot (5 nm step) of the IR photocurrent response of Ni/Au MSM test structure #1 fabricated on TDI, Mg-doped GaN (“normalized” for each wavelength by the pulse energy at that wavelength) shown Figure 162.

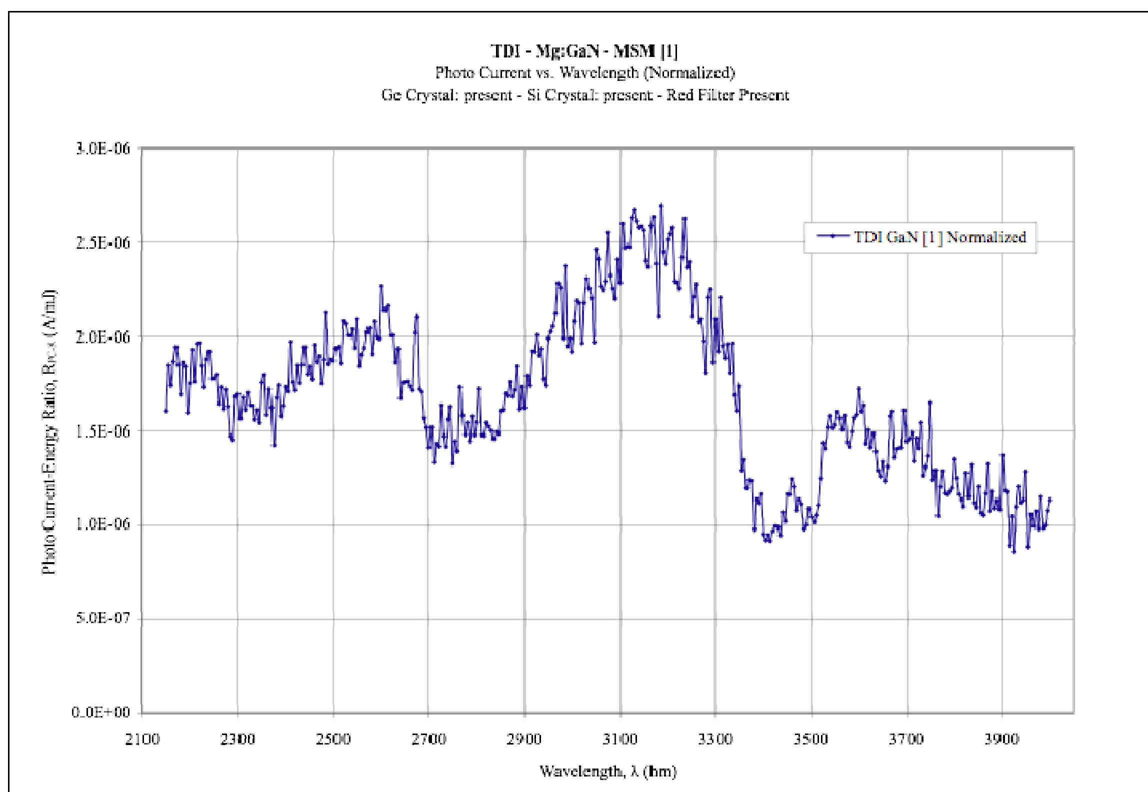

Figure 164: Plot (5 nm step) of the IR photocurrent response of Ni/Au MSM test structure #1 fabricated on TDI, Mg-doped GaN ("normalized" for each wavelength by the pulse energy at that wavelength) shown Figure 162.

Figure 165 shows the curve fitting of the observed peak of the plot (5 nm step) of the "normalized" IR photocurrent response of test structure #1 fabricated on TDI, Mg-doped GaN shown in Figure 164.

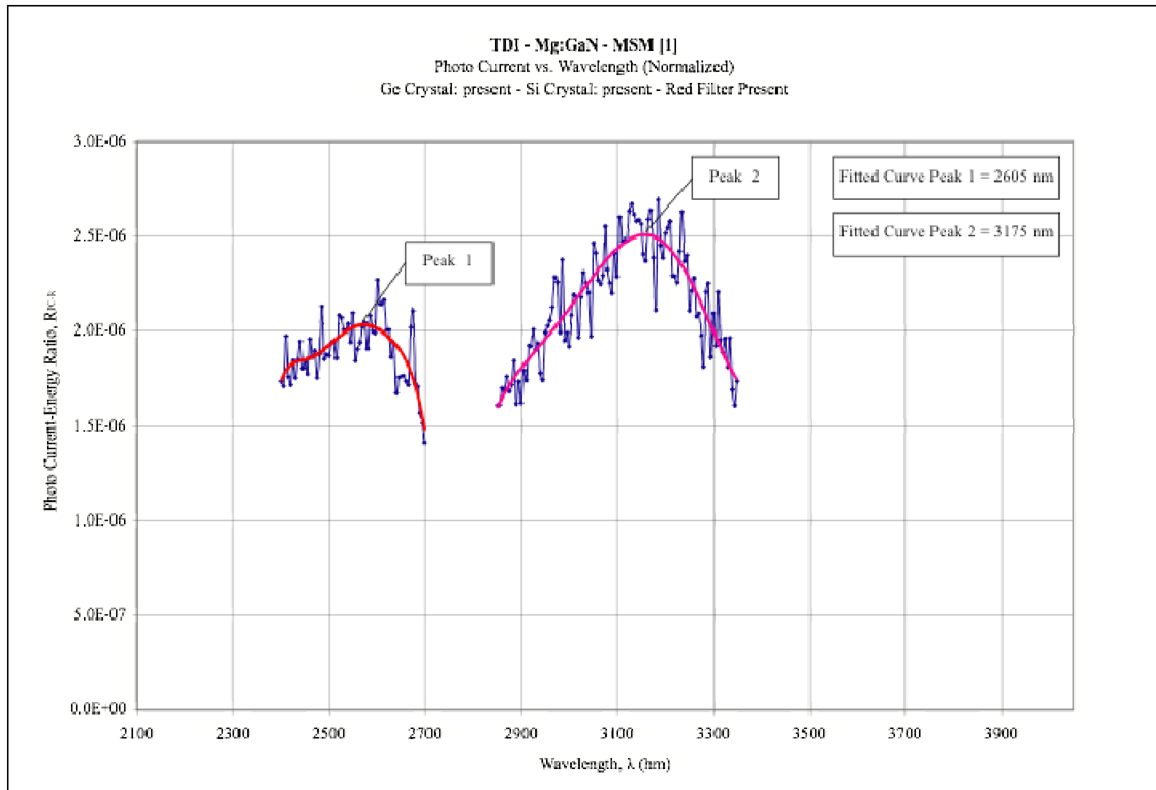

Figure 165: Curve fitting (polynomial) of the peak response observed in the high-resolution plot (5 nm step) shown in Figure 164.

Figure 166 shows the plot (5 nm step) of the IR photocurrent response of Ni/Au MSM test structure #2 fabricated on TDI, Mg-doped GaN ("normalized" for each wavelength by the pulse energy at that wavelength), and the optical power output available for IR optical pumping provided by the OPO/OPA system in the Mid IR range (2100 nm to 4000 nm). A peak in the IR photocurrent response is observed at ~3075 nm (~403 meV), and a secondary peak is observed at ~2675 nm (~464 meV); both are independent of the peak of the OPO/OPA system's power output located at ~2200 nm (~564 meV).

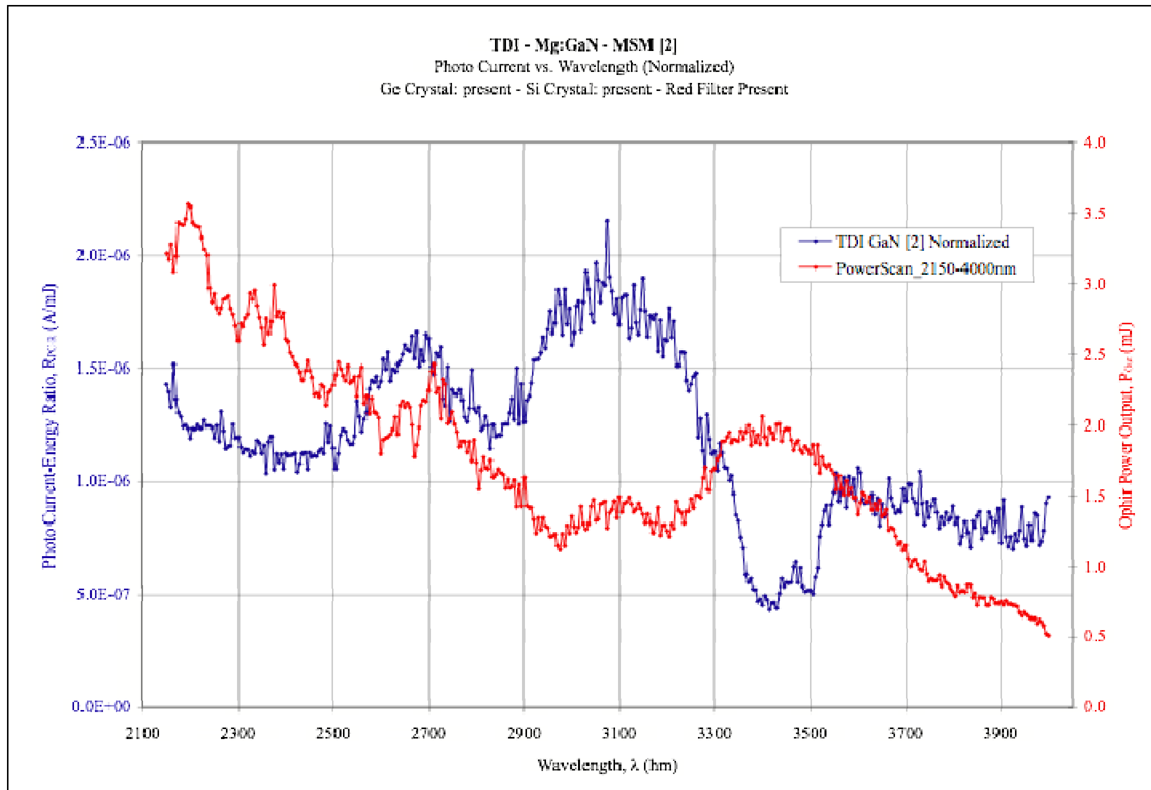

Figure 166: Plot (5 nm step) of the IR photocurrent response photocurrent response of Ni/Au MSM test structure #2 fabricated on TDI, Mg-doped GaN ("normalized" for each wavelength by the pulse energy at that wavelength), and the optical power output available for IR optical pumping provided by the OPO/OPA system in the Mid IR range (2100 nm to 4000 nm). A peak in the IR photocurrent response is observed at ~3075 nm (~403 meV), and a secondary peak is observed at ~2675 nm (~464 meV); both are independent of the peak of the OPO/OPA system's power output located at ~2200 nm (~564 meV).

Figure 167 shows the "raw" (not "normalized") plot (5 nm step) of the IR photocurrent response Ni/Au MSM test structure #2 fabricated on Epitex, Mg-doped $Al_{0.15}Ga_{0.95}N$, and the optical power output available for IR optical pumping provided by the OPO/OPA system in the Mid IR range (2100 nm to 4000 nm).

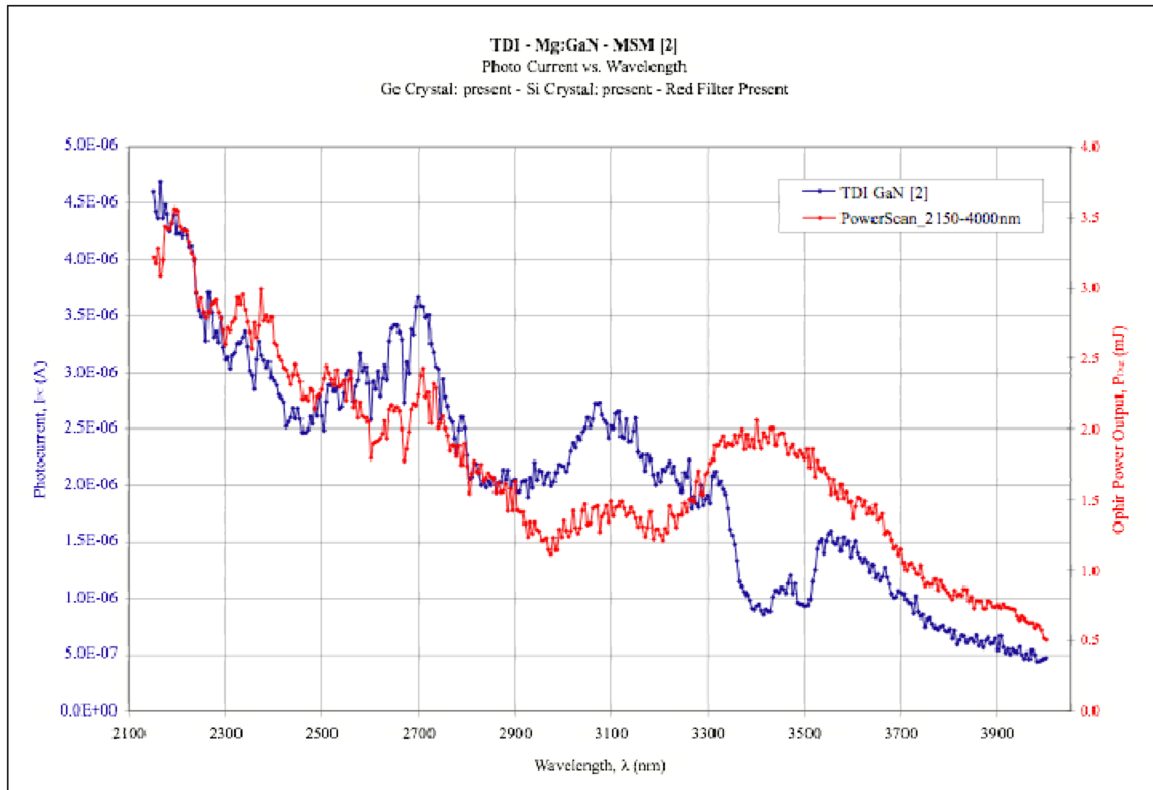

Figure 167: Plot (5 nm step) of the “raw” (not “normalized”) IR photocurrent response Ni/Au MSM test structure #2 fabricated on TDI, Mg-doped GaN, and the optical power output available for IR optical pumping provided by the OPO/OPA system in the Mid IR range (2100 nm to 4000 nm).

Figure 168 shows the plot (5 nm step) of the IR photocurrent response of Ni/Au MSM test structure #2 fabricated on TDI, Mg-doped GaN (“normalized” for each wavelength by the pulse energy at that wavelength) shown Figure 166.

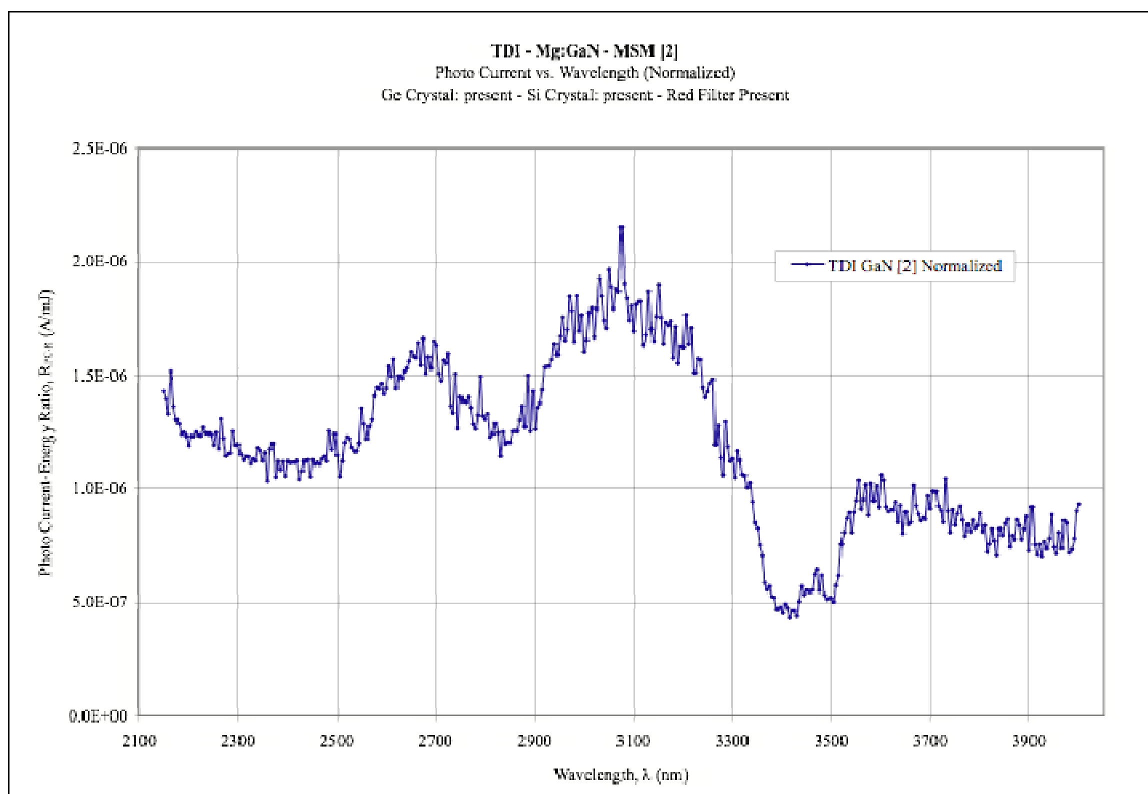

Figure 168: Plot (5 nm step) of the IR photocurrent response of Ni/Au MSM test structure #2 fabricated on TDI, Mg-doped GaN ("normalized" for each wavelength by the pulse energy at that wavelength) shown Figure 166.

Figure 169 shows the curve fitting of the observed peak of the plot (5 nm step) of the "normalized" IR photocurrent response of test structure #1 fabricated on TDI, Mg-doped GaN shown in Figure 168.

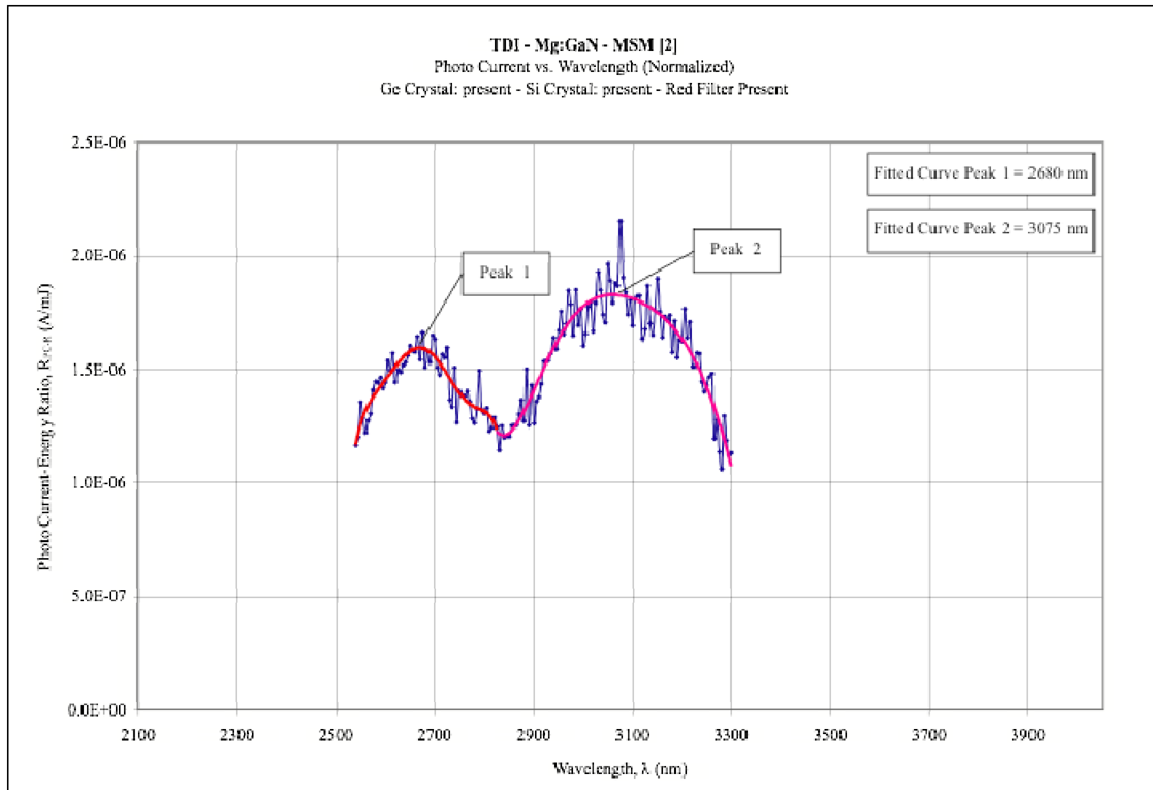

Figure 169: Curve fitting (polynomial) of the peak response observed in the high-resolution plot (5 nm step) shown in Figure 168.

Figure 170 shows a comprehensive plot (5 nm step) of the IR photocurrent response of Ni/Au MSM test structures fabricated on Honeywell, ATMI, and TDI Mg-doped GaN ("normalized" for each wavelength by the pulse energy at that wavelength), and the optical power output available for IR optical pumping provided by the OPO/OPA system in the Mid IR range (2100 nm to 4000 nm).

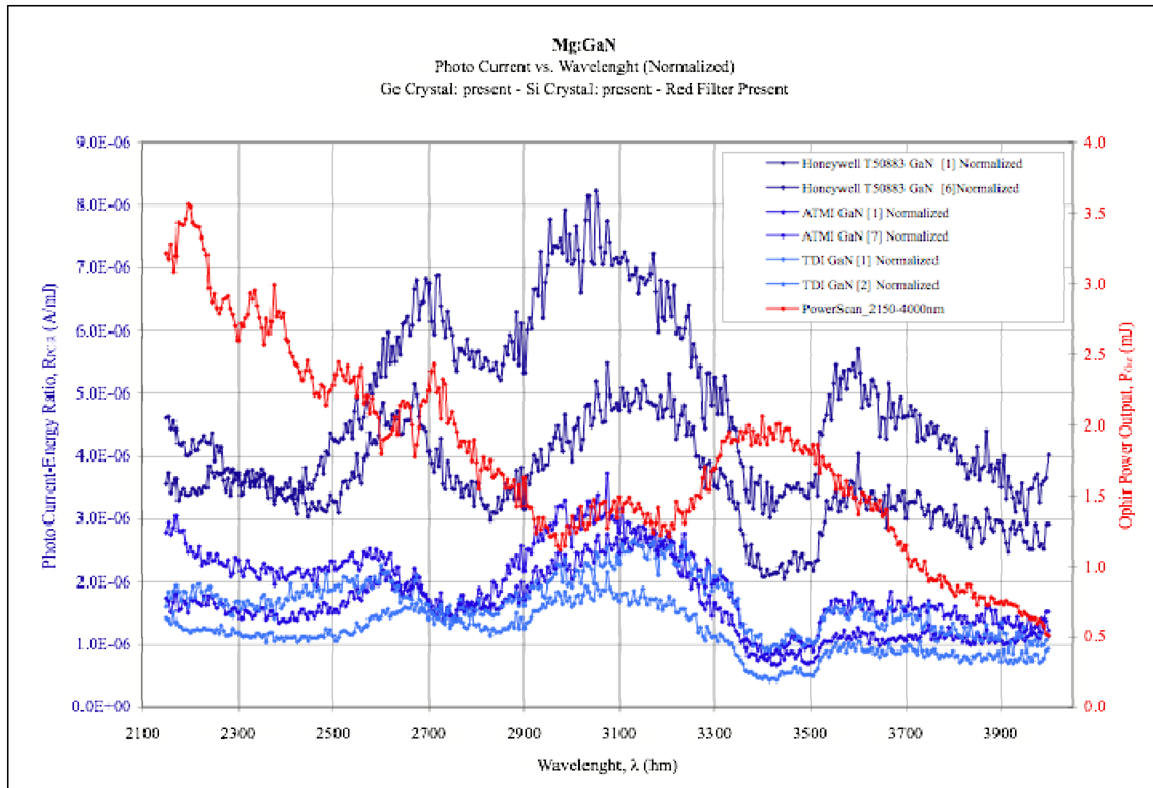

Figure 170: Comprehensive plot (5 nm step) of the IR photocurrent response of Ni/Au MSM test structures fabricated on Honeywell, ATMI, and TD, Mg-doped GaN ("normalized" for each wavelength by the pulse energy at that wavelength), and the optical power output available for IR optical pumping provided by the OPO/OPA system in the Mid IR range (2100 nm to 4000 nm).

6.6. Comprehensive Plot of the IR Photocurrent Response Peaks

Figure 171 shows a comprehensive plot the IR photocurrent response peak of the test structures as a function of their aluminum mole fraction; it includes the peak of the IR photocurrent response for each of the test structures investigated in this work.

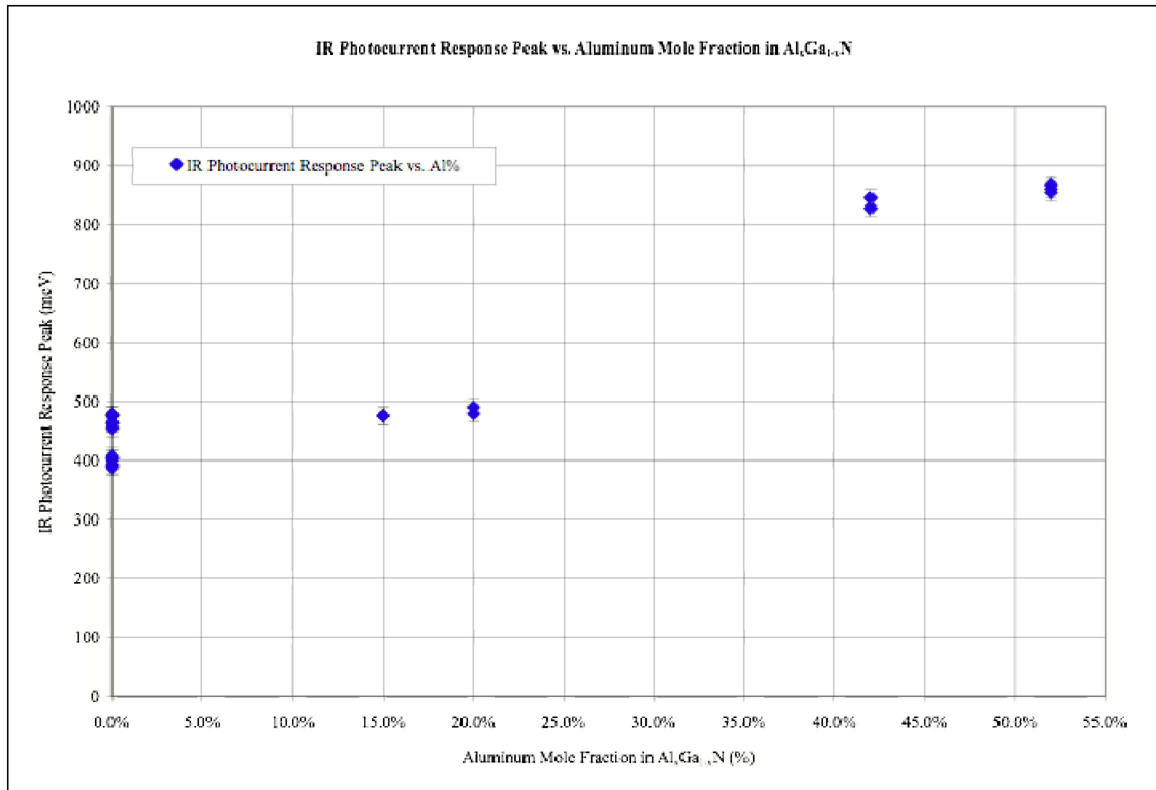

Figure 171: A comprehensive plot of the IR photocurrent response peak of the test structures as a function of their aluminum mole fraction composition. It includes the peak of the IR photocurrent response of each of the test structures investigated in this work.

6.7. Temperature Dependent Infrared Photocurrent Spectra from Mg-doped GaN Test Structures

Figure 172 shows the plot (5 nm step) of the temperature dependent IR photocurrent response of Ni/Au MSM test structure #1 fabricated on ATMI, Mg-doped GaN (“normalized” for each wavelength by the pulse energy at that wavelength), and the optical power output available for IR optical pumping provided by the OPO/OPA system in the Mid IR range (2100 nm to 4000 nm).

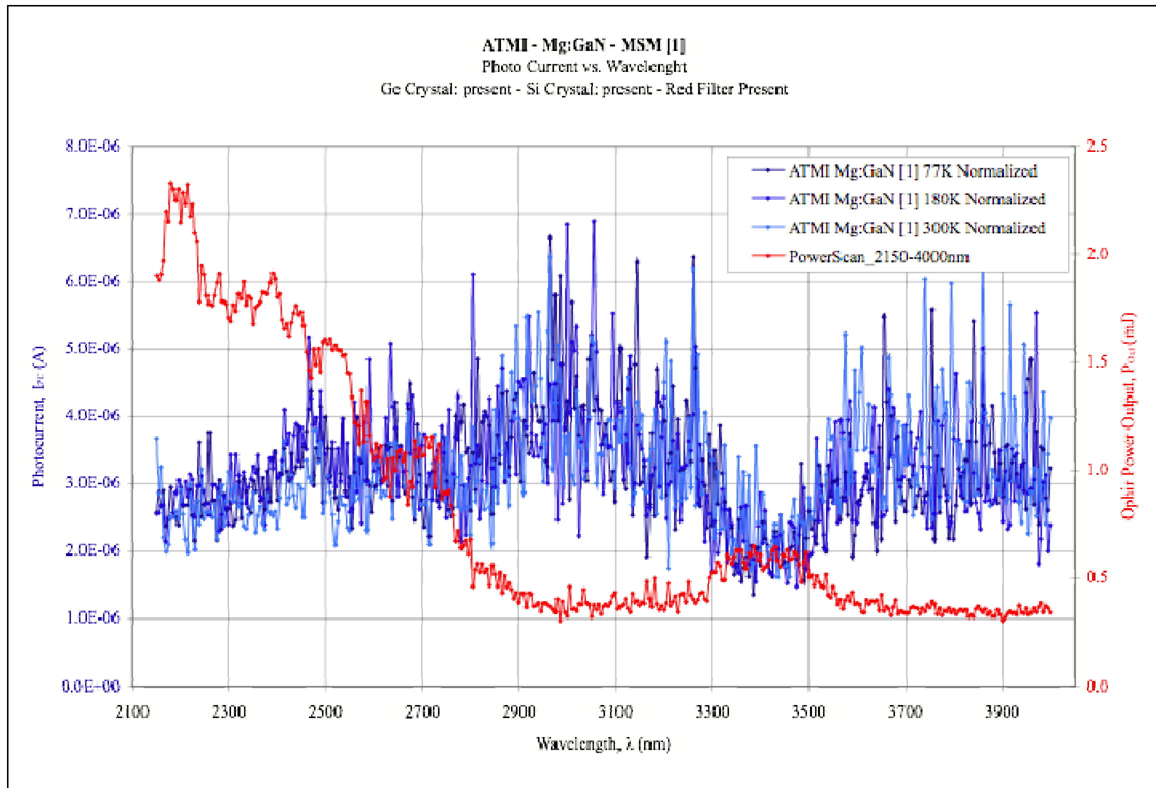

Figure 172: Plot (5 nm step) of the temperature dependent IR photocurrent response photocurrent response of Ni/Au MSM test structure #1 fabricated on ATMI, Mg-doped GaN ("normalized" for each wavelength by the pulse energy at that wavelength), and the optical power output available for IR optical pumping provided by the OPO/OPA system in the Mid IR range (2100 nm to 4000 nm).

Figure 173 shows the "raw" (not "normalized") plot (5 nm step) of the temperature IR photocurrent response Ni/Au MSM test structure #1 fabricated on ATMI, Mg-doped GaN, and the optical power output available for IR optical pumping provided by the OPO/OPA system in the Mid IR range (2100 nm to 4000 nm).

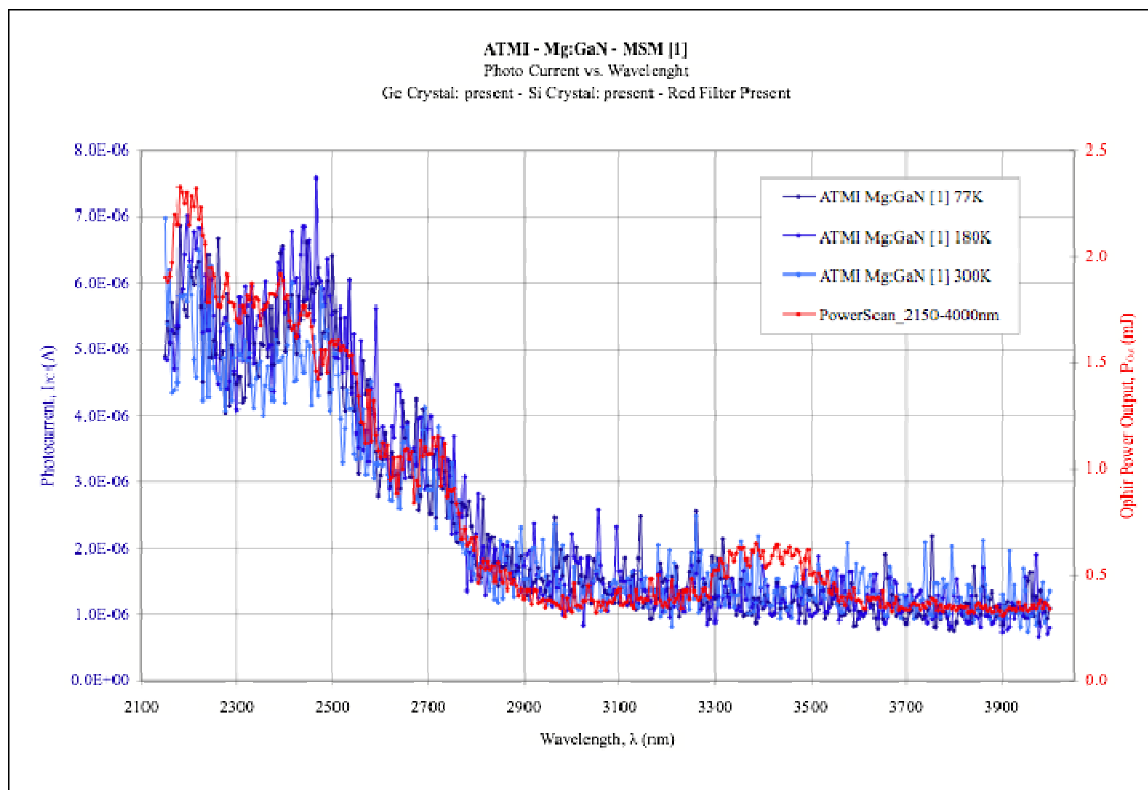

Figure 173: Plot (5 nm step) of the "raw" (not "normalized") temperature dependent IR photocurrent response Ni/Au MSM test structure #1 fabricated on ATMI, Mg-doped GaN, and the optical power output available for IR optical pumping provided by the OPO/OPA system in the Mid IR range (2100 nm to 4000 nm).

Figure 174 shows the time decay of the temperature dependent IR photocurrent response of Ni/Au MSM test structure #1 fabricated on ATMI, Mg-doped GaN.

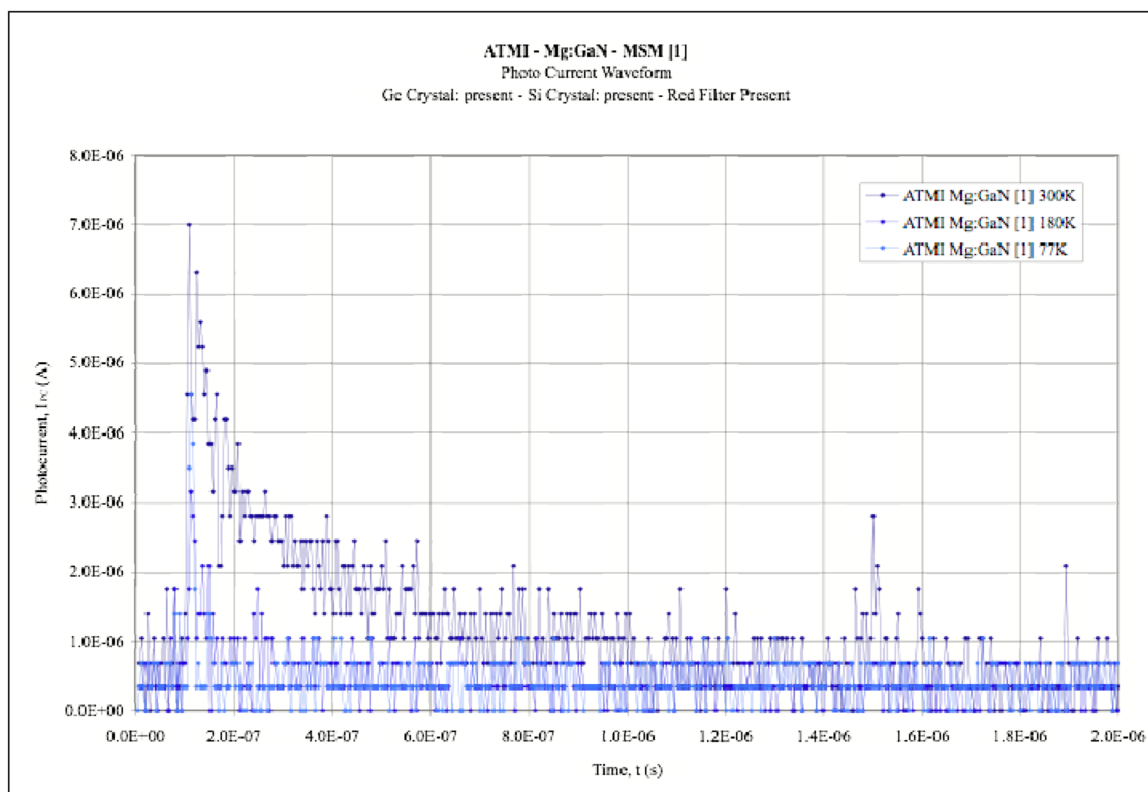

Figure 174: Time decay of the IR photocurrent response of Ni/Au MSM test structure #1 fabricated on ATMI, Mg-doped GaN.

Figure 175 shows the time decay of the IR photocurrent response of Ni/Au MSM test structure #1 fabricated on ATMI, Mg-doped GaN, at T= 300 °K.

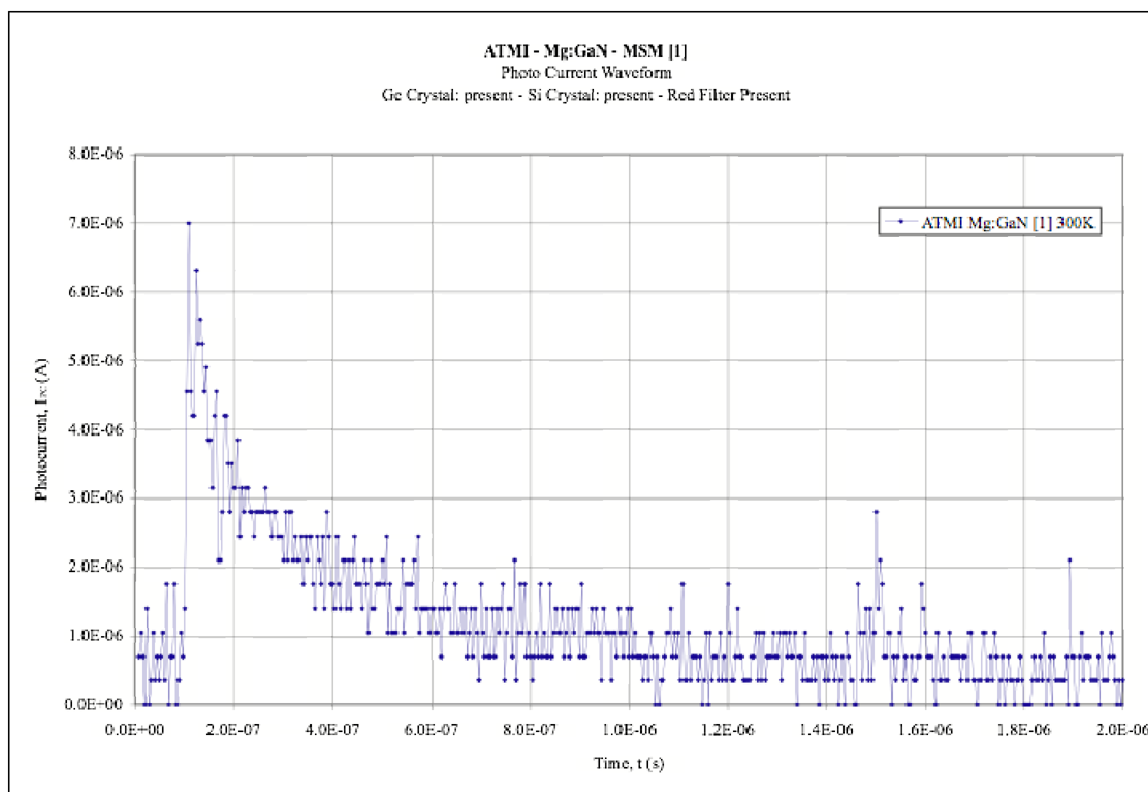

Figure 175: Time decay of the IR photocurrent response of Ni/Au MSM test structure #1 fabricated on ATMI, Mg-doped GaN at T = 300 °K.

Figure 176 shows the time decay of the IR photocurrent response of Ni/Au MSM test structure #1 fabricated on ATMI, Mg-doped GaN, at T= 180 °K.

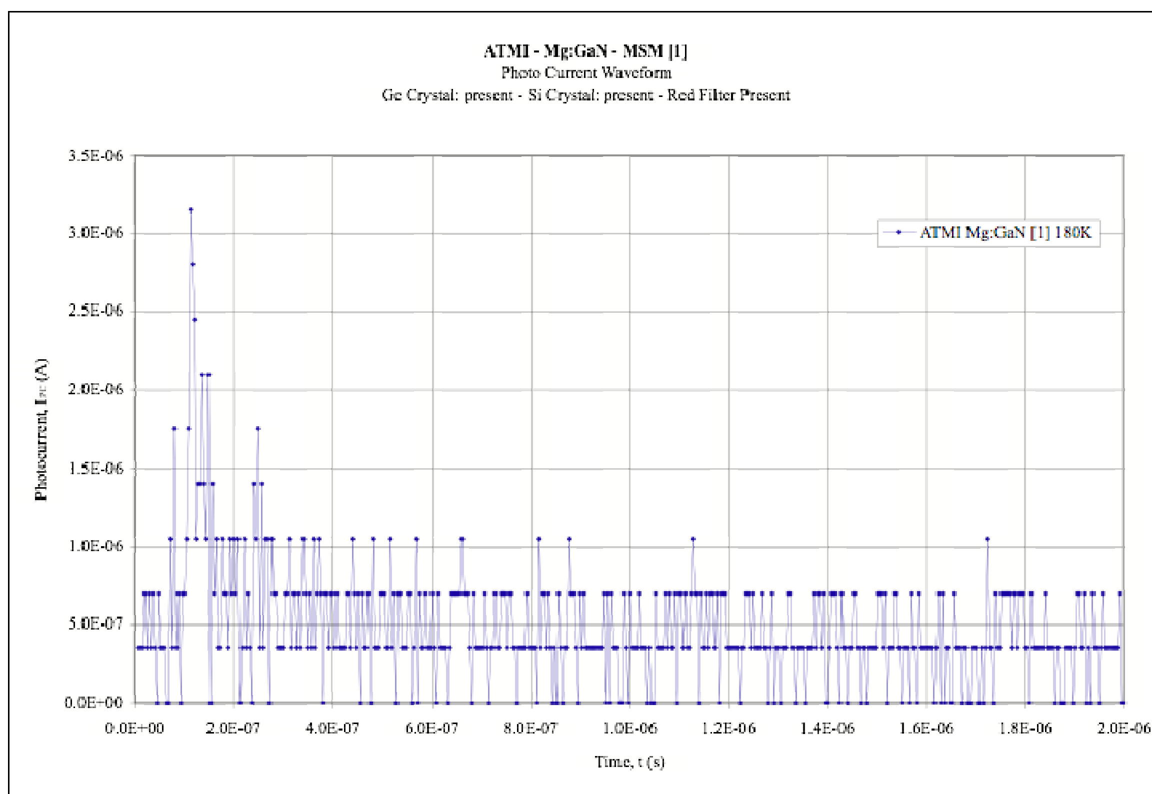

Figure 176: Time decay of the IR photocurrent response of Ni/Au MSM test structure #1 fabricated on ATMI, Mg-doped GaN at T = 180 °K.

Figure 177 shows the time decay of the IR photocurrent response of Ni/Au MSM test structure #1 fabricated on ATMI, Mg-doped GaN, at T= 77 °K.

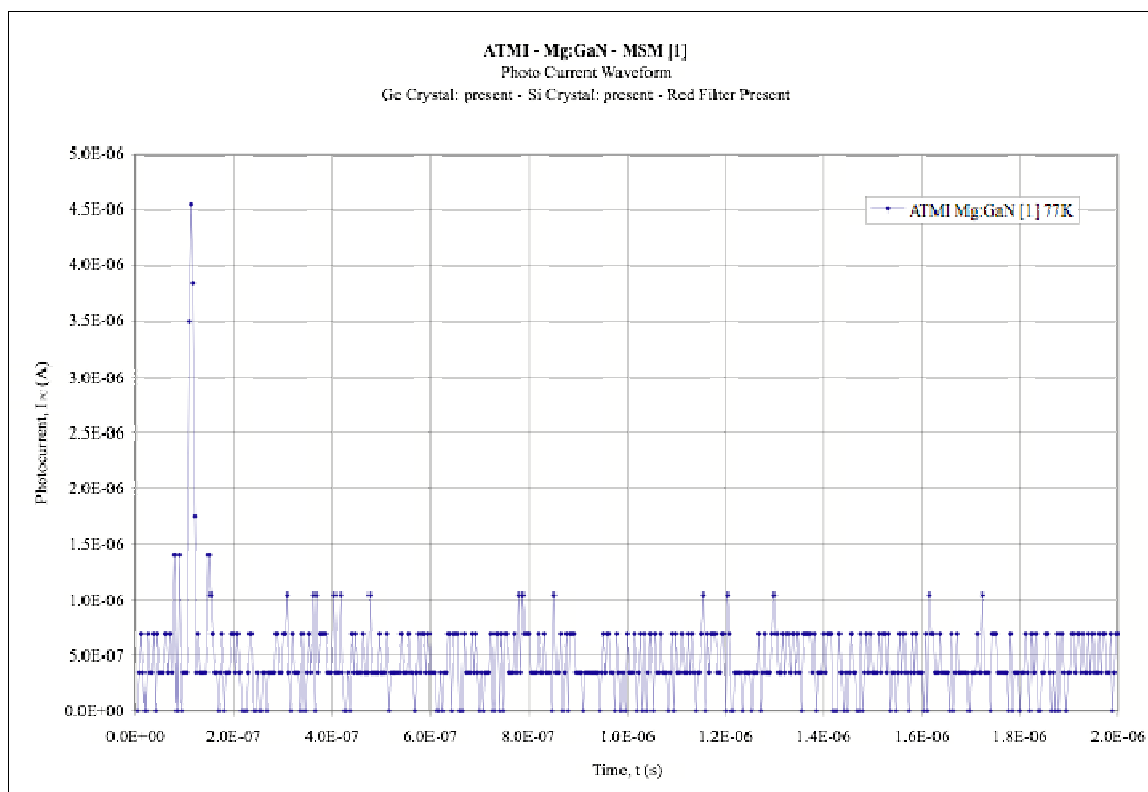

Figure 177: Time decay of the IR photocurrent response of Ni/Au MSM test structure #1 fabricated on ATMI, Mg-doped GaN at T = 77 °K.

6.8. Time Decay of the Infrared Photocurrent Spectra from Mg-doped GaN and $Al_xGa_{1-x}N$ Test Structures

Figure 178 shows the time decay of the IR photocurrent response of Ni/Au MSM test structure #1 fabricated on Honeywell, Mg-doped $Al_{0.52}Ga_{0.48}N$, as determined at the IR photocurrent peak response (1440 nm – 861 meV), and off peak response (1820 nm – 681 meV).

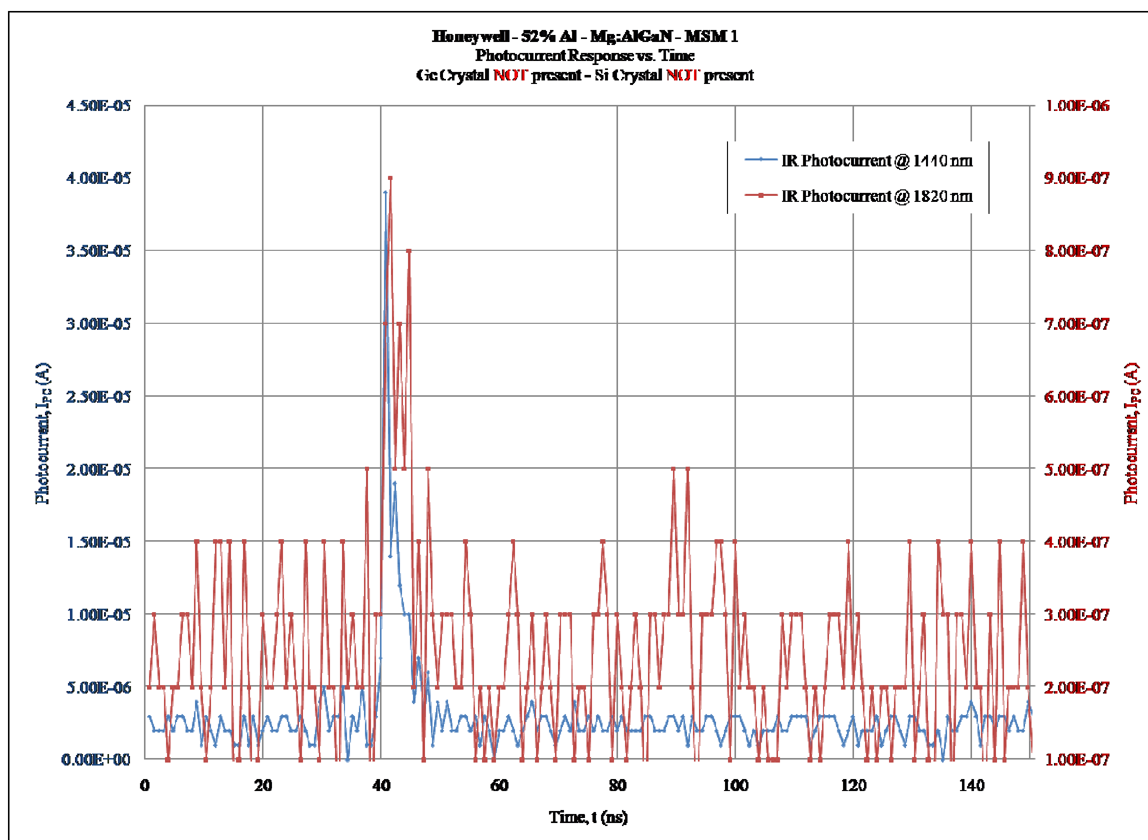

Figure 178: Time decay of the IR photocurrent response of Ni/Au MSM test structure #1 fabricated on Honeywell, Mg-doped $Al_{0.52}Ga_{0.48}N$, as determined at the IR photocurrent peak response (1440 nm – 861 meV), and off peak response (1820 nm – 681 meV).

Figure 179 shows the time decay of the IR photocurrent response of test structure #1 fabricated on Crystal IS, Mg-doped $Al_{0.42}Ga_{0.58}N$, as determined at the IR photocurrent peak response (1495 nm – 829 meV), and off peak response (1800 nm – 689 meV).

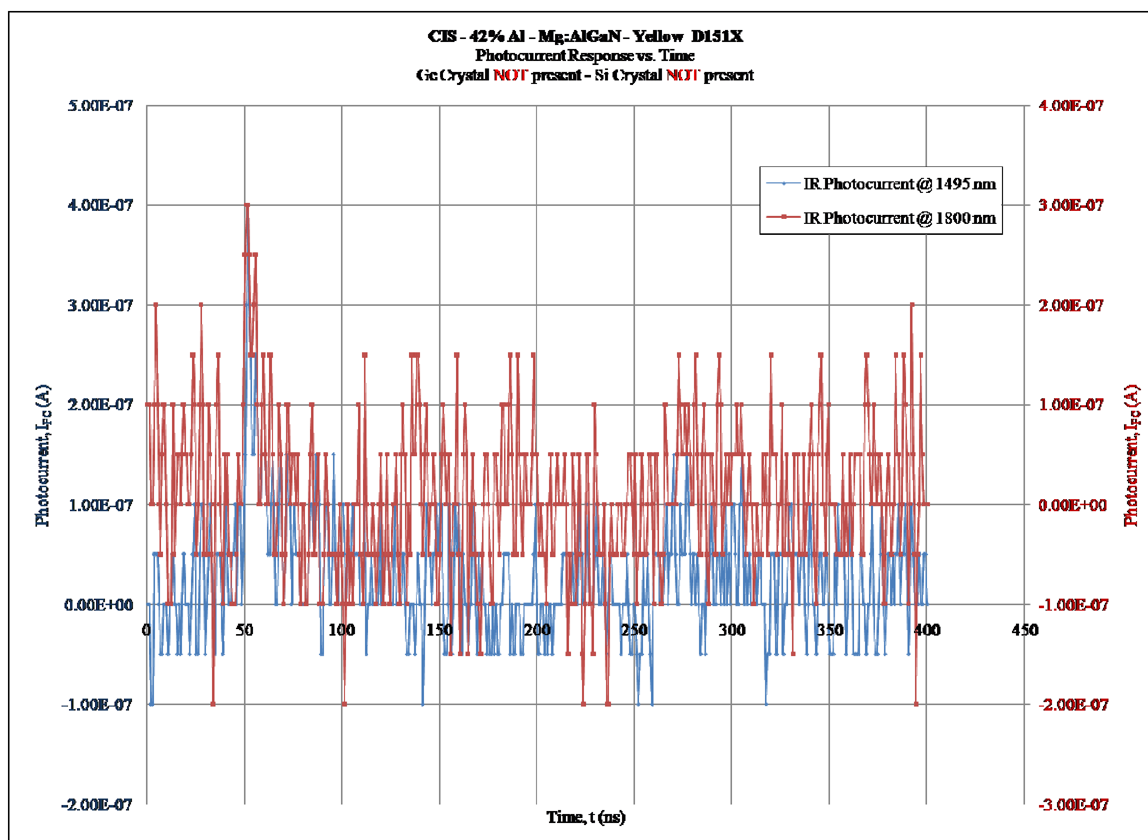

Figure 179: Time decay of the IR photocurrent response of test structure #1 fabricated on Crystal IS, Mg-doped $Al_{0.48}Ga_{0.52}N$, as determined at the IR photocurrent peak response (1495 nm – 829 meV), and off peak response (1800 nm – 689 meV).

Figure 180 shows the time decay of the IR photocurrent response of Ni/Au MSM test structure #3 fabricated on Honeywell, Mg-doped $Al_{0.20}Ga_{0.80}N$, as determined at the IR photocurrent peak response (2525 nm – 491 meV), and off peak response (3900 nm – 318 meV).

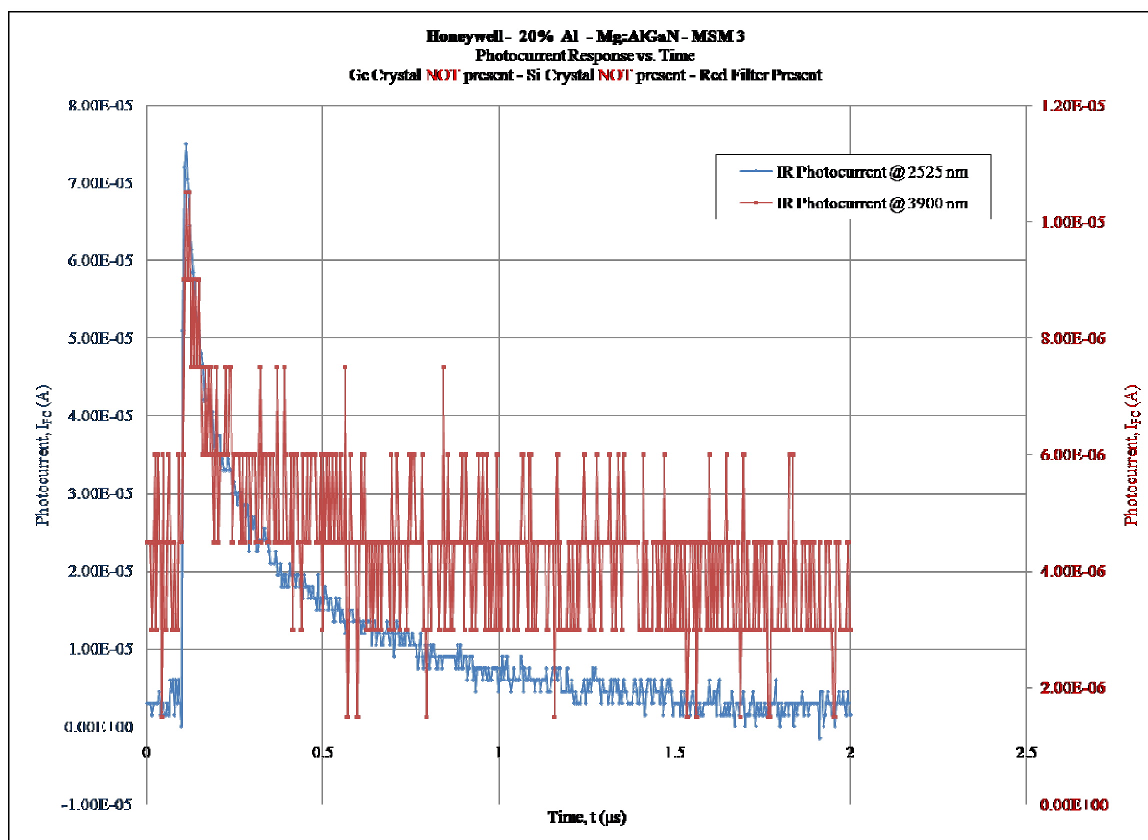

Figure 180: Time decay of the IR photocurrent response of Ni/Au MSM test structure #3 fabricated on Honeywell, Mg-doped $Al_{0.20}Ga_{0.80}N$, as determined at the IR photocurrent peak response (2525 nm – 491 meV), and off peak response (3900 nm – 318 meV).

Figure 181 shows the time decay of the IR photocurrent response of Ni/Au MSM test structure #3 fabricated on Epitex, Mg-doped $Al_{0.15}Ga_{0.85}N$, as determined at the IR photocurrent peak response (2605 nm – 476 meV), and off peak response (3900 nm – 318 meV).

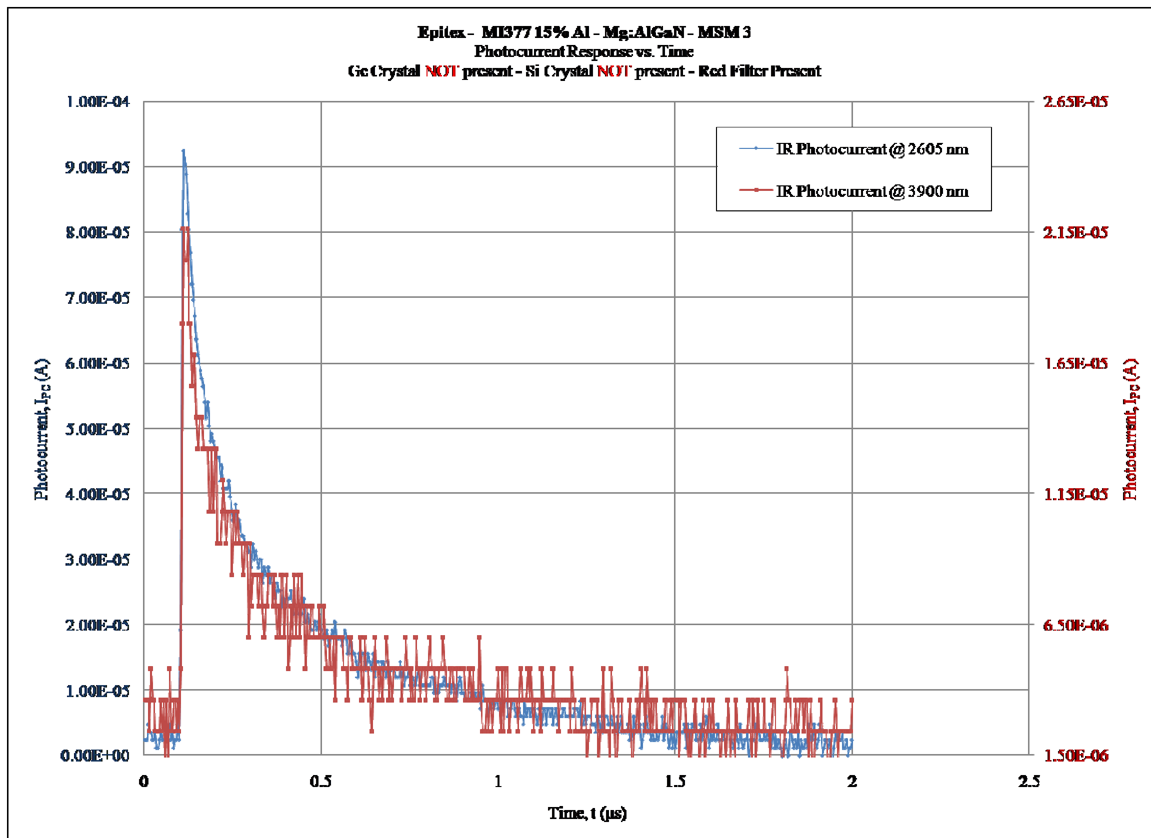

Figure 181: Time decay of the IR photocurrent response of Ni/Au MSM test structure #3 fabricated on Epitex, Mg-doped $Al_{0.15}Ga_{0.85}N$, as determined at the IR photocurrent peak response (2605 nm – 476 meV), and off peak response (3900 nm – 318 meV).

Figure 182 shows the time decay of the IR photocurrent response of Ni/Au MSM test structure #1 fabricated on Honeywell, Mg-doped GaN, as determined at the IR photocurrent peak response (3050 nm – 407 meV), and off peak response (3900 nm – 318 meV).

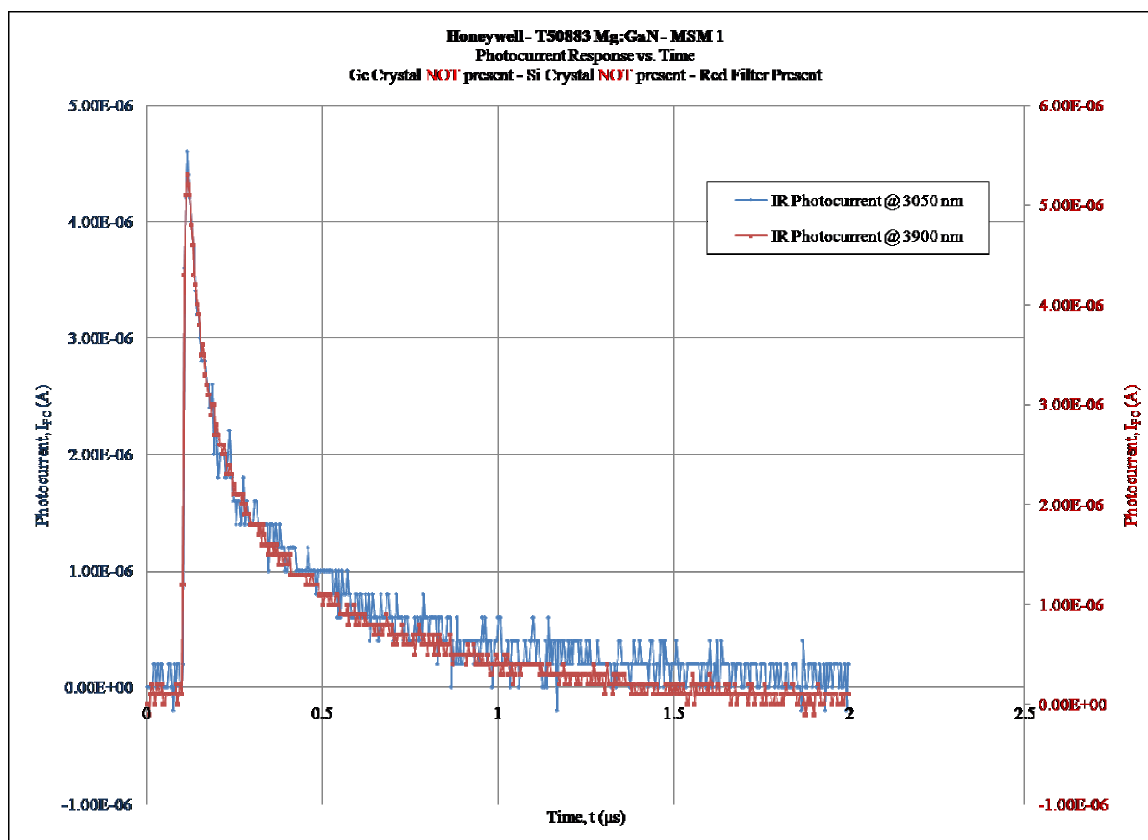

Figure 182: Time decay of the IR photocurrent response of Ni/Au MSM test structure #1 fabricated on Honeywell, Mg-doped GaN, as determined at the IR photocurrent peak response (3050 nm – 407 meV), and off peak response (3900 nm – 318 meV).

Figure 183 shows the time decay of the IR photocurrent response of Ni/Au MSM test structure #7 fabricated on ATMI, Mg-doped GaN, as determined at the IR photocurrent peak response (3075 nm – 403 meV), and off peak response (3950 nm – 314 meV).

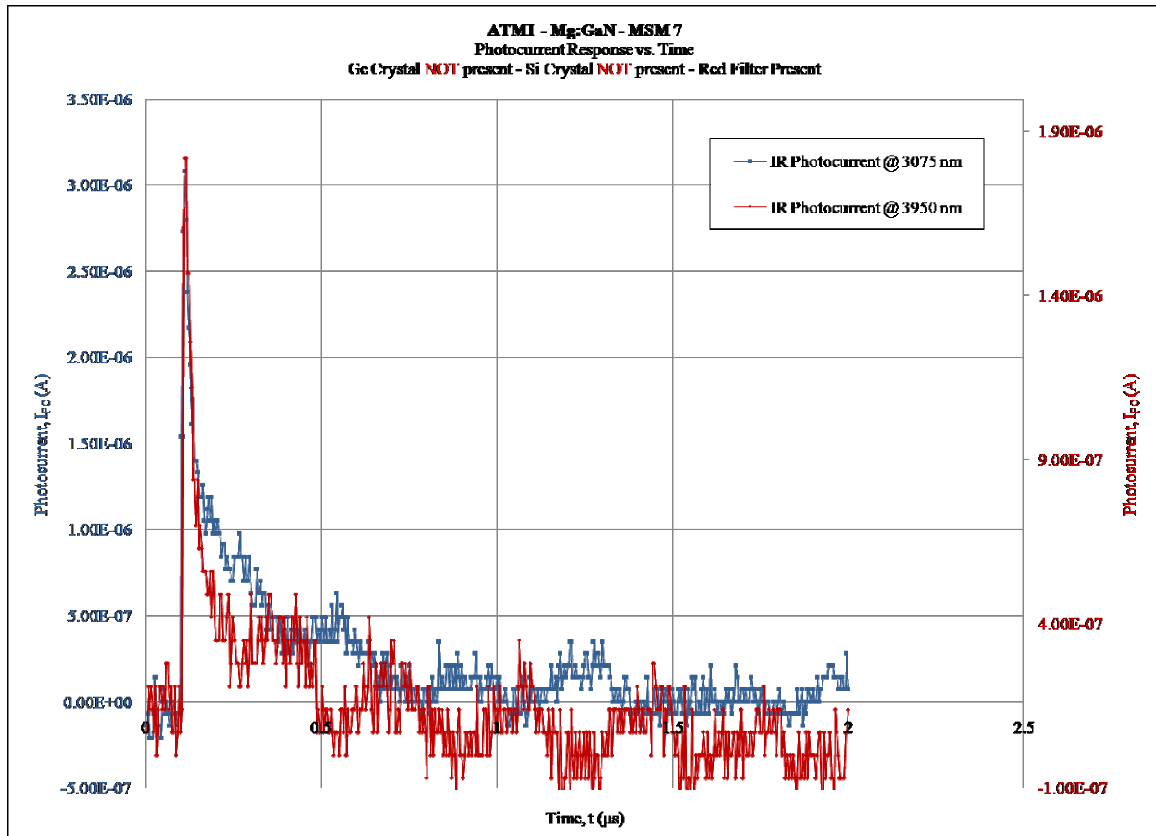

Figure 183: Time decay of the IR photocurrent response of Ni/Au MSM test structure #7 fabricated on ATMI, Mg-doped GaN, as determined at the IR photocurrent peak response (3075 nm – 403 meV), and off peak response (3950 nm – 314 meV).

Figure 183 shows the time decay of the IR photocurrent response of Ni/Au MSM test structure #2 fabricated on TDI, Mg-doped GaN, as determined at the IR photocurrent peak response (3075 nm – 403 meV), and off peak response (3900 nm – 318 meV).

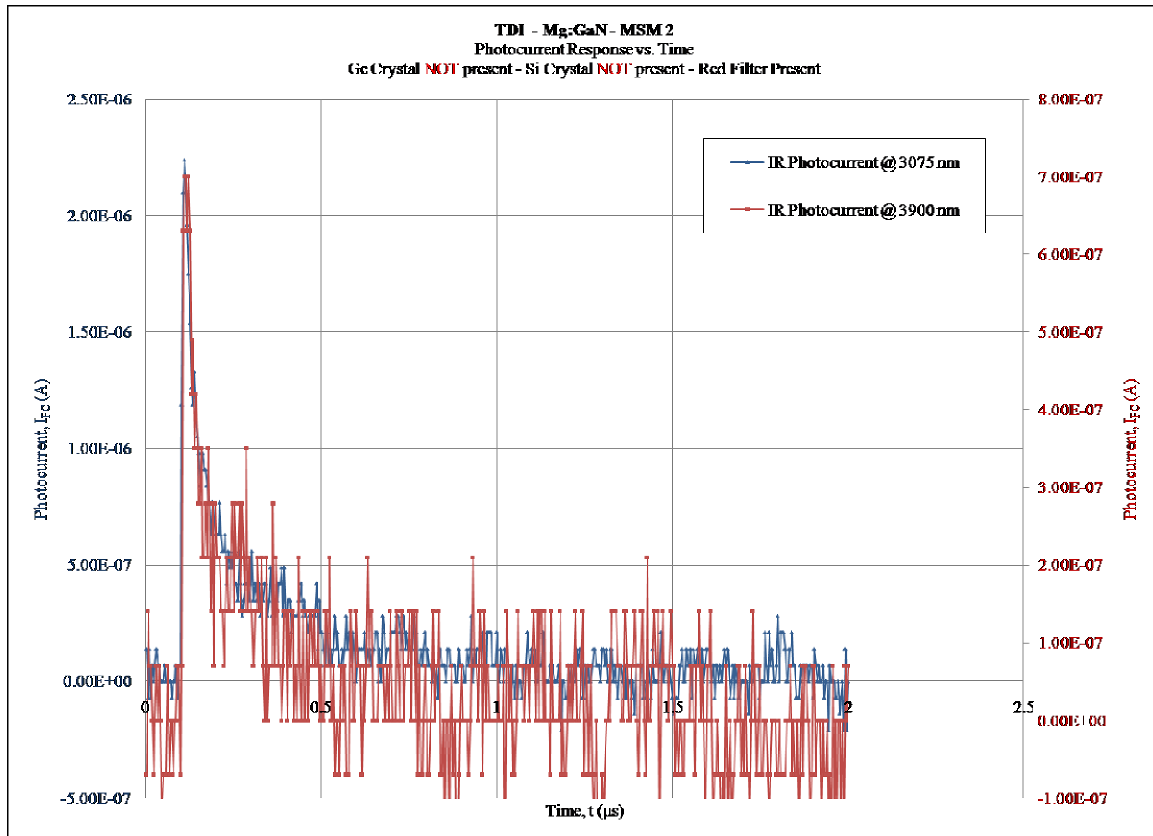

Figure 184: Time decay of the IR photocurrent response of Ni/Au MSM test structure #2 fabricated on TDI, Mg-doped GaN, as determined at the IR photocurrent peak response (3075 nm – 403 meV), and off peak response (3900 nm – 318 meV).

6.9. Effects on Forward Current and Light Output from Commercial UV III-nitride LEDs under IR Irradiation

Figure 185 shows a screenshot of the oscilloscope (Model TDS 524A, Tektronix, Beaverton, OR) with the transient enhanced UV emission (Ch2), and transient photocurrent (Ch1) of a Mid-IR pumped 365nm UV LED. The delay between photocurrent and light-pulse is due to transit time in the photomultiplier tube (PMT).

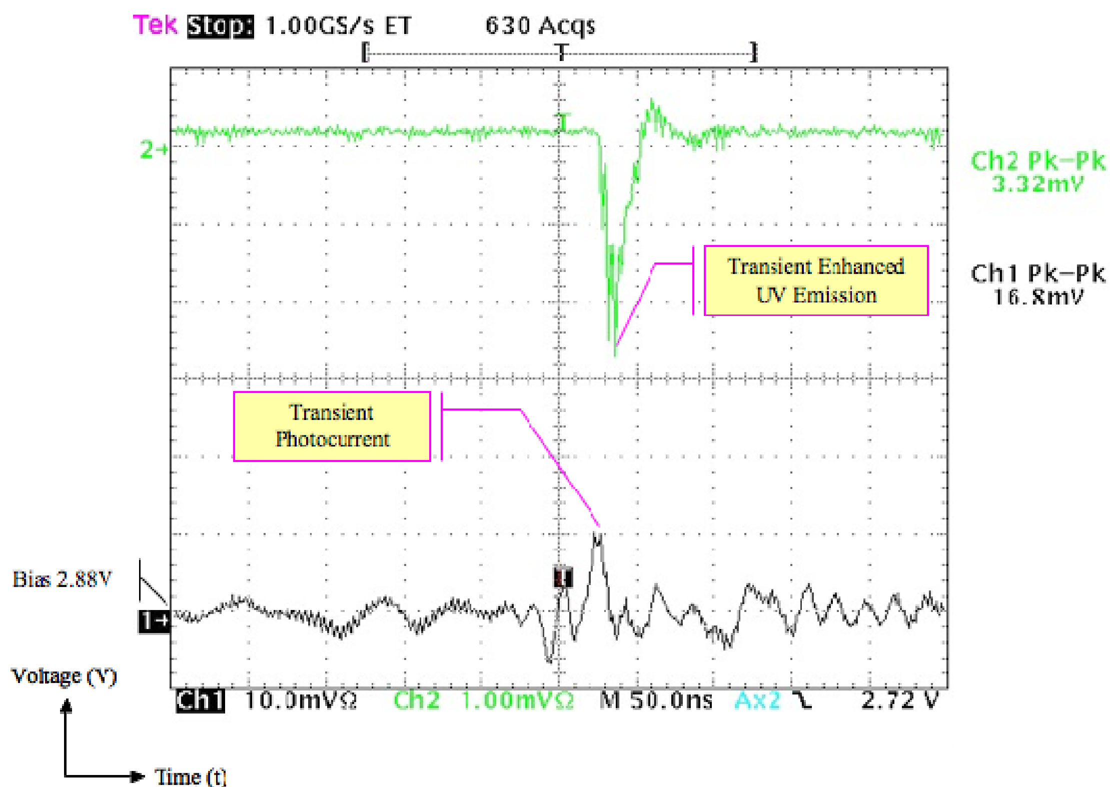

Figure 185: Screenshot of the oscilloscope (Model TDS 524A, Tektronix, Beaverton, OR) showing the transient enhanced UV emission (Ch2), and transient photocurrent (Ch1) of a Mid-IR pumped 365nm UV LED. The delay between photocurrent and light-pulse is due to transit time in the photomultiplier tube (PMT).

Figure 186 shows the OPO/OPA pulse energy available for mid-IR pumping of UV LEDs.

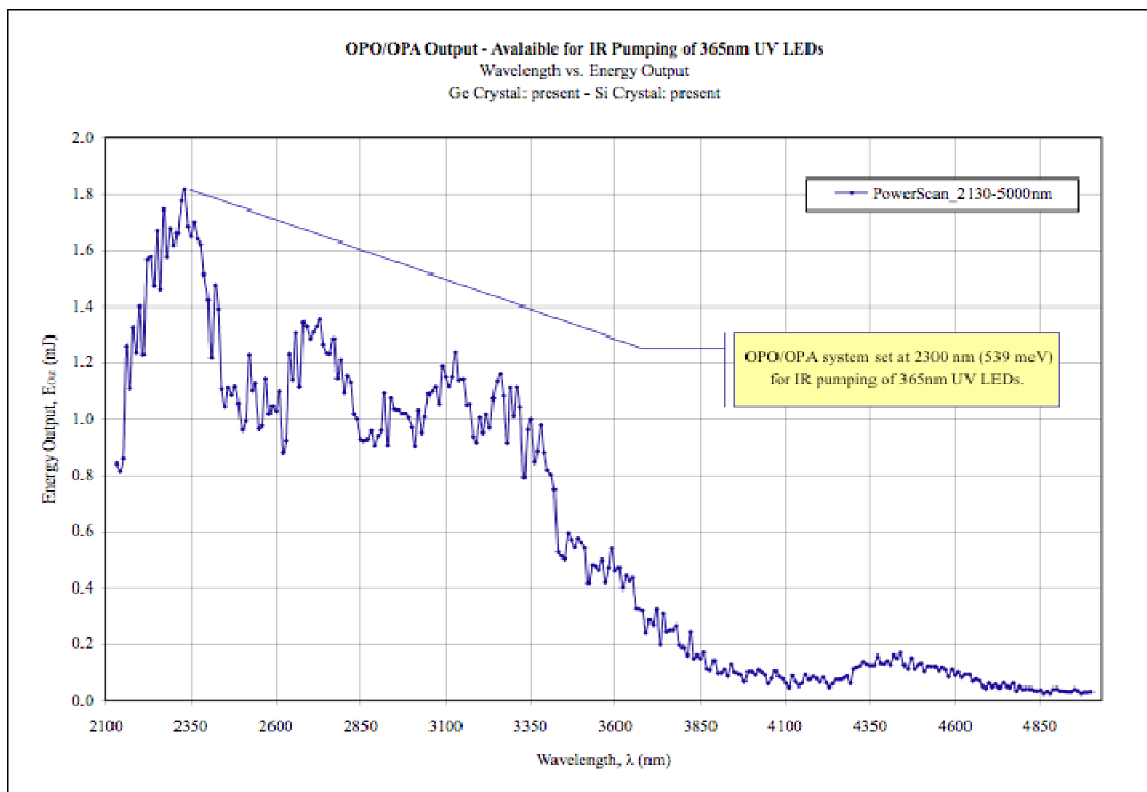

Figure 186: OPO/OPA pulse energy available for mid-IR pumping of UV LEDs.

Figure 187 shows emission spectra of a Mid-IR pumped commercial UV at nominal DC bias current over the temperature range 277 °K to 77 °K.

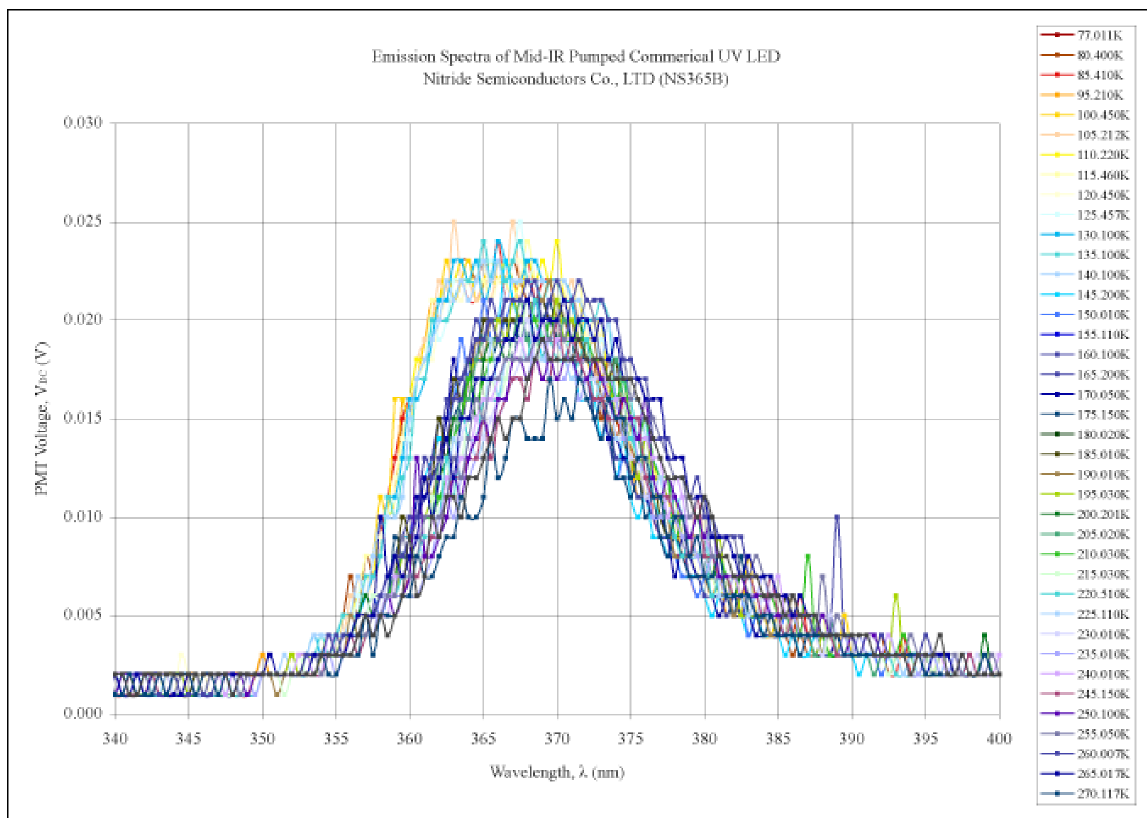

Figure 187: Emission spectra of a Mid-IR pumped commercial UV at nominal DC bias current over the temperature range 277 °K to 77 °K.

Figure 187 shows emission spectra of a Mid-IR pumped commercial UV at nominal DC bias current over the temperature range 277 °K to 77 °K.

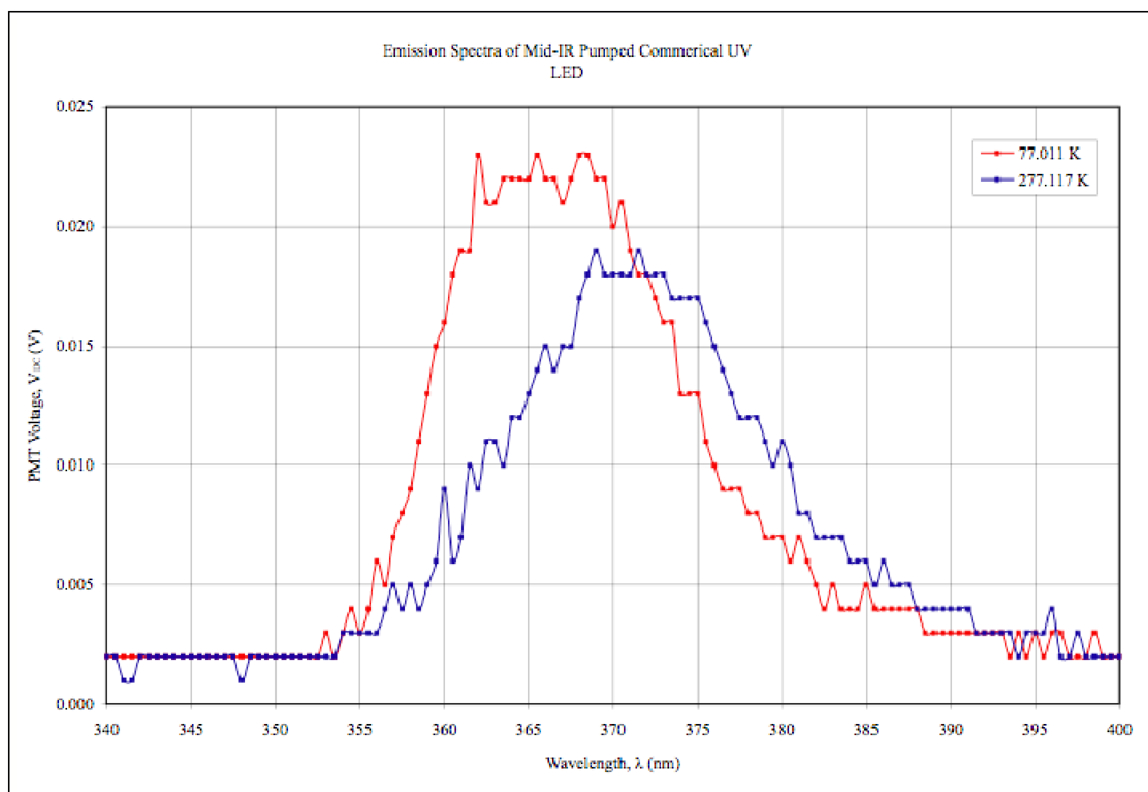

Figure 188: 277°K and 77°K spectra Emission spectra of a Mid-IR pumped commercial UV at nominal DC bias current, and dependence of peak emission photon energy on temperature.

CHAPTER 7: DISCUSSION AND CONCLUSIONS

In this work, IR photocurrent spectroscopy in Mg doped GaN, and Mg-doped $Al_xGa_{1-x}N$ ($0.15 < x < 0.52$) was conducted by means of a YAG-pumped OPO/OPA system tunable from 250 meV to 1.75 eV with the goal of observing and identifying energy levels associated with acceptor atoms of Mg in GaN and $Al_xGa_{1-x}N$. The results of the experiments performed in this work indicated that all of the Mg-doped GaN and $Al_xGa_{1-x}N$ test structures responded to IR irradiation in the wavelength range 1250 nm to 4000 nm with a photocurrent response; more precisely, a transient increase in photocurrent. Also, a non-zero photocurrent background was observed at all wavelengths. In other words, a photocurrent background response was always present, and never had a "zero magnitude". Two phenomena might explain the phenomenon of the transient, increased conductivity in the test structures investigated in this work. The first phenomenon is related to a transient, increased carrier density due to sample heating upon IR irradiation. The second phenomenon is related to a transient, increased carrier density due to IR-carrier optical pumping.

From a qualitative point of view, it is not likely that the Mg-doped GaN, and Mg-doped $Al_xGa_{1-x}N$ test structures will absorb the IR radiation ranging from 750 nm (1.65 eV) to 5000 nm (248 meV) because the GaN and $Al_xGa_{1-x}N$ films, as well as sapphire (the substrate on which the III-nitride films were epitaxially grown) are virtually transparent to the range of wavelengths above-mentioned; in addition, the OPO radiation

pulse duration is limited to only 3 ns with a rep rate of 10Hz and therefore a duty cycle of 30 parts per billion to avoid unintentional heating of the test structures. Moreover, TO5 headers (the special samples holders shown in Figure 88) were used to package the test structures; such sample holders are plated with gold, which is known to have good IR reflective properties. From a quantitative point of view, LeBoeuf *et al*. demonstrated that thermal activation of carriers, assuming thermal conduction into the GaN film by IR absorption in the sapphire substrate, is highly improbable, and that the absorbance in GaN is mostly due to dopants.[12]

The presence of a non-zero photocurrent background response to incoming IR radiation in the Mg-doped GaN, and Mg-doped $Al_xGa_{1-x}N$ investigated in this work can be associated with the presence of non-radiative, shallow native defects, and extrinsic impurities. Atoms of oxygen, which function as a shallow donors, or atoms of carbon, which function as shallow acceptors[218,219], are the kinds of extrinsic impurities that are most commonly observed; however, it might be possible that other kinds of elemental impurities are introduced during the epi-grown via source contamination. Unintentional incorporation of atoms of oxygen, and carbon typically occurs from a graphite component (crucibles, or susceptors to cite two examples) of an epitaxial growth reactor chamber, traces of oxygen in nitrogen plasma sources and/or nitrogen rich gas carriers[220]. In addition, a continuum of shallow levels with ionization energy ranging from 50 meV to 100 meV, as indicated by Seghier *et al.*[126], can be considered the cause of the above mentioned non zero photocurrent background response to incoming IR radiation in the Mg-doped GaN, and Mg-doped $Al_xGa_{1-x}N$ investigated in this work. Given that the OPO/OPA system used in this experiment allows a minimum photon energy of ~250

meV for IR photocurrent spectroscopy, no photocurrent response peaks relative to said shallow levels could be resolved.

The analysis of the data that plotted, made available in Figure 171, and organized in Table 9, suggested that the observed IR photocurrent peak response(s) for each of the Mg-doped GaN and Mg-doped $Al_xGa_{1-x}N$ test structures possibly showed a dependence on aluminum mole fraction in $Al_xGa_{1-x}N$; more precisely, we hypothesize that the data seemed to indicate that the energy depth of the observed IR photocurrent peak responses increase with increasing aluminum mole faction in $Al_xGa_{1-x}N$.

Table 9: IR photocurrent response peak of each of the test structures as a function of their aluminum mole fraction composition.

Sample ID	Al% Mole Fraction	IR Photocurrent Peak (nm)	IR Photocurrent Peak (meV)
TDI MSM [1]	0%	3175	391
ATMI MSM [7]	0%	3160	392
Honeywell MSM [1]	0%	3150	394
TDI MSM [2]	0%	3075	403
ATMI [1]	0%	3065	405
Honeywell MSM [6]	0%	3035	409
Honeywell MSM [6]	0%	2705	458
TDI MSM [2]	0%	2680	463
Honeywell MSM [1]	0%	2665	465
ATMI MSM [7]	0%	2605	476
TDI MSM [1]	0%	2605	476
ATMI MSM [1]	0%	2595	478
Epitex MSM [2]	15%	2605	476
Epitex MSM [3]	15%	2605	476
Honeywell MSM [4]	20%	2580	481
Honeywell MSM [3]	20%	2550	486
Crystal IS [D151X 1]	42%	1491	832
Crystal IS [D151X 2]	42%	1465	846
Honeywell [4a]	52%	1453	853
Honeywell [1]	52%	1430	867
Honeywell [6]	52%	1428	868
Honeywell [3]	52%	1426	870

Aluminum mole fraction dependent deep level centers have been observed by means of CV profiling, and/or cathodoluminescence spectroscopy by various groups, and reported in the literature.[218,219, 129] For the sake of this discussion, said aluminum mole fraction dependence deep levels centers were compared with the energy depth of the IR photocurrent response peaks observed in this experiment, and made available in the plot shown in Figure 189.

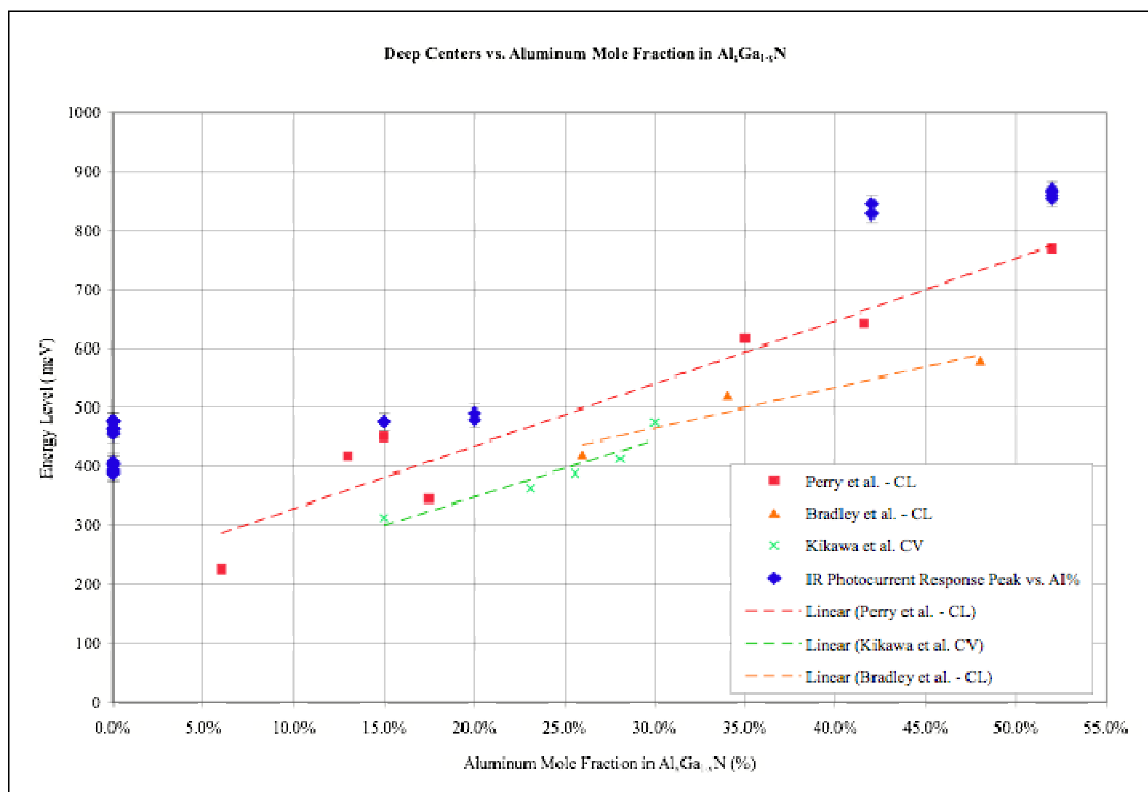

Figure 189: Comparison between the energy depth of the IR photocurrent response peaks observed in this experiment, and the energy depth of the Al mole fraction dependent deep centers observed by means of CV profiling and/or cathodoluminescence spectroscopy and reported in the literature.[218,219,129]

Again, the data comparison shown in Figure 189 could indicate that the observed IR photocurrent peak response(s) for each of the Mg-doped GaN and Mg-doped $Al_xGa_{1-x}N$ test structures possibly shows a dependence on aluminum mole fraction in $Al_xGa_{1-x}N$.

Data suggest that the energy depth of the observed IR photocurrent peak responses increase with increasing aluminum mole fraction in $Al_xGa_{1-x}N$, but it cannot be ascertained that this is a linear relationship. No test structure was fabricated on Mg-doped $Al_xGa_{1-x}N$ with an aluminum mole fraction ranging from 20% to 42%, nor was such a test structure available to be tested in terms of photocurrent spectroscopy, and so a more accurate model of the dependency cannot be confirmed at this time. Furthermore, in the graph shown in Figure 190, which plotted and compared photocurrent response peaks from test structures investigated in this experiment, an observed a peak broadening relative to the photocurrent response of low aluminum mole fraction (0% to 20%) test structures could be observed; in contrast, the peaks relative to the high aluminum mole fraction (42% to 52%) were observed to be much sharper. This observation suggested the plausible existence of two kinds of deep levels: one in the low aluminum mole fraction, and another one in high aluminum mole fraction test structures.

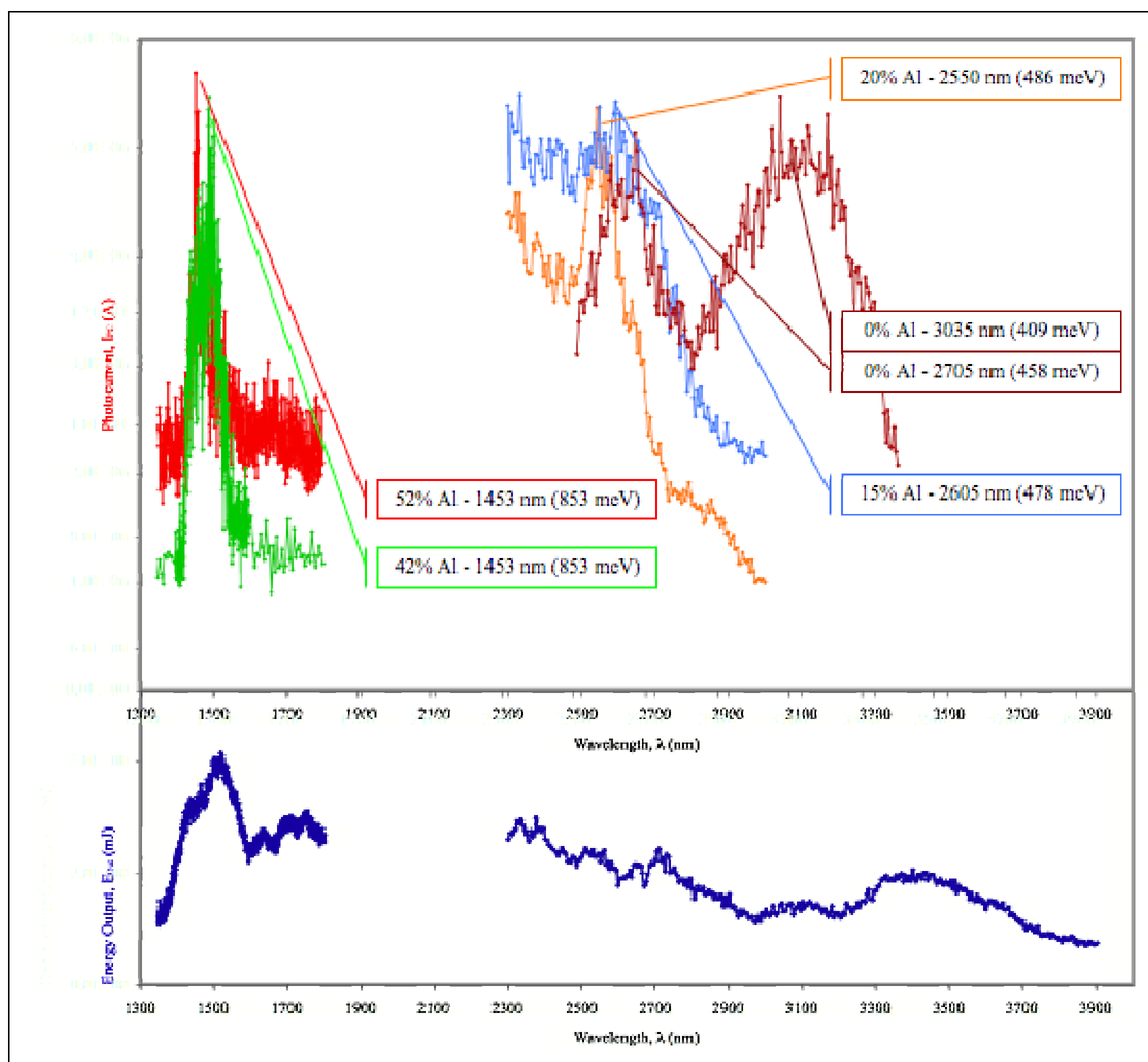

Figure 190: Comparison of photocurrent response peaks from test structures investigated in this experiment.

It is not possible at this time to determine the chemical nature of the deep centers observed in this work, although it is speculated that such deep centers can be associated with the concentration of Mg atoms incorporated in $Al_xGa_{1-x}N$, and the concentration of Mg-H complexes that survive ad-hoc anneal processes.[221] Such speculation finds some support in this thesis in light of the fact that all of the Mg-doped GaN, and Mg-doped $Al_xGa_{1-x}N$ films were grown epitaxially via MOCVD, which is a growth methodology

affected by hydrogen passivation of Mg atoms, and the formation of Mg-H complexes. In the effort to understand the electronic nature of the deep center observed in this work, a further analysis was however conducted on the results of the temperature dependent time decay of the IR photocurrent response shown in Figure 174. The graph shown in Figure 191, which plots the natural logarithm of the said time decay as a function of 1/kT, indicated that the slope of the obtained Arrhenius plot has a value of approximately 23 meV; such value is exactly that of the exciton binding energy.[222] Hence it must be assumed that the observed photocurrent response is due to electrons, considering that the Mg:GaN material is p-type and that holes are abundant in it.

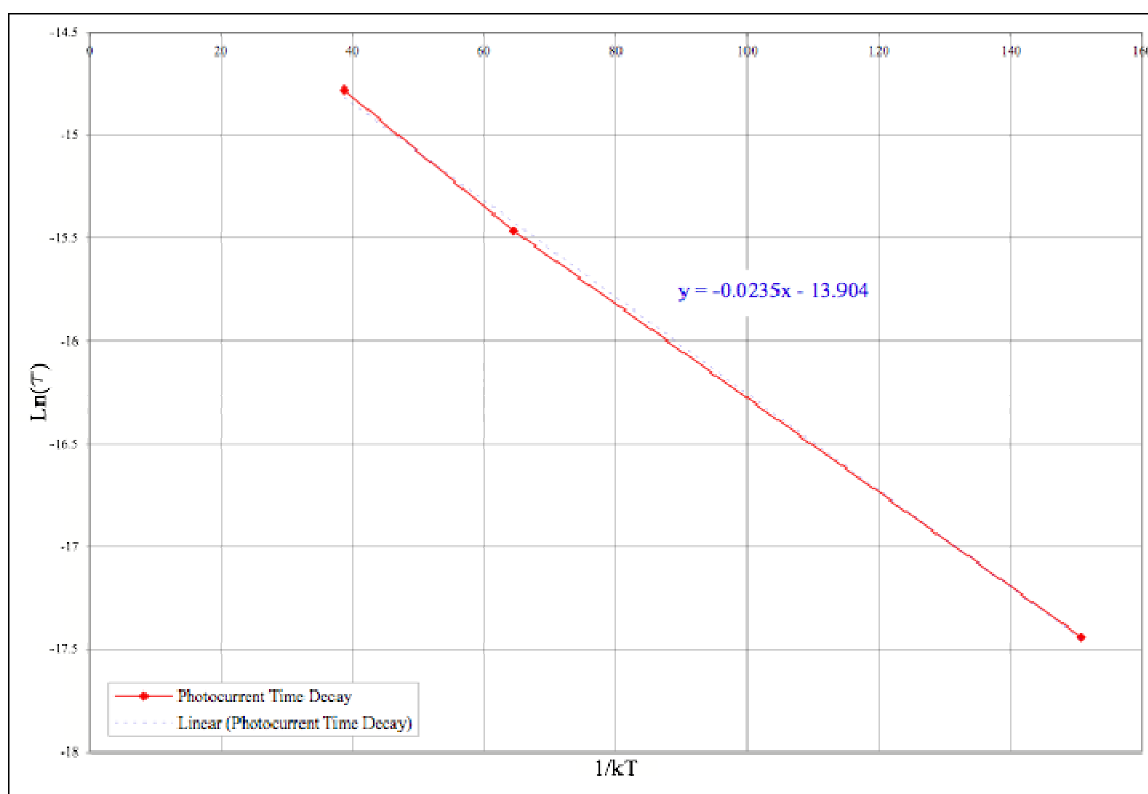

Figure 191: Arrhenius plot of the natural logarithm of temperature dependent IR photocurrent response of Ni/Au MSM test structure #1 fabricated on ATMI, Mg-doped GaN as a function of 1/kT.

From the analysis of Figure 174 through Figure 177, it was observed that at low temperature (77 °K), the photocurrent background is significantly lower than the photocurrent background at high temperature (300 °K); furthermore, it was observed that at low temperature, the magnitude of the photoexcited transient current is lower than the transient photoexcited current at high temperature. In addition, it was observed that at low temperature, time decay is of the order of ~40 ns, which is around the reported value of the minority carrier lifetime[223], whereas at high temperature the time decay is in the order of ~1000 ns, which is the value determined by Watanabe[224] for excess carrier lifetime. Assuming that IR photons excite deep donors at ~400 meV, it can be hypothesized that at 77 °K, ~400 meV photons ionize deep traps at an energy depth E_T; photoexcited electrons combine with abundant holes in p-GaN to form deep trap donor bound excitons. Carrying a net +e charge, these donor bound excitons have a large cross section, and hence short lifetime. At 300 °K, ~400 meV photons ionize deep traps at an energy depth E_T; however, since exciton energy is in the order of 20 to 30 meV, excitons do not form, ionized donors are screened by free electrons, and so donors have a smaller cross section, and a larger photocurrent lifetime. Such hypothesis is illustrated in Figure 192.

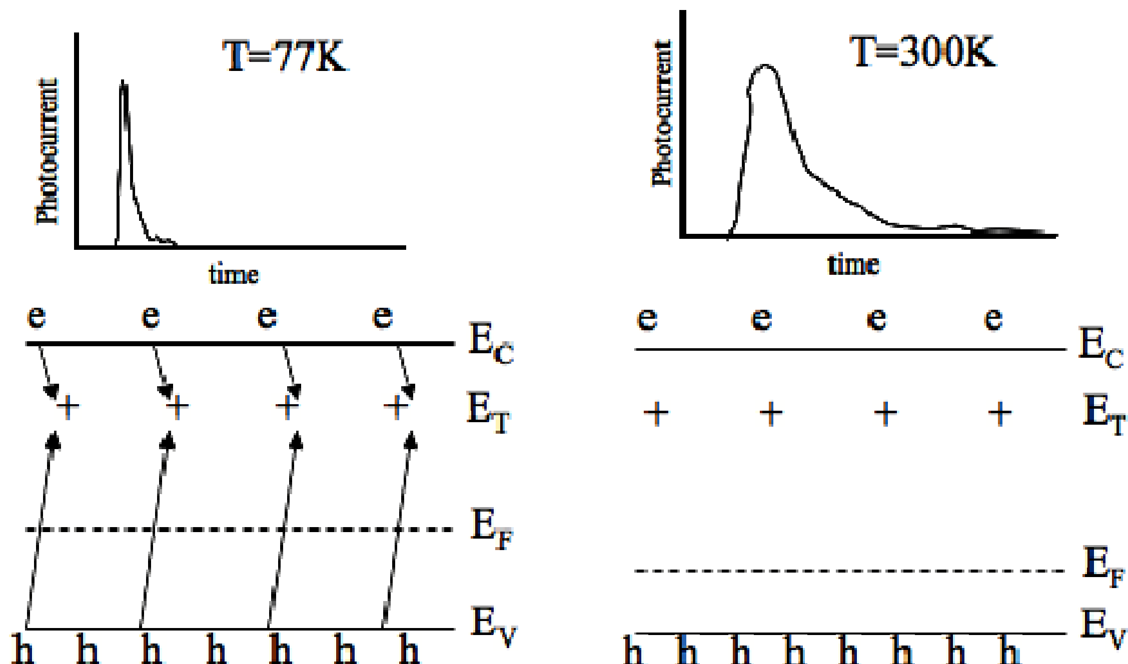

Figure 192: Schematics illustrating the proposed mechanism that explains the observations relative to results of the temperature dependent time decay of the IR photocurrent response shown in Figure 174 through Figure 177.

From the analysis of Figure 178 through Figure 184, it is observed that the room temperature time decay of the photocurrent response increased with decreasing aluminum mole fraction in $Al_xGa_{1-x}N$; more precisely, from ~40 ns for the 52%, up to 1 μs for GaN. Such phenomenon is very likely to be dominated by the value of the carrier mobility, which is known to decrease in III-nitride semiconductors as a function of increasing aluminum mole fraction. An increasing Al mole fraction is known to negatively affect the crystalline quality of $Al_xGa_{1-x}N$, and hence reduce the carrier mobility.

In this experiment, no enhanced photocurrent was observed at Mg acceptor energies; in fact, the observed energy levels of the IR photocurrent peak responses are significantly

larger than those of the Mg acceptor atoms in $Al_xGa_{1-x}N$, which have been cited in the literature, and plotted for the sake of the reader's comprehension in Figure 193.

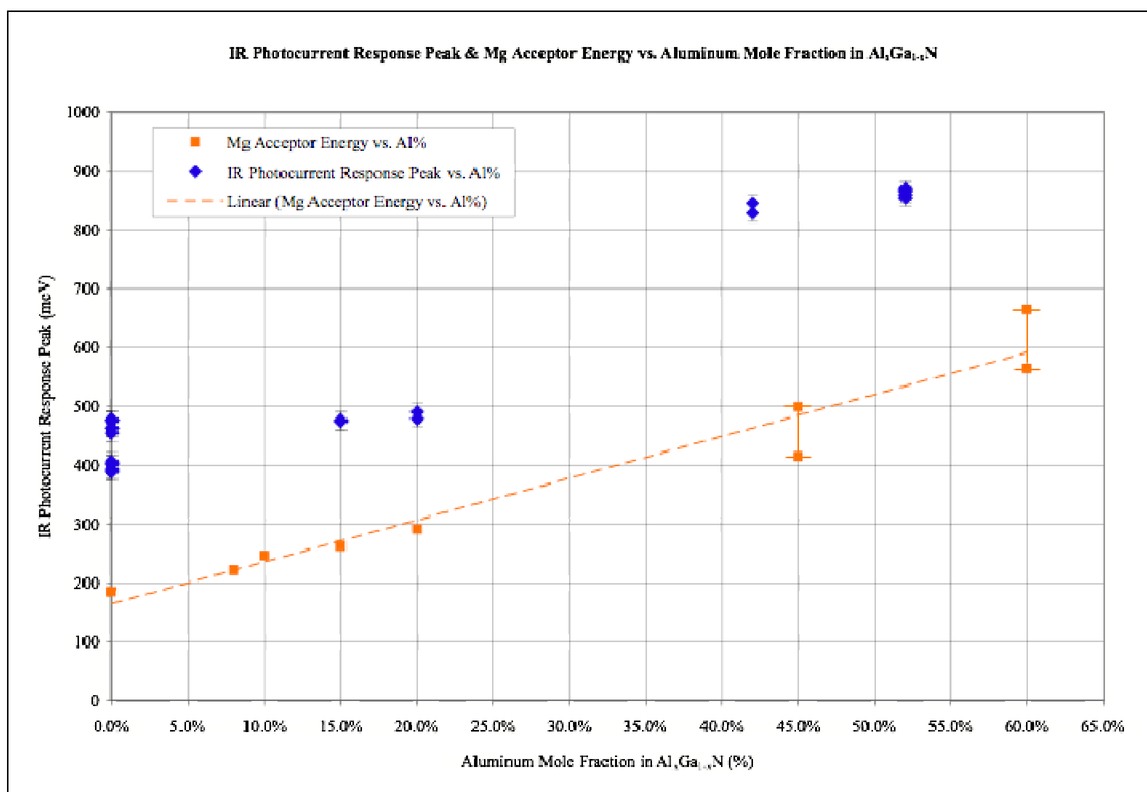

Figure 193: Plot of the IR photocurrent response peak of each of the Mg-doped GaN, and Mg-doped AlGaN test structures, and the Mg acceptor energy as a function of Al mole fraction as a extrapolated from Johnson [97].

As shown in Figure 193, the observed energy levels of the IR photocurrent peak responses are ~ 50% larger than the energy levels observed at Mg acceptor energies, and this fact should be considered as indication that the observed deep levels are not associated with acceptor ionization in Mg:GaN, and no optical ionization of Mg acceptors is observed in this experiment.

Experimental results relative to the IR optical pumping of commercial 365 nm UV LEDs however suggest that high intensity infrared can enhance conductivity and

electroluminescence,, as a transient enhancement in UV is observed in IR optically pumped, commercial 365 nm UV LEDs. In these supplemental experiments, commercial UV LEDs (NS365B - Nitride Semiconductor Co., Japan) were positively biased at a constant voltage of approximately 2.9V, and were irradiated with 2300 nm IR pulses; transient photocurrent, and UV optical output was simultaneously determined according following the schematics shown in Figure 194.

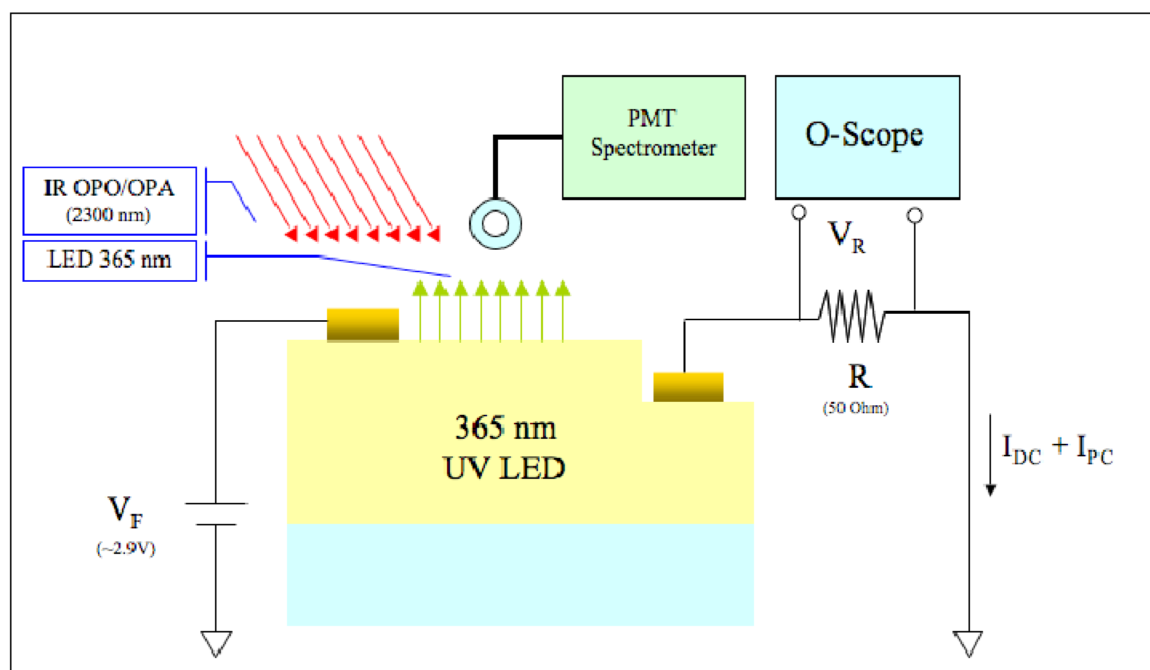

Figure 194: Schematics illustrating the test bed set up used to investigate the effects of IR optical pumping on commercial III-nitride 365nm UV LEDs.

As shown in Figure 185, both a transient IR photocurrent response, and enhanced UV optical output were observed in the IR optically pumped device; the screenshot of the oscilloscope (Model TDS 524A, Tektronix, Beaverton, OR) taken during the experiment, shows both a peak associated with the transient UV emission (Ch2), and a peak associated with the transient photocurrent (Ch1). The peak associated with the transient UV emission is delayed with respect to that of the transient photocurrent; this delay was

caused by the transit time in the photomultiplier tube. The experimental result of this supplemental experiment is significant, as it indicated that the transient UV emission could be plausibly caused by a transient excess hole concentration in under IR irradiation. In fact, the emission of III-nitride heterostructure UV (and Deep UV LEDs for that matter) is limited by low-hole concentration of its p-type layers; not by the electron concentration of its n-type layers.

Experimental results relative to the temperature dependent study of transient, enhanced UV emission from IR optically pumped, commercial 365 nm UV LEDs (shown in Figure 187) indicates that a transient, enhanced optical output is achieved even at very low temperature (77°K). This observation also suggests that thermal activation of carrier, or generation of electron-hole pairs is not likely in this experiment. In addition, as shown in Figure 188, a blue shift is observed in the transient UV output peak of optically pumped, commercial 365 nm UV LEDs at (77°K); temperature induced blueshift/redshift behavior is typical of all heterostructure based LEDs.

In conclusion, IR photocurrent spectroscopy is reported on test structures fabricated on Mg-doped GaN, and Mg-doped $Al_xGa_{1-x}N$ ($0.15 < x < 0.52$) by using a YAG-pumped OPO/OPA tunable from 250 meV to 1.75 eV, with the intention of identify energy levels associated with Mg in magnesium-doped GaN and $Al_xGa_{1-x}N$. Infrared photocurrent spectra are presented, and a non-zero background response was associated with shallow extrinsic impurities and/or a continuum of shallow levels with ionization energy ranging from 50 meV to 100 meV. In addition, peaks in the photocurrent response obtained from test structures are observed and associated with deep level donors. No evidence of acceptor ionization in magnesium-doped GaN and $Al_xGa_{1-x}N$ were observed. Finally,

experimental results on IR pumping of commercial 365nm UV LEDs indicate that an infrared enhanced UV optical output can be achieved.

7.1. Future Work

In this dissertation, photocurrent spectroscopy was conducted with the intention of observing and identifying energy levels associated with acceptor atoms of magnesium in Mg-doped $Al_xGa_{1-x}N$ with an aluminum mole fraction ranging 0% to 52%. Photocurrent response peaks at Mg energy levels in Mg-doped GaN, and $Al_xGa_{1-x}N$ would be expected to indicate transient optical ionization of acceptor atoms in III-nitride, and enable improved device performance through IR optical pumping in heterostructure LEDs and other p-n junction based devices. Furthermore, this would enable the creation of new class of optically pumped optoelectronic devices with enhanced performance, one extra degree of freedom, and the capability of controlling and modulating doping levels in wide bandgap materials, by generating transient excess carriers. However, the results of these experiments were not conclusive, as no photocurrent peak response was observed at Mg energy levels in Mg-doped GaN, and $Al_xGa_{1-x}N$.

The properties of III-nitrides, and GaN $Al_xGa_{1-x}N$ in particular, can vary greatly as a function of the epi-growth methodology; MOCVD, MBE, or HVPE to cite a few of them. In addition, properties of said compound semiconductors are affected by both technical, and human factors even when the same epi-growth methodology is used; in other words, no two reactors are created equal, nor are the epi-engineers that operate such reactors. Hence, future photocurrent spectroscopy should be conducted on homogeneous test structures; more precisely, test structures fabricated on Mg-doped GaN and $Al_xGa_{1-x}N$ films grown with the same exact condition, with the same epi-reactor. This kind of

experiment could be accomplished at UNC Charlotte in the near future in light of the fact that new III-nitride epi-growth reactors have been recently installed, or are in the process being installed. Granted that there is an established capability of growing ad-hoc III-nitride films, or the opportunity of having them made available by a collaborating third party, future work should deepen the investigation of the deep levels observed in this work, and verify their dependence on Al mole fraction.

Further work is also needed in order to understand the mechanism that enables transient, enhanced UV emission in heterostructure based UV LEDs, which was observed in this experiment, but which are not fully understood. This finding in particular may have a tremendous potential in terms of development of UV and Deep UV emitters and sensors, which is currently curbed by a lack of operating devices, and/or devices that operate at an unsatisfactory level in terms of optical power output or detection. Future investigations of IR pumping based III-nitride LEDs, with a well-defined and fully characterized heterostructure, should hence be conducted. Currently, a fundamental drawback of investigating the effects of IR pumping on forward biased commercial UV LEDs is that the information of their heterostructure is adamantly protected by either a trade secret, or intellectual property rights; without having access to this kind of information, attempts at modeling and predicting the mechanism that leads to the IR pumped, transient, enhanced UV emission would be virtually futile. Having stated that, future work on IR pumping on heterostructure LEDs should involve the fabrication of such devices preferably on campus, or by courtesy of a collaborating research group, if it can be arranged.

Finally, further work is necessary to determine the minimum level of IR optical input required by III-nitride heterostructure based LEDs and other p-n junction based devices to enable enhanced performance. This task will require the understanding of the phenomenon, and its modeling so that it will be possible to predict it.

REFERENCES

[1] Y. S. Park, "Wide bandgap III-Nitride semiconductors: opportunities for future optoelectronics", *Opto-electronics Review* 9(2), 117-124 (2001).

[2] M. Wraback, G. A. Garrett, A. V. Sampath, C. J. Collins, and H. Shen, "Make light, not heat: towards higher efficiency nitride semiconductor ultraviolet optical sources", *Proc. SPIE Int. Soc. Opt. Eng.* 5617, 209-220 (2004).

[3] A. Bensaula, D. Starikov, and C. Boney, "III-Nitrides-on-Silicon Chips for Detection of Live Bacteria in Enclosed Space Environments", Institute for Space Systems Operations 2001 Annual Report p. 72-76 Substrates" *NASA Contract No. NAS 3-22235 June 1983* (2001).

[4] D. Bykhovski, V. V. Kaminski, M. S. Shur, Q. C. Chen, and M. A. Khan, "Pyroelectricity in gallium nitride thin films", *Appl. Phys. Lett*. 69, 3254 (1996).

[5] H. Y. Zhang, X. H. He, Y. H.. Shih, M. Schurman, Z. C. Feng. And R. A. Stall, "Study of nonlinear optical effects in GaN:Mg epitaxial film", *Appl. Phys. Lett.* 69, 2953 (1996).

[6] J. Miragliotta, D. K. Wickenden, T. J. Kistenmacher, and W. A. Bryden, "Linear- and nonlinear- optical properties of GaN thin films", *J. Opt. Soc. Am.* B10, 1447 (1993).

[7] V. Tilak, P. Batoni, J. Jiang, and K. Knobloch, "Measurement of piezoelectric coefficient of gallium nitride using metal-insulator-semiconductor capacitors", *App. Phys. Lett.* 90, 043508 (2007).

[8] C. H. Ko *et al.,* "Photo-enhanced chemical wet etching of GaN", *Materials Science and Engineering*, N96 (2002).

[9] S. Montanari, "Fabrication and Characterization of Planar Gunn diodes for Monolithic Microwave Integrated Circuits", *Doctoral Dissertation,* University of Aachen, RWTH, Germany (2005).

[10] R. Kravets, M. Vanecek, C. Piccirillo, A. Mainwood, and M. E. Newton, "A quantitative study of the boron acceptor in diamond by Fourier-transform photocurrent spectroscopy", *Diamond & Related Materials* 13, 1785-1790 (2004).

[11] K. Hyunjung, M. Grimsditch, T. R. Anthony, A. K. Ramdas, and S. Rodriguez, "Infrared and Raman spectroscopy of acceptors in diamond: boron impurities", *Phys. Stat. Sol. (a)* 181, 51, (2000).

[12] S. F. LeBoeuf, E. B. Stokes, X. A. Cao, A. Ebong, and P. M. Sanvik, "Optical acceptor ionization in III-Nitrides", *Proc. ECS.* PV2002-2, 164 (2002).

[13] E. F. Schubert, Light Emitting Diodes, "LED Basics: electrical properties", Light-Emitting Diodes, 2nd Ed. Cambridge University Press (2006).

[14] E. Tiede, M. Thimann, K. Sensse, "Über phosphorescenzfähiges, durch Silicium aktiviertes Aluminumnitrid", *Chem. Berichte* 61, 1568 (1928).

[15] W. C. Johnson, J. B. Parson, M. C. Crew, "Nitrogen Compounds of Gallium III", *J. Phys. Chem.* 36, 2561 (1932).

[16] TDI, Techologies & Devices International, Inc. (Oxford Instruments), 12214 Plum Orchard Drive, Silver Spring, MD 20904, USA.

[17] Kyma Technologies, Inc., 8829 Midway West Road, Raleigh, NC 27617, USA.

[18] Lumilog, 2710 Chemin Saint Bernard, Les Moulins I, F-06220 Vallauris, France.

[19] Crystal IS, Inc., 70 Cohoes Avenue, Green Island, NY 12183, USA.

[20] H. Morkoç, Nitride Semiconductors and Devices, Springer Series in Material Science 32, R. Hull, R. M. Osgood Jr., H. Sakaki, and A. Zunder Eds. (1999).

[21] T. Yamane, F. Satoh, H. Murakami, Y. Kumagai, and A. Koukitu, "Growth of thick $Al_xGa_{1-x}N$ ternary alloy by hydride vapor-phase epitaxy", *J. Crys. Grow.* 300, 164-167 (2007).

[22] J. R. Creighton, G. T. Wang, and M. E. Coltrin, "Fundamental chemistry and modeling of group-III nitride MOVPE", *J. Crys. Grow.* 298, 2-7, (2007).

[23] X. L. Wang, d. G. Zhao, U. Jahn, K. Ploog, D. S. Jiang, H. Yang, and J. W. Liang, "The effects of LT AlN buffer thickness of the optical properties of AlGaN grown by MOCVD and Al composition inhomogeneity analysis", *J. Phys. D: Appl. Phys.* 40, 1113-1117 (2007).

[24] M. A. L. Johnson, Z. Yu, J. D. Brown, F. A. Koeck, N. A. El-Masry, H. S. Kong, J. A. Edmond, J. W. Cook Jr., and J. F. Schetzina, 'A critical comparison between MOVPE and MBE growth of III-V nitride semiconductor materials for opto-electronic device applications", *MRS Internet J. Nitride Semicond. Res.* 4S1, G5.10 (1999).

[25] T. Tanaka, A. Watanabe, H. Amano, Y. Kobayashi, I. Akasaki, S. Yamazaki, M. Koike, "p-type conduction in Mg-doped GaN and $Al_{0.08}Ga_{0.92}N$ grown by metalorganic vapor phase epitaxy", *Appl. Phys. Lett.* 65, 593 (1994).

[26] M. Suzuki, J. Nishio, M. Onomura, and C. Hongo, "Doping characteristics and electrical properties of Mg-doped AlGaN grown by atmospheric-pressure MOCVD", *J. Crys. Grow.* 189, 511 (1998).

[27] Lange's Handbook of Chemistry, 14th ed. (McGraw-Hill, New York, 1992).

[28] W. Kim, O. Aktas, A. E. Botchkarev, A. Salvador, S. N. Mohammad, H. Morkoç, "Reactive molecular beam epitaxy of wurtzite GaN: materials characteristics and growth kinetics", *J. Appl. Phys.* 79, 7657 (1994).

[29] W. C. Ke, C. S. Ku, H. Y. Huang, W. C. Chen, L. Lee, W. K. Chen, W. C. Chou, W. H. Chen, M. C. Lee, W. J. Lin, Y. C. Cheng, and Y. Y. Cherng, "Microphotoluminescence spectra of hillocks in $Al_{0.1}Ga_{0.89}N$ films", *Appl. Phys. Lett.* 85, 3047 (2004).

[30] R. N. Jacobs, L. Salamanca-Riba, M. He, G. L. Harris, P. Zhou, S. N. Mohammad, and J. B. Halpern, "Structural characterization of GaN nanowires fabricated via direct reaction of Ga vapor and ammonia", *Mat. Res. Soc. Symp. Proc.* 675, W9.4 (2001).

[31] T. J. Kropewnicki, and P. A. Kohl, "Hydrazine cyanurate as a nitrogen source for thin nitride film growth", *J. Vac. Sci. Technol.* 16, 1 (1998).

[32] S. A. Nikishin, H. Temkin, V. G. Antipov, A. I. Guriev, A. S. Zubrilov, V. A. Elyukhin, N. N. Faleev, R. N. Kyutt, and A. K. Chin, "Gas source molecular beam Epitaxy of GaN with hydrazine on spinel substrates", *Appl. Phys. Lett*. 72, 3261 (1998).

[33] V. G. Antipov, A. I. Guriev, V. A. Elyukhin, N. N. Faleev, Yu. A. Kudriavtsev, A. B. Lebedev, T.V. Shubina, A. S. Zubrilov, S. A. Nikishin, and H. Temkin, "GaN/GaAs(111)B grown by molecular beam Epitaxy using hydrazine", *Compound Semiconductor, 1997 IEEE International Symposium on Volume*, Issue, 8-11, Page(s) 15-23, (1997).

[34] S. Yuge, and H. Sugawara, "Megthod for manufacturing a GaN-based compound semiconductor light emitting device", *US Patent* 6,030,848 (2000).

[35] H. Amano, and A. Bando, "AlGaN substrate and production method thereof", *US Patent Application Publication* US 206/0225643 A1 (2006).

[36] Y. Ohba, T. Izumiya, and A. Hatano, 'AlGaN compound semiconductor material", *US Patent 5,076,860* (1991).

[37] T. Nagai, T. Kawashima, M. Imura, M. Iwaya, S. Kamiyama, H. Amano, and I. Akasaki, "Microstructure in nonpolar m-plane GaN and AlGaN films", *J. Crys. Grow.* 298, 288-292, (2007).

[38] C. N. Chen, K. F. Yarn, S. H. Chang, M. L. Hung, J. C. Chiang, I. Lo, W. T. Wang, M. H. Gau, H. F. Kao, and M. E. Lee, "On the giant anisotropy observed in m-plane GaN/AlGaN quantum wells by crystal-field effect", *CSICT-2006: 2006 8th International Conference on Solid-State and Integrated Circuit Technology, Proceedings*, *ICSICT-2006: 2006 8th International Conference on Solid-State and Integrated Circuit Technology, Proceedings*, 1459-1461 (2007).

[39] S. L. Selvarai, and T. Egawa, "Demonstration of AlGaN/GaN high electron mobility transistors on a-plane sapphire", *Japanese Jour. Appl. Phys.* Part 1, 47, 3332-3335 (2008).

[40] N. Imer, M. Schmidt, B. Haskell, S. Rajan, B Zhong, K. Kim, F. Wu, T. Mates, S. Keller, U. K. Mishra, S. Nakamura, J. S Speck, S. P. DenBaars, "Improved quality nonpolar a-plane GaN/AlGaN UV LEDs grown with sidewall lateral epitaxial overgrowth (SLEO), *Physica Status Solidi A*, 205, 1705-1712 (2008).

[41] M. Tsuda, H. Furukawa, A. Honshio, M. Iwaya, S. Kamiyama, H. Amano, and I. Akasaki, "Anisotropically, biaxial strain in a-plane AlGaN on GaN grown on r-plane", *Japanese J. Appl. Phys.* Part 1, 45, 2509-2513 (2006).

[42] M. A. Khan, Q. Chen, J. Yang. C. J. Sun, B. Lim, H. Temkin, J. Schetzina, and M. S. Shur, "UV, blue and green light emitting diodes based on GaN-InGaN multuple quantum wells over sapphire and (111) spinel substrates", *Materials Science & Engineering B* B43, 265-268 (1997).

[43] B. G. Streetman, and S. Banerjee, "The Hall Effect", Solid State Electronic Devices, 5th Ed., Prentice Hall, Upper Saddle River, NJ, 100-102

[44] W. Shockley, "Research and investigation of inverse epitaxial UHF power transistors," *Report No. Al-TOR-64-207*, Air Force Atomic Laboratory, Wright-Patterson Air Force Base, Ohio (1964).

[45] S. A. Bashar, "Study of indium tin oxide (ITO) for novel optoelectronic devices", *Doctoral Dissertation*, King's College, London, UK (1998).

[46] H. H. Berger, "Contact resistance on diffused resistor", *IEEE International Solid-State Circuits Conference*, Session XIII, 160-169 (1969).

[47] H. H. Berger, "Models for contacts to planar devices', *Solid State Electronics* 15, 2, 145-158 (1972).

[48] G. K. Reeves, "Specific contact resistance using a circular transmission line model", *Solid-State Electron.* 23, 487-490 (1980).

[49] J. Kriz, K. Gotterfield, C. Kaufmann ,and T. Gessner, “Determination of ohmic contacts on n-type 6H – polycrystalline 3C-SiC using circular transmission line structures”, *Diamond Relat. Matter* 7 (1), 11-80 (1998).

[50] S. Xue, Y. Han, Z. Wu, and Y. Lou,” Measurement of specific contact resistivity of ohmic contact on p-GaN”, *Chin. Journ. Semicond.* 26, 5, 965-969 (2005).

[51] C. Xu. Chuan, J. Wang, M. Wang, H. Jin, Y. Hao, and C. Wen, “Reeves’s circular transmission line model and its scope of application to extract specific contact resistance”, *Solid-State Electon.* 50, 843-847 (2006).

[52] G. S. Marlow, M.B. Das, “The effects of contact size and non-zero metal resistance on the determination of specific contact resistance”, *Solid-State Electron.* 25, 2, 91-94 (1982)

[53] A. Weimar, A. Lell, G. Bruderl, S. Bader, V. Harle, “Investigation of low-reistance metal contacts pn p-type GaN using the linear and circular transmission line method”, *Phys. Sta. Sol. (a)* 183,169-175 (2001)

[54] J. H. Klootwijk, C. E. Timmering, “ Merits and limitation of circular TLM structures for contact resistace determination for novel III-IV HBTs”, *Proc. IEEE Int. Conference on Microelectronic Tests Stuctuctures*, Vol 17, 247-252 (2004)

[55] B. Jacobs, M. C. J. C. M. Kramer, E. J. Geluk, F. Karouta, “Optimization of the Ti/Al/Ni/Au ohmic contacts on AlGaN/GaN FET structures”, *Journ. Crystal Growth* 241, 15-18 (2001)

[56] D. Mistele, F. Fedler, H. Klausing, T. Rotter, J. Stemmer, O. K. Semchinova, J. Aderhold, “ Investigation of Ni/Au contacts on p-GaN annealed in different atmospheres”, *Journ. Crystal Growth* 230, 564-568 (2001)

[57] H. Murramann, and D. Widmann, “Current crowding on metal contacts to planar devices”, *IEEE Trans. Elect. Dev* ED-16, No. 12, 1022-1024 (1969)
[58] H. P. Maruska, and J. J. Tietjen,”Preparation and properties of vapor-deposited single crystalline GaN”, *Appl. Phys. Lett.* 15, 327 (1969).

[59] H. Amano, M. Kito, K. Hiramatsu, and I. Akasaki, “Gallium arsenide and related compounds”, 1989 (eds) T. Ikoma, H. Watanabe, Bristol UKIOP 725 (1990).

[60] F. Wang, J. Li, S. S. Li, Xia J. B., and S. H. Wei, “Mg acceptors energy levels in AlxInyGa1-x-yN quaternary alloys: an approach to overcome the p-type doping bottleneck in nitrides”, *Phys. Rev. B.* 77, 113202 (2008).

[61] S. H. Wei, “Overcoming the doping bottleneck in semiconductors”, *Comput. Mater. Sci.* 30, 337 (2004).

[62] C. G. Van de Walle, and J. Neugebauer,"First-principles calculations for defects and impurities: applications to III-nitrides", *J. Appl. Phys.* 95, 3851 (2004).

[63] Y. Yan, J. Li, S. H. Wei, and M. M. Al-Jassim," Possible approach to overcome the doping asymmetry in wideband gap semiconductors", *Phys. Rev. Lett.* 98, 135506 (2007).

[64] C. G. Van de Walle, "Electrical conductivity control", Introduction to Nitride Semiconductor Blue Lasers and Light Emitting Diodes, Ed. S. Nakamura, and S. F. Chichibu, Taylor & Francis, New York, NY 10001, 67-90 (2000).

[65] D. C. Look, D. C. Reynolds, J. W. Hemsky, J. R. Sizelove, R. L. Jones, and R. J. Molnar, "Dislocation scattering in GaN", *Phys. Rev. Lett.* 79, 2273 (1999).

[66] J. Neugebauer, and C. G. Van de Walle, "Defects and doping in GaN", *Proceedings of the 22th International Conference on the Physics of Semiconductors*, edited by D. J. Lockwood (World Scientific Publishing Co Pte Ltd., Singapore), 2327 (1994).

[67] J. Neugebauer, and C. G. Van de Walle, "Role of defects in doping of GaN", *Proc. 23rd Int. Conf. Physics of Semiconductors*, Ed. M. Scheffler, and R. Zimmerman, World Scientific Publishing, Co Pte Ltd., Singapore, 2877 (1996).

[68] V. Fiorentini, F. Bernardini, A. Bosin, and D. Vanderbilt, *Proc. 23rd Int. Conf. Physics of Semiconductors*, Ed. M. Scheffler, and R. Zimmerman, World Scientific Publishing, Co Pte Ltd., Singapore, 2849 (1996).

[69] F. Bernardini, V. Fiorentini, and A. Bosin, "Theoretical evidence for efficient p-type doping of GaN using beryllium", *Appl. Phys. Lett.* 70, 2990 (1997).

[70] F. Mireles, and S. E. Ulloa, *Phys. Rev. B* 58, 3870 (1998).

[71] A. K. W. Salvador, Aktas Ö, Botchkarev A., Fan Z., and Morkoç H., "Near ultraviolet luminescence of Be doped GaN grown by reactive molecular beam epitaxy using ammonia", *Appl. Phys. Lett.* 69, 2696 (1996).

[72] F. J. Sánchez , F. Calle , M. A. Sánchez-Gárcía, E. Celleja, E. Muňoz, C. H. Molloy, D. J. Someford, F. K. Koschnick, K.. Michael, and J. M Spaeth," Luminescence of Be-doped GaN layers grown by molecular beam epitaxy on Si (111)", *Mater. Res. Soc. Internet J. Nitride* Semicond. Res. 3, 19 (1998).

[73] O. Brandt, H. Yang, H. Kostail, and K. H. Ploog, "High p-type conductivity in cubic GaN/GaAs(113)A by using Be as the acceptor and O as the codopant", *Appl. Phys. Lett.* 69, 2692 (1996).

[74] K. H. Ploog, and O. Brandt, "Doping of group III nitrides", *J. Vac. Sci. Technol. A.* 16, p. 1609 (1998).

[75] S. Nakamura, N. Iwasa, and S. Nagahama, "Cd-doped InGaN films grown on GaN films", *Jpn. J. Appl. Phys.* 32, L139 (1993).

[76] J. W. Lee, S. J. Pearton, J. C. Zolper, and R. A. Stall, "Hydrogen passivation of Ca acceptors in GaN", *Appl. Phys. Lett.* 68, 2102 (1996).

[77] J. I. Pankove, and J. A. Hutchby, "Photoluminescence of ion-implanted GaN", *J. Appl. Phys.* 47, 5387 (1976).

[78] E. Ejder, and H. G. Grimmeiss, "Optical investigation of Zn, Hg, and Li doped GaN", *J. Appl. Phys.* 5, 275 (1974).

[79] P. Boguslawski, E. L. Brigs, and J. Bernholc, "Amphoteric properties of substitutional carbon impurity in GaN and AlN", *Appl. Phys. Lett.* 69, 233 (1996).

[80] P. Boguslawski, and J. Bernholc, *Phys. Rev. B* 56, 9496 (1997).

[81] S. Fisher, C. Wetzel, E. E. Haller, and B. K, Meyer, "On p-Type Doping in GaN - Acceptor Binding Energies", *Appl. Phys. Lett.* 67, 1298 (1995).

[82] J. Neugebauer, and C. G. Van de Walle, *Festkörperprobleme/Advances in Solid State Physics* 35, Ed. R. Helbig R. (Braunschweig/Wiesbaden: Vieweg) 25 (1996).

[83] S. Nakamura, M. Senoh, and T. Mukai, "Highly P-Typed Mg-Doped GaN Films Grown with GaN Buffer Layers", *Jpn. J. Appl. Phys.* 30, L1708 (1991).

[84] A. Saxler, W. C. Mitchel, P. Kung, and M. Razeghi," Aluminum gallium nitride short-period superlattices doped with magnesium", *App Phys Lett.* 74, 2023 (1999).

[85] S. Nakamura, and S. F. Chichibu, Introduction to Nitride Semiconductor Blue Lasers and Light Emitting Diodes, Taylor & Francis, New York, NY 10001, 67-97 (2000).

[86] D. P. Bour, H. F. Chung, W. Götz, L. Romano, B. S. Krusor, D. Hofstetter,S. Rudaz, C. P. Kuo, F. A. Ponce, N. M. Johnson, M. G. Craford, and R. D. Bringans," Characterization of OMVPE-grown AlGaInP heterostructures", *Mat. Res. Soc. Symp. Proc*. 449, 509-518 (1997).

[87] J. W. Huang, T. F. Kuech, H. Lu, and I. Bhat," Electrical characterization of Mg-doped GaN grown by metalorganic vapor phase epitaxy", *Appl. Phys. Lett.* 68, 2392 (1996).

[88] C. Johnson, J. Y. Lin, H. X. Jiang, M. Asif Khan, and C. J. Sun, "Metastability and persistent photoconductivity in Mg-doped p-type GaN", *Appl. Phys. Lett.* 68, 1808, 1996.

[89] M. Katsuragawa, S. Sota, M. Komori, C. Anbe, Tetsuya Takeuchi, H. Sakai, H. Amano, and I. Akasaki, "Thermal ionization energy of Si and Mg in AlGaN", *J. Crys. Growth*, 189-190, 528-531(1998).

[90] W. Götz, R. S. Kern, C. H. Chen, H. Liu, D. A. Steigerwald, and R. M. Fletcher, "Hall-effect characterization of III-V nitride semiconductors for high efficiency light emitting diodes", *Mater. Sci. and Engin.* B 59, 211-217 (1999).

[91] D. Seghier, and H. P. Gislason, "Electrical characterization of Mg-related energy levels and the compensation mechanism in GaN:Mg", *Appl. Phys. Lett.* 88, 6483 (2000).

[92] Y. Nakano, and T. Jimbo," Electrical characterization of acceptor levels in Mg-doped GaN", *J. Appl. Phys.* 92, 5590 (2002).

[93] M. Smith, G. D. Chen, J. Y. Lin , and H. X. Jiang, A. Salvador , B. N. Sverdlov , A. Botchkarev , and H. Morkoç, B. Goldenberg, "Mechanisms of band-edge emission in Mg-doped p-type GaN" *Appl. Phys. Lett.* 68, 1883 (1996).

[94] M. D. Bremser, W. G. Perry, T. Zheleva, N. V. Edwards, O. H. Nam, N. Parikh, D. E. Aspnes, and R. F. Davis, "Growth, doping and characterization of $Al_xGa_{1-X}N$ thin film alloys on 6H-SiC(0001) substrates", MRS Internet J. Nitride Semicond. Res. 1, 8 (1996).

[95] M. D. Bremser, W. G. Perry, N. V. Edwards, T. Zheleva, N. Parikh, D. E. Aspnes, and R. F. Davis, "Growth and doping of $Al_xGa_{1-x}N$ deposited directly on α(6H)-SiC(0001) substrates via organometallic vapor phase epitaxy", Mat. Res. Soc. Symp. Proc. 395, 195 (1996).

[96] L. Chernyak, B. William, O. Lopatiuk, and M. Eickhoff, "Studies of electron trapping in III-Nitrides", *Proc. Electrochem. Soc.* 6, 512 (2004).

[97] M. Johnson, Associate Professor, NC State University, Materials Science and Engineering, *Personal E-mal Communication*, October 24, 2007.

[98] S. Yoshida, S. Misawa, and S. Gonda, "Properties of $Al_xGa_{1-x}N$ films prepared by reactive molecular beam epitaxy", *J. Appl. Phys.* 53, 6844 (1982).

[99] D. K. Wickenden, C. B. Bargeon, W. A. Bryden, J. Miragliova, T. J. Kistenmacher, "High quality self-nucleated $AlxGa_{1-x}$ N layers on (00.1) sapphire by low-pressure metalorganic chemical vapor deposition", *Appl. Phys. Lett.* 65, 2024 (1994).

[100] S. R. Lee, A. F. Wright, M. H. Crawford, G. A. Petersen, J. Han, and R. M. Biefeld, "The band-gap bowing of AlxGa1-xN alloys", *Appl. Phys. Lett.* 74, 3344 (1999).

[101] H. Angerer, D. Brunner, F. Freudenberg, O. Ambacher, M. Stutzmann, R. Hopler, T. Metzer, E. Born, G. Dollinger, A. Bergmaier, S. Karsh, and H. J. Korner, "Determination of the Al mole fraction and the band gap bowing of epitaxial $Al_xGa_{1-x}N$ films", *Appl. Phys. Lett.* 71, 1504 (1997).

[102] W. W. Lin, and Y. K. Kuo, "Band structures and bandgap bowing parameters of wurtzite and zincblend III-nitrides", *Proc. SPIE* 4913, 236 (2002).

[103] M. R. H. Khan, Y. Koide, H. Itoh, N. Sawaki, and I. Akasaki, "Edge Emission of $Al_xGa_{1-x}N$", *Solid State Commun.* 6, 509 (1986).
[104] J. Neugebauer, and C. G. Van de Walle," Hydrogen in GaN: novel aspects of a common impurity", *Phys. Rev. Lett.* 75, 4452 (1995).

[105] Y. Okamoto, M. Saito, and A. Oshiyama, "First-principles calculations on Mg impurity and Mg-H complex in GaN", *Jpn. J. Appl. Phys*. 35, L807 (1996).

[106] A. Y. Polyakov, N. B. Smirnov, A. V. Govorkov, K. H. Baik, S. J. Pearton, B. Luo, F. Ren, and J. M. Zavada, "Effects of hydrogen plasma treatment on electrical properties of p-AlGaN", *J. Vac. Sci. Technol. B Microelectron. Nanometer. Struct. B* 22, 2, 771-775 (2004).

[107] W. Kim, A. Salvador, A. E. Botchkarev, Ö. Aktas, S. N. Mohammad, H. Morkoç, "Mg-doped p-type GaN grown by reactive molecular beam epitaxy", *Appl. Phys. Lett.* 69, 559 (1996).

[108] H. Amano, M. Kito, K. Hiramatsu, I. Akasaki, "P-Type Conduction in Mg-Doped GaN Treated with Low-Energy Electron Beam Irradiation (LEEBI)", *Jpn. J. Appl. Phys.* 28, L2112 (1989).

[109] S. Nakamura, T. Mukai, M. Senoh, "High-Power GaN P-N Junction Blue-Light-Emitting Diodes", *Jpn. J. Appl. Phys*. 30, L1998 (1991).

[110] Y. Nakano, O. Fujishima, and T. Kachi, "High-temperature annealing behavior of p-type doping characteristics in Mg-doped GaN", *J. Electrochem. Soc.* 151**,** G574-G577 (2004).

[111] W. Götz, N. M. Johnson, N. M. Chen, H. Liu, C. Kuo, and W. Imler, "Activation energies of Si donors in GaN", *Appl. Phys. Lett*. 68, 3114 (1996).

[112] J. Li, T. N. Oder, M. L. Nakami, J. Y. Lin, and H. X. Jiang, "Optical and electrical properties of Mg-doped p-type $Al_xGa_{1-x}N$", *Appl. Phys. Lett.* 80, 1210 (2002).

[113] Y. Hongbo, E. Erkin, and E. Ozbay, "MOCVD growth and electrical studies of p-type AlGaN with AL fraction 0.35", *J. Crys. Grow.* 289, 419 (2006).

[114] C. G. Moe, H. Masui, C. M. C. Shmidt, L. Shen, B. Moran, S. Newman, K. Vampola, T. Mates, S. Keller, J. S. Speck, S. P. DenBaars, C. Hussel, and D. Emerson, "Milliwatt Power Deep Ultraviolet Light Emitting Diodes Grown on Silicon Carbide", *Jpn. J. Appl. Phys.* 44, 17, L502 (2005).

[115] M. L. Nakarmi, K. H. Kim, M. Khizar, Z. Y. Fan, J. Y. Lin, and H. X. Jiang, "Electrical and optical properties of Mg-doped $Al_{0.7}Ga_{0.3}N$ alloys", *Appl. Phys. Lett.* 86, 092108 (2005).

[116] X. D. Chen, Y. Huang, S. Fung, C. D. Beling, C. C. Ling, J. K. Sheu. M. L. Lee, G. C. Chi, and S. J Chang, "Deep level defect in Si-implanted GaNn^{+}-p junction", *Appl. Phys. Lett.* 82, 3671 (2003).

[117] O. Breitenstein, "DTLS Manual", Max Planck Institute of Microstructure Physics, Weinberg, Germany, (May 2003). Available: http://www.mpi-halle.mpg.de/coffeeseminar/dlts/ (Jan. 31st, 2009).

[118] P. Hacke, T. Detchprohm, K. Hiramatsu, N. Sasaki, "Analysis of deep levels in *n*-type GaN by transient capacitance methods", *J. Appl. Phys.* 76, 304 (1994).

[119] W. Götz, N. M. Johnson, H. Amano, and N. Akasaki, "Deep level defects in *n*-type GaN", *Appl. Phys. Lett.* 65, 463 (1994).

[120] W. I. Lee, T. C. Hunag, J. D. Guo, and M. S. Feng, "Effects of column III alkyl sources on deep levels in GaN grown by organometallic vapor phase epitaxy", *Appl. Phys. Lett. 67*, 1721 (1995).

[121] J. M. Martin, S. Garcia, I. Martil, G. Gonzalez-Diaz, E. Castan, and S. Duenas, "Deep-level transient spectroscopy and electrical characterization of ion-implanted *p-n* junctions into undoped InP", *J. Appl. Phys.* 78 (9), 5325 (1995).

[122] Q. S. Zhu, H. Nagai, Y. Kawaguchi, K. Hiramatsu, and N. Sawaki, "Effect of thermal annealing on hole trap levels in Mg-doped GaN grown by MOVPE", *J. Vac. Sci. Technol*. A 18(1), 261, Jan/Feb 2000

[123] M. J. Legodi, S. S. Hullavarad, S. A. Goodman, M. Hayes, and F. D. Auret,"Defect characterization by DLTS of AlGaN-UV Schottky photodetectors", *Physica B & C* 308, 1189-1192 (2002).

[124] T. Mizutani, T. Okino, K. Kawada, Y. Ohno, S. Kishimoto, and K. Maezawa,"Drain current DLTS of AlGaN/GaN HEMTs", *Phys. Stat. Sol. (a)* 200, 1, 195–198 (2003).

[125] D. Seghier, and H. P. Gislason, "Dx-like defects in AlGaN/GaN structures by means of noise spectroscopy", *Mater. Sci. Semicond. Process*. 9, 1, 41-44 (2006).

[126] D. Seghier, and H. P. Gislason, "Shallow and deep defects in $Al_xGa_{1-x}N$ structures", *Physica B* 401-402, 335-338 (2007).

[127] W. Gotz, N. M. Johnson, M. D. Bremser, and R. F. Davis, “A donorlike deep level defect in $Al_{0.12}Ga_{0.88}N$ characterized by capacitance transient spectroscopies”, *Appl. Phys. Lett.* 69, 2379 (1996).

[128] X. Z. Dang, C. D. Wang. E. T. Yu, K. S. Boutros, J. M. Redwing, “Persistent photoconductivity and defect levels in *n*-type AlGaN/GaN heterostructures”, *Appl. Phys. Lett.* 72, 2745 (1998).

[129] J. Kikawa, K. Imada, T. Yamada, T. Tsuchiya, Y. Hiroyama, M. Iwami, T. Araki, A. Suzuki, and Y. Nanishi, “Al mole fraction dependence of deep levels in AlGaN/GaN-HEMT structures estimated by CV profiling”, *Mater. Res. Soc. Symp. Proc.* 892, 195-202 (2006).

[130] E. F. Schubert, W. Grieshaber, and I. D. Goepfert, “Enhancement of deep acceptor activation in semiconductors by superlattice doping”, *Appl. Phys. Lett.* 69, 3737 (1996).

[131] G. Jaffé, “Theory of Conductivity of Semiconductors”, *Phys. Rev*. 85, 2, 354-363 (1952).

[132] R. S. Muller, and T. I. Kamins, with Mansun C., “Metal-Semiconductor Contacts”, Device Electronics for Integrated Circuits, 3rd Ed., John Wiley & Sons, Inc., New York, NY, 139-170 (2003).

[133] K. F. Brennan, “Junctions”, The Physics of Semiconductors, Cambridge University Press, Cambridge, UK, 544-606 (1999).

[134] D. W. Kim, and H. K. Baik, “Current conduction mechanism of Si/Ti-based ohmic contacts to n-GaN”, *App. Phys. Lett.* 77, p. 1011 (2000).

[135] B. Van Zeghbroeck, “Electrostatic Analysis”, Physics of Semiconductor Devices, http://ece-www.colorado.edu/~bart/book/book/title.htm (2004).

[136] E. H. Rhoderick and R. H. Williams, Metal-Semiconductor Contacts, 2nd Ed., Clarendon Press, Oxford, UK, 1-48 (1988).

[137] L. Pauling, *J. Am. Chem. Soc.* 54, 3570 (1932).

[138] L. Pauling, The Nature of the Chemical Bonds, 3rd Ed., Cornell University Press, Ithaca (1960).

[139] H. B. Michaelson, *J. Appl. Phys.* 48, 4729 (1977).

[140] V. Bougrov , M. E. Levinshtein, S. L. Rumyantsev, A. Zubrilov, Properties of Advanced SemiconductorMaterials GaN, AlN, InN, BN, SiC, SiGe . Eds. Levinshtein M.E., Rumyantsev S.L., Shur M.S., John Wiley & Sons, Inc., New York, 1-30 (2001).

[141] T. P Chow, Ghezzo, "SiC power devices", III-Nitride, SiC, and Diamond Materials for Electronic Devices, Eds. Gaskill D.K, Brandt C.D. and Nemanich R.J., *Material Research Society Symposium Proceedings,* Pittsburgh, PA. **423** 69-73 (1996).

[142] B. Monemar, J.P. Bergman, H. Amano, I. Akasaki, T. Detchprohm, K. Hiramatsu, N. Sawaki, *International Symposium on Blue Laser and Light Emiting Diodes*, Chiba University, Japan, March 5-7 (1996).

[143] J. S. Foresi, T.D Moustakas, "Metal contacts to gallium nitride", *Appl. Phys. Lett.* 62, 22 (1993).

[144] S. Nakamura, M. Senoh, S. Nagahama, N. Iwasa, T. Yamada, T. Matsushita, H. Kihoku, Y. Sugimoto , *Japanese Journ. Appl. Physics Part 2*, 35, L74 (1996).

[145] S. Nakamura, T. Mukai, M.Senoh, "Candela-class high-brightness InGaN/AlGaN double-heterostructure blue-light-emitting diodes", *Applied Physics Lett.* 64, 1687 (1994).

[146] J. M. DeLucca *et al.,* "Ohmic contacts formed by electro deposition and physical vapor deposition on p-GaN", *Applied Physics Letters* 73, 23 (1998).

[147] J. K. Ho, C. Jong, C. C. Chien, C. N. Huang, K. K. Shih, L. Chen, F. R. Chen, J. J. Kai, "Low resistance ohmic contacts to p-type GaN achieved by oxidation of Ni/Au films", *Journ. Appl. Phys.* 86, 8, 4491-4497 (1999).

[148] Y. J. Lin, "Electrical properties of Ni/Au and au contacts on p-type GaN", *Journ. Vac. Schi. Technol.* B 23,1 (2005).

[149] S. H. Wang and S. E. Mohney, and R. Birkhahn, "Environmental and thermal aging of Au/Ni/p-GaN ohmic contacts annealed in air", *Journ. Appl. Phys*. 91, 6, 3711-3716 (2002).

[150] K. N. Patel, Non-linear current-voltage modeling based on the Circular Transmission Line Model (CTLM) of p-type and n-type Gallium Nitride in novel quantum dot light emitting diodes, *Master's Thesis*, Univ. NC Charlotte (Fall 2007).

[151] J. G. Pagan, "Quantum dot light emitting diode", *Doctoral Dissertation*, Univ. NC-Charlotte (2006).

[152] A. P. Zhang, B. Lou, J.W. Johnson, F. Ren, J. Han, S .J. Pearton, "Role of annealing conditions and surface treatment on ohmi contacts to p-GaN and P-AlGaN/GaN superlattices", *App. Phys. Lett.*, 79, 22, 3636-3638 (2001).

[153] L. C. Chen, J. K. Ho, C. S. Jong, C. C. Chiu, K. K. Shih, F. F. Chen, J. J. Kai, L. Chang' "Oxidized Ni/Pt and Ni/Au ohmic contacts to p-type GaN", *App. Phys. Lett.* 76, 25, 3703-3705 (2000).

[154] D. Qiao, L.S. yu, S. S. Lau, J.Y Lin, H. X. Jiang, H. C. Chang, *Appl. Phys. Lett.*, 88, 4196 (2000).

[155] Y. Koide, H. Ishikawa, S. Kobayashi, S. Yamasaki, S. Ngai, J. Umezaki, M. Koike, M. Murakami, "Dependence of electrical properties on work functions of metals contacting to p-type GaN", *Applied Surface Science*, 117/118, 373-379, (1997).

[156] Y. J. Lin, "Electrical properties of Ni/Au and au contacts on p-type GaN", *Journ. Vac. Schi. Technol. B* 23,1 (2005).

[157] I. M. Chan, T. Y. Hsu, and F. C. Hong, "Enhanced hole injections in organic light-emitting devices by depositing nickel oxide on indium tin oxide anode", *Appl. Phys. Lett.* 81, 1899 (2002).

[158] S. P. Mitoff, "Electrical conductivity and thermodynamic equilibrium in nickel oxide", *J. Chem. Phys.* 35, 882 (1961).

[159] B. Sasi, K. G. Gopchandran, P. K. Manoj, P. Koshy, P. Prabhakara Rao, and V. K. Vaidyan, "Preparation of transparent and semiconducting NiO films", *Vacuum* 68, 2, 149-154 (2002).

[160] B. Sasi, and K. G. Gopchandran, "Nanostructured mesoporous nickel oxide thin films", *Nanotechnology* 18, 115613-115622 (2007).

[161] C. Y. Hu, Z. X. Qin, Z. Z. Chen, H. Yang, K. Wu, Q. Wang, Z. J. Yang, T. J. Yu, X. D. Hu, G. Y. Zhang, "Microstructure evolution of oxidized Ni/Au ohmic contacts to p-GaN studied by X-ray diffraction," *Mat. Sci. in Semiconductor Processing*, 8, 515-519. (2005).

[162] B. Liu, E. Lambers, W. B. Alexander, P. H. Holloway, "Effects of a Ni cap layer on transparent Ni/Au ohmic contacts to p-GaN," J. *Vac. Sci. Technol. B* 20 (4) (2002).

[163] T. Maeda, Y. Koide, and M. Murakami, *Appl. Phys. Lett.* 75, 4145 (1999).

[164] J. C. Jan, K. Asokan, J. W. Chiou, W. F. Pong, P. K. Tseng, M. H. Tsai, Y. Chen, F. R. Chen, and J. K. Ho, *Appl. Phys. Lett.* 78, 2718 (2001).

[165] H. W. Jang, J. K. Kim, S. Y. Kim. H. K. Yu, and J. L. Lee, "Ohmic contacts for high power LEDs", *Phys. Status Solidi a* 201, 2831 (2004).

[166] B. A. Hull, S. E. Mohney, U. Chowdhary, and R. D. Dupuis, "Ohmic contacts to p-type $Al_{0.45}GaN_{0.55}N$", *J. Appl. Phys.* 96, 7325 (2004).

[167] C. S. Lee, Y. J. Lin, and C. T. Lee, "Mechanism investigation of NiOx in Au/Ni/p-type GaN Ohmic contacts annealed in air", *Appl. Phys. Lett* 79, 3815 (2001).

[168] B. H. Jun, H. Hirayama, and Y. Aoyagi, "Nonalloyed Ohmic formation for p-type AlGaN with p-type GaN capping layers using Ohmic resessed technique", *Japan J. Appl. Phys.* 41, 581 (2002).

[169] T. V. Blank, Y. A. Goldberg, E. V. Kalinina, O. V. Konstantinov, A. E. Nikolaev, A. V. Fomin, and A. E. Cherenkov, "Mechanism of the current flow in Pd-(Heavily doped p-$Al_xGa_{1-x}N$) Ohmic contact", *Semiconductors* 35, 529 (2001).

[170] H. K. Kim, T. Y. Seong, I. Adesida, C. W. Tang, and K. M. Lau, "Low-resistance Pt/Pd/Au Ohmic contacts to p-type AlGaN", *Appl. Phys. Lett.* 84, 10, 1710-1712 (2004).

[171] Y. J. Lin, and Y. L. Chu, "Effects of the thickness of capping layers on electrical properties of Ni Ohmic contacts to p-AlGaN and p-GaN using Ohmic recessed technique, *Semicond. Sci. Technol.* 21, 1172-1175 (2006).

[172] Th. Gessmann, Y. L. Li, E. L. Waldron, J. W. Graff, E. F. Schubert, and J. K. Sheu, "Novel type of Ohmic contacts to p-doped GaN using polarization fields in thin $In_xGa_{1-x}N$ capping layers", *J. Electron. Mater.* 31, 416 (2002).

[173] Th. Gessmann, Y. L. Li, E. L. Waldron, J. W. Graff, E. F. Schubert, and J. K. Sheu, "Ohmic contacts to p-type GaN mediated by polarization fields in thin $In_xGa_{1-x}N$ cap-layers ", *Appl. Phys. Lett.* 80, 986-988 (2002).

[174] Th. Gessmann, J. W. Graff, Y. L. Li, Waldron E. L., and E. F. Schubert, "Ohmic contact technology in III nitrides using polarization effects of cap layers", *J. Appl. Phys.* 92, 3740 (2002).

[175] K. Kumakura, T. Makimoto, and N. Kobayashi, "Ohmic contact to p-GaN using a strained InGaN contact layer and its thermal stability", *Japan J. Appl. Phys.* 42, 2254 (2003).

[176] M. E. Lin, Z. Ma, F. Y. Huang, Z. Fan, L. H. Allen, and H. Morkoç, "Low resistance ohmic contacts on wide band-gap GaN", *Appl. Phys. Lett.* 64, 1003 (1994).

[177] Y. J. Lin, "Hole-transport barrier and band bending at the indium tin oxide/polymer/p-AlGaN interface", *Appl. Phys. Lett.* 89, 152121 (2006).

[178] Y. Cao, G. Y. Zhang, R. Menon, and A. J. Heeger, "Polymer light emitting diodes with polyethylene dioxythiophene polystyren sulfonate as the transparent anode", *Synth. Met.* 87, 171 (1997).

[179] J. C. Scott, S. A. Carter, S. Karg, and M. Angelopoulos, “Polymeric anodes for organic light-emitting diodes”, *Synth. Met.* 85, 1197 (1997).

[180] W. R. Salaneck, M. Lögdlund, M. Fahlman, G. Greczynski, and T. Kluger, “The electronic structure of polymer-metal interfaces studied by Ultraviolet Photoelectron Spectroscopy”, *Mater. Sci. Eng.* R. 34, 121 (2001).

[181] J. Neugebauer, and C. G. Van de Walle, “Gallium vacancies and the yellow luminescence in GaN”, *Appl. Phys. Lett.* 69, 503 (1996).

[182] S. E. Mohney, and X. Lin, *J. Electron. Mater.* 25, 811 (1996).

[183] D. W. Jenkins, J. D. Dow, and M. H. Tsai, “N vacancies in $Al_xGa_{1-x}N$”, *J. Appl. Phys.* 72, 4130 (1992).

[184] L. Chen, F. Chen, J. J. Kai, L. Chang, J. K. Ho, C. S Jong, C. Chiu, C. N Huang, C. Y Chen, “Microstructural investigation of oxidized Ni/Au ohmic contact to p-type GaN”, *J. Appl. Phys.* 86, 7, 3826-3832 (1999).

[185] Q. Z. Liu, S. S. Lau, “Review of the metal-GaN contact technology”, *Solid State Electronics* 42, 5, 677-691 (1998).

[186] S. J. Pearton, J. C Zolper, R. J. Shul, F. Ren, “ GaN: Processing, defects and devices,” Applied physics reviews, *J. Appl. Phys.* 86, 1, 1-78 (1999).

[187] A. Vertiatchikh, E. Kaminsky, J. Teetsov, and K. Robinson, “Structural properties of alloyes Ti/Al/Ti/Au and Ti/Al/Mo/Au Ohmic contacts to AlGaN/GaN”, *Solid-State Electronics* 50, 1425-1429 (2006).

[188] Y. Sun, and L. F. Eastman, “Low-resistance Ohmic contacts developed on undoped AlGaN/GaN-based high electron mobility transistors with AlN interlayer”, *J. Vac. Sci. Technol. B* 24 (6), 2723-2725 (2006).

[189] S. Kaciulis, L. Pandolfi, S. Viticoli, M. Peroni, and A. Passaseo, “Characterization of Ohmic contacts on GaN/AlGaN heterostructures”, *Applied Surface Science* 253, 1055-1064 (2006).

[190] A. N. Bright, P. J. Thomas, M. Weyland, D. M. Tricker, C. J. Humphreys, and R. Davies, “Correlation of contact resistance with microstructure for Au/Ni/Al/Ti/AlGaN/GaN ohmic contacts using transmission electron microscopy”, *J. Appl. Phys.* 89, 3143 (2001).

[191] R. C. Fitch, J. K. Gillespie, N. Moser, G. Jessen, T. Jenkins, R. Dettmer, D.Via, A. Crespo, A. M. Dabiran, P. P. Chow, A. Osinsky, J. R. La Roche, F. Ren, and S. J. Pearton, "Comparison of Ir and Ni-based Ohmic contacts for AlGaN/GaN high electron mobility transistors", *J. Vac. Sci. Technol.* B 22, 2, 619-623 (2004).

[192] R. C. Glass, L. M. Spellman, and R. F. Davis, "Low energy ion-assisted deposition of titanium nitride ohmic contacts on alpha (6H)-silicon carbide", *Appl. Phys. Lett*. 59, 2868-2870 (1991).

[193] F. M. Mohammed, L. Wang, L. Adesida, and E. Piner, "The Role of barrier layer on Ohmic performance of Ti/Al-based contact metallizations on AlGaN/GaN heterostructures", *J. Appl. Phys.* 100, 23708 (2006).

[194] Z. Fan, S. N. Mohammad, W. Kim, Ö. Aktas, A. E. Botchkarev, and H. Morkoç, "Very low resistance multilayer Ohmic contact to *n*-GaN", *Appl. Phys. Lett.* 68, 1672 (1996).

[195] D. F. Wang, F. Shiwei, C. Lu, A. Motayed, M. Jah, S. N. Mohammad, K. A. Jones, and L. S. Riba, "Low-resistance Ti/Al/Ti/Ay multilayer Ohmic contact to n-GaN", *J. Appl. Phys.* 89, 6214 (2001)

[196] E. F. Chor, D. Zhang, H. Gong, G. L. Chen, and T. Y. F. Liew, "Electrical characterization and metallurgical analysis of Pd-containing multilayer contacts on GaN", *J. Appl. Phys.* 90, 1242 (2001).

[197] S. J. Cai, R. Li, Y. L. Chen, L. Wong, W. G. Wu, S. G. Thomas, and K. L. Wang, "High performance AlGaN/GaN HEMT with improved Ohmic contacts", *Electron. Lett.* 34, 2354 (1998).

[198] V. Kumar, L. Zhou, D. Selvanathan, and I. Adesida, "Thermally-stable low-resistance Ti/Al/Mo/Au multilayer Ohmic contacts on n-GaN", *J. Appl. Phys.* 92, 1712 (2002).

[199] V. Reddy, S. H. Kim, and T. Y. Seong,"electrical and structural properties of low-resistance Ti/Al/Re/Au Ohmic contacts to n-type GaN", *J. Electron. Mater.* 33, 395 (2004).

[200] R. C. Fitch, J. K. Gillespie, N. Moser, T. Jenkins, J. Sewell, D. Via, A. Crespo, A. M. Dabiran, P. P. Chow, A. Osinsky, J. R. La Roche, F. Ren, and S. J. Pearton, "Properties of Ir-based Ohmic contacts to AlGaN/GaN high electron mobility transistors", *Appl. Phys. Lett.* 84, 1485 (2004).

[201] T. Nakayama, H. Miyamoto, Y. Ando, Y Okamoto, T. Inoue, K. Hataya, and M. Kuzuhara, "Low-contact-resistance and smooth-surface Ti/Al/Nb/Au ohmic electrode on AlGaN/GaN heterostructure" *Appl. Phys. Lett.* 85, 3775 (2004).

[202] D. Mistele, F. Fedler, H. Klausing, T. Rotter, J. Stemmer, O. K. Semchinova, and J. Aderhold, " Investigation of Ni/Au contacts on p-GaN annealed in different atmospheres", *Journ. Crystal Growth* 230, 564-568 (2001).

[203] K. Nishizono, M. Okada, M. Kamei, D. Kikuta, K. Tominaga, Y. Ohno, and J. P. Ao, "Metal/Al-doped ZnO Ohmic contact for AlGaN/GaN high electron mobility transistor", *Appl. Phys. Lett.* 84, 3996 (2004).

[204] D. Selvanathan, F. M. Mohammed, J. O. Bae, I. Adesida, and K. H. A. Bogart, "Investigation of surface treatment schemes on n-type GaN and Al0.20Ga0.80N", *J. Vac. Sci. Technol. B*, 23, 6, 2538-2544 (2005).

[205] J. K. Kim, J. L. Lee, J. W. Lee, H. E. Shin, Y. J. Park, and T. Kim, "Low resistance Pd/Au Ohmic contacts to p-GaN using surface treatment", *Appl. Phys. Lett.* 73, 2953 (1998).

[206] J. K. Kim, J. L. Lee, J. W. Lee, Y. J. Park, and T. Kim, "Effect of surface treatment by (NH4)2Sx solution on the reduction of Ohmic contact resistivity of p-type GaN, *J. Vac. Sci.* B 17, 2, 497-499 (1999).

[207] A. P. Zhang, B. Lou, J. W. Johnson, F. Ren, J. Han, S. J. Pearton, " Role of annealing conditions and surface treatment on ohmic contacts to p-GaN and p-AlGaN/GaN superlattices", App. *Phys. Lett.* 79, 22, 3636-3638 (2001).

[208] K. A. Rickert, A. B. Ellis, J. K. Kim, J. L. Lee, F. J. Himpsel, F. Dwikusuma, T. F.Kuech, "X-ray photoemmision determination of the Schottky barrier height of metal contacts on n-GaN and p-GaN", *Journ. Appl. Phys.* 92, 11, 6671-6678 (2002).

[209] A. Motayed, M. Jah, A. Sharma, W. T. Anderson, C. W. Litton, S. N. Mohammad, "Two-step surface treatment technique: realization of nonalloyed low-resistance Ti/Al/Ti/Au Ohmic contact to n-GaN", *J. Vac. Sci. Technol.* B 22, 2, 663-667 (2004).

[210] J. S. Jang, S. J. Park, and T. Y. Seong, "Formation of low resistance Pt Ohmic contacts to p-GaN using two-step surface treatment", *J. Vac. Sci. Technol.* B, 17, 6, 2667-2670 (1999).

[211] I. Cimalia, F. Will, K. Tonisch, M. Niebelschutz, V. Cimalia, V. Lebedev, G. Kittler, M. Himmerlich, S. Krischok, J. A. Schaefer, M. Gebinoga, A. Schober, T. Friedrich, and O. Ambacher, "AlGaN/GaN biosensor – effect of device processing steps on the surface properties and biocompatibility", *Sensors and Actuators B: Chemical* 123, 2, 740-748 (2007).

[212] R. Lui, T. Dai, L. Zhu, H. Pan, K. Xu, B. Zhang, Z. Yang, G. Zhang, Z. Gan, and X. Hu, "The reactive ion etching characteristics of AlGaN/GaN SLx and etch-induced damage study of n-GaN using $Cl_2/SiCl_4$/Ar plasma", *Journal of Crystal Growth* 298, 375-378 (2007).

[213] D. Selvanathan, L. Zhou, V. Kumar, and I. Adesida, "Low resistance Ti/Al/Mo/Au Ohmic contacts for AlGaN/GaN heterostructure field effect transistors", *Phys. Stat. Sol. (a)* 194, No. 2 (2002).

[214] D. Buttari, A. Chini, T. Palacios, R. Coffie, L. Shen, H. Xing, S. Heikman, L. McCarthy, A. Chakraborty, S. Keller, and U. K. Misra, "Origin of etch time in Cl_2 dry etching of AlGaN/GaN structures", *Appl. Phys. Lett.* 83, 4779 (2003).

[215] X. J. Zhou, K. Qiu, C. J. Ji, F. Zhong, X. H. Li, and Y. Q. Wang, "Low-resistance Ohmic contact on undoped AlGaN/GaN heterostructures with surface treatment using CCl_2F_2 reactive ion etching" *Appl. Phys. Lett.* 91, 103511 (2007).

[216] T. C. Shen, G. B. Gao, H. Morkoç, "Recent development in ohmic contacts for III- V compound semiconductors", *J. Vac. Sci. Technol.* B 10, 2113 (1992).

[217] M. E. Lin, Z. Ma, F. Y. Huang, Z. Fan, L. H. Allen, H. Morkoç, "Low resistance Ohmic contacts on wide band-gap GaN", *Appl. Phys. Lett.* 64, 1003 (1994).

[218] W. G. Perry, M. B. Bremser, and R. F. Davis, "Cathodoluminescence studies of deep level emission bands of $Al_xGa_{1-x}N$ films deposited on 6H-SiC(0001)", *J. Appl. Phys.* 83, 1, 469-475 (1998).

[219] S. T. Bradley, S. H. Goss, L. J. Brillson, J. Hwang, and W. Schaff, "Deep level defects and doping in high Al mole fraction AlGaN", *J. Vac. Sci. Technol.* B21, 6, 2558-2563 (2003).

[220] H. Kim, F. J. Faith, and T. G. Anderson, "Unintentional incorporation of B, As, and O impurities in GaN grown by molecular beam epitaxy", J. Electron. Mater. 30, 1343-1347 (2001).

[221] S. J. Ching, B. Karunagaran, C. H. Hong,, H. J. Lee, and E. K. Suh, "Photocurrent spectroscopy investigations of Mg-related defect levels in p-type GaN", J. Korean Phys. Soc. 48, 460-463 (2006).

[222] J. F. Muth, J. H. Lee. I. K. Shmagin, R. M. Kolbas, H. C. Casey Jr., B. P. Keller, U. K. Mishra, and S. P. DenBaars, "Absorption coefficient, energy gap, exciton binding energy, and recombination lifetime on GaN obtained from transmission measurements", *Appl. Phys. Lett.* 71, 2572 (1997).

[223] Z. Z. Bandic, P. M. Bridger, E. C. Piquette, T. C. McGill, "The values of minority carrier diffusion lengths and lifetimes in GaN and their implications for bipolar devices", *Solid-State Electronics* 44, 221 (2000).

[224] H. Watanabe, M. Kato, M. Ichimura, E. Arai, M. Kanechika, O. Ishiguro, and T. Kachi, "Excess carrier lifetime measurement for plasma-etched GaN by the microwave photoconductivity decay method", J. Journ. Appl. Phys. 46, 35, (2007).

APPENDIX A: AUTHOR'S CURRENT LIST OF PUBLICATIONS

P.Batoni, E. B. Stokes, S. F. LeBoeuf, and T. Hohava, "Photocurrent Spectroscopy Investigation of Deep Level Defects in Mg-doped GaN and Mg-doped $Al_xGa_{1-x}N$ (0.20 < x < 0.52)", Appl. Phys. Lett. Pending (Feb. 2009).

J. Li, P. Batoni, and R. Tsu, "Heteroepitaxial 4H-SiC on c-plane sapphire by C60 and Si solid source MBE", Appl. Phys. Lett. Pending (Jan. 2009).

K. N. Patel, E. B. Stokes, J. G. Pagan, C. C. Burkhart, M. D. Hodge, and P. Batoni, "Circular Transmission Line Model (CTML) Analysis for Non-linear VI Characteristics on MBE p-GaN, 212th ECS Meeting Washington DC, October 2007, (2007).

P. Batoni, K. Patel, C. C. Burkhart, T. K. Shah, V. Iyengar, M. T. Ahrens, S. T. Morton, S. M. Bobbio, and E. B. Stokes, "Very Low Pressure Magnetic Reactive Ion Etching of GaN and $Al_xGa_{1-x}N$ Using Dichlorodifluoromethane (Halocarbon 12)", Journal of Electronic Materials (2007).

K. N. Patel, Edward B. Stokes, Jennifer G. Pagan, C. C. Burkhart, M. D. Hodge, and P. Batoni, "Circular Transmission Line Model (CTLM) analysis for non-linear VI characteristics on MBE p-GaN", 212th ECS Meeting in Washington, DC, in October 2007, (2007).

V. Tilak, P. Batoni**,** J. Jiang, and A. Knobloc, "Measurement of Piezoelectric Coefficient of GaN using Metal-Insulator-Semiconductor Capacitors", App. Phys. Lett. 90, 1 (2007).

V. Tilak, P. Batoni, J. Jiang, and A. Knobloc, "AlGaN High Temperature Pressure Sensor", presented at the Materials for Microelectronics and Nanoengineering 2006 conference, Journal of Material Science: Materials in Electronics (2006).

M. D. Hodge, E. B. Stokes, and P. Batoni, "Ionization of Acceptor in Be-Doped $Al_{0.42}Ga_{0.58}N$ with IR Optical Pumping", presented at the 210th ECS Meeting/ XXI Congreso de la Sociedad Mexicana de Electroquimica October 2006, Cancun, Mexico, (2006)

P. Batoni, T. K. Shah, D. M. Hodge, T. J. Suleski, and E. B. Stokes, "Self-induced surface texturing of Al_2O_3 by means of Inductively Coupled Plasma Reactive Ion Etching in Cl_2 chemistry", presented at the Lester Eastman Conference on High Performance Devices August 2006, Cornell University, Ithaca, New York, USA. International Journal of High Speed Electronics and Systems, Vol. XX, No. X (2006 1-4).

T. J. Suleski, Y. Chuang, D. J. Spivey, P. Batoni, and E. B. Stokes. "Nanotexturing in Ultraviolet Light-Emitting Diodes for Enhanced Light Extraction", OSA Journal of the Optical Society of America A (2006).

V. Yang, E. B. Stokes, P. Batoni, and R. A. Hudgins, "Temperature Study of Blue and Green Light Emitting Diodes", ECS Electrochemical and Solid-State Letters (2006).

P. Batoni, K. Patel, C. C. Burkhart, T. K. Shah, V. Iyengar, M. T. Ahrens, S. T. Morton, B. A. Martin, S. M. Bobbio, and E. B. tokes, "Very Low Pressure Magnetic Reactive Ion Etching of GaN Using Dichlorodifluoromethane (Halocarbon 12)", ECS Transactions, v 1, n 2, State-of-the-Art Program on Compound Semiconductors (SOTAPOCS XLIII) -and- Nitride and Wide Bandgap Semiconductors for Sensors, Photonics, and Electronics VI, 2005, p 158-168, (2005)

P. Batoni, E. B. Stokes, S. F. LeBoeuf, N. V. Yang, J. G. Pagan, and. R. A. Hudgins, "Enhanced UV Emission by Means of Infrared Optical Pumping in UV Light Emitting Diodes", ECS Transactions, v 1, n 2, State-of-the-Art Program on Compound Semiconductors (SOTAPOCS XLIII) -and- Nitride and Wide Bandgap Semiconductors for Sensors, Photonics, and Electronics VI, 2005, p 202-207, (2005)

P. Batoni, K. Patel, C. C. Burkhart, T. K. Shah, V. Iyengar, M. T. Ahrens, S. T. Morton, B. A. Martin, S. M. Bobbio, and E. B. Stokes, "Very Low Pressure Magnetic Reactive Ion Etching of GaN Using Dichlorodifluoromethane (Halocarbon 12)", Meeting Abstracts, v MA 2005-02, 208th Meeting of The Electrochemical Society - Meeting Abstracts, 2005, p 1570, (2005)

P. Batoni, E. B. Stokes, S. F. LeBoeuf, N. V. Yang, J. G. Pagan, and. R. A. Hudgins, "Enhanced UV Emission by Means of Infrared Optical Pumping in UV Light Emitting Diodes", Meeting Abstracts, v MA 2005-02, 208th Meeting of The Electrochemical Society - Meeting Abstracts, 2005, p 1575, (2005).